

UNIVERSITY OF CRETE

DOCTORAL THESIS

---

# Dynamics of field-induced phases in spin-1 antiferromagnetic chains

---

*Author:*  
Christina PSAROUDAKI

*Supervisor:*  
Prof. Dr. Xenophon ZOTOS  
*Co-supervisor:*  
Prof. Dr. Nikos Papanicolaou

*A thesis submitted in fulfilment of the requirements  
for the degree of Doctor of Philosophy*

*in the*

December 17, 2014



UNIVERSITY OF CRETE

# *Abstract*

Department of Physics

Doctor of Philosophy

## **Dynamics of field-induced phases in spin-1 antiferromagnetic chains**

by Christina PSAROUDAKI

This thesis is devoted to the study of a class of antiferromagnetic spin-1 chains with a strong easy plane anisotropy in the presence of magnetic field  $H$ . At zero temperature the system undergoes two quantum phase transitions at critical fields  $H_1$  and  $H_2$ . Reliable and detailed theoretical analysis is provided on the Electron Spin Resonance (ESR) spectrum, thermodynamics and the thermal transport of the model. The tools at hand range from exact analytical solutions and to numerical simulation techniques. The  $S = 1$  antiferromagnet in a magnetic field can be systematically mapped onto an  $S = 1/2$   $XXZ$  chain in a longitudinal magnetic field. This effective  $S = 1/2$  description has been extensively used in order to gain a better physical understanding of the original  $S = 1$  chain.

For the Electron Spin Resonance spectrum, apart from the theoretical analysis, high-field ESR experimental studies of the compound  $NiCl_2 - 4SC(NH_2)_2$  (abbreviated as DTN) are presented and found consistent with theoretical predictions. The most interesting feature is the experimental signature of the single-ion two-magnon bound state.

Part of this thesis is devoted to the magnetic-field and temperature dependence of magnetization and specific heat for the whole field-region and a wide range of temperatures, with special emphasis at the critical behaviour of these quantities at the critical fields. Finally, the calculation of dynamic correlation functions pertinent to the study of thermal transport is addressed for the  $S = 1$  model with easy plane anisotropy and the  $S = 1/2$   $XXZ$  model in the presence of finite magnetic field.

# *Acknowledgements*

It is a pleasant task to express my gratitude to all those who contributed in many ways to the success of this study and made this thesis possible. First and foremost, I am thankful to my PhD supervisors, Professors Nikos Papanicolaou and Xenophon Zotos, for unconditionally supporting me during all these years. In particular, I gratefully acknowledge Prof. Papanicolaou for his patience, help, genuine caring, concern and faith in me. He has been supportive, motivating, encouraging and for this I cannot thank him enough. I am also thankful to Prof. Zotos for his contributions of time, ideas and guidance to make my Ph.D. experience possible and productive.

My gratitude is also extended to Dr. Sergei Zvyagin, not only for serving as my committee member, but primarily for our wonderful collaboration and his hospitality during my visit to the National High Magnetic Field Laboratory in Tallahassee. Also, I take this opportunity to sincerely acknowledge the members of the Physics department of University of Crete.

Also, I am indebted to many student colleagues for providing a stimulating and fun filled environment. In particular many thanks go to Dr. Yiannis Iatrakis, who has always been a tremendous help no matter the task, Dr. Alexandros Metavitsiadis and Dr. Yiannis Constantinou. I also thank my friends for providing the support and friendship that I needed. To include them all is an impossible task. Of course no acknowledgements would be complete without giving thanks to family. My mother and sister deserve special mention here for their constant support and sincere encouragement.

This work was funded by the Marie Curie Initial Training Network LOTHERM Project (FP7-238475).

# Contents

|  |            |
|--|------------|
| <b>Abstract</b>  | <b>i</b>   |
| <b>Acknowledgements</b>  | <b>ii</b>  |
| <b>Contents</b>  | <b>iii</b> |
| <b>Introduction</b>  | <b>1</b>   |
| <b>1 Quantum Spin-1 Chains</b>                                   | <b>6</b>   |
| 1.1 Haldane Phase  | 7          |
| 1.2 Easy plane anisotropy  | 11         |
| 1.2.1 Microscopic origin   | 12         |
| 1.2.2 Phase Transitions  | 13         |
| 1.3 Large - D Limit  | 14         |
| 1.3.1 Field-induced quantum phase transitions                    | 16         |
| 1.3.2 Excitations in the Paramagnetic Phase                      | 20         |
| 1.3.3 Excitations in the Fully Ferromagnetic Phase               | 26         |
| 1.4 Three Dimensional Model                                      | 30         |
| 1.5 Effective $S=1/2$ description of the $S=1$ chain             | 32         |
| <b>2 Electron Spin Resonance</b>                                 | <b>37</b>  |
| 2.1 Resonance Theory   | 38         |
| 2.2 ESR studies for the AFM $S = 1$ chain with strong anisotropy | 42         |
| 2.2.1 One-Dimensional ESR spectrum                               | 42         |
| 2.2.2 Numerical Calculation of the Power Absorption              | 48         |
| 2.2.3 Three-Dimensional ESR spectrum                             | 53         |
| 2.3 Application to DTN: Experimental Data                        | 54         |
| 2.4 ESR studies for the effective $S=1/2$ Hamiltonian            | 63         |
| 2.5 Discussion   | 66         |
| <b>3 Thermodynamics</b>  | <b>68</b>  |
| 3.0.1 $S = 1$ chain with strong anisotropy                       | 68         |
| 3.0.2 Effective $S = 1/2$ chain                                  | 69         |
| 3.1 Magnetization  | 70         |
| 3.2 Specific Heat  | 73         |
| 3.3 Discussion   | 77         |
| <b>4 Thermal Transport</b>                                       | <b>78</b>  |
| 4.1 Transport Theory   | 81         |

|   |   |            |
|---|---|------------|
| 4.2   | Thermal Transport in the $S = 1$ large- $D$ chain . . . . .   | 86         |
| 4.3   | Thermal Transport in the $S = 1/2$ XXZ chain . . . . .  | 90         |
| 4.3.1   | Spin Conductivity . . . . .   | 92         |
| 4.3.2   | Thermal Conductivity . . . . .  | 98         |
| 4.3.3   | Magnetothermal effects . . . . .  | 108        |
| 4.4   | Discussion . . . . .  | 112        |
| <b>Conclusions</b>                                |   | <b>114</b> |
| <b>A Two-magnons bound states in the 3D model</b> |   | <b>117</b> |
| <b>B Analytical Techniques</b>                    |   | <b>126</b> |
| B.1   | ESR spectrum for the $S=1/2$ XXZ chain using the Bethe ansatz technique                               | 126        |
| B.2   | Spin Drude weight for the $S=1/2$ XXZ chain using the Bethe ansatz technique . . . . .                | 129        |
| B.3   | Quantum Transfer Matrix Approach (QTM) . . . . .  | 130        |
| B.4   | Bosonization of the $S=1/2$ chain: Calculation of the Spin Drude weight at zero temperature . . . . . | 136        |
| <b>C Numerical Techniques</b>                     |   | <b>140</b> |
| C.1   | Exact Diagonalization (ED) . . . . .  | 140        |
| C.2   | Finite Temperature Lanczos Method (FTLM) . . . . .  | 141        |
| C.3   | Transfer Matrix Renormalization Group (TMRG) . . . . .  | 143        |
| <b>Bibliography</b>                               |   | <b>145</b> |
| <b>List of Figures</b>                            |   | <b>164</b> |

# Introduction

Quantum magnetism can be traced back more than 90 years ago, when Ising in 1925 [1] and later Bethe in 1931 [2] investigated quantum mechanical one-dimensional models used in the study of magnetic materials. Nevertheless it is still a rapidly developing field producing new phenomena and being at the core of the contemporary research in condensed matter physics.

Magnetic properties arise from electronic spin, whose existence follows directly from relativistic considerations [3]. Possible magnetic interactions between magnetic moments (spins) are recognised to be the key to a microscopic theory describing the majority of phenomena related to magnetism. In general, the term magnetic interaction is used to describe the dependence of the interaction energy of two or more magnetic moments from their relative orientation [4].

The starting point of describing a system of localised magnetic moments, in particular ferromagnetic or antiferromagnetic insulators, is the Heisenberg exchange interaction. The exchange energy is that contribution to the interaction energy of a system of electrons which arises from the use of antisymmetrized wave functions as opposed to single products of one electron wave functions [3]. If Pauli exclusion principle is combined with the usual electrostatic Coulomb interaction between electrons could lead to an effective exchange interaction between the magnetised moments (spins). This effect was discovered simultaneously and independently by Dirac and Heisenberg in 1926. Under certain approximations it may be represented as an effective interaction Hamiltonian of the form:

$$\mathcal{H} = \pm \sum_{i,j} J_{ij} \mathbf{S}_i \cdot \mathbf{S}_j . \quad (0.0.1)$$

The exchange coupling  $J_{ij}$  is determined as a matrix element of the Coulomb interaction between orbital states. Thus the exchange interaction, which is a purely electrostatic effect, may be expressed as a spin–spin interaction. The Hamiltonian of Eq.(0.0.1) was extended to describe interacting ions localised in lattice sites, having more than one unpaired electron. In this case, the interaction is expressed in terms of the total ionic spin. Exchange interactions are usually supplemented by terms describing spin and lattice anisotropies, external fields, spin orbit coupling, etc.

The quantum nature of magnetic models becomes more elevated when one restricts to low dimensional, small spin  $S$  models which are studied at low temperatures. The reduced dimensionality is of high importance, since quantum fluctuations become stronger and lead to fascinating critical phenomena. By applying a magnetic field or exerting pressure on the system, quantum fluctuations can be continuously or discretely tuned across a phase boundary and drive the system to a new collective quantum phase. The point separating these two phases is a quantum critical point (QCP) and the transition across it is a quantum phase transition (QPT). Contrary to thermal phase transitions QPTs occur at zero temperature [5].

A completely different route towards QPT transitions in quantum magnets is represented by the effect of non-magnetic doping. When doping the system with non-magnetic impurities, novel inhomogeneous phases emerge from the interplay between geometric randomness and quantum fluctuations. The system inhomogeneity is found to strongly affect phase transitions. The existence of accessible quantum magnets has provided the possibility to experimentally demonstrate different kinds of quantum phase transitions and quantum critical phenomena.

Apart from the study of the various quantum phases realized in a magnetic system, transport properties of one-dimensional spin systems have also attracted theoretical and experimental interest. This rapidly progressing field has been motivated by the experimental evidence that magnetic excitations can contribute significantly to the thermal conductivity of various quasi-one and two dimensional materials. While the thermodynamic properties of low dimensional quantum magnets have been intensively studied, the transport properties are more challenging for experimental and theoretical physicists. From a theoretical perspective, the principle difficulty lies in the fact that transport theory requires the computation of nontrivial correlation functions.

The only strongly correlated systems for which we have a complete solution of their dynamics are the integrable ones. Exactly because of their integrability, these systems exhibit unconventional ballistic (non-diffusive) thermal transport [6], and many studies have been devoted to the question of whether integrability can stop a current from decaying completely. On the contrary, the theoretical work that has focused on transport properties of nonintegrable models revealed that, within linear response theory, ballistic transport is not realized [7].

From the theoretical point of view the field is extremely broad and the study of dynamical and ground state properties requires a large variety of methods, such as the Bethe ansatz technique for integrable models, quantum field theory approaches and methods of many-body theory, perturbational approaches and many different numerical methods such as exact diagonalization, density matrix renormalization group (DMRG) and Quantum Monte Carlo (QMC) calculations.

The study of magnetic systems is not an exclusively theoretical field. The experimental interest in low-dimensional magnets developed into a field of its own providing a unique possibility to study and verify a rich variety of the properties of quantum models. Magnets in restricted dimensions do have a physical realization since they exist as three dimensional (3D) compounds with exchange interactions much stronger in one or two spatial directions than in the remaining ones. The long-standing research on quantum systems revealed that often, excellent agreement between theoretical predictions and experiments has been found as far as ground-state properties, excitation spectra, thermodynamic or transport properties are concerned. Quantum magnetism has proven to be a successful example for a fruitful interplay between theory and experiment and a vast and varied topic that drives contemporary research, both fundamental and applied.

This thesis is devoted to the study of a class of antiferromagnetic spin-1 chains with a strong easy plane anisotropy in the presence of magnetic field  $H$ . At zero temperature the system undergoes a phase transition at a critical field  $H_1$  above which nonzero spontaneous magnetization develops in the ground state and the spectrum of magnetic excitations becomes gapless. A further transition occurs at a second critical field  $H_2$  above which the ground state is a fully ordered ferromagnetic state. The system can be found in three different quantum phases defined as:

1. A paramagnetic phase for  $H < H_1$  characterized by a singlet ground state and gapped lowest excitations. At  $H_1$  level crossing occurs so that the system enters a new phase through a second order phase transition.
2. An intermediate phase for  $H_1 < H < H_2$  with a ground state that becomes increasingly ferromagnetic while gapless excitations are expected. Magnetization develops in the ground state that ranges from zero to one. At  $H_2$  a second transition occurs.
3. A ferromagnetic phase for  $H > H_2$  where the ground state is a completely ordered ferromagnetic state with a gapped excitation spectrum.

Another framework of these phase transitions is presented if the  $S = 1$  system is thought of as a spin fluid formally described as a gas of hard-core bosons. The Bose gas is populated only above  $H_1$  and the phase transition corresponds to Bose-Einstein condensation in the dilute limit. This phase extends up to  $H_2$  where the system is described as a Mott insulator in the bosonic language. This problem is of obvious theoretical interest since there exist experimental realizations of spin-1 chains with large easy-plane anisotropy, for example the organic compound  $NiCl_2 - SC(NH_2)_2$ , (dichloro-tetrakis thiourea-nickel(II), abbreviated as DTN), that has attracted considerable experimental and theoretical attention [8].

We are in a position to claim reliable theoretical analysis on the Electron Spin Resonance (ESR) spectrum, Thermodynamics and the Thermal Transport of the model. The tools at hand range from exact analytical solutions and to numerical simulation

techniques. In order to familiarize the reader with these techniques, three Appendices are added at the end of this thesis.

This thesis is organized as follows:

- *In Chapter 1:* The main properties of the 1D  $S = 1$  Haldane chain, as well as several approaches concerning the difference between integer and half-integer spin chains, are presented in this chapter. The inclusion of a single ion anisotropy to the Heisenberg Hamiltonian is discussed. We concentrate on the limit of strong anisotropy where the ground state properties and elementary excitations of the paramagnetic phase for  $H < H_1$  and the fully ferromagnetic phase for  $H > H_2$  are calculated. Special emphasis is put on the field-induced quantum phase transitions. A generalisation of the energy-momentum dispersions of the elementary excitations in the presence of three-dimensional couplings is presented.

Finally, we show that the  $S = 1$  Heisenberg AFM with strong easy-plane anisotropy in a magnetic field can be systematically mapped onto an  $S = 1/2$   $XXZ$  Heisenberg model in a longitudinal magnetic field. This mapping enables us to gain a better physical understanding of the original  $S = 1$  model. For all quantities studied in the following chapters, results for both the  $S = 1$  and  $S = 1/2$  model are presented and compared in order to test the effectiveness of the mapping.

- *In Chapter 2:* The chapter begins with a synopsis of the fundamentals of ESR theory. Having established the required basis in Chapter 1, a detailed theoretical study of the ESR spectrum of a  $S = 1$  chain with strong anisotropy is presented. Special emphasis is given on the contribution of a special two-magnon single-ion bound state. A numerical analysis through exact diagonalization and a corresponding simulation of the relevant dynamic susceptibilities provides an additional tool in analyzing important features of the ESR spectrum. Attention is also given to generalize our results including three-dimensional couplings.

In a subsequent section high-field ESR experimental studies of  $NiCl_2-4SC(NH_2)_2$  (DTN) are presented and found consistent with theoretical predictions. Perhaps, the most interesting feature is the experimental signature of the single-ion two-magnon bound state. Furthermore, the theoretical analysis is completed by calculating the low-lying ESR spectrum throughout the intermediate region using the mapping to the effective  $S = 1/2$  model. The chapter closes with general conclusions mostly concentrated on the agreement between theoretical predictions and experimental findings.

- *In Chapter 3:* This chapter is devoted to the calculation of the thermodynamic quantities, such as magnetization  $M$  and the specific heat  $C_v$  for both the  $S = 1$  model using a variety of numerical techniques, and the effective  $S = 1/2$  model. It

is important that this calculation is done for the original Hamiltonian directly in some numerical ways in order to test the validity of the approximations used while performing the mapping. We examine both the magnetic-field and temperature dependence of  $M$  and  $C_v$  for the whole field-region and a wide range of  $T$ , with special emphasis at the critical behaviour of magnetization and specific heat at the critical fields. For all quantities studied here, results for both the  $S = 1$  and  $S = 1/2$  model are presented and compared.

- *In Chapter 4:* In this chapter we address the calculation of dynamic correlation functions pertinent to the study of thermal transport of the  $S = 1$  large- $D$  model and  $S = 1/2$   $XXZ$  model in the presence of finite magnetic field. In the first part, the transport theory is presented within the framework of linear response theory, and relevant issues are discussed. Next, the thermal conductivity of the  $S = 1$  model is presented, as it is calculated using the FTLM method on a chain up to  $L = 16$  sites. The frequency dependence of the conductivity is explored for a wide range of magnetic fields and various temperatures. In addition the  $S = 1/2$   $XXZ$  chain is considered, and the comparison between the two models reveals that the magnetic field dependence of the Drude weight of the effective model includes all characteristic features of the  $S = 1$  low- $\omega$  behaviour.

For the  $S = 1/2$  chain, attention is also given in the magnetic field dependence of the spin Drude weight and the magnetothermal corrections to the thermal conductivity, a term that originates from the coupling of the heat and spin currents in the presence of magnetic field. An analysis on relevant transport experiments can be found in a subsequent section. Finally, two quantities relevant to the magnetothermal effect in spin systems are provided, the magnetic Seebeck coefficient  $S$  and the figure of merit  $ZT$ .

# Chapter 1

## Quantum Spin-1 Chains

Haldane [9] first argued in 1983 that spin- $S$ , one dimensional Heisenberg Antiferromagnets (AFM) have an excitation gap and a finite correlation length for an integer, but not half integer, spin  $S$ . He therefore suggested that there is a fundamental difference between half-integer and integer AFM spin chains, with quantitative implications to the physical properties of each model, which crucially depend on the existence of a gap. His argument was based on a field theoretical treatment of the problem, where he related the large- $S$  AFM to the  $O(3)$  nonlinear sigma model (NL $\sigma$ M) quantum field theory.

Haldane's conjecture challenged the conventional picture originally given by Bethe in his pioneering work [2], where the exact treatment of the  $S = 1/2$  chain predicts a many body ground state, with no gap to the excited states, and with spin correlations that decay slowly as a power law of distance. The spin-wave spectrum for the  $S=1/2$  quantum chain was derived by des Cloizeaux and Pearson [10] in 1962. One has to note that, since the Mermin-Wagner theorem [12] does not allow long range order in one dimension, the power-law correlations correspond to quasi-long-range order and the massless excitations are not true Goldstone bosons [11].

The one-dimensional quantum chain is also different with the picture valid in higher-dimensions, where the behaviour of the AFM Heisenberg chains is given by simple spin-wave theory [13, 14]. Within this theory, two Goldstone modes are predicted, which correspond to the breaking of the  $SO(3)$  symmetry to  $SO(2)$  rotations about the  $z$  axis. The simplest and most studied example of an integer- $S$  chain is the  $S = 1$  AFM spin chain, which has been studied in numerous numerical and analytical works. The mapping of the large- $S$  chain onto the NL $\sigma$ M is not rigorous, and an exact solution of the quantum problem is still missing. Having that in mind, the numerical methods developed so far, have served to establish reliable results about the existence of a finite gap between the singlet ground state and excited states and of a finite correlation length. The main properties of the  $S=1$  chain, as well as several approaches concerning the difference between integer and half-integer spin chains, are presented in the subsequent

subsections. A review of the experiments that confirm the existence of a gap in Haldane chains can be found at the end of this section.

## 1.1 Haldane Phase

The ground state of the one dimensional  $S=1$  Heisenberg chain is a spin singlet, and the lowest excitation is a massive triplet with  $S=1$ . Early numerical calculations [15, 16] based on an exact diagonalization of a finite chain of length up to  $N=12$ , showed that the systems is characterised by nonmagnetic singlet ground state with a nonzero gap and an exponential decay of the spin–correlation functions.

Larger systems of  $N = 32$  became accessible with an efficient Monte Carlo method [17–19]. These studies support Haldane’s prediction that a gap exists in the excitation spectrum for an infinite chain. They suggested a gap of  $\Delta = 0.41J$  at momentum  $\pi$ , and the ground state energy was found equal to  $E_0/NJ = -1.4015$ . At this point a coherent picture was formed with the lowest excitation being a triplet with a dispersion  $E(k) = \Delta + u^2(k - \pi)^2/(2\Delta) + \dots$  and with the next-lowest excitation being the two–magnon continuum beginning at  $E = 2\Delta$  and  $k=0$  [20].

Even though with Monte Carlo methods longer chains can easily be studied, the results have statistical as well as systematic errors with the latter being much more troublesome. Real-space renormalization-group methods have also been applied by White to spin chains [21, 22], which is a substantially better method than Monte Carlo and similar in accuracy with results obtained from exact diagonalization, but one can treat lattices hundreds of sites long. Improved results for the ground-state energy per site of the infinite chain is found to be  $E_0/NJ = -1.401484038971$  and Haldane gap at momentum  $\pi$  was provided,  $\Delta = 0.41050$ . Open-ended  $S = 1$  chains have effective  $S = 1/2$  spins on each end, with exponential decay of the local spin moment away from the ends, with decay length  $\xi = 6.03$ . Many low–lying excited states were found, including one– and two–magnon states, for several different chain lengths. Since the magnons have  $S = 1$ , the two–magnon states are singlets  $S = 0$ , triplets  $S = 1$  and quintuplets  $S = 2$ . For magnons with momenta near  $\pi$ , the magnon–magnon interaction in the triplet channel is shown to be attractive, while in the singlet and quintuplet channels it is repulsive. The above described picture is summarized in Fig. (1.1.2) .

Exact diagonalization technique by the Lanczos method [23] was later used to reach finite chains up to  $N=22$ . The estimated values for the Haldane gap and the ground state energy are close to the ones calculated by White, but a more accurate estimate of the spin-spin correlation function was made possible, which is well fit by  $e^{(-r/\xi)}$ , with  $\xi = 6.2$ . Therefore, the predictions of Haldane about the existence of an excitation gap and a finite correlation length for a  $S = 1$  Heisenberg AFM chain have completely been confirmed by numerical means.

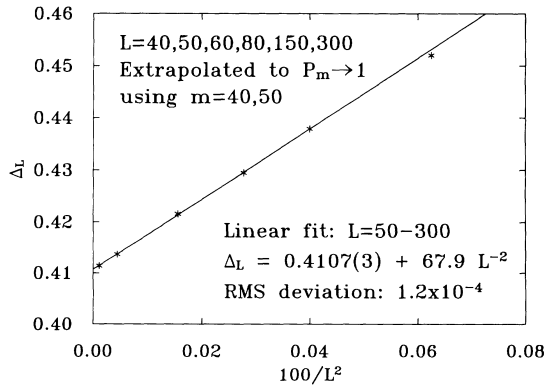


**Figure 1.1.1:** The Haldane gap as a function of lattice size  $L$ , as it has been calculated by the real-space renormalization-group method. The figure is taken from [21].

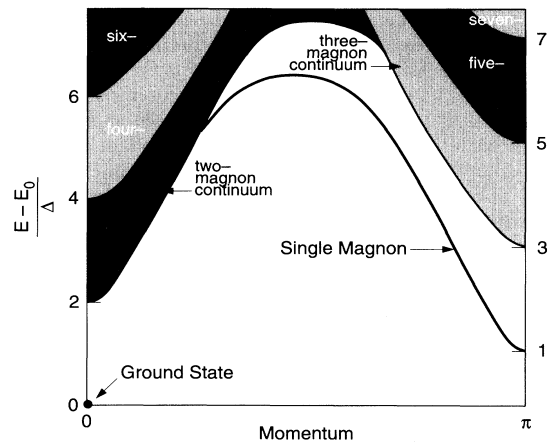


**Figure 1.1.2:** Low-lying states for an infinite  $S=1$  chain. The figure is taken from [22].

**Large- $S$  mapping onto the  $NL\sigma M$ :** At this point, we review some of the basic assumptions made by Haldane in order to map the spin- $S$  chain onto the  $NL\sigma$  Model. For our purposes it is sufficient to survey the most important results obtained without giving details on the exact derivation on the model. The reader can refer in the original paper [9] or review papers such as [11] and [24] for the full treatment of the problem. The starting point is the spin- $S$  isotropic AFM Heisenberg chain with nearest neighbors interactions, described by the Hamiltonian:

$$\mathcal{H} = J \sum_n \mathbf{S}_n \cdot \mathbf{S}_{n+1}. \quad (1.1.1)$$

Since we are interested in the long-wavelength low-energy modes, it is convenient to define the  $\mathbf{m}$  and  $\mathbf{l}$  fields as slowly varying quantities on the scale of the lattice, given by:

$$\mathbf{m}(2n + \frac{1}{2}) = (\mathbf{S}_{2n+1} - \mathbf{S}_{2n})/2, \quad \mathbf{l}(2n + \frac{1}{2}) = (\mathbf{S}_{2n+1} + \mathbf{S}_{2n})/2. \quad (1.1.2)$$

The commutation relations between fields  $\mathbf{m}$  and  $\mathbf{l}$  in the  $S \rightarrow \infty$  are of the type that occur in quantum field theory. If we calculate the Hamiltonian (3.0.2) in a gradient expansion, keeping terms up to  $\mathbf{m}^2$  and  $\mathbf{l}^2$ , we arrive at the following effective Hamiltonian:

$$\mathcal{H} = \frac{u}{2} [g^2 (1 - \frac{\theta}{4\pi} \mathbf{m})^2 + \mathbf{m}^2/g^2]. \quad (1.1.3)$$

with velocity  $u = 2JS$ , coupling constant  $g = 2/S$  and topological angle  $\theta = 2\pi S$ . The field  $\mathbf{m}$  is constrained to have a unit magnitude,  $\mathbf{m}^2 = 1$ . This Hamiltonian follows from the action:

$$\mathcal{S} = \frac{1}{2g} \int dx_0 dx_1 \partial_\mu \mathbf{m} \partial^\mu \mathbf{m} + i2\pi S Q. \quad (1.1.4)$$

The first term is known as the  $O(3)$  NL $\sigma$ M and the second is a topological term, where the integer-valued quantity  $Q$  is given by

$$Q = \frac{1}{4\pi} \int d^2\mathbf{m} \cdot (\partial_0\mathbf{m} \times \partial_1\mathbf{m}), \quad (1.1.5)$$

and measures the winding number of how many times the vector  $\mathbf{m}$  sweeps the unit sphere when  $x$  sweeps the 2D space time. Since  $e^{-S}$  is a periodic function of  $\theta = 2\pi S$ , all physical properties of the model are periodic in  $\theta$ . Thus, for integer- $S$  chains we effectively have  $\theta = 0$ , and without the topological term the partition function of the quantum AF spin- $S$  chain is equivalent to that of a classical 2D ferromagnet at the effective temperature  $T_{eff} = g$  in the continuum approximation. The equivalence between a  $d$ -dimensional quantum many body system and a  $(d+1)$ -dimensional classical statistical mechanical system is known as *classical-quantum correspondence*. It is known [25, 26] that at finite temperature the 2D classical AFM has a finite correlation length  $\xi \propto e^{2\pi/T_{eff}}$  which corresponds in the original spin chain at  $T = 0$  to a finite Haldane gap  $\Delta \propto JS e^{\pi S}$ . The disorder due to thermal fluctuations in the classical model corresponds to quantum fluctuations in the quantum model. Thus the ground state is disordered with a massive triplet as the lowest excitation. Note that, a semiclassical analysis of Hamiltonian Eq. (1.1.3) would reproduce the results of spin-wave theory to first order in  $1/S$ , namely two free massless Goldstone bosons.

For half-integer spins, the partition function carries a phase  $e^{-i2\pi S Q}$ , which leads to interference of configurations with different  $Q$  and at the absence of the gap. A more detailed analysis of the half-integer case can be found in [11], where the connection between topological effects and the generation of a mass is explored.

As it was pointed out by Affleck in [34], due to the  $\mathbf{m}^2 = 1$  constraint, the Eq. (1.1.3) is a highly nonlinear theory. A much simpler theory was introduced, where from a renormalization group transformation, the linear version of the model arises. The constraint is relaxed and a repulsive  $\mathbf{m}^4$  is added. A simple mean-field theory is obtained by assuming that the interaction strength between particles is small, and this theory contains a triplet of bosons with rest energy  $\Delta$ . An alternative field theory for the  $S = 1$  Heisenberg model with a single ion anisotropy and quadratic exchange was suggested by Tsvetlik [35]. This model is a simple theory of three Majorana fermions, where a variant of the Jordan-Wigner transformation was used.

**The Lieb-Shultz-Mattis theorem and the VBS model:** From the discussion above, it became evident that there is a difference between integer and half-integer spin chains, since the two models map onto different field theories in the  $S \rightarrow \infty$  limit. While the behavior of the integer- $S$  chain is better understood in terms of the NL $\sigma$ M, the existence of the topological term in the action Eq. (1.1.4) makes the picture for the

half-integer chain ( $\theta = \pi$ ) more complicated. A more clear resolution is provided by the Lieb–Schultz–Mattis theorem [27] for the  $S = 1/2$  chain, later extended to arbitrary half-integer  $S$  [28] and to finite magnetization [29]. The theorem proves in a rigorous way that if we have a half-integer spin Hamiltonian  $\mathcal{H}$  such that,

- (a) includes only short-range exchange interactions (local),
- (b) respects translational symmetry by  $a$  lattice constants,
- (c) respects rotational symmetry,

then either  $\mathcal{H}$  has a unique ground state with zero gap, or the ground state is degenerate corresponding to spontaneously broken parity. It follows that if a spontaneous breaking of the translational symmetry is excluded, a spin- $S$  Heisenberg chain can *only* be gapped if  $S$  is integer. An example of an exactly solvable  $S = 1/2$  chain with broken parity is the following:

$$\mathcal{H} = \sum_n J \left( \mathbf{S}_n \cdot \mathbf{S}_{n+1} + \frac{1}{2} \mathbf{S}_n \cdot \mathbf{S}_{n+2} \right), \quad (1.1.6)$$

first introduced in [30]. For an even periodic chain, there are two ground states with broken parity that can be represented by a simple dimer configuration, and a finite gap above them. Another exactly solvable model with integer spin- $S$  is the so-called valence bond solid (VBS) model, like the one introduced by Affleck, Kennedy, Lieb and Tasaki in [31] for  $S = 1$  also known as AKLT model with a Hamiltonian:

$$\mathcal{H} = \sum_n \left[ \mathbf{S}_n \cdot \mathbf{S}_{n+1} + \frac{1}{3} (\mathbf{S}_n \cdot \mathbf{S}_{n+1})^2 \right]. \quad (1.1.7)$$

The ground state of Eq. (1.1.7) can be constructed by regarding every spin operator as a symmetrized product of 2  $S = 1/2$  operators and linking each  $S = 1/2$  spin to its neighbor from the nearest site with a single bond, see Fig. 1.1.3. For periodic boundary conditions, the singlet ground state is unique.

If the VBS state is used as a variational trial function for the Haldane chain, it will result a ground state energy equal to  $E_0 = -4/3$ , a value very close to the one obtained numerically  $E_0 = -1.41$ . On the other hand, the correlation length for the VBS state is determined as  $\xi = 0.9$ , a value much different to the one calculated for the Haldane chain  $\xi = 6.3$ . Therefore, the VBS model provides an intuitive picture of what the singlet ground state might look like and the existence of the gap, but it can not be used for calculations.

At this point, a clarification should be made for the  $S = 1$  bilinear-biquadratic chain, which may be written in the most general form as:

$$\mathcal{H} = \sum_n \left[ \mathbf{S}_n \cdot \mathbf{S}_{n+1} - \beta (\mathbf{S}_n \cdot \mathbf{S}_{n+1})^2 \right]. \quad (1.1.8)$$



**Figure 1.1.3:** The ground state of the AKLT Hamiltonian with a single valence bond connecting every neighboring pair of sites.

The AKLT Hamiltonian is given for  $\beta = -1/3$ . Another exactly solvable model can be constructed using  $\beta = 1$ . In this case, the model can be solved by the Bethe ansatz technique [32], and as proven, the gap vanishes and the correlation length diverges. This suggests that a transition should occur at a critical  $\beta_{cr}$ , between the two phases, or maybe the existence of a more complicated phase diagram. According to [33], the well established phases of the phase diagram are a Haldane, a ferromagnetic one, and the dimerized one. The  $\beta = 1$  corresponds to a critical point.

**Experimental Verification:** The first experimental evidence for the existence of the Haldane gap came from neutron scattering experiments [43] in 1986 for the nearly isotropic AFM chain  $CsNiCl_3$ . Experimental data supported the Haldane conjecture of a gap of about  $0.4J$  at  $k = \pi$ . The most experimentally studied  $S = 1$  isotropic compound is the  $Ni(C_2H_8N_2)_2NO_2(ClO_4)$  abbreviated as NENP. Two finite gaps at  $k = \pi$  were measured for this compound [44], that correspond to two branches of the triplet that are split by the presence of an effective anisotropy.

## 1.2 Easy plane anisotropy

The Hamiltonian of the isotropic Heisenberg system described Eq. (3.0.2) does not exhaust all possible effective interactions that one might include. Among the other possibilities, a single ion anisotropy of the form  $D \sum_n (S_n^z)^2$  can be added, describing the tendency of the spins to align along the  $z$  axis for  $D < 0$ , or along the  $x - y$  plane for  $D > 0$ . The physical properties of the system strongly depend on the strength of anisotropy  $D$ . The inclusion of this type of anisotropy will yield the following Hamiltonian:

$$\mathcal{H} = \sum_n [\pm JS_n \cdot \mathbf{S}_{n+1} + D(S_n^z)^2] \quad (1.2.1)$$

The importance of this type of Hamiltonian becomes apparent if one considers that Eq.(1.2.1) provides an adequate phenomenological theory for the magnetic properties of real materials, such as  $CsNiF_3$  (a FM with  $J/D \simeq 2.6$  [45]),  $CsFeCl_3$  (a FM with  $J/D \simeq 1/4$  [46]),  $CsFeBr_3$  (an AFM with  $J/D \simeq 1/5$  [47]), NENP (an AFM with  $J/D = 5.9$  [48]) and DTN (AFM with  $J/D = 1/4$  [49]). In fact, in most of the known

$S = 1$  magnets, the Heisenberg exchange is complemented by single-ion anisotropy. The interplay between these interactions with external magnetic field and lattice geometry can result in a rich variety of quantum phases and phenomena.

### 1.2.1 Microscopic origin

Such a contribution arises from the following mechanism [3]. Apart from the intraatomic Coulomb term, and the possible contribution from the crystal field, the spin-orbit and the Zeeman term should be considered. The former corresponds to the interaction between the electron spin and the field produced by its orbital motion, whereas the latter appears due to the presence of a uniform external magnetic field  $\mathbf{H}$ . These two terms are:

$$\mathcal{H}_{s-o} + \mathcal{H}_Z = \lambda \mathbf{L} \cdot \mathbf{S} - \mu_B (\mathbf{L} + 2\mathbf{S}) \cdot \mathbf{H}. \quad (1.2.2)$$

The idea is to project out the orbital dependence, and since there is no mixing of orbital and spin states, the eigenfunctions of Eq.(1.2.2) are of the form  $|\Gamma, \gamma\rangle |S, M_s\rangle$ , where  $\Gamma$  and  $\gamma$  indicate the representation and the particular basis state chosen (see [3]). By the use of perturbation theory, the correction to the orbitally nondegenerate ground state  $|\Gamma, \gamma\rangle$  to second order in perturbation theory reads:

$$\mathcal{H}_{eff} = 2\mu_B \mathbf{H} \cdot \mathbf{S} - \sum_{\Gamma', \gamma'} \frac{|\langle \Gamma', \gamma' | \mu_B \mathbf{H} \cdot \mathbf{L} + \lambda \mathbf{L} \cdot \mathbf{S} | \Gamma, \gamma \rangle|^2}{E_{\Gamma', \gamma'} - E_{\Gamma, \gamma}}. \quad (1.2.3)$$

As a result, since the calculation was done within the orbital space, the effective spin Hamiltonian  $\mathcal{H}_{eff}$  depends only on the spin operators and should be diagonalized within the spin subspace. Expanding the square, the  $\mathcal{H}_{eff}$  can be written as:

$$\mathcal{H}_{eff} = \sum_{\mu, \nu} (\mu_B g_{\mu\nu} H_\mu S_\nu - \lambda^2 \Lambda_{\mu\nu} S_\mu S_\nu - \mu_B^2 \Lambda_{\mu\nu} H_\mu H_\nu), \quad (1.2.4)$$

where

$$\Lambda_{\mu\nu} = \sum_{\mu, \nu} \frac{\langle \Gamma, \gamma | L_\mu | \Gamma', \gamma' \rangle \langle \Gamma', \gamma' | L_\nu | \Gamma, \gamma \rangle}{E_{\Gamma', \gamma'} - E_{\Gamma, \gamma}}, \quad g_{\mu\nu} = 2(\delta_{\mu\nu} - \lambda \Lambda_{\mu\nu}). \quad (1.2.5)$$

The second term represents the fine structure, or *single ion anisotropy*, and since it reflects the symmetry of the crystal it could be in general anisotropic. In a cubic crystal  $\Lambda_{xx} = \Lambda_{yy} = \Lambda_{zz}$ , and the anisotropy term reduces to a constant. If the  $z$  axis is of highest symmetry, the  $\Lambda$  tensor will have  $\Lambda_{xx} = \Lambda_{yy} = \Lambda_\perp$  eigenvalues along the perpendicular directions to  $z$ , and different  $\Lambda_{zz} = \Lambda_\parallel$  along  $z$ . In that case, the effective Hamiltonian

without the last term becomes:

$$\mathcal{H}_{eff} = g_{\parallel}\mu_B H_z S_z + g_{\perp}\mu_B (H_x S_x + H_y S_y) + D (S_z^2 - S(S+1)) + \frac{1}{3}S(S+1)(2\Lambda_{\perp} + \Lambda_{\parallel}), \quad (1.2.6)$$

where  $D = \lambda(\Lambda_{\parallel} - \Lambda_{\perp})^2$ . Note that the quadratic anisotropy term vanishes identically in the case  $S = 1/2$ .

### 1.2.2 Phase Transitions

As mentioned earlier the properties of the system strongly depend on the strength of anisotropy  $D$ . The case  $D = 0$  has been extensively studied in the literature, and as discussed earlier, the ground state is a singlet with a massive degenerate triplet as the next-lowest excitation. When positive  $D > 0$  interaction is introduced, acting as a perturbation to the isotropic Hamiltonian, the rotational symmetry breaks down to the rotation along the  $z$  axis. Thus, the triplet splits into a higher in energy singlet with  $S^z = 0$ , and a lower lying doublet  $S^z = \pm 1$ . Accordingly, The Haldane gap is split into two components, one gap  $\Delta_-$  between the ground state and the  $S^z = \pm 1$  and one  $\Delta_+$  between the ground state and the  $S^z = 0$  component of the triplet. The former decreases with  $D$ , whereas the latter increases. In [36], chains up to 16 were studied by a Lancz s method and chains up to 32 by a quantum Monte Carlo simulation. The gaps  $\Delta_+$  and  $\Delta_-$  are estimated for values of  $D$  up to 0.25, as  $\Delta_+ = 0.41 + 1.41D$  and  $\Delta_- = 0.41 - 0.57D$ .

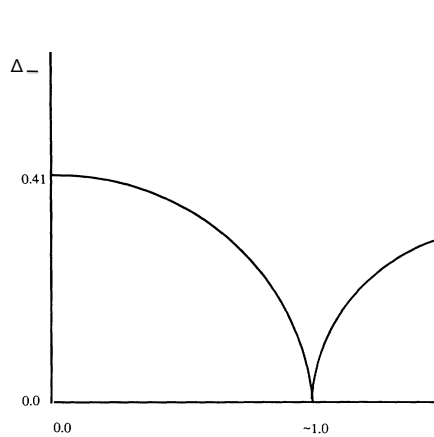


**Figure 1.2.1:** Gap of the spin-1 AF chain as a function of the single-ion easy-plane anisotropy  $D$ . The Haldane phase extends from  $D = 0$  up to  $D = 1$ . Figure is taken from [36].

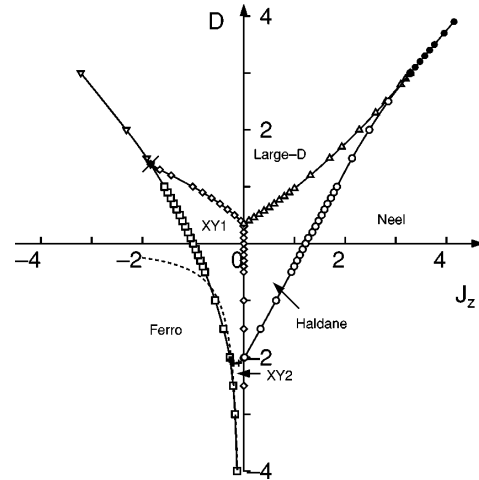


**Figure 1.2.2:** The phase diagram of  $S = 1$  XXZ chains with uniaxial single-ion-type anisotropy. The solid lines and symbols are the transition lines. Figure is taken from [38].

When  $D$  is increased the Haldane gap is diminished until it vanishes. At this point a transition occurs, so when  $D$  is further increased we observe the rise of a gap of different

nature. For large  $D$  the ground state is the direct product of states with  $S^z = 0$  because, due to the large anisotropy, all spins are forced to lie in the XY plane. It is therefore natural to expect a phase transition at a critical  $D_{cr}$ , which can be either an isolated point, as shown in Fig. 1.2.1, or a collection of values of  $D$ , a phase with non-zero width in  $D$ . Early numerical calculations [37] showed that the transition occurs clearly in a narrow region, and most likely there is only one isolated point with  $D_{cr} = 0.99J$ . This is clarified in more recent studies [38, 39], where the critical value is reestimated  $D_{cr} = 0.968J$  with better accuracy.

Interesting physics arises if one considers a slightly more complex Hamiltonian, allowing anisotropies in the exchange interaction:

$$\mathcal{H} = \sum_n (J(S_i^x S_{i+1}^x + S_i^y S_{i+1}^y) + J_z S_i^z S_{i+1}^z + D(S_i^z)^2). \quad (1.2.7)$$

The ground-state phase diagram of this model consists of the Haldane phase, the large- $D$  phase, two XY phases, the ferromagnetic phase, and the Néel phase [38–40]. Between these phases, various types of phase transitions take place, as they are summarized in Fig. 1.2.2. It is fascinating that such a rather simple model exhibits a very complex diagram.

### 1.3 Large – D Limit

We will now focus on the isotropic version of Hamiltonian (1.2.7), where there exist two distinct coupling regimes controlled by the anisotropy constant  $D$ . The transition between the two regimes is marked by the critical value  $D_{cr}$ . In the previous section we summarized some important results concerning the properties of the  $D < D_{cr}$  region, but here we shall be interested in strong anisotropies. In this limit, a gap of a different nature reappears above the critical value and is present in both antiferromagnetic (AFM) and ferromagnetic (FM) chains. This problem is of obvious theoretical interest since there exist several experimental realizations of spin-1 chains with large easy-plane anisotropy, for example the organic compound  $NiCl_2 - SC(NH_2)_2$ , (dichloro-tetrakis thiourea-nickel(II), abbreviated as DTN), that has attracted considerable experimental and theoretical attention [8, 41, 42]. In this section we examine the ground state properties of the model in the presence of magnetic field along the hard axis.

A way to attack the situation is by the usual semiclassical approach, which has proven to be a useful tool to provide the essential aspects of the excitation spectrum for systems which exhibit (anti)ferromagnetic order in their ground state. Unfortunately, the standard semiclassical theory of magnetism fails in one dimension owing to strong quantum fluctuations, and in the present problem, predicts no gap for either weak or strong easy-plane anisotropy. Moreover, the semiclassical calculation of the Haldane

Hamiltonian suggests that the antiferromagnetic magnon is a spin-1 state with twofold, instead of the expected threefold, multiplicity. Therefore, the usual semiclassical theory of magnetism is clearly inapplicable for all couplings.

A more sophisticated spin-wave approach based on a  $1/n$  expansion was developed in [50, 51] in order to account for magnetic systems with planar behavior and systems involving quartic exchange interactions [52]. The method enables one to study magnets with weak as well as strong single-site anisotropies, and predicts a sharp crossover transition for intermediate couplings. This critical behavior was found at  $D_{cr} = 4J$  and, as is often the case with semiclassical methods, this theory fails to predict the correct critical coupling. Note that numerical simulations indicate that the true critical coupling is at  $D_{cr} = 0.968J$  [39].

The accuracy of the modified semiclassical approximation is challenged through a direct strong-coupling expansion for the  $T = 0$  dynamics; that is, an expansion in powers of  $J/D$  [53], where the exchange interaction is treated as a perturbation. The strong-coupling expansion, not only provides analytical approximations for the dispersion of elementary excitations, but also yields valuable information on certain bound states [54] that can be observed through the two-point longitudinal correlation function. This bound state is missed by the semiclassical theory for more or less the same reason that the familiar Holstein-Primakoff expansion does not yield direct information for the two-magnon bound states known to exist in ferromagnets. More calculational details on the strong coupling expansion will be given in 1.3.2.

We now restrict our study in the one dimensional AFM chain. In the presence of magnetic field  $\mathbf{H}$  along the hard axis ( $z$ ), the Hamiltonian reads:

$$\mathcal{H} = \sum_{n=1}^N [J\mathbf{S}_n \cdot \mathbf{S}_{n+1} + D(S_n^z)^2 + g\mu_B H S_n^z], \quad (1.3.1)$$

where both  $D$  and  $J$  are taken to be positive. It is convenient to scale out the anisotropy constant by measuring energy in units of  $D$ . The remaining independent parameters are:

$$\rho = J/D, \quad h = g\mu_B H/D. \quad (1.3.2)$$

We are interested in the  $\rho \gg 1$  limit, but no restriction is imposed for  $h$ . Important for the discussion of the properties of model (1.3.1) is the presence of symmetries leading to good quantum numbers such as wave vector  $k$  (translation) and  $S^z$  (rotation about  $z$ -axis).

In the limit of infinite  $D$ , spins uncouple and Eq.(1.3.1) reduces to a sum of single-site Hamiltonians, the spectrum of which may be obtained trivially. The ground state is then the direct product of states with vanishing azimuthal spin,  $S_n^z = 0$  for each site

n:

$$|\Omega\rangle = |1, 0\rangle \otimes |1, 0\rangle \otimes |1, 0\rangle \otimes \dots \otimes |1, 0\rangle, \quad (1.3.3)$$

and has vanishing energy. This phase is called *quantum paramagnetic phase* because the dominant anisotropy term forces each spin to be in a nonmagnetic state with  $S_n^z = 0$  and no order is expected down to zero temperature  $T = 0$ .

At zero magnetic field,  $h = 0$ , the first excited states can be constructed by assigning the value  $S_n^z = \pm 1$  to one site, with eigenvalues  $\epsilon_{\pm} = 1$  in rationalized units (or  $\epsilon_{\pm} = D$ ). The degeneracy of the lowest excited states is lifted in the presence of magnetic field, because the eigenvalues are given by  $\epsilon_{\pm} = 1 \pm h$ ; there are  $N$  independent states that are obtained by exciting any single site to an azimuthal spin  $S^z = 1$  with energy  $\epsilon_+ = 1 + h$  and  $N$  independent states that are obtained by exciting any single site to an azimuthal spin  $S^z = -1$  with energy  $\epsilon_- = 1 - h$ . We shall refer to these states as exciton and antiexciton, correspondingly. Next excited states correspond to states with more than one non-vanishing azimuthal spin of either sign; there exist  $N(N-1)/2$  two exciton states with  $S^z = 2$  and energy  $E_{++} = 2\epsilon_+$ ,  $N(N-1)/2$  two antiexciton states with  $S^z = -2$  and energy  $E_{--} = 2\epsilon_-$ ,  $N(N-1)$  exciton-antiexciton states with  $S^z = 0$  and energy  $E_{+-} = \epsilon_+ + \epsilon_-$ , and so on.



**Figure 1.3.1:** Schematic representation of the ground state Eq. 1.3.3 of the  $S = 1$  AFM Heisenberg chain. Yellow indicates a site with azimuthal spin  $S^z = 0$ .

A pertinent question is how this picture changes in the presence of small but nonvanishing exchange interaction. The ground state is given by Eq.(1.3.3), and the elementary excitations are  $S^z = 1$  excitons and  $S^z = -1$  antiexcitons. Since we turned on the exchange interaction, their energy  $\epsilon_{\pm}(k) = \epsilon(k) \pm h$  becomes dispersive and, for the AFM case considered here, the smallest gap  $\Delta_0$  occurs at the zone boundary  $k = \pi$ . It is the purpose of section 1.3.2 to provide analytical expressions for  $\epsilon(k)$  using the strong coupling expansion.

### 1.3.1 Field-induced quantum phase transitions

This subsection is devoted on the interesting physics that arises if one succeeds to close the gap by the magnetic field. The application of magnetic field along the  $z$  direction induces a zero-temperature quantum phase transition at a critical field  $h_1$ , above which magnetization develops in the ground state. At this point level crossing occurs and the azimuthal spin of the ground state is no longer zero but increases with increasing field. The value of  $h_1$  is defined by the gap  $\Delta_0$ ,  $h_1 = \Delta_0$ . Thus the system enters

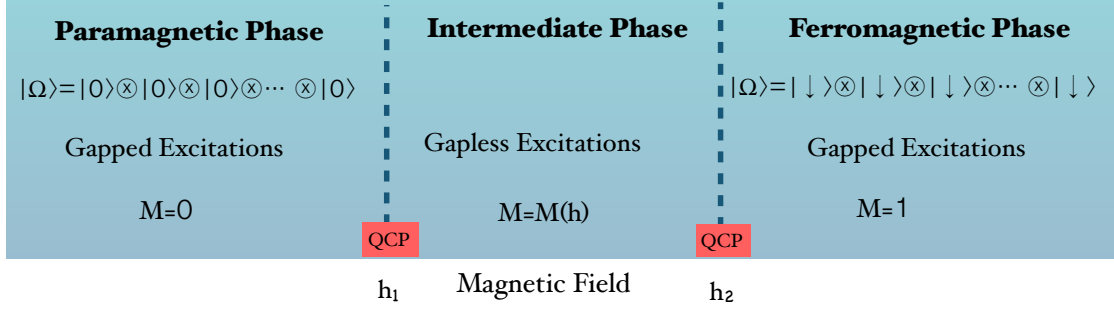


**Figure 1.3.2:** Diagram of the various phases of model (1.3.1) as a function of magnetic field. Vertical lines correspond to field-induced phase transitions located at critical fields  $h_1$  and  $h_2$ . Paramagnetic phase is characterized by a singlet ground state with  $S_i^z = 0$  at any site, and lowest excitations have a gap. At  $h_1$  level crossing occurs and the ground state becomes increasingly ferromagnetic, while gapless excitations are expected. Magnetization develops in the ground state that ranges from zero to one. At  $h_2$  a second transition occurs, where the ground state is a completely ordered ferromagnetic state with a gapped excitation spectrum.

an intermediate phase through a field-induced quantum phase transition. The magnon spectrum is expected to be gapless in the intermediate phase but its detailed structure is now difficult to calculate. A systematic  $1/D$  expansion is not feasible while semiclassical methods are generally inaccurate at strong anisotropy.

The theoretical model of Eq.(1.3.1) becomes again tractable for sufficiently strong fields  $h > h_2$  where the ground state is a completely ordered ferromagnetic state and the gapped excitation spectrum  $\omega(k)$  of a magnon can be calculated exactly. Thus the ordered state is stable when the field exceeds a second critical value given by the lowest gap of the magnon dispersion, that again occurs at  $k = \pi$ . Apart from the single magnon and the two-magnon continuum, the physical picture gets more involved thanks to the existence of two-magnon bound states. One of them is of special importance in the analysis of the ESR spectrum. Section 1.3.3 surveys the essential results concerning the elementary excitations of this phase.

It is relevant to note that at one-dimension and  $h_1 < h < h_2$ , quasi-long-range phase coherence occurs. This corresponds to uniform magnetic moment in the direction of the applied field  $z$  and a power-law decay of the staggered magnetization orthogonal to the applied field [55], i.e.,

$$\langle S_i^a S_j^b \rangle \propto (-1)^{i-j} \frac{\delta_{ab}}{|i-j|^\eta} \quad (a, b = x, y). \quad (1.3.4)$$

In the presence of weak 3D couplings, this will turned into true long-range order. This magnetic ordering has been identified as an  $XY$ -ordered state that exists in the interval  $h_1 < h < h_2$  and it is dome shaped, reaching a peak somewhere between the two critical fields.

Both of these phase transitions are second order, and the order parameter is the

$z$  component of magnetization,  $M$  with discontinuous derivative at  $h_1$  and  $h_2$ . The dynamical exponent  $z$  of the inverse correlation length  $1/\xi$  determines the power-law exponent of the single-particle dispersion  $\omega_k$  at the magnetic-field-induced quantum critical points (QCP) [5],  $\omega_k \propto k^z$ . We will later see that  $\omega_k \propto k^2$  at  $h_1$  and  $h_2$ , hence the dynamical exponent is  $z = 2$ . The quadratic shape of the single-particle excitations cannot be modified as  $h \rightarrow h_1$  (or  $h \rightarrow h_2$ ), and the only effect of the applied field is to close (or open) the gap.

Another framework of these phase transitions may be considered if the  $S = 1$  system is thought of as a spin fluid formally described as a gas of hard-core bosons (for a review see [8]). The  $S^z = 0$  state is mapped into a state with zero bosons per site, the  $S^z = -1$  with one boson per site and the  $S^z = 1$  with two bosons per site, see Fig. 1.3.3. The particle concentration is tuned by applying an external magnetic field which plays the role of a chemical potential and the density of bosons corresponds to magnetization. Therefore, the ground state for  $h < h_1$  is an empty state in the bosonic language and there is a gap for creating a single boson. The Bose gas is populated only above  $h_1$ , and the phase transition corresponds to Bose-Einstein condensation in the dilute limit. This phase extends up to  $h_2$ , where the spins become fully polarized and the ground state contains one hard-core boson in each site (Mott insulator in the bosonic language).

Actually, this spin-particle correspondence has been pointed out some time ago for the 1D Haldane chain [34, 55], where a Landau-Ginsburg formulation of the  $S = 1$  model was developed and some exact results concerning the critical behavior of this theory were derived. Some caution is necessary with regard to a few crucial points of this correspondence. The first has to do with the dimensionality  $d$  of the system. For one-dimensional  $U(1)$  invariant models, the connection between magnetic spin systems and gases of particles became clear after the Jordan-Wigner transformation [56]. The transformation consists of a nonlocal mapping between  $S = 1/2$  spin operators and creation and annihilation operators of spinless fermions, that provide a natural realization of two-level systems. This exact mapping can be generalized in  $S = 1$  systems by using a generalized Jordan-Wigner transformation [58], or by considering the low-energy limit of the spin Hamiltonian, where the  $S^z = 1$  element with a gap  $\sim 2h_1$  at  $h \simeq h_1$  becomes irrelevant and may be integrated out. The result is a two-level  $S = 1/2$  effective Hamiltonian, and its derivation is the subject of section 1.5.

Since the field-induced QCP in 1D is described by a free-fermion theory, it is easy to compute the exponents of thermodynamic properties as a function of  $\mu$  and  $T$ . At  $T = 0$  the fermion density is given by  $\rho \propto \sqrt{\mu}$ , a result that implies that  $M \propto \sqrt{h - h_1}$  near  $h_1$  and  $M \propto \sqrt{h_2 - h}$  near  $h_2$ . This is verified by an independent numerical calculation of the magnetization of model (1.3.1) and is presented in Chapter 3, where thermodynamical quantities are studied. Derivation of the same result using a bosonic

language is possible making use of the known result for the ground-state energy as a function of density in the Bose fluid [57].

For spatial dimension  $d \geq 2$ , a simpler mapping can be used known as Matsubara–Marsuda transformation [59], where  $S = 1/2$  operators are mapped into hard-core bosons. This transformation can also be generalized for higher spin-values [60]. The raising and lowering spin operators are mapped into creation and annihilation bosonic operators that satisfy the same commutation relations. The application of magnetic field plays the role of the chemical potential and closes the gap at  $h = h_1$ . At this point the ground state is populated by bosons that normally condense into a BEC state. The BEC state is the particle state of the  $XY$  AFM ordered state and the QCP that separates the quantum paramagnetic and the  $XY$ -ordered state belongs to the BEC universality class in effective dimension  $D = d + z = d + 2$ . The same applies to the second QCP at  $h_2$ . The asymptotic behavior of the critical fields at low temperatures is  $h_1(T) - h_1(T = 0) \propto T^{d/2}$ , and can be used as an experimental signature of the BEC in quantum magnets. Actually, the power-law behavior of the observed phase boundary of DTN [61]  $h_1(T) - h_1(0) \propto T^\alpha$  has been identified as  $\alpha = 1.47 \pm 0.10$  consistent with the 3D BEC universality class.

There are several reasons for studying BECs in quantum magnets. Among them is that they have provided experimental tests of the scaling laws of thermodynamic quantities near a BEC QCP ([8] and references within) and a basis to study a variety of exotic phenomena related to bosonic physics. We should emphasize that a key condition for observing a BEC is the number conservation that is naturally present in the

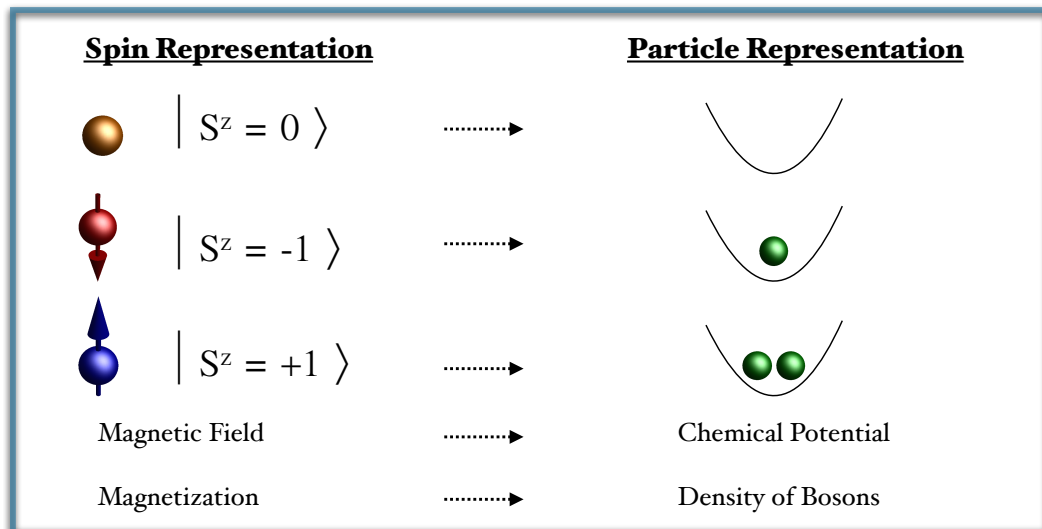


**Figure 1.3.3:** Diagram of the spin–particle correspondence. The  $S^z = 0$  state is mapped into a state with zero bosons per site, the  $S^z = -1$  with one boson per site and the  $S^z = 1$  with two bosons per site. Magnetic field plays the role of the chemical potential and the density of bosons corresponds to magnetization.

case of cold-atoms. In the magnetic language, the boson number corresponds to the longitudinal magnetization along  $z$  axis and the number conservation to uniaxial symmetry. In real crystals the uniaxial symmetry is approximate, since the symmetry can be broken either by crystal field anisotropy, effective spin-spin interactions induced by spin-orbit coupling or dipole-dipole interactions. These terms are almost always present and become relevant at low temperatures compared to the magnitude of the symmetry-breaking term. For this reason the notion of BEC applied to spin systems is always an approximate concept [8].

In the present thesis, a theoretical analysis is formulated that does not depend on the spin-particle correspondence. The main reason is that the bosonic description of Hamiltonian (1.3.1) that is developed in terms of schwinger bosons [42] is not reliable for intermediate anisotropies, even though it goes beyond the usual semiclassical expansion. For example, the critical coupling that separates the Haldane phase from the large- $D$  phase is predicted equal to  $D_{cr} = 4J$  in 1D [62], while numerical calculations revealed that the true coupling is at  $D_{cr} = 0.968J$  [39]. Therefore, for intermediate anisotropies we are mostly interested, detailed predictions should be searched for using alternative methods.

The objective in developing a complete theoretical description of model 1.3.1 will become apparent in the following chapters, where thermodynamical and dynamical quantities will be considered. For the time being, let us concentrate of the ground state properties and elementary excitations of the paramagnetic phase for  $h < h_1$  and the fully ferromagnetic phase for  $h > h_2$ .

### 1.3.2 Excitations in the Paramagnetic Phase

Here we will present analytical results for the dispersion of an exciton or antiexciton mode obtained within the strong-coupling expansion. In addition, an exciton-antiexciton mode is formed that could be observed through the two-point longitudinal dynamic correlation function. The discussion follows Ref. [53], adjusting the parameters in the isotropic AFM case we are interested.

As a first step to carry out the strong-coupling expansion, the Hamiltonian (1.3.1) is written as:

$$\mathcal{H}/D = \mathcal{H}_0 - V\rho = \sum_{n=1}^N (S_n^z)^2 - \rho \sum_{n=1}^N \left[ \frac{1}{2} (S_n^+ S_{n+1}^- + S_n^- S_{n-1}^+) + S_n^z S_{n+1}^z \right], \quad (1.3.5)$$

where  $\rho = J/D$ ,  $\mathcal{H}_0$  is the unperturbed Hamiltonian and the term  $-V\rho$  is treated as a small perturbation within a systematic expansion in powers of  $\rho$ . Including the

first-order correction, the ground state is given by:

$$|\Omega'\rangle = |\Omega\rangle + \frac{\rho}{2} \sum_n (|n, \overline{n+1}\rangle + |\overline{n}, n+1\rangle) + \mathcal{O}(\rho^2), \quad (1.3.6)$$

provided that state  $|n_1, \overline{n}_2\rangle$  differs from the ground state at sites  $n_1$  and  $n_2$  where the azimuthal spin is  $+1$  and  $-1$  respectively. The ground state energy to fourth order in  $\rho$  is:

$$E_{GS} = N(\rho^2 + \frac{\rho^3}{2} + \frac{\rho^4}{4} + \dots). \quad (1.3.7)$$

Similarly, elementary excitations are searched for in the form:

$$|k\rangle = \frac{1}{\sqrt{N}} \sum_n e^{ikn} |n\rangle, \quad |\overline{k}\rangle = \frac{1}{\sqrt{N}} \sum_n e^{ikn} |\overline{n}\rangle, \quad (1.3.8)$$

where state  $|n\rangle$  ( $|\overline{n}\rangle$ ) carries nonvanishing azimuthal spin  $+1$  ( $-1$ ) only at site  $n$ . These states will be referred to as excitons and antiexcitons, and are eigenstates of  $\mathcal{H}_0$ .

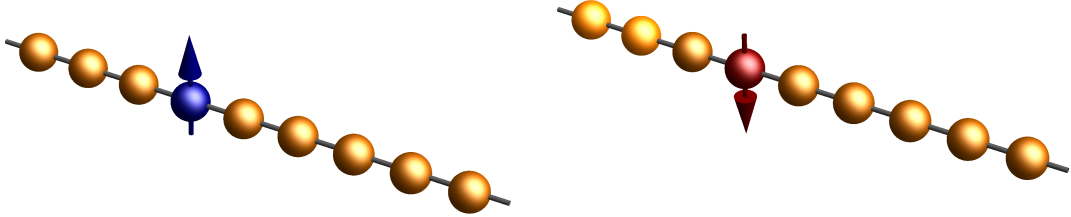


**Figure 1.3.4:** Illustration of the elementary excitations of the  $S = 1$  AFM Heisenberg chain with strong easy-plane anisotropy in the paramagnetic phase. From left to right: Exciton with  $S^z = +1$  and antiexciton with  $S^z = -1$ . Yellow indicates a site with azimuthal spin  $S^z = 0$ , red with  $S^z = -1$  and blue with  $S^z = +1$ .

To leading order the one-exciton state is given by:

$$\begin{aligned} |\Psi_k\rangle = |k\rangle &+ \frac{\rho}{2\sqrt{N}} \sum_n e^{ikn} (2 \cos k |n+1, \overline{n}, n-1\rangle \\ &+ \sum_{m(m \neq n, n \pm 1)} (|m, \overline{m+1}, n\rangle + |\overline{m}, m+1, n\rangle)) + \mathcal{O}(\rho^2), \end{aligned} \quad (1.3.9)$$

and the one-antiexciton state is:

$$\begin{aligned} |\overline{\Psi}_k\rangle = |\overline{k}\rangle &+ \frac{\rho}{2\sqrt{N}} \sum_n e^{ikn} (2 \cos k |\overline{n+1}, n, \overline{n-1}\rangle \\ &+ \sum_{m(m \neq n, n \pm 1)} (|m, \overline{m+1}, \overline{n}\rangle + |\overline{m}, m+1, \overline{n}\rangle)) + \mathcal{O}(\rho^2). \end{aligned} \quad (1.3.10)$$

States  $|n_1, \overline{n}_2, n_3\rangle$  can be found by generalizing the notation introduced earlier. The exciton and antiexciton dispersion is a rapidly converging sequence in terms of  $\rho$  and up

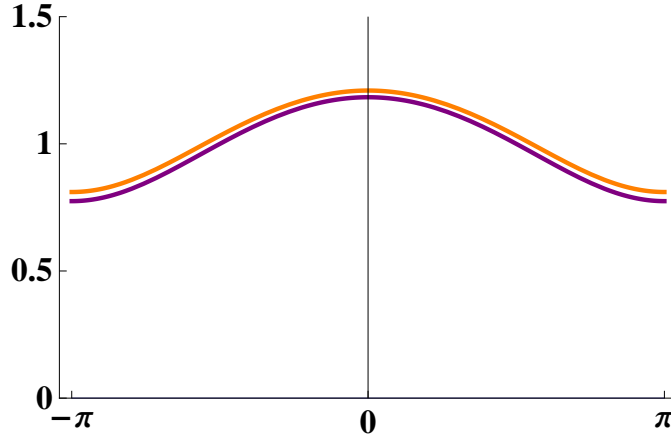


**Figure 1.3.5:** Energy–momentum dispersion of the (anti)exciton dispersion for a typical coupling  $\rho = 0.1$ . Orange line corresponds to the strong–coupling expansion result given in Eq.(1.3.11) and purple line to the modified semiclassical method given in Eq.(1.3.12).

to third order is:

$$\epsilon(k) = 1 + 2\rho\cos k + \rho^2(1 + 2\sin^2 k) - \rho^3 \left( \frac{1}{2}(1 + 8\sin^2 k)\cos k - 2\sin^2 k \right). \quad (1.3.11)$$

A comparison between the results obtained by the strong–coupling method and the ones obtained using the modified semiclassical method developed in [50] is possible. The latter method has provided the following analytical expression for the exciton or antiexciton energy–momentum dispersion:

$$\epsilon_{SC}(k) = \sqrt{1 - 4 \cos k} \rho. \quad (1.3.12)$$

In Fig. 1.3.5 we depict the energy–momentum dispersion (1.3.11) and (1.3.12) for a typical coupling  $\rho = 0.1$ . While Eq.(1.3.11) gives an excellent approximation in this region of couplings, the observed discrepancy between the two curves reveals that Eq.(1.3.12) fails to do so. Note that a mass gap of the doubly degenerate anti(exciton) mode is developed:

$$\Delta_0 = \epsilon(k = \pi) = (1 - 2\rho + \rho^2 + \frac{\rho^3}{2} + \dots). \quad (1.3.13)$$

For  $\rho = 0.1$  the  $\mathcal{O}(\rho^3)$  term corresponds to the 0.062% of the total value, and for  $\rho = 0.25$  to the 1.37%, which makes it reasonable to assume that the strong–coupling series up to third order remains reliable for intermediate couplings  $\rho \sim 0.25$ . Nevertheless, several more terms beyond the third order have recently become available [63].

Before we turn our attention to two–body states, let us consider the case of finite magnetic field  $h$  along the  $z$  axis. For nonzero but sufficiently low fields the  $S^z = 0$

ground state remains unaffected while the degeneracy of the  $S^z = \pm 1$  states is lifted to yield a twofold dispersion:

$$\epsilon_{\pm}(k) = \epsilon(k) \pm h. \quad (1.3.14)$$

Therefore, the anti(exciton) frequencies of Eq.(1.3.14) remain positive throughout the Brillouin zone as long as  $h < h_1$  where  $h_1$  is a critical field defined from:

$$h_1 = \Delta_0 = \epsilon(k = \pi) = (1 - 2\rho + \rho^2 + \frac{\rho^3}{2} + \dots). \quad (1.3.15)$$

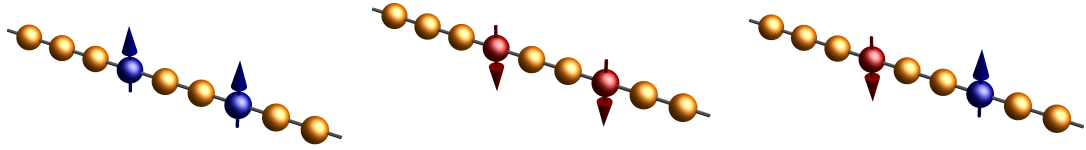


**Figure 1.3.6:** Illustration of two-body states. From left to right: exciton–exciton pairs ( $ee$ ) with  $S^z = 2$ , antiexciton–antiexciton pairs ( $\bar{e}\bar{e}$ ) with  $S^z = -2$  and exciton–antiexciton pairs ( $e\bar{e}$ ) with  $S^z = 0$ .

To complete the analysis of low-lying excitations in the paramagnetic phase we are considering two-body states, namely exciton–exciton pairs ( $ee$ ) with  $S^z = 2$ , antiexciton–antiexciton pairs ( $\bar{e}\bar{e}$ ) with  $S^z = -2$ , and exciton–antiexciton pairs ( $e\bar{e}$ ) with  $S^z = 0$ . We first analyze the  $ee$  sector. In the strong coupling limit, this sector consists of states of the form  $|n_1, n_2\rangle$ , with  $n_1 \neq n_2$ . The main point of this calculation is that Hamiltonian (1.3.5) can be diagonalized by an elementary Bethe ansatz, in close analogy with calculations of two-magnon states in isotropic ferromagnetic chain of arbitrary spin [64] or the anisotropic chain [65, 66]. Thus we consider the eigenvalue problem:

$$V|\psi\rangle = E|\psi\rangle \quad |\psi\rangle = \sum_{n_1 < n_2} C_{n_1, n_2} |n_1, n_2\rangle, \quad (1.3.16)$$

where coefficients  $C_{n_1, n_2}$  satisfy the system of linear equations:

$$\begin{aligned} E C_{n_1, n_2} &= C_{n_1-1, n_2} + C_{n_1+1, n_2} + C_{n_1, n_2+1} + C_{n_1, n_2-1} \quad \text{for } n_1 < n_2 - 1 \\ E C_{n, n+1} &= -C_{n, n+1} + C_{n-1, n+1} + C_{n, n+2}. \end{aligned} \quad (1.3.17)$$

The system of equations given by Eq.(1.3.17) is solved by the Bethe ansatz:

$$\begin{aligned} C_{n_1, n_2} &= \exp[i(k_1 n_1 + k_2 n_2 + \phi/2)] + \exp[i(k_1 n_2 + k_2 n_1 - \phi/2)] \\ E &= 2(\cos k_1 + \cos k_2). \end{aligned} \quad (1.3.18)$$

Wavenumbers  $k_1$ ,  $k_2$  and the phase shift  $\phi$  are related by:

$$\cot(\phi/2) = \frac{-\sin[(k_1 - k_2)/2]}{2\cos[(k_1 + k_2)/2] + \cos[(k_1 - k_2)/2]} . \quad (1.3.19)$$

If one imposes periodic boundary conditions  $C_{n_1, n_2} = C_{n_2, n_1 + N}$ , the wavenumbers and phase shifts are constrained as:

$$Nk_1 - \phi = 2\pi\lambda_1, \quad Nk_2 + \phi = 2\pi\lambda_2, \quad (1.3.20)$$

where  $\lambda_1$  and  $\lambda_2$  are integers, provided that  $0 \leq \lambda_1 \leq \lambda_2 \leq N - 1$ . The leading approximation to the excitation energy of an ( $ee$ ) pair is given by:

$$\Omega_{k_1, k_2} = 2h + 2[1 - \rho(\cos k_1 + \cos k_2)] . \quad (1.3.21)$$

For any set of integers  $\lambda_1$  and  $\lambda_2$  in the range  $0 \leq \lambda_1 \leq \lambda_2 \leq N - 1$ , equations (1.3.18), (1.3.19) and (1.3.20) provide a solution of the eigenvalue problem (1.3.16). There exist essentially two categories of solutions. The first one corresponds to  $\lambda_1 < \lambda_2 - 1$  and yields real wavenumbers  $k_1$  and  $k_2$ . The excitation energies of these solutions fall into a two-body continuum parametrized in terms of the total crystal momentum  $k = k_1 + k_2$ . The boundaries of the two-body continuum restricted to the fundamental Brillouin zone are located:

$$\Omega_k^\pm = 2h + 2[1 \pm 2\rho \cos(k/2)] . \quad (1.3.22)$$

The second category of solutions corresponds to  $\lambda_1 = \lambda_2$  or  $\lambda_1 = \lambda_2 - 1$  and may lead to complex wavenumbers of the form  $k_1 = u + iv$  and  $k_2 = u - iv$ . From Eq.(1.3.20) we find that  $\phi = iNu$  for  $\lambda_1 = \lambda_2$  and  $\phi = iNu + \pi$  for  $\lambda_1 = \lambda_2 - 1$ . Substituting these relations in Eq.(1.3.19) and taking the thermodynamic limit  $N \rightarrow \infty$  we find that:

$$2\cos(u) = -e^{-u}, \quad u = (k_1 + k_2)/2 = k/2, \quad v = (k_1 - k_2)/(2i) . \quad (1.3.23)$$

The excitation energy calculated by inserting (1.3.23) into (1.3.21) is:

$$\Omega_k^{ee} = 2h + 2[1 + \rho(1/2 + 2\cos(k/2)^2)] . \quad (1.3.24)$$

A consequence of Eq.(1.3.23) is that complex solutions exist only when  $-1/2 \leq \cos(k/2) \leq 0$  and the usual folding of the zone leads to the condition:

$$2\pi/3 \leq |k| \leq \pi . \quad (1.3.25)$$

A solution with complex wavenumbers describes a bound state of two excitons, with energy-momentum dispersion given by Eq.(1.3.24), that lies above the continuum and

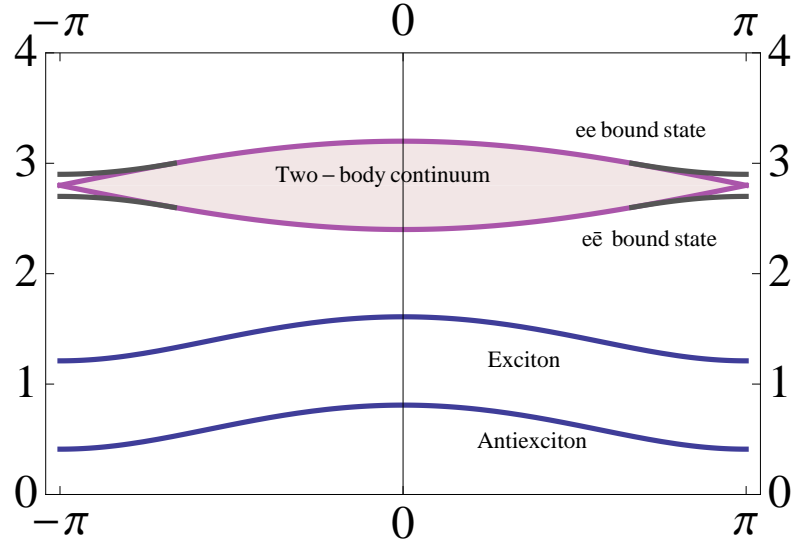


**Figure 1.3.7:** A schematic view of the energy–momentum dispersions of magnetic excitations in an  $S = 1$  AFM Heisenberg chain with strong easy-plane anisotropy for  $\rho = 0.1$  and  $h = 0.4 < h_1$ . Blue lines correspond to the exciton and antiexciton mode, and purple lines indicate the boundaries of the two–body continuum. Black lines denote the bound states. The  $ee$  ( $\bar{e}\bar{e}$ ) bound state lies above (below) the continuum, while the  $e\bar{e}$  bound state emerges below the continuum.

merges with the continuum at the cut–off momentum  $k = k_0$ . Below  $k_0$  the bound state is unstable. The analysis of the antiexciton–antiexciton sector ( $\bar{e}\bar{e}$ ) with  $S^z = -2$  is completely analogous and leads to a bound state with the same dispersion as in Eq.(1.3.24).

Thus we shall investigate the exciton–antiexciton ( $e\bar{e}$ ) sector. In the strong coupling limit this sector is spanned by states of the form  $|n_1, \bar{n}_2\rangle$ . The corresponding eigenvalue problem is solved by the following wavefunctions:

$$|\psi\rangle^\pm = \sum_{n_1 < n_2} C_{n_1, n_2} |n_1, n_2\rangle^\pm, \quad \text{where} \quad |n_1, n_2\rangle^\pm = \frac{1}{\sqrt{2}} [|n_1, \bar{n}_2\rangle \pm |n_2, \bar{n}_1\rangle]. \quad (1.3.26)$$

The coefficients are given by Eq.(1.3.18) but the wavenumbers and phase shift are now related by:

$$\cot(\phi/2) = \frac{\sin[(k_1 - k_2)/2]}{2\cos[(k_1 + k_2)/2] - \cos[(k_1 - k_2)/2]}, \quad (1.3.27)$$

A difference also arises in the periodic boundary condition that reads  $C_{n_1, n_2} = C_{n_2, n_1+N}$  or  $C_{n_1, n_2} = -C_{n_2, n_1+N}$ , for symmetric or antisymmetric combinations in Eq.(1.3.26) respectively. Expressing these relations in terms of the wavenumbers and the phase shift leads to Eq.(1.3.20) in both cases, but the  $\lambda_1$  and  $\lambda_2$  are integers in the first case and half–integers in the second. In the thermodynamic limit, the boundaries of the ( $e\bar{e}$ ) continuum coincide with the ones given in Eq.(1.3.22) while the dispersion

for the bound state is:

$$\Omega_k^{e\bar{e}} = 2h + 2 \left[ 1 - \rho(1/2 + 2 \cos(k/2))^2 \right]. \quad (1.3.28)$$

Hence, the bound state emerges below the continuum. Fig. 1.3.7 illustrates the main results presented here for a typical coupling  $\rho = 0.1$  and magnetic field  $h = 0.4$ . All dispersions are in units of  $D$ .

### 1.3.3 Excitations in the Fully Ferromagnetic Phase

Here we shall be concerned with the excitation spectrum of Hamiltonian (1.3.1), assuming that the magnetic field is large enough that complete ferrromagnetic order is achieved in the ground state. The critical field  $h_2$  that marks this second phase transition, corresponds to the lowest gap of a single magnon. Our purpose is to summarize all information necessary for a complete analysis of the excitation spectrum along the lines of [65]. To begin with, the ground state of the system is now given by:

$$|\Omega\rangle = |1, -1\rangle \otimes |1, -1\rangle \otimes |1, -1\rangle \otimes \dots \otimes |1, -1\rangle, \quad (1.3.29)$$

that is, all spins point along the negative  $z$  axis, with an energy  $E_0 = N(1 + \rho - h)$ . The single magnon eigenstate is:

$$|\psi_1\rangle = \frac{1}{\sqrt{N}} \sum_{n=1}^N e^{ikn} |n\rangle, \quad (1.3.30)$$

where  $k$  is the crystal momentum and the state  $|n\rangle$  denotes a state with site  $n$  carrying azimuthal spin 0, while the azimuthal spin equals  $-1$  at all other sites. The eigenvalue of  $|\psi_1\rangle$  equals  $E_0 + \omega(k)$ , where:

$$\omega(k) = h - 1 + 2 \rho(\cos k - 1), \quad (1.3.31)$$

with the lowest gap at  $k = \pi$ . Therefore,  $h_2 = 1 + 4 \rho$  is the second critical field, below which energy–momentum dispersion of the magnon becomes negative.

Similarly, two–magnon eigenstates are searched for in the form:

$$|\psi_2\rangle = \sum_{n=1}^{N-1} \sum_{m=n+1}^N c_{n,m} |n, m\rangle + \sum_{n=1}^N d_n |n, n\rangle, \quad (1.3.32)$$

where states  $|n, m\rangle$  with  $n \neq m$  differs from the ground state at sites  $n$  and  $m$  where the azimuthal spin is equal zero, while state  $|n, n\rangle$  differs only at site  $n$  where the azimuthal spin is equal to  $+1$ . The task is to determine coefficients  $c_{m,n}$  and  $d_n$  so that

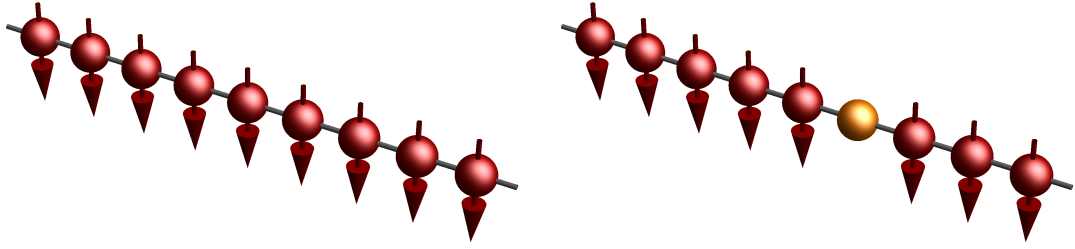


**Figure 1.3.8:** Illustration of the ground state and magnon excitation of the  $S = 1$  AFM Heisenberg chain with strong easy plane anisotropy in the fully ferromagnetic phase.

$|\psi_2\rangle$  becomes an eigenstate of the Hamiltonian:

$$\mathcal{H}|\psi_2\rangle = E_2|\psi_2\rangle = (E_0 + E)|\psi\rangle. \quad (1.3.33)$$

Coefficients  $c_{n,m}$  are given by the familiar Bethe Ansatz:

$$\begin{aligned} c_{n,m} &= \exp[i(k_1 n + k_2 m + \phi/2)] + \exp[i(k_1 m + k_2 n - \phi/2)] \\ d_n &= \frac{\cos(k_1 - \phi/2) + \cos(k_2 + \phi/2)}{\cos k_1 + \cos k_2 - 1/\rho} e^{(k_1+k_2)n}, \end{aligned} \quad (1.3.34)$$

and the phase  $\phi$  must satisfy the constraint:

$$\begin{aligned} \cot(\phi/2) &= \frac{(1+Q)\sin[(k_1 - k_2)/2]}{2\cos[(k_1 + k_2)/2] - (1+Q)\sin[(k_1 - k_2)/2]} \\ Q &\equiv \frac{1 + \cos(k_1 + k_2)}{\cos k_1 + \cos k_2 - 1/\rho}. \end{aligned} \quad (1.3.35)$$

If periodic boundary conditions are enforced, we arrive at the relations:

$$Nk_1 - \phi = 2\pi\lambda_1, \quad Nk_2 + \phi = 2\pi\lambda_2, \quad (1.3.36)$$

where  $\lambda_1$  and  $\lambda_2$  are integers that may be restricted to  $0 \leq \lambda_1 \leq \lambda_2 \leq N - 1$ . Finally, the eigenvalue of  $|\psi_2\rangle$  is given by:

$$E = 2(h - 1) - 4\rho \left[ 1 - \frac{1}{2}(\cos k_1 + \cos k_2) \right]. \quad (1.3.37)$$

The boundaries of the two-magnon continuum are located at  $2(h - h_2) - 4\rho(1 \pm \cos(k/2))$  with  $k = k_1 + k_2$ . The two-magnon bound states are characterized by complex wave numbers  $k_1 = u + iv$  and  $k_2 = u - iv$  that may occur when  $\lambda_2 = \lambda_1$  or  $\lambda_2 = \lambda_1 + 1$ , that lead to  $\phi = iNu$  or  $\phi = iNu + \pi$  respectively. In both cases the algebraic constraint

(1.3.35) reduces to the cubic equation in the thermodynamic limit:

$$\rho x^3 - \frac{x^2}{\cos u} + (\rho + 2)x - 2\rho \cos u = 0, \quad (1.3.38)$$

where  $x = e^{-u}$  ( $x$  may be restricted in the  $0 < x < 1$  range) and  $u = (k_1 + k_2)/2$ . Accordingly the excitation energy (1.3.37) reads:

$$E = 2(h - h_2) + 4\rho \left[ 1 + \frac{1}{2} \left( x + \frac{1}{x} \right) \cos u \right]. \quad (1.3.39)$$

Therefore, for any given value of  $u$  for which Eq.(1.3.38) has a root in the interval  $[0, 1]$ , Eq.(1.3.39) yields the excitation energy of the corresponding bound state parametrized by the total crystal momentum  $k = k_1 + k_2$  folded into the fundamental Brillouin zone. If we consider Eq.(1.3.38) near the zone boundary, two real roots emerge, the  $x \approx -\rho \cos u$  provided that  $\cos u < 0$  and  $x \approx 2 \cos u$  provided that  $\cos u > 0$ . These two cases will be referred to as the single-ion bound state and the exchange bound state, respectively. For the first case, we choose to change the variable as:

$$x = \rho \cos(k/2) z, \quad \text{where} \quad z = 1 - \frac{\rho^3 z^3 \cos^2(k/2)}{2 - \rho z}. \quad (1.3.40)$$

For each  $k$  in the range  $[-\pi, \pi]$  the cubic equation can be solved easily by iteration process starting with  $z = 1$ . Actually, for  $\rho \ll 1$  a single iteration yields a sufficiently accurate description of the single-ion bound state:

$$x \approx \rho \left[ 1 - \frac{\rho^3}{2 - \rho} \cos^2(k/2) \right] \cos(k/2), \quad (1.3.41)$$

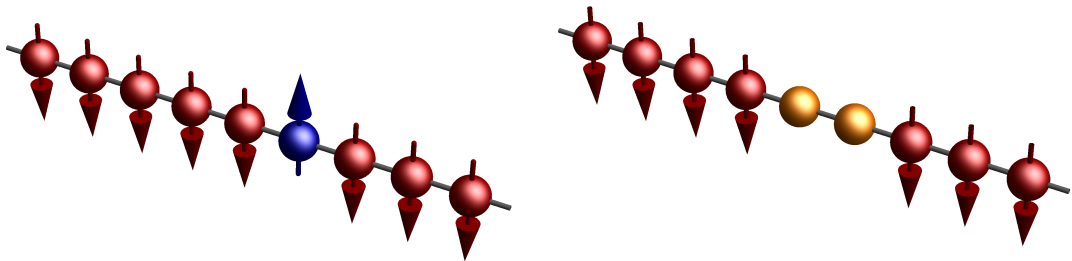


**Figure 1.3.9:** Illustration of the two-magnon states. The bound character of the single-ion state manifests itself in the enhanced probability that the two magnons are at the same site. Similarly for the exchange bound state, that the two spins are on neighboring sites of the chain.

and the exact dispersion (1.3.39) is approximated to third order by:

$$E(k) = 2(h - h_c) + 2 \left[ 1 + 2\rho + \left( \rho^2 + \frac{1}{2}\rho^3 \right) \cos^2(k/2) \right]. \quad (1.3.42)$$

Similarly, the exchange bound state is obtained by changing the variables as:

$$x = 2 \cos(k/2) w, \quad \text{where} \quad w = 1 - \frac{4\rho w^3 \cos^2(k/2)}{\rho - 2w}. \quad (1.3.43)$$

Again we solve the cubic equation by simple iteration starting with  $w = 1$ . The energy–momentum dispersion of the single–ion bound state, as well as the exchange bound state and the single magnon are depicted in Fig. 1.3.10 for  $\rho = 0.1$ . We complete the description by noting that the exchange bound state branches off above the continuum. The single–ion dispersion approaches the continuum as  $\rho$  becomes larger, but never touches its upper side. Instead the single–ion and exchange dispersions merge at the zone boundary for  $\rho = 2$  and exchange roles for  $\rho > 2$ .

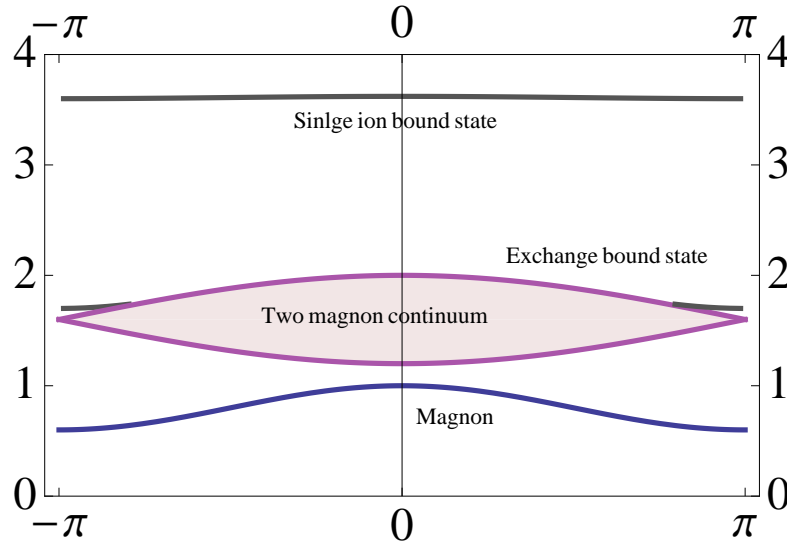


**Figure 1.3.10:** One and two–magnons excitation energies (in units of  $D$ ) for an AFM chain with a small exchange interaction  $\rho = 0.1$  and a typical field  $h = 2 > h_2$ . Blue line corresponds to the single magnon and purple lines indicate the boundaries of the two–magnon continuum. Black lines denote the bound states. The single–ion bound state is well separated above the continuum, while the exchange bound state branches off the continuum near the zone boundary.

In order to gain a better insight about the nature of two–magnons bound states we consider the following limiting cases. First, when  $\rho = 0$  the moments uncouple and the two–magnon bound states can be constructed either by reducing the azimuthal spin by two units at a single site with excitation energy  $\Omega_I = 2h$  or by reducing its value by one unit at two different sites with excitation energy  $\Omega_{II} = -2 + 2h$ . In the presence of exchange interaction, the eigenvalue problem of Eq.(1.3.33) becomes in general more complicated with solutions given in Eqs.(1.3.39), (1.3.40) and (1.3.43). Nevertheless, we

can consider a special case if we require:

$$\begin{aligned} d_n &= (-1)^n, & c_{n,m} &= 0 & \text{with } E &= -4\rho + 2h = \Omega_I \\ c_{n,n+1} &= (-1)^n & c_{n,m} &= 0 = d_n & \text{with } E &= -3\rho - 2 + 2h = \Omega_{II}, \end{aligned} \quad (1.3.44)$$

It can be shown that the single-ion bound state restricted to the zone boundary  $k = \pi$  corresponds to  $\Omega_I$ , while the exchange bound state corresponds to  $\Omega_{II}$ . Of course, such a distinction is possible only at the zone boundary and becomes less meaningful inside the zone.

## 1.4 Three Dimensional Model

The results developed in the preceding sections are completely general for the one-dimensional AFM chain with strong easy plane anisotropy. It is the purpose of this section to generalize the energy-momentum dispersions of the elementary excitation in the presence of three-dimensional couplings. In order to motivate this approach, it is pertinent to consider that real materials are not truly one dimensional, but rather quasi-one-dimensional, where exchange interactions perpendicular to the chain  $J_{\perp}$  are finite, but much smaller than the one along the chain  $J$ . For example, a physical realization of a  $S = 1$  chain in the large- $D$  limit is the organic compound  $NiCl_2 - SC(NH_2)_2$  abbreviated as DTN, that is considered to be the quasi-one-dimensional limit of a three dimensional (3D) system, with  $J_{\perp}/J \simeq 0.18$ . In Chapter 2. we present results of systematic high-field electron spin resonance (ESR) experimental and theoretical studies of this compound, hence the necessity of developing a three-dimensional theoretical analysis. As a starting point, we consider the Hamiltonian:

$$\mathcal{H} = \sum_{i,\nu} J_{\nu}(\mathbf{S}_i \cdot \mathbf{S}_{i+e_{\nu}}) + \sum_i [D(S_i^z)^2 + g\mu_B H S_i^z], \quad (1.4.1)$$

where  $i$  denotes a generic site of a 3D lattice and  $e_{\nu}$  with  $\nu = x, y, z$  count nearest neighbors. The exchange constants  $J_{\nu} = \{J_x, J_y, J_z\}$  may depend on the specific lattice direction and are assumed to be significantly smaller than the easy-plane anisotropy ( $J_{\nu} \ll D$ ). Here and in later discussions we assume that  $J_x = J_y \ll J_z$ . The presence of three-dimensional couplings does not make any significant changes in the overall picture. In short, in the low-field region  $H < H_1$  the ground state carries zero azimuthal spin ( $S^z = 0$ ) while magnon excitations with  $S^z = \pm 1$  are separated by a gap. These magnons are the 3D generalization of excitons and antiexcitons. In the high-field region,  $H > H_2$ , the system has a ferromagnetic ground state and single-particle excitations correspond to eigenstates with a single spin flip relative to the fully ordered ground state. These magnons acquire a nonzero energy gap that increases linearly with the

applied magnetic field. The two-magnon states come in three varieties: a two magnon continuum, a single ion bound state and an exchange bound state. Note that in this section, we are concerned only with the excitations that are relevant to the analysis of the ESR spectrum. For reasons that will become apparent later, bound states in the paramagnetic phase and the exchange bound state in the fully ferromagnetic phase will not be taken into account.

Let us examine the excitations in the case where  $H < H_1$ . The analysis has been done in [67], where a systematic  $1/D$  expansion was developed, carried to third order. The approach is based on a new representation of integer spin  $S$  via bosonic operators, considering the exchange interaction as a perturbation and using the diagram technique. At zero field  $H = 0$  the magnon spectrum consists of two degenerate branches with  $S^z = \pm 1$  and energy-momentum dispersion  $\epsilon(\mathbf{k})$  calculated through a systematic  $1/D$  expansion carried to third order:

$$\begin{aligned} \epsilon(\mathbf{k}) = & D + 2 \sum_{\nu} J_{\nu} \cos k_{\nu} + \frac{1}{D} \left[ 3 \sum_{\nu} J_{\nu}^2 - 2 \left( \sum_{\nu} J_{\nu} \cos k_{\nu} \right)^2 \right] \\ & + \frac{1}{D^2} \left[ 2 \sum_{\nu} J_{\nu}^3 + 4 \left( \sum_{\nu} J_{\nu} \cos k_{\nu} \right)^3 + \frac{5}{2} \sum_{\nu} J_{\nu}^3 \cos k_{\nu} \right. \\ & \left. - 7 \left( \sum_{\mu} J_{\mu}^2 \right) \left( \sum_{\nu} J_{\nu} \cos k_{\nu} \right) - 2 \left( \sum_{\mu} J_{\mu} \cos k_{\mu} \right) \left( \sum_{\nu} J_{\nu}^2 \cos k_{\nu} \right) \right] \end{aligned} \quad (1.4.2)$$

Note that Eq.(1.4.2) coincides with Eq.(1.3.11) under the substitution  $J_x = 0 = J_y$ . For nonzero but sufficiently low fields the  $S^z = 0$  ground state remains unaffected while the degeneracy of the  $S^z = \pm 1$  magnon states is lifted to yield a twofold dispersion:

$$\epsilon(\mathbf{k}) = \epsilon(\mathbf{k}) \pm g\mu_B H. \quad (1.4.3)$$

The critical field  $H_1$  is defined by the smallest gap of dispersion  $\epsilon(\mathbf{k})$ , that occurs at  $k = (\pi, \pi, \pi)$ :

$$\begin{aligned} g\mu_B H_1 = \epsilon(\pi, \pi, \pi) = & D - 2 \sum_{\nu} J_{\nu} + \frac{3}{D} \sum_{\nu} J_{\nu}^2 - \frac{2}{D} \left( \sum_{\nu} J_{\nu} \right)^2 \\ & - \frac{1}{2D^2} \sum_{\nu} J_{\nu}^3 - \frac{4}{D^2} \left( \sum_{\nu} J_{\nu} \right)^3 + \frac{5}{D^2} \left( \sum_{\nu} J_{\nu}^2 \right) \left( \sum_{\mu} J_{\mu} \right) \end{aligned} \quad (1.4.4)$$

When the field  $H$  exceeds its critical value  $H_1$  level crossing occurs and the azimuthal spin of the ground state no longer vanishes but increases with increasing field. A systematic  $1/D$  expansion is not feasible while semiclassical methods are generally inaccurate at strong anisotropy. The same applies for the one-dimensional chain as well. The theoretical model of Eq.(1.4.1) becomes again tractable for sufficiently strong

fields where the ground state is a completely ordered ferromagnetic state with energy  $E_0 = N(D + J_x + J_y + J_z - g\mu_B H)$ . Since the system under consideration is translationally invariant, the single-magnon problem is exactly diagonalized in the basis of well-defined momentum. The energy-momentum dispersion of single-magnon states is given by:

$$\omega(\mathbf{k}) = g\mu_B H - D - 2(J_x + J_y + J_z) + 2(J_x \cos k_x + J_y \cos k_y + J_z \cos k_z) \quad (1.4.5)$$

The lowest gap of this dispersion occurs at  $\mathbf{k} = (\pi, \pi, \pi)$  and is equal to  $g\mu_B H - D - 4(J_x + J_y + J_z)$ . Thus the ordered state is stable when the field exceeds a critical value given by:

$$g\mu_B H_2 = D + 4(J_x + J_y + J_z) \quad (1.4.6)$$

We now turn our attention to two-body states, and more specifically we are interested to calculate the energy-momentum dispersion of the single-ion bound state. We have already discussed that an exact calculation of such states is possible in the 1D model through an elementary Bethe Ansatz. However, a Bethe Ansatz is not applicable to the 3D model studied in this section. Thus we resort to a more direct method developed long time ago by Wortis [68] for the calculation of two-magnon bound states in ferromagnets with arbitrary lattice dimension. The method is here generalized to account for easy-plane anisotropy with strength  $D$  and is employed in conjunction with the  $1/D$  expansion when analytical treatment is no longer feasible. For our purposes it will be sufficient to reproduce the final result of this calculation, while the precise derivation is described in detail in Appendix A. The energy-momentum dispersion of the single-ion bound state in the presence of three dimensional couplings is:

$$E(\mathbf{k}) = 2g\mu_B H + \sum_{m=\{x,y,z\}} \left[ -4J_m + \cos^2(k_m/2) \left( \frac{2J_m^2}{D} + \frac{J_m^3}{D^2} \right) \right]. \quad (1.4.7)$$

This result will prove to be of major importance in explaining experimental data of ESR measurements on real materials. At this point, the 3D generalization of the 1D results has reached to an end. The rest of the two-magnon states are not relevant to the analysis of the ESR spectrum and are thus omitted.

## 1.5 Effective $S=1/2$ description of the $S=1$ chain

In the present section we show that the  $S = 1$  Heisenberg AFM with strong easy-plane anisotropy in a magnetic field can be systematically mapped onto a  $S = 1/2$  XXZ Heisenberg model in a longitudinal magnetic field. A similar analysis has been carried out for non-frustrated and frustrated  $S = 1/2$  ladders in a magnetic field [69] and is valid in the critical region where the magnetization goes from zero to saturation.

This mapping enables us to gain a better physical understanding of the original  $S = 1$  model. For all quantities studied in the following chapters, results for both the  $S = 1$  and  $S = 1/2$  model are presented and compared in order to test the effectiveness of the mapping, and results from the exactly solvable XXZ model are collated to complete the theoretical description.

While the mapping should be possible at any dimension, here we restrict our analysis in the 1D case. The original  $S = 1$  Hamiltonian reads:

$$\mathcal{H} = D \sum_{n=1}^N [\rho \mathbf{S}_n \cdot \mathbf{S}_{n+1} + (S_n^z)^2 + h S_n^z] , \quad (1.5.1)$$

For  $h < h_1$  the ground state  $|\Omega\rangle$  and lowest excitations  $|\Psi_1\rangle$  and  $|\Psi_2\rangle$  (antiexcitons and excitons) are:

$$\begin{aligned} |\Omega\rangle &= |1, 0\rangle \otimes |1, 0\rangle \otimes |1, 0\rangle \otimes |1, 0\rangle \otimes \cdots \otimes |1, 0\rangle , \\ |\Psi_{1,2}\rangle &= \frac{1}{\sqrt{N}} \sum_n e^{ikn} |n_{\mp}\rangle , \end{aligned} \quad (1.5.2)$$

where states  $|n_{-}\rangle$  and  $|n_{+}\rangle$  carry nonzero azimuthal spin equal to  $-1$  and  $+1$  respectively only at the site  $n$ . At zero magnetic field the states  $|\Psi_1\rangle$  and  $|\Psi_2\rangle$  are degenerate with a known energy momentum dispersion  $\epsilon(k)$  (1.3.11) for 1D or (1.4.2) for 3D. This degeneracy is lifted at nonzero magnetic field  $h$  due to the Zeeman energy. Upon increasing  $h$  the state  $|\Psi_1\rangle$  approaches the ground state, whereas the energy difference of states  $|\Psi_1\rangle$  and  $|\Psi_2\rangle$  equals  $2h$  and becomes larger. Close to  $h_1$  the low-energy space is spanned only by states  $|\Psi_1\rangle$  and  $|\Omega\rangle$  and the contribution of  $|\Psi_2\rangle$  can be neglected, see Fig. 1.5.1. A new  $S = 1/2$  representation can be used:

$$\begin{aligned} |\tilde{\Omega}\rangle &= |\downarrow\rangle \otimes |\downarrow\rangle \otimes |\downarrow\rangle \otimes |\downarrow\rangle \otimes \cdots \otimes |\downarrow\rangle , \\ |\tilde{\Psi}_1\rangle &= \frac{1}{\sqrt{N}} \sum_n e^{ikn} |\tilde{n}\rangle , \end{aligned} \quad (1.5.3)$$

where state  $|\tilde{n}\rangle$  differs from  $|\tilde{\Omega}\rangle$  by a spin-up at site  $n$ . From now on, we are using the  $\tilde{A}$  notation for a state or an operator that acts on the  $S = 1/2$  space. The idea is to project the original Hamiltonian into the low-energy subspace (1.5.2) using the  $S = 1/2$  representation of Eq.(1.5.3). The  $S = 1$  spin operators are mapped as follows:

$$\begin{aligned} S_n^+ S_{n+1}^- + S_i^- S_{n+1}^+ &\longrightarrow 2(\tilde{S}_n^+ \tilde{S}_{n+1}^- + \tilde{S}_i^- \tilde{S}_{n+1}^+) \\ S_i^z S_{i+1}^z &\longrightarrow \tilde{S}_i^z \tilde{S}_{i+1}^z + \frac{1}{2}(\tilde{S}_i^z + S_{i+1}^z) + \frac{1}{4} \\ S_i^z &\longrightarrow -\tilde{S}_i^z - \frac{1}{2} \\ (S_i^z)^2 &\longrightarrow \tilde{S}_i^z + \frac{1}{2} \end{aligned} \quad (1.5.4)$$

Therefore, the resulting effective Hamiltonian is:

$$\tilde{\mathcal{H}} = D \sum_n \left[ 2\rho \left( \tilde{S}_n^x \tilde{S}_{n+1}^x + \tilde{S}_n^y \tilde{S}_{n+1}^y + \Delta \tilde{S}_n^z \tilde{S}_{n+1}^z \right) + \tilde{h} \tilde{S}_n^z \right] + \mathcal{H}_0, \quad (1.5.5)$$

where  $\Delta = 1/2$  and

$$\begin{aligned} \tilde{h} &= -\rho - 1 + h \\ \mathcal{H}_0 &= \sum_n \left( \frac{J}{4} + \frac{D}{4} - \frac{H}{2} \right) \end{aligned} \quad (1.5.6)$$

A mapping based on similar considerations is possible for  $h \rightarrow h_2$ , using the single magnon state and the ferromagnetic (FM) ground state:

$$\begin{aligned} |\Omega'\rangle &= |1, -1\rangle \otimes |1, -1\rangle \otimes |1, -1\rangle \otimes |1, -1\rangle \otimes \cdots \otimes |1, -1\rangle, \\ |\Psi'\rangle &= \frac{1}{\sqrt{N}} \sum_n e^{ikn} |n\rangle, \end{aligned} \quad (1.5.7)$$

where state  $|n\rangle$  differs from the ground state by the fact that  $S_n^z = 0$ . By identifying these two states with the  $S = 1/2$  states given in Eq. (1.5.3) the spin operators are mapped as follows

$$\begin{aligned} S_n^+ S_{n+1}^- + S_i^- S_{n+1}^+ &\longrightarrow 2(\tilde{S}_n^+ \tilde{S}_{n+1}^- + \tilde{S}_i^- \tilde{S}_{n+1}^+) \\ S_i^z S_{i+1}^z &\longrightarrow \tilde{S}_i^z \tilde{S}_{i+1}^z + \frac{1}{2}(\tilde{S}_i^z + \tilde{S}_{i+1}^z) + \frac{1}{4} \\ S_i^z &\longrightarrow -\tilde{S}_i^z - \frac{1}{2} \\ (S_i^z)^2 &\longrightarrow -\tilde{S}_i^z - \frac{1}{2} \end{aligned} \quad (1.5.8)$$

and the resulting model is again described by Hamiltonian (1.5.5).

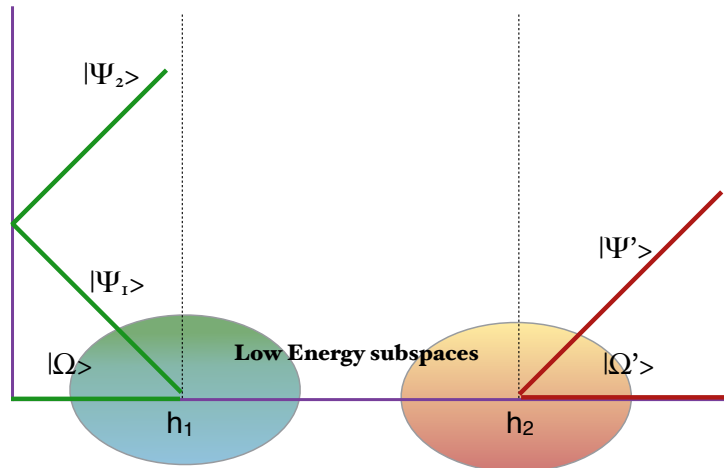


**Figure 1.5.1:** Illustration of the low-energy subspaces (1.5.2) and (1.5.7) in the vicinity of  $h_1$  and  $h_2$ .

To summarize, the original  $S = 1$  Hamiltonian reduces to that of the  $S = 1/2$  *XXZ* Heisenberg AFM chain in the presence of longitudinal magnetic field:

$$\tilde{\mathcal{H}} = D \sum_n \left[ 2\rho \left( \tilde{S}_n^x \tilde{S}_{n+1}^x + \tilde{S}_n^y \tilde{S}_{n+1}^y + \Delta \tilde{S}_n^z \tilde{S}_{n+1}^z \right) + \tilde{h} \tilde{S}_n^z \right], \quad (1.5.9)$$

where  $\Delta = 1/2$  and  $\tilde{h} = -\rho - 1 + h$ . Ferromagnetic order in the ground state is established when the magnetic field exceeds the critical value  $\tilde{h}_c = 2\rho(\Delta + 1)$ . The whole phase can be described by the effective Hamiltonian (1.5.9), where

1. the gapped phase of model (1.5.1) for  $h < h_1$  corresponds to the negatively FM ordered state of model (1.5.9) for  $\tilde{h} < -\tilde{h}_c$ ,
2. the gapless phase of (1.5.1) for  $h_1 < h < h_2$  corresponds to gapless phase of model (1.5.9) for  $-\tilde{h}_c < \tilde{h} < \tilde{h}_c$ ,
3. and the FM state of model (1.5.1) for  $h > h_2$  corresponds to the positively FM ordered state of model (1.5.9) for  $\tilde{h} > \tilde{h}_c$ .

In order to explore the effectiveness of this mapping, a first direct test can be given if we compare the critical fields obtained by the two models. For the first critical field, model (1.5.9) predicts  $h_1 = 1 - 2\rho$ , which coincides with Eq. (1.3.15) only at first order in terms of  $\rho$ , whereas both models predict the same value for the second critical field given by  $h_2 = 1 + 4\rho$ . This is an indication that the mapping should be more accurate close to  $h_2$  rather than  $h_1$ .

The obvious advantage of this mapping is that the  $S = 1/2$  *XXZ* chain is one of the most important models in one-dimension and has played an essential role in the development of exact solutions, in particular of the Bethe ansatz technique. This technique gives explicit analytic expressions for its eigenfunction and eigenvalues, and the thermodynamics can be calculated through a set of nonlinear integral equations. For arbitrary value of  $\Delta$ , the  $S = 1/2$  *XXZ* model is characterized by the following phases:

1. For  $\Delta < -1$  the *XXZ* chain is in the ferromagnetic Ising phase: the ground state is the saturated state with all spins aligned in either  $z$  or  $-z$  direction with magnetization  $S^z = \pm N/2$ . The low-lying excited states in the ferromagnetic phase are magnons with the total spin quantum number  $S^z = N/2 - 1$  with a gap at  $k = 0$  equal to  $|\Delta| - 1$ . At  $\Delta = -1$  the discrete symmetry of spin reflection  $S^z \rightarrow -S^z$  generalizes to the continuous rotational symmetry and the spectrum becomes gapless. Eigenstates in the subspace with two spin deviations,  $S^z = N/2 - 2$  can be found exactly by solving the scattering problem of two magnons. This results in the existence of bound states below the two magnon continuum.
2. For  $\Delta > +1$  the *XXZ* chain is in the antiferromagnetic Ising or Néel phase with broken symmetry and one from 2 degenerate ground states, the  $S = 1/2$  remnants of the classical Néel states. The ground states have  $S^z = 0$  but finite sublattice

magnetization. The elementary excitations are constructed by turning around one spin that breaks two bonds and leads to a state with energy  $\Delta$ , degenerate with all states resulting from turning around an arbitrary number of subsequent spins. These states have  $S^z = \pm 1$  ( $S^z = 0$ ) for an odd (even) number of turned spins, they are called two-domain wall states and are exact eigenstates in the the Ising limit  $\Delta \rightarrow \infty$ . These states are no more eigenstates when  $\Delta^{-1}$  is finite, but for  $\Delta^{-1} \ll 1$ , they can be dealt with in perturbation theory, leading to the excitation spectrum in the first order in  $1/\Delta$ . The excitation spectrum is composed of two entities, domain walls which propagate independently with momenta  $k_1$ , and  $k_2$ . The elementary excitations thus form a continuum with the relative momentum of the two domain walls serving as an internal degree of freedom.

3. For  $-1 < \Delta < +1$  the  $XXZ$  chain is in the  $XY$ -planar phase, characterized by uniaxial symmetry of the easy-plane type and a gapless excitation continuum for sufficiently low magnetic field. This phase is the most interesting from the theoretical perspective; for  $\Delta = 0$  the model reduces to the isotropic  $XY$  model (also known as the  $XX$  model), corresponding to free fermions on a lattice. The point  $\Delta = 1/2$  also turns out to be very interesting, as it develops additional symmetries. For sufficiently strong external magnetic field the ground state becomes fully ferromagnetic and the lowest excitations are exactly known. Actually, this is true for arbitrary value of  $\Delta$ . The ferromagnetic ground state becomes unstable when the lowest spin wave frequency becomes negative. This allows to determine the critical field  $\tilde{h}_c$  that corresponds to the boundary of the ferromagnetic phase, with  $\tilde{h}_c = 2\rho(1 + \Delta)$ .

In the present thesis we shall be interested in the  $\Delta = 1/2$  case that lies in the  $XY$ -planar regime. Thermodynamical and dynamical quantities, known exactly for the  $S = 1/2$  model, will be collated and compared with the  $S = 1$  model, in order to complete the theoretical description of the latter. The  $S = 1/2$   $XXZ$  model has been extensively studied over the years, using a variety of powerful methods such as Bethe ansatz and bosonization. Since this is not a place to develop such techniques, they will be introduced, where necessary, in a rather ad hoc manner. For a detailed analysis the reader can refer to [70], where an introduction to the coordinate Bethe ansatz approach and to the thermodynamics of the model can be found, or to [71] where Algebraic Bethe ansatz and advanced techniques toward the calculation of correlation functions are presented.

## Chapter 2

# Electron Spin Resonance

Electron Spin Resonance (ESR) spectroscopy is an important experimental method which directly probes magnetic properties of materials with unpaired electrons. It is a magnetic resonance technique, that permits the gathering of precise highly detailed magnetic information of a type not obtained in other ways. ESR was invented by the Soviet physicist Zavoisky in 1944 and was further developed by Brebis Bleaney and his group at Oxford University in the next decade. It has been used for over 60 years to study a variety of magnetic materials. Although ESR spectroscopy is supposed to be a mature field, the activity has proceeded at a vigorous pace, pouring out many new concepts. Correspondingly, while the theory of ESR has been studied for a long time [73–75], there remain some important open problems, especially for strongly interacting systems.

The technique depends on the fact that transitions among the levels of the magnetic system can be detected by monitoring the power absorbed from an alternating magnetic field, just as ordinary atomic transitions are detected by absorption of light. The experimental requirements are reasonably clear. The specimen containing the magnetic material is placed in a uniform magnetic field and a small alternating magnetic field is applied. We then arrange to detect the absorption of energy when the frequency  $\omega$  of the alternating field is equal to one of the transition frequencies of the system,  $\hbar\omega = \Delta E$ . Quantitatively, the magnetic resonance frequencies fall typically in the microwave region, 1-10 GHz for applied fields of a few kilogauss. In practice, the ESR spectrum is generated by keeping the frequency incident on the sample stable and varying the uniform magnetic field until the energy difference matches the energy of the microwaves. Comparing the observed transitions with model calculations then lets us detect the energy levels, characterize the materials and explore interesting quantum phenomena.

In Sec. 2.1, a synopsis of the fundamentals of ESR theory is given, followed in 2.2 by a detailed theoretical study of the ESR spectrum of a  $S = 1$  chain with strong anisotropy. Special emphasis is given on the contribution of the two-magnon single-ion bound state.

A numerical analysis through exact diagonalization and a corresponding simulation of the relevant dynamic susceptibilities provides an additional tool in analyzing important features of the ESR spectrum. Attention is also given to generalize our results including three-dimensional couplings. In Sec. 2.3 high-field ESR experimental studies of  $NiCl_2 - 4SC(NH_2)_2$  (DTN) are presented and found consistent with theoretical predictions. Perhaps, the most interesting feature is the experimental signature of the single-ion two-magnon bound state. Furthermore, the theoretical analysis is completed in Sec. 2.4 by calculating the low-lying ESR spectrum throughout the intermediate region using the mapping to the effective  $S = 1/2$  model. The chapter closes with general conclusions mostly concentrated on the agreement between theoretical predictions and experimental findings.

## 2.1 Resonance Theory

In this section we present theoretical concepts for the description of resonance phenomena. The essential aspects of ESR may be illustrated by considering the case of a spin Hamiltonian  $\mathcal{H}_0$  that is invariant under rotations about the  $z$  axis, i.e. the eigenstates and allowed energies are characterized by the azimuthal spin  $m$ . The application of a magnetic field  $\mathbf{H}$  produces an interaction energy  $g\mu_B\mathbf{H}\cdot\mathbf{S}$ . Taking the field to be along the  $z$  direction, the energy levels are shifted by an amount  $\pm g\mu_B H m$  and the system is described by the Hamiltonian

$$\mathcal{H} = \mathcal{H}_0 + \sum_n g\mu_B H S_n^z. \quad (2.1.1)$$

We shall denote the eigenvalues of energy of this many-spin Hamiltonian as  $E_a$ ,  $E_b$  and so on, with corresponding many-spin wave functions  $|a\rangle$ ,  $|b\rangle$ . The presence of such a set of energy levels can be detected by some form of spectral absorption, an interaction that will cause transitions between levels. To satisfy the conservation of energy, the interaction must be time dependent and of such an angular frequency  $\omega$  that  $\hbar\omega = \Delta E$ , where  $\Delta E$  is the difference between the initial and final energy level. Moreover, the interaction must have non vanishing matrix element joining the initial and final states. The coupling most commonly used to produce magnetic resonances is an alternating magnetic field applied perpendicular to the static field. To formalize this idea we consider the time-dependent Zeeman Hamiltonian:

$$H_{pert} = -g\mu_B H_x \sum_n S_n^x \cos(\omega t), \quad (2.1.2)$$

assuming a linearly polarized field. The magnitude of  $H_x$  is usually small, so we can treat this as an additional time-dependent perturbation inducing transitions between

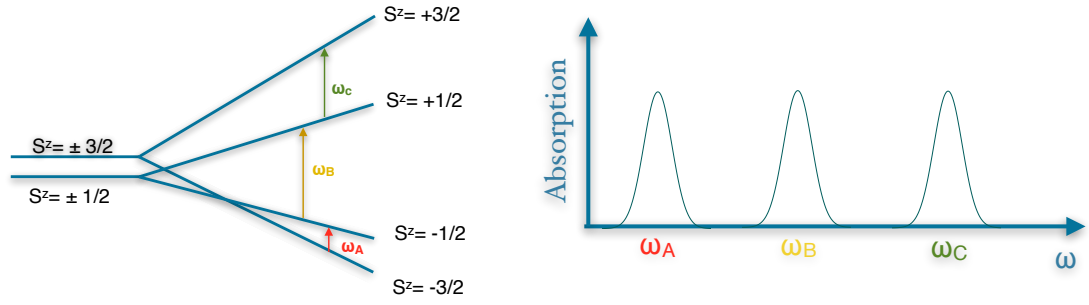


**Figure 2.1.1:** Left: Illustrations of the possible ESR transitions in a magnetic system. It is assumed that the uniform magnetic field is along the symmetry axis of the model, causing a splitting of the energy levels. Right: Sketch of the expected ESR absorption spectrum as a function of frequency.

the energy levels of the unperturbed system. A strong selection rule emerges from this calculation because the operator  $S^x$  must have matrix elements between states  $m$  and  $m'$   $\langle m|S^x|m'\rangle$  which vanish unless  $m' = m \pm 1$ .

Now we are interested in obtaining expressions for the absorption in terms of the wavefunctions and energy levels of the system under study [72]. The states  $|a\rangle$  and  $|b\rangle$  are eigenstates of the Hamiltonian (2.1.1). The most general wavefunction would be a linear combination of such eigenstates:

$$\Psi = \sum_a c_a |a\rangle e^{-iE_a t/\hbar}, \quad (2.1.3)$$

where the  $c_a$ 's are complex constants. The probability  $p(a)$  of finding the system in the eigenstate  $a$  is  $|c_a|^2$ . If the system is in thermal equilibrium, the probability of occupation  $p(a)$  is given by the Boltzmann factor

$$p(E_a) = \frac{e^{-E_a/(kT)}}{\sum_{E_c} e^{-E_c/(kT)}}, \quad (2.1.4)$$

where the sum goes over the entire eigenvalue spectrum. The denominator is the partition function  $Z$  that guarantees the total probability of finding the system in any of the eigenstates is equal to unity, i.e.  $\sum_{E_a} p(E_a) = 1$ . The absorption rate  $P_{ab}$ , due to transitions between between states  $a$  and  $b$ , is given in terms of the probability per second  $W_{ab}$ , that a transition would be induced from  $a$  to  $b$  if the system was entirely in state  $a$  initially:

$$P_{ab} = \hbar\omega W_{ab} (p(E_b) - p(E_a)). \quad (2.1.5)$$

To calculate  $W_{ab}$  we are using elementary quantum mechanics. Suppose we have a time-dependent perturbation  $H_{pert}$  given by:

$$H_{pert} = Fe^{-i\omega t} + Ge^{i\omega t}, \quad (2.1.6)$$

where  $F$  and  $G$  are operators. For  $H_{pert}$  to be Hermitian,  $F$  and  $G$  are related as:

$$\langle a|F|b\rangle = \langle b|G|a\rangle^*, \quad (2.1.7)$$

for all states  $|a\rangle$  and  $|b\rangle$ . Under the action of such a perturbation we can write that  $W_{ab}$  is time independent and is given by the formula:

$$W_{ab} = \frac{2\pi}{\hbar} |\langle a|F|b\rangle|^2 \delta(E_a - E_b - \hbar\omega), \quad (2.1.8)$$

provided that all calculations are for times  $t > \tau$ , where  $\tau$  is a characteristic time that satisfies the conditions: (a) the populations change only a small amount in  $\tau$  and (b) the possible states between which absorption can occur must be spread in energy continuously over a range  $\delta E$  such that  $\delta E \gg \hbar/\tau$ . These conditions are violated if the perturbation matrix element  $|\langle a|F|b\rangle|$  exceeds the line width, and it does when a very strong alternating field is applied. By summing all states with  $E_a > E_b$  we find the average power absorbed  $P(\omega)$  from an alternating magnetic field with frequency  $\omega$ :

$$P(\omega) = \frac{2\pi}{\hbar} \frac{H_x^2}{4} \hbar\omega \sum_{E_a > E_b} (p(E_b) - p(E_a)) |\langle a|\mu_x|b\rangle|^2 \delta(E_a - E_b - \hbar\omega), \quad (2.1.9)$$

where  $\mu_x = \sum_n S_n^x$  is the total spin in the  $x$  direction. This formula explicitly connects the macroscopic quantity  $P$  and microscopic quantities such as eigenstates, matrix elements and energy levels of the system. As long as  $E_a > E_b$ , only positive  $\omega$  will give absorption because of the  $\delta$  function. If we remove the restriction  $E_a > E_b$ , the meaning of  $P$  is extended to negative  $\omega$ .

A simple inspection of Eq.(2.1.9) reveals that for a state  $|a\rangle$  characterized by a given azimuthal spin  $m$  and wavevector  $k$  and for a state  $|b\rangle$  with  $m'$  and  $k'$ , the matrix elements  $\langle a|\mu_x|b\rangle$  are nonzero only when the following selection rules apply:

$$\begin{aligned} \Delta m &= m' - m = \pm 1 \\ \Delta k &= k' - k = 0 \end{aligned} \quad (2.1.10)$$

In the presence of the time-dependent Zeeman Hamiltonian (2.1.2), the induced magnetization in the  $\alpha$  direction is given by:

$$M_\alpha(\omega) = -(g\mu_B)^2 \chi_{\alpha x}(\omega) H_x(\omega), \quad \text{with} \quad \alpha = \{x, y, z\} \quad (2.1.11)$$

Within linear response theory, the spin magnetic susceptibility  $\chi_{\alpha\beta}$  is:

$$\chi_{\alpha\beta} = \frac{1}{Z} \sum_{a,b} (e^{-\beta E_b} - e^{-\beta E_a}) \frac{\langle b|S^\alpha|a\rangle \langle a|S^\beta|b\rangle}{E_a - E_b - \omega - i\eta}, \quad (2.1.12)$$

If we break susceptibility to its real and imaginary part,  $\chi_{\alpha\beta}(\omega) = \chi'_{\alpha\beta}(\omega) + i\chi''_{\alpha\beta}(\omega)$  and use the following identity:

$$\frac{1}{x \pm i\eta} = P(1/x) \mp i\pi\delta(x), \quad (2.1.13)$$

we arrive at the formula:

$$\chi''_{xx}(\omega) = \chi''(\omega) = \pi \sum_{a,b} (p(E_b) - p(E_a)) |\langle a|\mu_x|b\rangle|^2 \delta(E_a - E_b - \hbar\omega). \quad (2.1.14)$$

Combining Eq.(2.1.9) and Eq.(2.1.14) we find that

$$P(\omega) = \frac{\omega}{2} \chi''(\omega) H_x^2. \quad (2.1.15)$$

This equation provides a simple connection between the power absorbed,  $\chi''(\omega)$  and the strength of the alternating field and we shall use it as a basis for the calculation of  $P$ . Note that since  $p(E_b) - p(E_a)$  changes sign when  $a$  and  $b$  are interchanged,  $\chi''(\omega)$  is an odd function of  $\omega$ . Moreover, we recognize that the validity of Eqs. (2.1.14) and (2.1.15) does not depend on the assumptions made here, namely a  $U(1)$  invariant Hamiltonian  $\mathcal{H}_0$  and a uniform magnetic field along the  $z$  direction. Additionally, it is also possible to observe absorption of the electromagnetic wave polarized parallel to the static magnetic field, so called Voigt configuration. The standard configuration for an electromagnetic field polarized perpendicular to the static magnetic field is called Faraday configuration.

It is difficult to theoretically study the ESR spectrum, because the absorption spectrum is related to dynamical correlation functions. An analytical calculation of  $\chi''(\omega)$  is out of question except in very special cases [76]. Traditionally, one has to make crude approximations, such as the high-temperature approximation [72], the classical spin approximation and the decoupling of correlation functions. However, these approximations break down when the many-body correlations become important. Field-theory techniques can be used to describe the universal low-energy large-distance behavior [77] and numerical methods can be a perfect tool when analytical methods fail.

## 2.2 ESR studies for the AFM $S = 1$ chain with strong anisotropy

In this section we present a theoretical study of ESR in  $S = 1$  chains with strong planar anisotropy and an exchange interaction that is antiferromagnetic. The analysis extends throughout the various phases of the system, namely the paramagnetic phase for  $h < h_1$ , the intermediate phase for  $h_1 < h < h_2$  and the ferromagnetic phase for  $h > h_2$ . The essential features of the ESR spectrum have been accounted for the 1D model in an earlier work of Papanicolaou *et. al.* in [76], where they provided a calculation of ESR for large- $D$  systems and exchange interaction that is either FM or AFM. This work is employed in the present thesis to discuss some open questions, with special emphasis on the remaining discrepancies between theory and experiment. A three-dimensional analysis is also developed to provide predictions that go beyond the quasi-one-dimensional limit and are closer to the experimental data of DTN. Yet there are several questions that are difficult to settle analytically, such as the calculation of intensities of the various ESR modes and the structure of the spectrum in the intermediate phase. Thus, in Sec. 2.2.2 we carry out calculations within a 1D model through exact diagonalization on finite chains and a corresponding simulation of the relevant dynamic susceptibilities. Most of the results were originally presented in Ref. [49].

### 2.2.1 One-Dimensional ESR spectrum

We remind the reader that the  $S = 1$  AFM magnetic chains are governed by the Hamiltonian:

$$\mathcal{H} = \sum_n ((S_n^z)^2 + \rho(\mathbf{S}_n \cdot \mathbf{S}_{n+1}) + h S_n^z), \quad (2.2.1)$$

with  $\rho = J/D$  and  $h = g\mu_B H/D$ . To complete the description of rationalized units we note that  $\beta = 1/T$ , where  $T$  is units of  $D$ , and the unit of frequency  $\omega$  is  $D/\hbar$ . Therefore the Planck constant will not appear explicitly in our calculations. The region of interest is  $D \gg J$  or  $\rho \ll 1$ .

On the basis of the preceding explicit results presented in Chapter 1, we now discuss various features of ESR. Before we turn our attention to the full problem with finite  $\rho$  it is illustrative to discuss the limit of vanishing exchange anisotropy,  $\rho = 0$ , that provides a valuable guide for understanding magnetic chains with  $\rho \ll 1$ .

**Vanishing exchange constant  $\rho = 0$ :** This limit provides the only possibility for an exact analytical calculation of  $\chi''(\omega)$ . At  $\rho = 0$  the spins uncouple and the eigenstates are given by the  $S = 1$  basis  $|1, 0\rangle$ ,  $|1, \pm 1\rangle$  with eigenvalues  $\epsilon_0 = 0$  and  $\epsilon_{\pm} = 1 \pm h$  correspondingly. Note that level crossing occurs at  $h_{cr} = 1$ , where the energy  $\epsilon_-$  becomes equal to  $\epsilon_0$ .

The partition function  $z$  at a single site is  $z = 1 + e^{-\beta\epsilon_+} + e^{-\beta\epsilon_-}$ . A straightforward calculation of Eq. (2.1.14) yields:

$$\begin{aligned} \chi''(\omega) = & \frac{N\pi}{2z} \left[ (1 - e^{-\beta\epsilon_+})\delta(\epsilon_+ - \omega) + (1 - e^{-\beta\epsilon_-})\delta(\epsilon_- - \omega) \right. \\ & \left. + (e^{-\beta\epsilon_+} - 1)\delta(\epsilon_+ + \omega) + (e^{-\beta\epsilon_-} - 1)\delta(\epsilon_- + \omega) \right], \end{aligned} \quad (2.2.2)$$

where  $N$  is the total number of spins. As expected,  $\chi''(\omega)$  is an odd function of frequency and only two of the four terms survive at positive frequencies. The ESR analysis depend on the strength of the bias field  $h$ ; there are two different phases marked by the critical field  $h_{cr}$ .

- (a) For  $h < h_{cr} = 1$  the energy levels are ordered as  $\epsilon_0 < \epsilon_- < \epsilon_+$  and only the first two terms in Eq.(2.2.2) survive for positive  $\omega$ . Both of them respect the selection rule  $\Delta m = \pm 1$ . The first corresponds to  $\Delta m = 1$  transitions from the ground state  $|1, 0\rangle$  to the state  $|1, 1\rangle$  with resonance frequency  $\omega_A = \epsilon_+ - \epsilon_0 = 1 + h$ , while the second to  $\Delta m = -1$  transitions from the ground state to the  $|1, -1\rangle$  with resonance frequency  $\omega_B = \epsilon_- - \epsilon_0 = 1 - h$ . The corresponding intensities of these transitions may be inferred from the coefficients of the  $\delta$  functions multiplied by  $\omega$ . Note that the intensity of the ESR line  $\omega_B$  vanishes at  $h = 1$ .
- (b) For  $h > h_{cr} = 1$  the energy levels are ordered as  $\epsilon_- < \epsilon_0 < \epsilon_+$ . At positive frequencies, only the first and fourth terms in Eq.(2.2.2) survive. The fourth term corresponds to a  $\Delta m = 1$  transition from the ground state  $|1, -1\rangle$  to  $|1, 0\rangle$  with resonance frequency  $\omega_C = \epsilon_0 - \epsilon_- = h - 1$ , and the first to a  $\Delta m = 1$  transition from  $|1, 0\rangle$  to  $|1, 1\rangle$  with resonance frequency  $\omega_D = \epsilon_+ - \epsilon_0 = h + 1$ . This is a transition between excited states and its intensity vanishes at zero temperature.

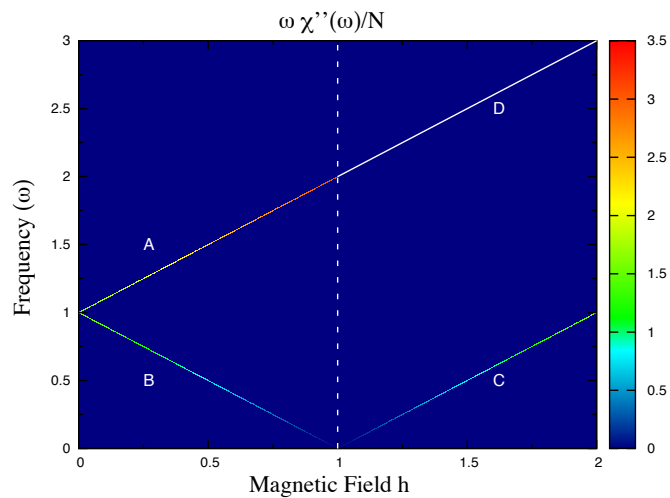


**Figure 2.2.1:** Field dependence of the resonance lines at vanishing exchange interaction and zero temperature. Colored surface represents the ESR intensity  $P \sim \omega\chi''(\omega)$ , where  $\chi''(\omega)$  is given by Eq.(2.2.2). The intensity of  $\omega_D$  vanishes at zero temperature, because the transition takes place between excited states.

These results are summarized in Fig. 2.2.1 in which we plot the resonance frequencies  $\omega_A$ ,  $\omega_B$ ,  $\omega_C$  and  $\omega_D$  as a function of field  $h$ . Line  $\omega_D$  for  $h > 1$  is the continuation of line  $\omega_A$  for  $h < 1$ . All ESR lines are straight because the uniform field preserves the azimuthal symmetry of the problem. If the uniform field was applied in the basal plane, e.g.  $\mathbf{h} = (h, 0, 0)$ , the analysis would be similar with resonance frequencies  $\omega \sim \sqrt{\text{const.} + h^2}$ .

An important assumption made to derive Eq.(2.2.2) is that sums extend over all eigenstates of the single-spin Hamiltonian  $W = (S^z)^2 + h S^z$ . To make a connection with the full spin Hamiltonian (2.2.1) one has to sum over all eigenstates of the complete chain with  $N$  spins. Following the discussion at the end of section 1.3 it is easy to notice that for  $h < 1$  all  $\Delta m = 1$  transitions of the  $N$ -spin Hamiltonian lead to a common resonance frequency  $\omega_A$  and all  $\Delta m = -1$  transitions lead to a common frequency  $\omega_B$ . The corresponding contributions to the intensity add up coherently to produce the correct linear dependence on  $N$  anticipated in Eq.(2.2.2). The same applies for  $h > 1$ , where all transitions lead to common frequencies  $\omega_{C,D}$ .

**Finite  $\rho \ll 1$  exchange constant:** When the exchange interaction is turned on, the various processes do not lead to a common transition frequency, making the calculation of  $\chi''(\omega)$  impossible. However, at low temperatures the ESR spectrum is dominated from transitions between the ground state and the lowest-excited states, or between excited states that obey the selection rules of Eq.(2.1.10) but with vanishing intensity at  $T = 0$ . Therefore, we are keeping only the first few terms in Eq.(2.1.14) to obtain the main results at low temperature.

For  $h < h_1$ , ESR transitions from the ground state take place only to  $k = 0$  excitons and antiexcitons (see Fig. 2.2.2) with corresponding resonance frequencies:

$$\begin{aligned}\omega_A = \epsilon_+(k = \pi) &= (1 + 2\rho + \rho^2 - \frac{1}{2}\rho^3 + \dots) + h \\ \omega_B = \epsilon_-(k = \pi) &= (1 + 2\rho + \rho^2 - \frac{1}{2}\rho^3 + \dots) - h.\end{aligned}\quad (2.2.3)$$

These lines differ from their  $\rho = 0$  counterparts by an upward displacement. (Anti)exciton dispersion  $\epsilon_{\pm}(k)$  is given in Eqs.(1.3.11)-(1.3.14). The most important contributions in  $\chi''(\omega)$  are given by these transitions that lead to:

$$\chi''(\omega) \approx \frac{N\pi f_0}{2Z} \left[ (1 - e^{-\beta\omega_A})\delta(\omega_A - \omega) + (1 - e^{-\beta\omega_B})\delta(\omega_B - \omega) \right], \quad (2.2.4)$$

where the amplitude  $f_0$  is given by [78]:

$$f_0 = 1 - 2\rho + \frac{3}{3}\rho^2 + \dots \quad (2.2.5)$$

At the limit of  $T = 0$ , the partition function becomes equal to 1 and  $\chi''$  becomes:

$$\chi''(\omega) = \frac{N\pi f_0}{2} (\delta(\omega_A - \omega) + \delta(\omega_B - \omega)). \quad (2.2.6)$$

Eq.(2.2.6) is exact in the limit of zero temperature, and the only approximation is the one related to the fact that  $\omega_A$ ,  $\omega_B$  and  $f_0$  are given as series up to third order in  $\rho$ . At finite temperatures, line broadening of sharp lines  $\omega_{A,B}$  occurs thanks to higher-order processes. For example,  $\Delta m = 1$  transitions from the exciton state to the two-body exciton-exciton sector, or from the antiexciton to the exciton-antiexciton sector will yield a signal that contributes to broadening of line  $\omega_A$ . Similarly,  $\Delta m = -1$  transitions, from the antiexciton state to the antiexciton-antiexciton sector, or from the exciton to the exciton-antiexciton sector contribute to broadening of line  $\omega_B$ . A related fact is that the maxima of power absorption may acquire a mild temperature dependence.

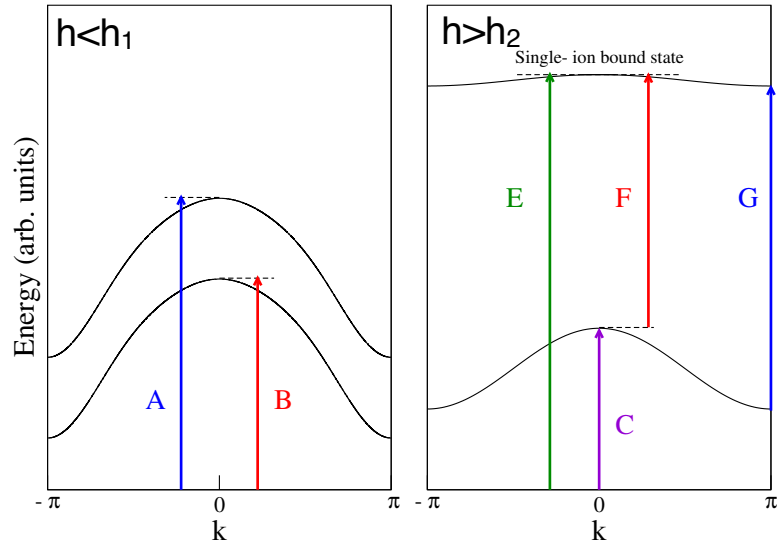


**Figure 2.2.2:** A schematic view of the energy-momentum dispersions of magnetic excitations in an  $S = 1$  Heisenberg chain with strong easy-plane ( $D > 0$ ) anisotropy for two typical fields  $h < h_1$  (left) and  $h > h_2$  (right). Note that the ESR transitions denoted by  $A$ ,  $B$ ,  $C$ ,  $E$  and  $F$  occur at  $k = 0$ , whereas transition  $G$  occurs at  $k = \pi$ . Two-particle continua are not shown for simplicity.

For  $h > h_2$  the only ESR transition that survives in the  $T \rightarrow 0$  limit is the one between the ferromagnetic ground state and a single magnon at  $k = 0$  (see Fig. 2.2.2) with resonance frequency:

$$\omega_C = \omega(k = 0) = h - 1, \quad (2.2.7)$$

where  $\omega(k)$  is the magnon dispersion given in Eq.(1.3.31). Line  $\omega_C$  is  $\rho$  independent and coincides with the corresponding frequency in the limit  $\rho = 0$ . The single-magnon

contribution to susceptibility is

$$\chi_1''(\omega) = \frac{N\pi}{2Z}(1 - e^{-\beta\omega_C})\delta(\omega_C - \omega). \quad (2.2.8)$$

The complete susceptibility  $\chi''(\omega)$  coincides exactly with Eq.(2.2.8) in the limit of zero temperature. At finite, but small, temperature there are additional allowed  $\Delta m = \pm 1$  contributions to the spectrum, which originate from transitions between the single-magnon state and a two magnon state. A transition between a magnon and a state in the two-magnon continuum or an exchange bound state yields signal that is roughly superimposed with the basic magnon line  $C$  and contributes to its broadening. On the contrary, transitions between a magnon and a single-ion bound state make a distinct contribution to susceptibility that is clearly separated from the magnon resonance  $C$  (see Fig. 2.2.2). These are absent at zero temperature but may occur with nonvanishing intensity at finite temperature. The corresponding resonance frequencies are then given by  $\omega_{FG}(k) = E(k) - \omega(k)$ , where  $E(k)$  is the dispersion of the single-ion bound state given in Eqs.(1.3.39)-(1.3.43). Note that in this case transitions occur for every  $k$  in the Brillouin zone, and resonance frequencies are expected to be observed throughout a band  $\omega_F < \omega < \omega_G$ , where the boundary lines are defined as:

$$\begin{aligned} \omega_F &= E(k=0) - \omega(k=0) = h + 1 - 4\rho + 2\rho^2 + \rho^3 + \dots, \\ \omega_G &= E(k=\pi) - \omega(k=\pi) = h + 1. \end{aligned} \quad (2.2.9)$$

Frequency  $\omega_G$  is an exact result independent of the exchange constants, in analogy with the resonance frequency  $\omega_C$  of Eq.(2.2.7). Moreover, it coincides with its  $\rho = 0$  counterpart  $\omega_D$  but is no longer the continuation of the exciton line  $A$  that acquires a nontrivial  $\rho$ -dependence given by Eq.(2.2.3). Therefore absorption by the single-ion bound state is distributed over a frequency band with a width

$$\Delta_\rho = \omega_G - \omega_F = 4\rho - 2\rho^2 - \rho^3 + \dots \quad (2.2.10)$$

Next task is to determine the distribution of power absorption over the  $FG$  band. Contributions from a single-magnon to a two-magnon state are isolated in Eq.(2.1.14)

$$\chi_2''(\omega) \approx \frac{N}{Z}(1 - e^{-\beta\omega}) \int_0^\pi dk e^{-\beta\omega(k)} |f(k)|^2 \delta(E(k) - \omega(k) - \omega), \quad (2.2.11)$$

where  $f(k) = \langle \psi_2(k) | \mu_x | \psi_1(k) \rangle$  is the matrix element of the total moment between the normalized wavefunctions of a magnon  $|\psi_1(k)\rangle$  given in Eq.(1.3.30) and two-magnons  $|\psi_2(k)\rangle$  given in Eq.(1.3.32). Using the explicit wave functions, the matrix element is

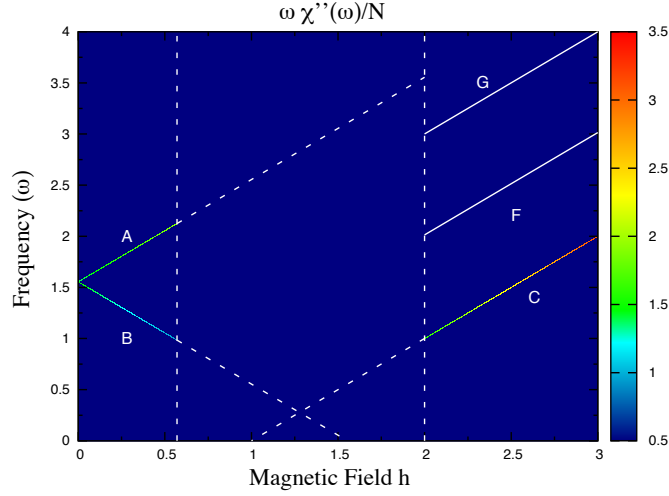


**Figure 2.2.3:** Field dependence of the ESR spectrum for an AFM chain with a small exchange interaction  $\rho = 0.25$  at zero temperature. Colored surface represents the ESR intensity  $P \sim \omega \chi'(\omega)$ , where  $\chi''(\omega)$  is given by Eq.(2.2.6) and (2.2.8). The location of critical fields  $h_1 = 0.57$  and  $h_2 = 2$  is indicated by vertical dashed lines. At the zero- $T$  limit, there is an absence of intensity of the  $FG$  band. The resonance lines  $A$ ,  $B$ , and  $C$  are continued as dashed lines into the intermediate phase  $h_1 < h < h_2$  to indicate the lack of analytical calculations of the low-lying excitation spectrum for such field values.

calculated as:

$$\begin{aligned}
 |f(k)|^2 &= \frac{X}{2Y}, \\
 X &= \left[ 1 - \frac{2(x - \cos(k/2))}{1 - 2x \cos(k/2) + x^2} \left( x + \frac{1}{x} - \frac{1}{\rho \cos(k/2)} \right) \right], \\
 Y &= 1 + \frac{1}{1 - x^2} \left( x + \frac{1}{x} - \frac{1}{\rho \cos(k/2)} \right), \tag{2.2.12}
 \end{aligned}$$

where  $x$  satisfies the cubic equation (1.3.40) and is given by the approximate expression (1.3.41). Performing the  $k$  integration in Eq.(2.2.11) yields

$$\chi''_2(\omega) = \frac{N}{Z} (1 - e^{-\beta\omega}) e^{-\beta\omega(k)} d(k), \tag{2.2.13}$$

where

$$d(k) = \frac{|f(k)|^2}{\left| \frac{d(E(k) - \omega(k))}{dk} \right|} \tag{2.2.14}$$

As was argued in Ref. [76] the intensity is expected to display a characteristic double peak, an enhancement around the band edges, although nonvanishing absorption occurs throughout the  $FG$  band. Therefore, both frequencies  $F$  and  $G$  are associated with the single-ion bound state and are relevant for the analysis of actual experiments.

Finally, we return briefly to the possibility of a  $\Delta S^z = 2$  transition between the ordered ground state and a  $k = 0$  single-ion bound state, which would lead to a resonance

frequency

$$\omega_E = \omega_F + \omega_C \quad (2.2.15)$$

but zero intensity thanks to the axial symmetry adopted in our theoretical model. However, in real experimental setups, field misalignment or deviations from strict axial symmetry of the crystal may render mode  $E$  observable.

There are several questions that have not been answered so far, such as the calculation of the full  $\chi''(\omega)$  at finite  $T$ , and most importantly the structure of the spectrum in the intermediate phase. Thus, in the following section we carry out calculations through exact diagonalization on finite chains and a corresponding simulation of the  $\chi''(\omega)$  for a wide range of magnetic fields.

### 2.2.2 Numerical Calculation of the Power Absorption

In order to elucidate the issues raised in the preceding section, we carry out an explicit calculation of power absorption. Since the analytical calculation of  $\chi''(\omega)$  is out of question, we resort to a numerical calculation based on Eq.(2.1.14) and a complete diagonalization of the  $S = 1$  Hamiltonian of Eq.(2.2.1) defined on a finite periodic chains with size  $N$  as large as 12. Actually, explicit results presented below were obtained on a chain with  $N = 10$ , whereas  $N = 12$  chains were occasionally used for consistency checks. Details on the exact diagonalization (ED) technique used are briefly discussed in Appendix. B.

A test about the efficiency of the numerical calculation on a finite chain can be provided by comparing the numerically obtained gap of the (anti)exciton dispersion at  $k = \pi$  with the one calculated at the thermodynamic limit given by Eq.(1.3.11). Inspection of Fig. 2.2.4 reveals that the finite chain numerical calculation provides an accurate estimate of critical field  $h_1$  for anisotropies up to  $\rho \simeq 0.8$ . In calculations presented in this section, we adopt the value  $\rho = 0.25$  in order to achieve semi-quantitative agreement with experimental data of DTN that will be presented in Sec. 2.3.

On a finite chain Eq.(2.1.14) yields a susceptibility that is a sum of weighted  $\delta$ -functions and is thus rather spiky. Hence we adopted an empirical smoothing process to obtain an intensity

$$I = I(f, h, \tau) \quad (2.2.16)$$

that is a reasonably smooth function of frequency  $f = \omega/(2\pi)$ , magnetic field  $h$ , and temperature  $\tau = T/D$ . Our main task is then to analyze the calculated intensity as a function of all three variables.

In Fig. 2.2.5 we depict the intensity  $I(f, h, \tau)$  as a function of frequency  $f$  for  $\rho = 0.25$ , at a fixed temperature  $\tau = 0.2$  and four typical values of magnetic field  $h$ . For

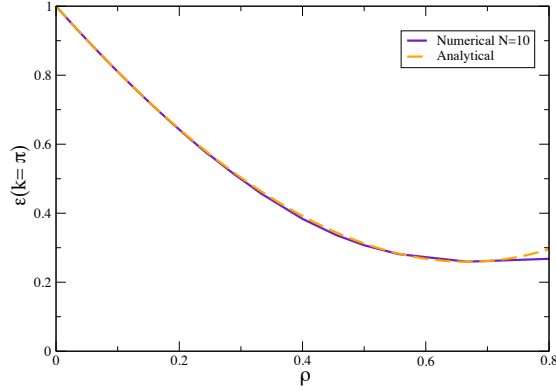


**Figure 2.2.4:** Energy gap of the (anti)exciton dispersion at  $k = \pi$ . Orange line corresponds to the theoretical value obtained within a strong-coupling expansion in the thermodynamic limit and purple line to the one obtained through a numerical exact diagonalization of a finite chain of length  $N = 10$ .

$h < h_1$  lines  $A$  and  $B$  coincide exactly with resonance frequencies  $\omega_A$  and  $\omega_B$  and line-broadening occurs thanks to higher-order processes that take place at finite temperature. In the intermediate region, lines  $\omega_{A,B}$  are extended but they lose their intensity as  $h \rightarrow h_m$ , where  $h_m = (h_1 + h_2)/2$  denotes approximately the center of the intermediate region. Moreover, an additional line is developed that roughly coincides with the extension of resonance line  $\omega_G$ , one of the boundaries of the  $FG$  band. For  $h_m < h < h_2$ , an extension of resonance line  $C$  appears, while line  $G$  loses its intensity and vanishes at  $h > h_2$ . In the ferromagnetic phase, only line  $C$  is present, because temperature is low to yield a significant signal for the single-ion bound state.

In order to establish a coherent picture of the ESR spectrum in the intermediate phase at relatively low temperatures, we calculate the intensity  $I(f, h, \tau)$  for a wide range of magnetic fields and we are thus in position to track the evolution of ESR lines as the magnetic field varies. In Fig. 2.2.6 we present our results for the (colored) surface  $I = I(f, h)$  at fixed temperature  $\tau = 0.2$  which is a typical relatively low temperature of experimental interest [42]. Superimposed in the same figure are the analytical predictions for the two critical fields  $h_1 = 0.57$  and  $h_2 = 2$ , as well as corresponding predictions for the resonance lines  $A, B$  for  $h < h_1$  and  $C, F, G$  for  $h > h_2$ .

Several important facts have already become apparent in Fig. 2.2.6 which we analyse in turn:

- (a) In the paramagnetic phase, we note that the magnon resonance lines  $A$  and  $B$  coincide with the maxima of the calculated intensity as expected in the low-temperature region. Nevertheless, the chosen temperature is sufficiently high to account for the anticipated line broadening which is also apparent.
- (b) In the intermediate region  $h_1 < h < h_2$ , where analytical predictions are practically absent, the most conspicuous feature is a tail of line  $G$  with strong intensity which persists even at very low temperatures. Therefore, the  $G$ -tail corresponds to some

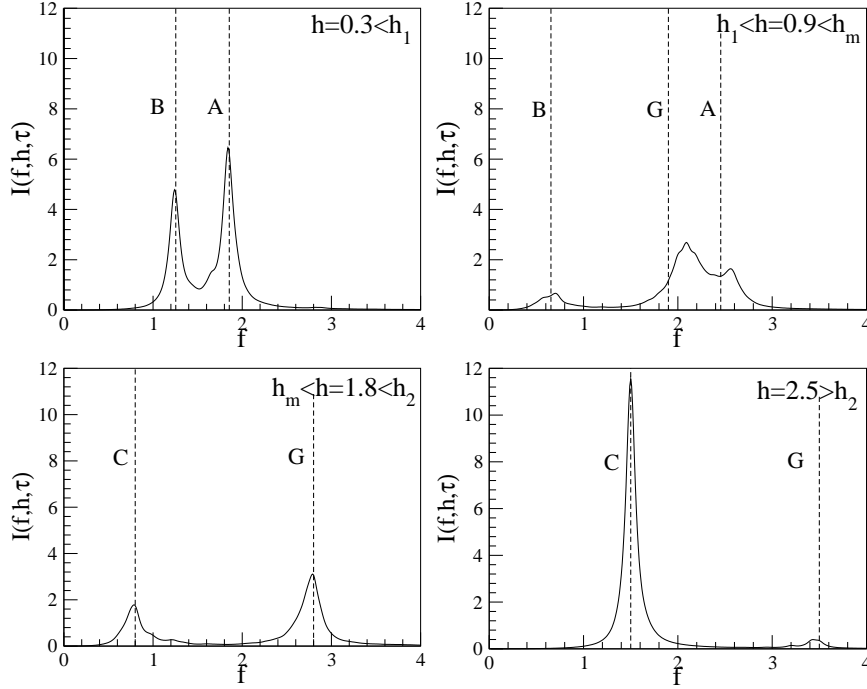


**Figure 2.2.5:** Calculated normalized intensity  $I(f, h, \tau)$  as a function of frequency  $f$  for  $\rho = 0.25$  at a fixed temperature  $\tau = 0.2$  and four typical values of magnetic field  $h$ . Field  $h_m = (h_1 + h_2)/2$  denotes approximately the center of the intermediate phase. Vertical lines  $A$ ,  $B$ ,  $C$  indicate the location of resonance frequencies  $\omega_A$ ,  $\omega_B$  and  $\omega_C$ , while line  $G$  indicates the position of the one of the boundaries of the single-ion (FG) band.

sort of a collective excitation that appears in the intermediate phase as a shadow of the single-ion two-magnon bound state, and requires further theoretical investigation. On the other hand, mode  $F$  acquires a tail into the intermediate region with intensity that diminishes at low temperature and is thus invisible in Fig. 2.2.6. We note that the lines  $A$ ,  $B$  and  $C$  also acquire tails but with intensity that gradually vanishes as one approaches the center of the intermediate phase.

- (c) In the ferromagnetic phase, Fig. 2.2.6 indicates absence of measurable intensity in the single-ion (FG) band at the relatively low temperature  $\tau = 0.2$ . The ESR spectrum is dominated by resonance line  $C$ .

Fig. 2.2.6 completes the missing parts of Fig. 2.2.3 in the intermediate region and at finite temperature. The structure of tails of lines  $A$  and  $C$  becomes apparent in Fig. 2.2.7 which focuses on the low-frequency end of the intermediate phase. Thus we reveal a  $V$ -like structure with intensity that gradually vanishes as one approaches the center. This picture apparently contradicts the result of Cox *et al* [80] who predict by a similar calculation a  $Y$ -like structure with intensity that remains finite and practically constant near the center. On the other hand, our result is consistent with a rounding of a  $V$  into a  $U$  structure predicted to occur in the presence of a small Dzyaloshinskii–Moriya anisotropy treated by a semiclassical method [82].

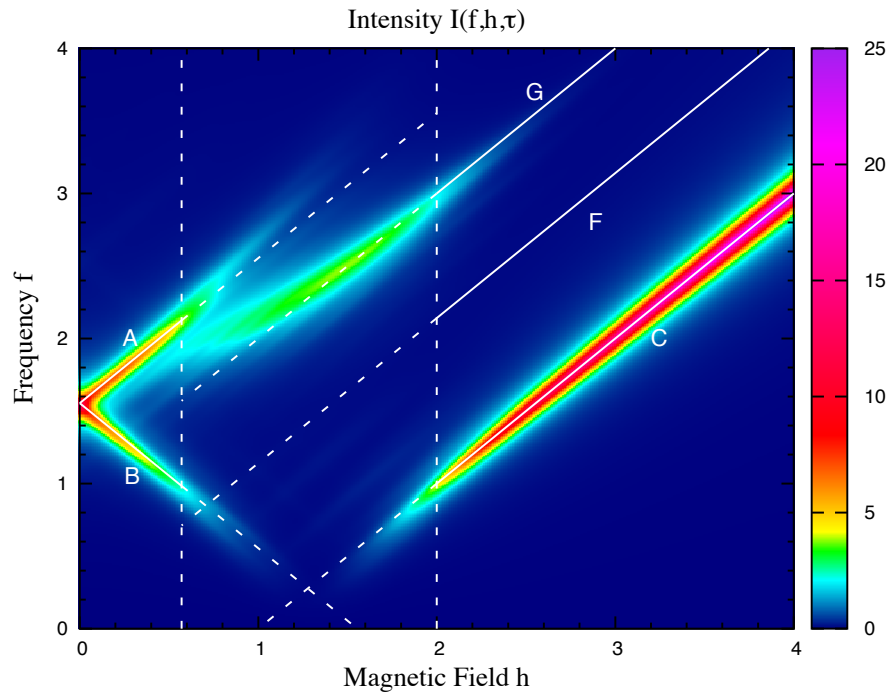


**Figure 2.2.6:** Colored surface represents the normalized ESR intensity  $I(f, h, \tau)$  calculated for a spin chain with  $N = 10$  as a function of frequency  $f$  and magnetic field  $h$ , at fixed temperature  $\tau = 0.2$ . Solid lines correspond to analytical results and are deliberately extended as dashed lines into the intermediate region  $h_1 < h < h_2$ . The location of critical fields  $h_1 = 0.57$  and  $h_2 = 2$  is indicated by vertical dashed lines.

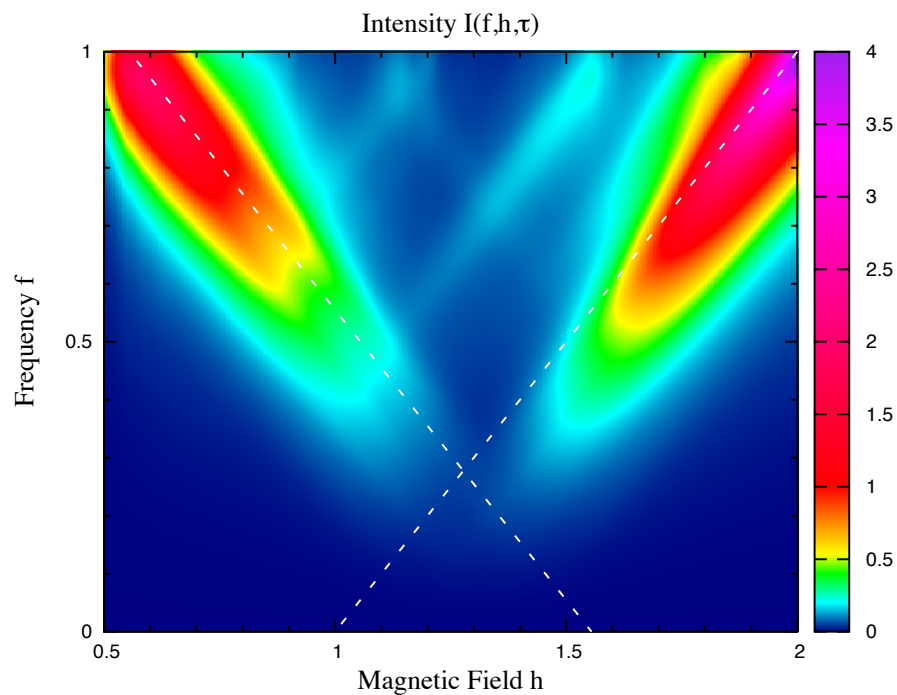


**Figure 2.2.7:** Same as Fig. 2.2.6 but now focusing on the low-frequency end of the intermediate phase  $h_1 < h < h_2$ . Note the formation of a V-like structure with rapidly decreasing intensity as one approaches the center of the intermediate phase.

Next we focus on the appearance of the  $FG$  band upon increasing of temperature. In Fig. 2.2.8 we depict the intensity as a function of frequency at a fixed field  $h = 2.5 > h_2$  and selected values of temperature. At the lowest temperature  $\tau = 0.1$  considered in Fig. 2.2.8, the dominant feature is the magnon resonance  $C$  while there is no sign for a single-ion bound state. On the contrary, the  $FG$  band is activated already at temperature  $\tau = 0.5$  and is further enhanced at higher temperature, as is evident in the  $\tau = 1$  and  $\tau = 2$  entries. Also evident is the formation of a double peak in the  $FG$  region, with the dominant peak occurring near the  $G$  boundary while a peak of lower intensity develops near the  $F$  boundary. The relative enhancement of the intensity near the  $G$  boundary is likely due to the fact that it involves transitions between  $k = \pi$  single magnons and  $k = \pi$  single-ion bound states, where the magnon acquires its lowest gap and is thus more heavily populated at finite temperature than, say,  $k = 0$  magnons. Therefore, theory suggests a dominant peak near the  $G$  boundary followed by a secondary peak (a knee) near the  $F$  boundary, but the two peaks are partners in a doubly-peaked  $FG$  band that cannot be separated in any meaningful way.

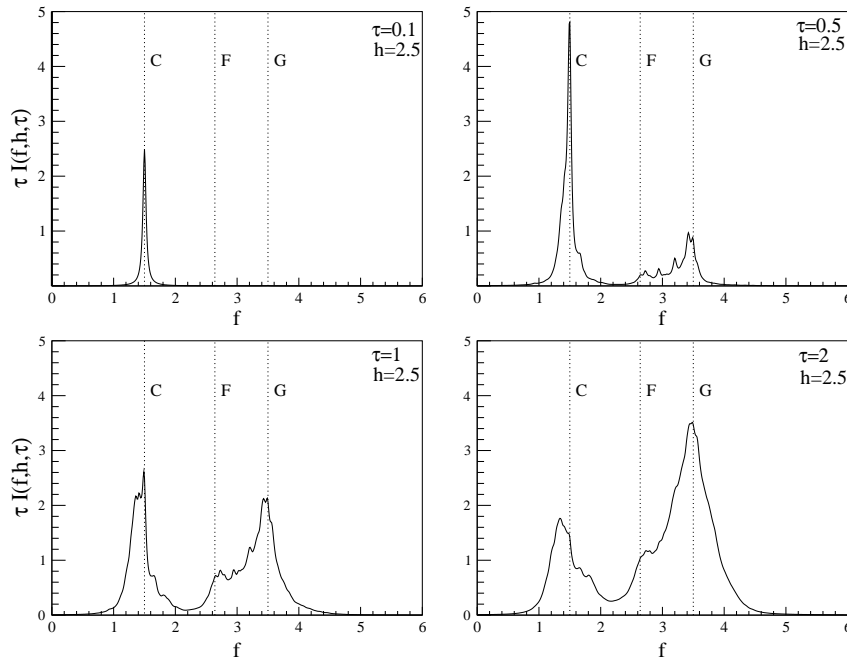


**Figure 2.2.8:** Calculated normalized intensity  $I(f, h, \tau)$  scaled with temperature  $\tau$ , as a function of frequency  $f$  at a fixed field  $h = 2.5$  and four typical values of temperature  $\tau$ . Vertical lines  $C$ ,  $F$  and  $G$  indicate the location of the single-magnon resonance  $C$  and the boundaries of the single-ion ( $FG$ ) band.

The same applies for the whole field region  $h > h_2 = 2$  as demonstrated in Fig. 2.2.9 which displays the intensity in the ferromagnetic phase and temperature  $\tau = 2$ . The calculated  $FG$  band is highly populated at this temperature with most of the intensity concentrated near the  $G$  boundary. This provides unambiguous evidence for the existence of a single-ion two-magnon bound state.

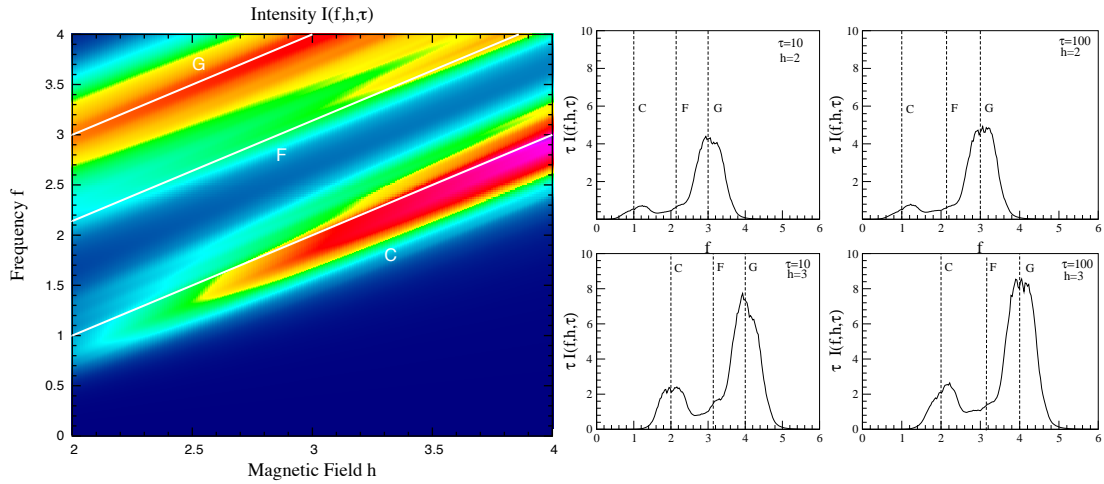


**Figure 2.2.9:** Same as Fig. 2.2.6 but with intensity now calculated at a much higher temperature  $\tau = 2$ . Note that we concentrate on the high-field region  $h > h_2$  in order to emphasize the significant enhancement of intensity in the  $FG$  band (especially near the  $G$  boundary).

**Figure 2.2.10:** Calculated normalized intensity  $I(f, h, \tau)$  scaled with temperature  $\tau$ , as a function of frequency  $f$  at two fixed field  $h = 2.5, 3$  and two typical values of temperature  $\tau = 10, 100$ . In the high- $\tau$  limit, intensity scales as  $\Phi(f, h)/\tau$  as a function of temperature.

Upon increasing of temperature, line  $G$  in enhanced and becomes dominant in the high- $\tau$  limit. In this limit, the temperature-dependence of the intensity is approximated by  $I(f, h, \tau) \simeq \Phi(f, h)/\tau$ , where function  $\Phi(f, h)$  does not depend on  $\tau$ . This is evident in Fig. 2.2.10, where we plot intensity scaled with temperature  $\tau$  as a function of  $f$  for two fields in the ferromagnetic phase,  $h = 2.5, 3$  and two values of temperature  $\tau = 10, 100$ .

The numerical study presented so far, yields important insights into the underlying physics of model (2.2.1). Yet, a number of features such as the shift of resonance field and the behaviour of the intensity of the various modes as a function of temperature have not been explored. We postpone further discussion until Sec. 2.3 where the numerical data will be compared to experimental investigations on the same quantities. To conclude, one of the most important elements of our analysis so far is the suggestion that the single-ion bound state makes a distinct contribution to the ESR spectrum and its effect can be identified by the presence of a doubly-peaked  $FG$  band with nonvanishing intensity at sufficient high temperature.

### 2.2.3 Three-Dimensional ESR spectrum

A theoretical analysis of the ESR spectrum observed in real materials requires, in most of the cases, the inclusion of 3D couplings. The essential features of the 1D model are expected to remain unaffected, while the resonance lines will shift as a result of the presence of couplings perpendicular to the chain. Here we are presenting explicit results

of resonance frequencies  $A$  and  $B$  for  $h < h_1$  and  $C$ ,  $G$  and  $F$  for  $h > h_2$ , and will be used to compare with experimental data and estimate exchange couplings of DTN. Based on the preceding explicit results presented in Sec. 1.4, the resonance frequencies are:

$$\begin{aligned} \omega_{A,B} = & D + 2 \sum_{\nu} J_{\nu} + \frac{1}{D} \left[ 3 \sum_{\nu} J_{\nu}^2 - 2 \left( \sum_{\nu} J_{\nu} \right)^2 \right] \\ & + \frac{1}{D^2} \left[ 4 \left( \sum_{\nu} J_{\nu} \right)^3 + \frac{9}{2} \sum_{\nu} J_{\nu}^3 - 9 \left( \sum_{\mu} J_{\mu}^2 \right) \left( \sum_{\nu} J_{\nu} \right) \right] \pm g\mu_B H, \quad (2.2.17) \end{aligned}$$

and

$$\begin{aligned} \omega_C &= g\mu_B H - D \\ \omega_G &= g\mu_B H + D \\ \omega_F &= g\mu_B H + D - 4(J_x + J_y + J_z) \\ &+ \frac{2}{D}(J_x^2 + J_y^2 + J_z^2) + \frac{1}{D^2}(J_x^3 + J_y^3 + J_z^3). \quad (2.2.18) \end{aligned}$$

Note that resonance frequencies  $\omega_C$  and  $\omega_G$  are independent of the exchange couplings, as in the 1D case. Recovery of the one-dimensional results are through the formal substitution  $J_x = J_y = 0$  and  $J_z = J$ .

### 2.3 Application to DTN: Experimental Data

Besides the theoretical analysis, experimental studies of DTN ( $NiCl_2 - 4SC(NH_2)_2$ ) are presented with a special emphasis on single-ion two-magnon bound states. DTN has been investigated for its quantum magnetism and extensive information about its magnetic and magneto-elastic properties is available [41, 42, 61, 79, 82, 83, 85–87].

The nickel(II) ion is a sensitive probe of crystalline field distortions. In an  $S = 1$   $Ni^{++}$  spin system an axially symmetric distortion of the proper sign can split the triplet into a lower singlet separated from an excited doublet by an energy  $|D|$  [83]. The energy level diagram of DTN is such that the  $S = 1$  triplet is split by single-ion anisotropy into a  $S^z = 0$  ground state and  $S^z = \pm 1$  excited states with an energy gap of  $D \sim 10$  K [42, 83].

The  $Ni$  magnetic spins were shown to occupy a tetragonal body-centered structure, space group I4, with two molecules in the unit cell [83, 84], see Fig. 2.3.1. The thioureas are bonded to the nickel by means of the sulfur atoms in a square array, as shown schematically in Fig. 2.3.2. The bond lengths are  $Ni - Cl = 2.40 \pm 0.02$  Å in the upper

plane and  $2.52 \pm 0.02 \text{ \AA}$  in the lower plane,  $Ni-S = 2.46 \pm 0.004 \text{ \AA}$ ,  $S-C = 1.73 \pm 0.03 \text{ \AA}$ , and  $C-N = 1.33 \pm 0.04 \text{ \AA}$ . The chlorine atom below the plane is  $3.30 \text{ \AA}$  from the nitrogen atoms of its neighbors. The structure as a whole consists of molecules all oriented in the same way and held together by  $Cl-Ni$  hydrogen bonds.

Zero-field inelastic-neutron-scattering data [41] and ESR measurements in applied fields [42] indicate that the magnetic interaction is through the super-exchange  $Ni-Cl-Ni$  path along the tetragonal  $c$  axis, with the antiferromagnetic exchange parameter equals to  $J = 2.2 \text{ K}$ . The coupling along the  $a$  and  $b$  axes are significantly weaker,  $J_{\perp} = J_a = J_b = 0.18 \text{ K}$  and no couplings were found to within the experimental resolution along the (1,1,1) direction [41].  $Ni$  spins are strongly coupled along the  $c$  axis, making DTN a system of weakly interacting  $S = 1$  chains. Therefore, DTN is considered to be the quasi-one-dimensional limit of a three-dimensional (3D) system, where the exchange couplings perpendicular to the chain  $J_{\perp}$  are finite but much smaller than  $J$ ,  $J_{\perp}/J \simeq 0.08$ . Since  $D$  exceeds  $2z_0|J|$ , a transition to long range magnetic order cannot occur in zero external field according to Moriya's criterion [81]. Perpendicular couplings become significant when the application of a field  $H \parallel z$  axis minimizes the energy gap and a transition to long-range order can be established at low enough temperatures.

The intermediate phase in DTN has been experimentally identified as a 3D XY AFM ordered phase that can be regarded as a Bose-Einstein condensate (BEC) of magnons below some critical temperature  $T_N$  [61]. As shown in Fig. 2.3.3, antiferromagnetic exchange between the  $Ni$  atoms produces the XY long-range order in a dome-shaped region of the  $T-H$  phase diagram between  $H_1 = 2.1 \text{ T}$ , where the magnetic ground state is induced, and  $H_2 = 12 \text{ T}$  where the spins align with the applied magnetic field [42].

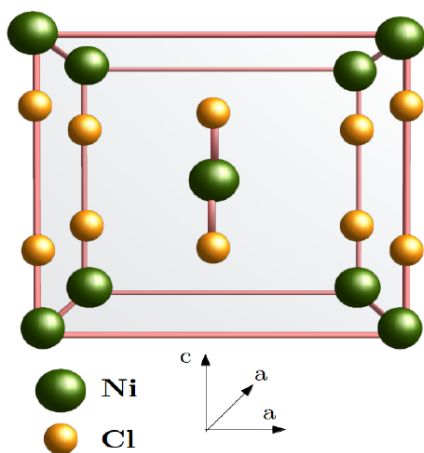


**Figure 2.3.1:** One unit cell of of the full crystal structure of  $NiCl_2 - 4SC(NH_2)_2$ . The  $Ni$  magnetic spins (green) occupy a tetragonal body-centered structure with antiferromagnetic interactions between nearest neighbors.

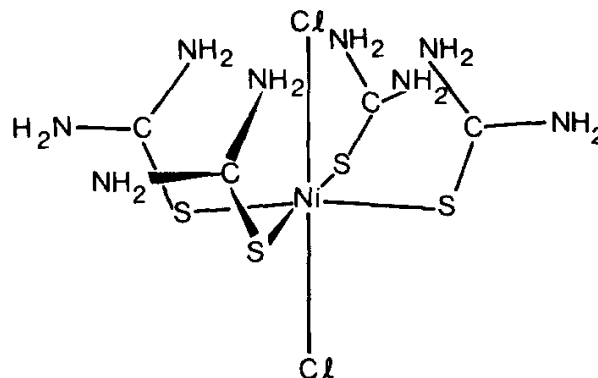


**Figure 2.3.2:** Molecular structure of  $NiCl_2 - 4SC(NH_2)_2$ . Figure taken from [83].

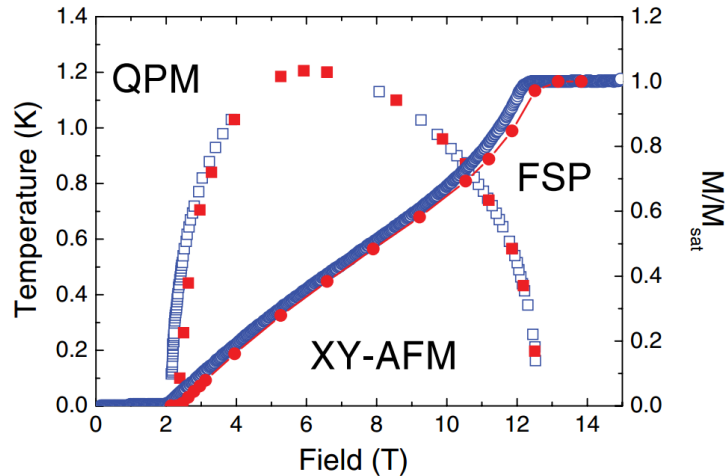


**Figure 2.3.3:** Temperature–field diagram of the AFM-ordered phase obtained from magnetocaloric-effect measurements (opened squares), and the magnetization data taken at  $T = 16$  mK (opened circles). Closed squares and circles denote results of the quantum Monte Carlo calculations. Figure taken from [42].

3D long-range order occurs approximately below 1 K. Critical fields  $H_1$  and  $H_2$  delimit the region of magnetic-field-induced long-range order. Magnetization is zero between 0 and  $H_1$ , then increases roughly linearly between  $H_1$  and  $H_2$  as the spins cant in the direction of the applied magnetic field, and then saturates above  $H_2$ .

Here we present results of systematic high-field electron spin resonance (ESR) experimental studies. Actually, Zvyagin et al. [42, 79] had carried out detailed ESR measurements of magnetic excitations in a wide field range up to 25 T for this compound and the resulting picture was found to be generally consistent with early theoretical predictions of [76]. Yet, there were some remaining discrepancies between theory and experiment that are clarified through new set of ESR experiments [49].

A frequency range of 50-700 GHz was used with a tunable-frequency submillimeter-wave ESR spectrometer [88] equipped with Backward Wave Oscillators as radiation sources and a 25 T resistive magnet. A transmission-type probe with a sample in the Faraday geometry was employed (with the light propagation vector directed along the applied magnetic field  $H$  and the tetragonal  $c$  axis of the sample). High-quality single crystals of DTN with a typical size of about  $3 \times 3 \times 5$  mm<sup>3</sup> (from a new batch, grown from aqueous solutions of thiourea and nickel chloride) were used. A silicon-based Dow Corning High Vacuum Grease 976 V was used to fix samples inside the probe. Particular attention was paid to measuring the temperature dependence of the observed ESR modes, especially in order to unambiguously resolve the contribution of two-magnon bound states in the high-field region  $H > H_2$ .

In a typical ESR experiment, the ESR spectrum is generated by keeping the frequency incident on the sample stable and varying the uniform magnetic field. In Fig. 2.3.4 we present ESR transmittance spectra for three characteristic frequencies and a wide field

range up to 25 T. The specific choice of frequencies is such that all possible modes appear in the figure. The essential features of the observed ESR spectrum are illustrated in Fig. 2.3.6 together with the theoretical predictions presented in Sec. 2.2.3.

The set of parameters  $J_{x,y,z}$ ,  $g$  and  $D$  employed to calculate the branches of the ESR spectrum shown by straight lines  $A$ ,  $B$ ,  $C$ ,  $F$  and  $G$  are chosen as follows. The simplest possibility is to fit the zero-field magnon dispersion given by Eq.(1.4.2) to the dispersion measured via inelastic neutron scattering [41]. A good fit is obtained, see Fig. 2.3.7, with the choice of parameters [89]:

$$D = 7.72 \text{ K}, \quad J_x = J_y = 0.2 \text{ K}, \quad J_z = 1.86 \text{ K}. \quad (2.3.1)$$

In particular,  $\epsilon_0 = \epsilon(k=0) = 257 \text{ GHz}$ , is in fair agreement with the experimental value  $\epsilon_0 = 267 \text{ GHz}$  independently obtained through ESR. Consequently, the theoretically predicted branches  $A$  and  $B$  in the ESR spectrum agree with experiment if we further choose a gyromagnetic ratio  $g = 2.22$ . The critical field calculated from Eq.(1.4.4) is  $H_1 = 2.08 \text{ T}$ , in excellent agreement with the experimental value  $H_1 = 2.1 \text{ T}$ .

Thus the preceding choice of parameters yields a sufficiently accurate description of the low-field region  $H < H_1$ . But such a choice leads to poor quantitative predictions in the high-field region  $H > H_2$ . For example, the critical field  $H_2$  calculated from Eq.(1.4.6) is  $H_2 = 11.24 \text{ T}$ , to be compared with the experimental  $H_2 = 12.6 \text{ T}$ . Similarly, the exact magnon branch  $\omega_C$  of Eq.(2.2.18) substantially disagrees with experiment when  $D = 7.72 \text{ K}$ .

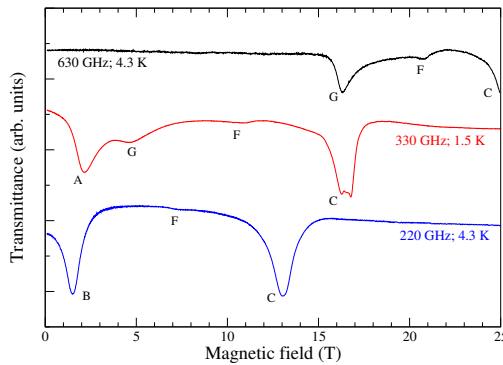


**Figure 2.3.4:** ESR transmittance spectra for three characteristic frequencies and a wide field range up to 25 T. Note that the specific choice of frequencies is such that all possible modes appear in the figure.

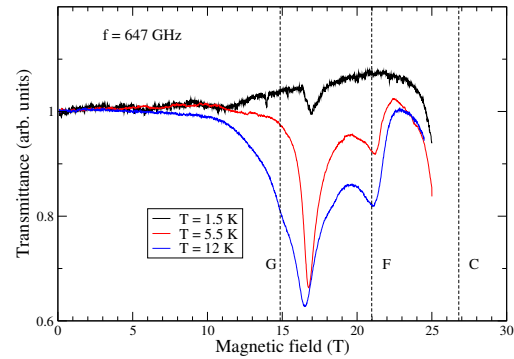


**Figure 2.3.5:** ESR transmittance spectra in DTN taken at frequency 647 GHz for three representative temperature values. Note that experiments were performed in magnetic fields up to 25 T and thus the single-magnon ( $C$ ) resonance is not shown in this figure.

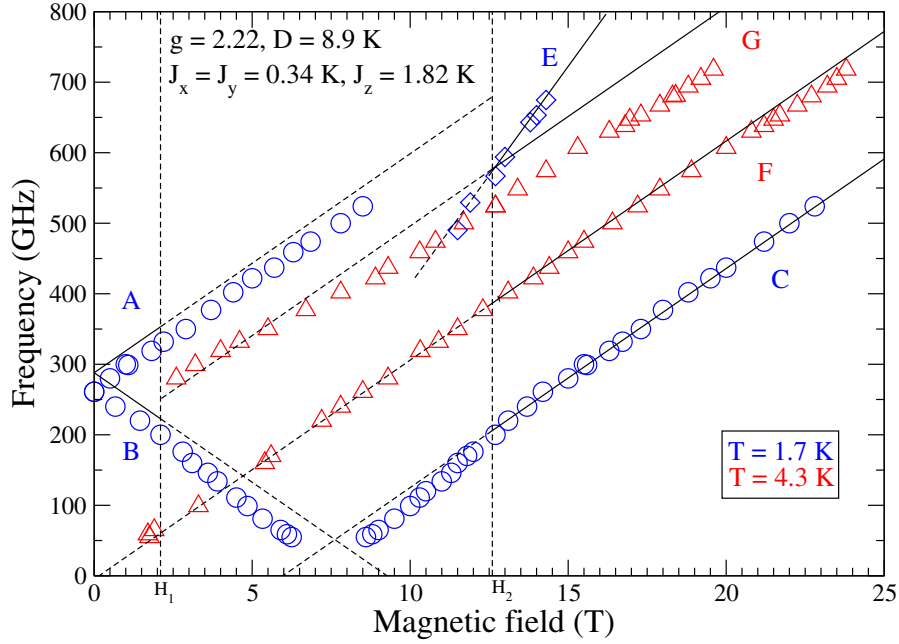


**Figure 2.3.6:** Frequency-field dependence of magnetic excitations in DTN, with a uniform magnetic field  $H$  applied along the tetragonal  $c$  axis. Blue symbols denote experimental data taken at  $T = 1.7$  K and red symbols at  $T = 4.3$  K. Note that the mode  $E$  was observed in the Voight configuration [42, 79] while the rest of the modes were observed in the Voight as well as in the Faraday geometry. Solid lines correspond to results of calculations presented in Sec. 2.2.3 and are continued as dashed lines into the intermediate region  $H_1 < H < H_2$ . The location of critical fields  $H_1 = 2.1$  T and  $H_2 = 12.6$  T is indicated by vertical dashed lines.

Instead, an excellent fit of mode  $C$  is obtained using the parameters [42]

$$g = 2.22, \quad D = 8.9 \text{ K}. \quad (2.3.2)$$

We adopt these values and fix the remaining (exchange) constants via a least-square fit of the zero-field dispersion of Eq.(1.4.2) to the experimental dispersion, see Fig. 2.3.7, to obtain

$$J_x = J_y = 0.34 \text{ K}, \quad J_z = 1.82 \text{ K}, \quad (2.3.3)$$

which are significantly different from  $J_x = J_y = 0.18$  K and  $J_z = 2.2$  K obtained in Ref.[42] using a self-consistent semiclassical method to calculate the zero-field magnon dispersion. Here, to be consistent, we employ the parameters of Eq.(2.3.2) and Eq.(2.3.3) to calculate the critical fields  $H_1 = 2.30$  T and  $H_2 = 12.68$  T which are in rough agreement with the experimental  $H_1 = 2.1$  T and  $H_2 = 12.6$  T. Using the same set of parameters, ESR branches  $A$ ,  $B$ ,  $C$ ,  $F$  and  $G$  shown in Fig. 2.3.6 are again in rough agreement with experiment.

We return briefly to the possibility of a  $\Delta S^z = 2$  transition between the ordered ground state and a  $k = 0$  single-ion bound state, which would lead to a resonance

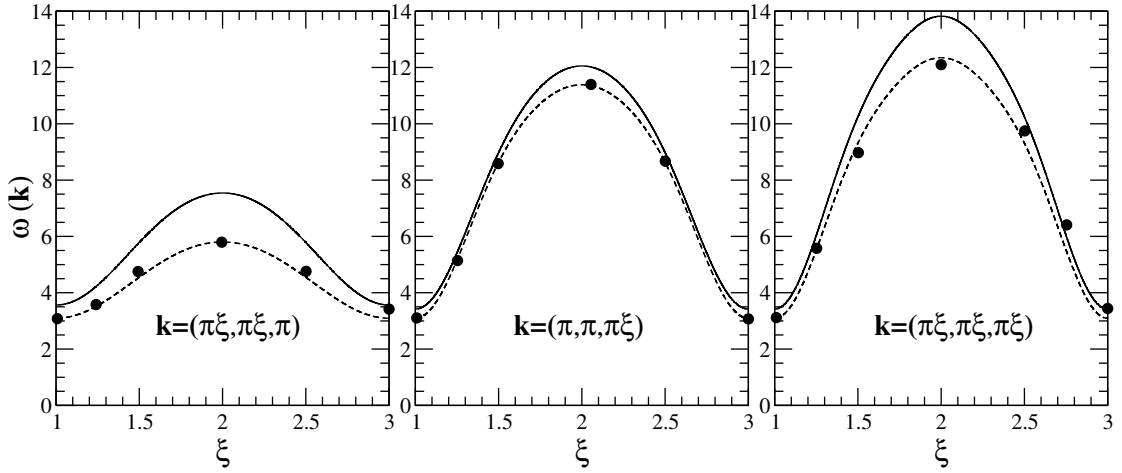


**Figure 2.3.7:** DTN dispersion of magnetic excitations at zero field calculated along three directions in the Brillouin zone using Eq.(1.4.2) and parameters taken from Eq.(2.3.1) (dashed lines) and Eqs.(2.3.2)–(2.3.3) (solid lines). Symbols denote inelastic neutron scattering data taken from [41]. Energy is measured in degrees K.

frequency:

$$\omega_E = E(\mathbf{k} = 0) = \omega_F + \omega_C \quad (2.3.4)$$

but zero intensity thanks to the axial symmetry adopted in our theoretical models. However, crystal symmetry is compatible with some deviations from strict axial symmetry which apart from a tiny field misalignment may render mode  $E$  observable. In fact, such a mode was previously observed in DTN with a sample in the Voigt geometry [42, 79] and is included in Fig. 2.3.6.

We now turn our attention to the single-ion  $FG$  band. Note that the band is absent at relatively low-temperature of about  $T = 1.7$  K, and one has to increase temperature around  $T = 4.3$  K to get nonvanishing intensity (see Fig. 2.3.6). As was discussed in Sec. 2.2.2, the intensity is expected to display a characteristic double peak as a function of frequency at fixed external field, or as a function of field at fixed frequency. Therefore, both frequencies  $F$  and  $G$  are associated with the single-ion bound state and are relevant for the analysis of actual experiments. In this respect, it is worth mentioning that the absorption corresponding to mode  $G$  was initially observed in previous experiments [79]. This absorption was interpreted as an artifact originating in the superficial layer of DTN crystals attacked by a GE-varnish solvent used to fix the sample within the sample holder.

However, our theoretical analysis suggests that the  $G$  mode is actually an inseparable partner in a doubly-peaked  $FG$  band associated with the single-ion bound state. Indeed, our current experiment supports such an interpretation, as shown in Fig. 2.3.5 where the transmittance measured at fixed frequency  $f = 647$  GHz displays a characteristic double peak as a function of the applied field. Also note that the double peak is uneven with most power absorbed for frequencies near the  $G$  boundary, an experimental fact that is

consistent with the numerical calculation of power absorption presented in Sec. 2.2.2. Another important feature of Fig. 2.3.5 is the apparent vanishing of intensity at relatively low temperatures (e.g.,  $T = 1.5$  K), an experimental fact that is consistent with our interpretation of the  $FG$  resonance band as the result of transitions between excited states; namely, transitions between single magnons and single-ion two-magnon bound states.

Some of the features of the observed spectrum can be explained through the 1D numerical calculation of the intensity  $I(f, h, \tau)$  developed in Sec. 2.2.2. First, a digression concerning the choice of parameters within the 1D model. Recall that the single-magnon resonance frequency  $\omega_C$  is an exact prediction of the 1D as well as the 3D model. Therefore, we adopt in this section the choice of the gyromagnetic ratio  $g$  and anisotropy  $D$  already made in Eq.(2.3.2) and the only remaining parameter is the exchange constant  $J$  or, equivalently, the dimensionless ratio  $J/D$ . A semi-quantitative agreement with experiment is obtained with the choice:

$$g = 2.22, \quad D = 8.9 \text{ K}, \quad \frac{J}{D} = \frac{1}{4}, \quad (2.3.5)$$

which will be adopted in all calculations within the 1D model.

**Table 2.3.1:** Rationalized variables introduced in Sec. 2.2.2 are given in units.

| Frequency $f$            | Magnetic Field $h$ | Temperature $\tau$ |
|--------------------------|--------------------|--------------------|
| $D/2\pi\hbar=185.45$ GHz | $g\mu_B H/D=6$ T   | $T/D=8.9$ K        |

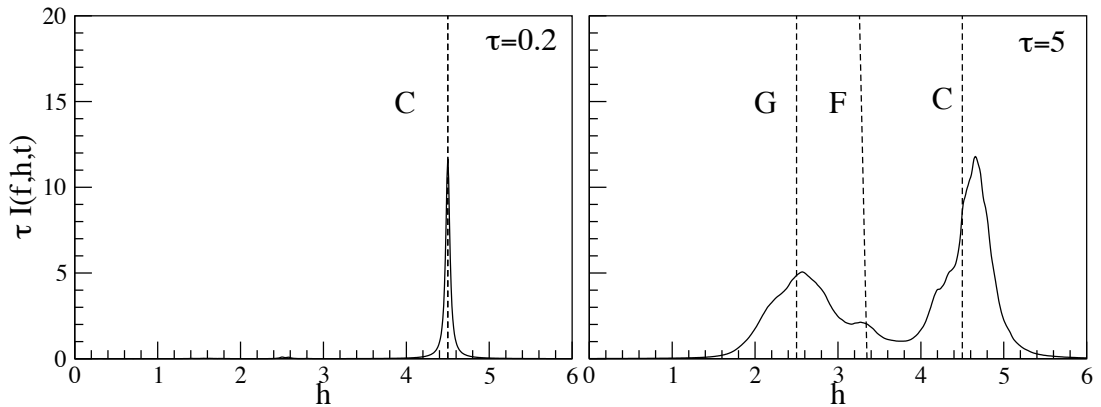


**Figure 2.3.8:** Calculated normalized intensity  $I(f, h, \tau)$  scaled with temperature  $\tau$  as a function of magnetic field  $h$  at a fixed frequency  $f = 3.5$  (649 GHz) and two values of temperature  $\tau = 0.2, 5$  (1.78 K, 44.5K). Note that resonance field of line  $C$  shifts from its zero-temperature limit upon increasing of temperature.

Since with the 1D numerical technique the intensity  $I(f, h, \tau)$  can be calculated as a function of all three variables, it is illustrative to plot  $I$  as a function of magnetic field at fixed frequency and temperature, in order to simulate the experimental ESR

transmittance spectra. Formulas that describe resonance lines  $A$ ,  $B$  and  $C$ ,  $G$ ,  $F$  are now expressed in terms of the magnetic field. For example, resonance line  $C$  is now located at  $h_C = f + 1$  (in rationalized units). In Fig. 2.3.8 we present the intensity  $I(f, h, \tau)$  scaled with temperature  $\tau$  as a function of magnetic field  $h$  at a fixed frequency  $f = 3.5$  (649 GHz) and two values of temperature  $\tau = 0.2, 5$  (1.78 K, 44.5K). We note that at low temperatures (first entry) line  $C$  is centered around  $h_C = f + 1 = 4.5$ , while there is a shift of the resonance field as we increase the temperature (second entry).

It is of theoretical as well as experimental interest to analyze the resonance field shift  $h_C(\tau)$ . Some caution is necessary with respect to the definition of  $h_C(\tau)$ , which no longer corresponds to its zero-temperature limit given by  $h_C(\tau = 0) = f + 1$  but to the maximum of the intensity in the neighborhood of  $h_C(\tau = 0)$ . In Fig. 2.3.9 we plot  $H_C(T)$  as a function of  $T$ , calculated within the 1D model; superimposed are experimental data extracted from the maxima of the ESR transmittance spectra. The theoretical curve indicates that at very low temperatures there is a shift at lower values than  $H_C(T = 0)$ , while at around  $T = 2$  K the shift moves at higher values until it reaches a maximum around 11 K. A further increase of temperature will cause the curve to decrease until it reaches an approximate value at high- $T$ . We note that there is quantitative agreement between theory and experiment, specially in the low- $T$  region of the diagram.

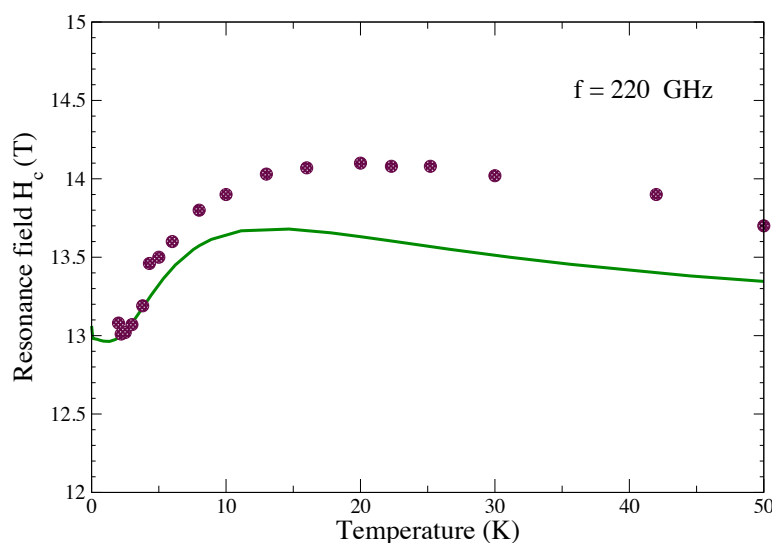


**Figure 2.3.9:** The temperature dependence of resonance field  $H_C$  at frequency  $f = 220$  GHz. Symbols denote experimental data.

The theoretical findings of Sec. 2.2.2, with a dominant peak near the  $G$  boundary followed by a secondary peak (a knee) near the  $F$  boundary are consistent with the experimental results of the type shown in Fig. 2.3.5, with due attention to the fact that Fig. 2.3.5 depicts the transmittance as a function of applied field at fixed frequency. In any case, both theory and experiment suggest that the two peaks are partners in a doubly-peaked  $FG$  band that cannot be separated in any meaningful way. Thus it is

difficult to measure or calculate their relative intensity. Nevertheless, it is possible to calculate the total intensity of the  $FG$  band:

$$I_{FG} = \int_a^b I(f, h, \tau) dh, \quad (2.3.6)$$

where integration extends over a field interval  $a \leq h \leq b$  chosen empirically so that it encompasses the entire  $FG$  band. The total intensity of Eq.(2.3.6) is depicted in Fig. 2.3.10 as a function of temperature at fixed frequency  $f = 647$  GHz, together with experimental results obtained by applying a similar integration process to data of the type shown in Fig. 2.3.5. Taking into account that intensity is displayed in “arbitrary units”, the qualitative agreement between theory and experiment shown in Fig. 2.3.10 is satisfactory and fully consistent with our current interpretation of the ESR signal of the single-ion two-magnon bound state.

The same procedure was followed for the integrated intensity of line  $C$  (denoted as  $I_C$ ) and the results are presented in Fig. 2.3.10. The agreement is not so satisfactory, specially in the vicinity of small temperatures. Nevertheless, both theory and experiment suggest that there is a difference between the behavior of  $I_{FG}$  and  $I_C$ , with the former exhibiting a peak at a finite  $T$ , while the latter smoothly decreases with increasing  $T$  and no peaks is observed. This qualitative difference can be explained as follows. The intensity of ESR depends on the difference in thermal population between the energy levels pertaining to the ESR transition. If there is an energy gap between the ground state and the lowest excited state, the thermal population of the excited state is larger at larger temperature. On the other hand, the difference in thermal population within excited states becomes small with increasing temperature. Consequently, the intensity of the ESR transition within excited states exhibits a peak at a finite  $T$ .

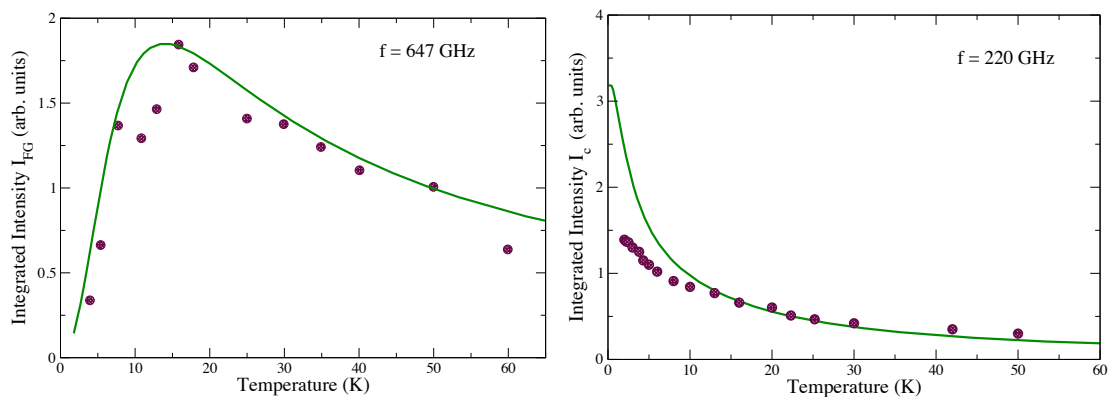


**Figure 2.3.10:** Integrated intensity  $I_{FG}$  at fixed frequency  $f = 647$  GHz (left) and  $I_C$  at fixed frequency  $f = 220$  GHz (right) as a function of temperature calculated within the 1D model. Symbols denote experimental data extracted from field integration of ESR spectra.

## 2.4 ESR studies for the effective $S=1/2$ Hamiltonian

One of the main conclusions of the above sections is that the essential features of the ESR spectrum observed in DTN are accounted for by the strictly 1D  $S = 1$  model (2.2.1). Yet, even within this 1D model, detailed calculation of the ESR spectrum has been difficult especially for fields in the intermediate phase.

It is the purpose of the present section to investigate the structure of the zero-temperature low-lying ESR spectrum throughout the intermediate region  $h_1 < h < h_2$  using the mapping to the effective  $S = 1/2$  model (1.5.9) for which a rigorous solution can be obtained using the Bethe ansatz. These results have been originally presented in [90].

As a preparation for our main result, we recall that the extent of the intermediate phase predicted by the  $S = 1/2$   $XXZ$  model is given by  $-\tilde{h}_c < \tilde{h} < \tilde{h}_c$ , where  $\tilde{h}_c = 2J(1 + \Delta) = 3J$  for  $\Delta = 1/2$ . Upon translating this prediction in terms of the original field  $h = \tilde{h} + \rho + 1$ , the extent of the intermediate phase is given by

$$h_1 = 1 - 2\rho, \quad h_2 = 1 + 4\rho, \quad (2.4.1)$$

where  $h_2$  coincides with the exact upper critical field predicted by the  $S = 1$  model, whereas  $h_1$  is an approximate prediction for the lower critical field that is consistent with Eq. (1.3.15), restricted to first order in the  $J/D$  expansion. Accordingly, the field dependence of the ESR spectrum outside the intermediate phase is given by

$$\begin{aligned} \omega_B &= 1 + 2\rho - h \quad \text{for } h < h_1, \\ \omega_C &= h - 1 \quad \text{for } h > h_2, \end{aligned} \quad (2.4.2)$$

where  $\omega_C$  is the  $k = 0$  value of the magnon dispersion for  $\tilde{h} > \tilde{h}_c$ , and  $\omega_B$  is the corresponding value for  $\tilde{h} < -\tilde{h}_c$ . Note that  $\omega_C$  coincides with the exact value of the corresponding prediction in the  $S = 1$  model, whereas  $\omega_B$  is again the first order approximation within a systematic  $1/D$  expansion.

The preceding elementary calculation of the ESR spectrum cannot be simply extended into the intermediate phase even within the effective  $S = 1/2$  model. However, recent developments in the Bethe ansatz method [91, 92], allow the semi analytical evaluation of matrix elements between eigenstates in the  $S = 1/2$  Heisenberg model for any magnetization: the calculations reduce to the numerical evaluation of determinants of the order of the size of the spin system. When applied to the ESR operator  $|\langle m | \tilde{S}_{\text{tot}}^- | \tilde{\Omega} \rangle|^2$ , where  $|\tilde{\Omega}\rangle$  is the ground state,  $|m\rangle$  an excited state and  $\tilde{S}_{\text{tot}}^- = \sum_n \tilde{S}_n^-$ , it is found that there is essentially only one excited state,  $|m^*\rangle$ , that has significant weight in the spectrum. This state is a highly unusual one in the Bethe ansatz literature. While usually eigenstates are characterized by sets of real pseudomomenta  $\lambda$  or pseudomomenta with

imaginary parts symmetrically arranged around the real axis (“strings”), this state has all the  $\lambda$ 's real except one that is complex with an imaginary part  $i\pi/2$ . The existence of this state was recently discussed [93] and it physically corresponds to a uniform change of the  $\tilde{S}^z$  component of the magnetization by 1. It is fascinating that the ESR experiments exactly probe this state and its dynamics.

From a computational point of view, it turns out to be rather difficult to find the pseudomomenta  $\lambda$  for this state. The nonlinear Bethe ansatz equations at finite magnetization, in general, do not converge by iteration. To circumvent this problem, it was suggested [94] to study chains with an odd number  $N$  of spins, where indeed the problem is far less crucial [92]. In the following we present data for the magnetic field  $\tilde{H}$  dependence of the ESR resonance frequency  $\omega_{m^*} = \epsilon_{m^*} - \epsilon_{\tilde{\Omega}}$  and of the ESR matrix element  $|\langle m^* | \tilde{S}_{\text{tot}}^- | \tilde{\Omega} \rangle|^2$  for  $N = 51$ . The quantum numbers characterizing the ground state  $|\tilde{\Omega}\rangle$  with  $M$  reversed spins are given by  $I_{j=1,M} = -M/2 + 1, \dots, +M/2$ , corresponding to a magnetization  $\tilde{S}^z = N/2 - M$ . The excited state  $|m^*\rangle$  has  $M + 1$  reversed spins and is characterized by the quantum numbers  $I_{j=1,M} = -M/2 + 1/2, \dots, +M/2 - 1/2$ ,  $I_M = (N + M)/2$ .

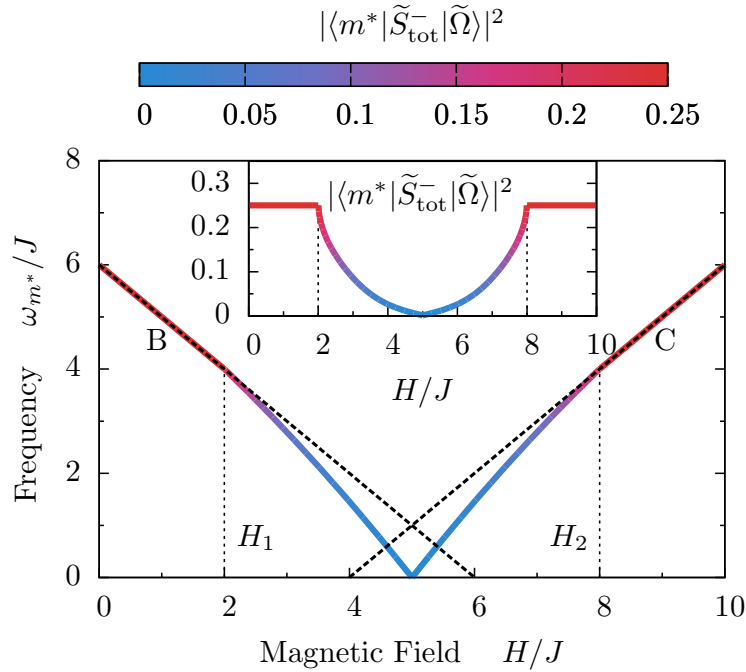


**Figure 2.4.1:** Field dependence of  $T = 0$  low-lying ESR lines calculated from the effective  $S = 1/2$  model diagonalized through the Bethe ansatz. Lines  $B$  and  $C$  are the straight lines  $\omega_B$  and  $\omega_C$  given in Eq. (2.4.2) for fields outside the intermediate phase but bend downwards in a nontrivial manner upon entering the intermediate phase to meet at the center and thus form a  $V$ -like structure. The inset depicts the field dependence of the matrix element  $|\langle m^* | \tilde{S}_{\text{tot}}^- | \tilde{\Omega} \rangle|^2$ , which is directly relevant for the calculation of the intensity of ESR modes. Vertical dotted lines indicate the location of the critical fields  $h_1$  and  $h_2$  calculated from Eq. (2.4.1).

The results of this intriguing calculation are summarized in Fig. 2.4.1, which depicts the field dependence of the low-lying ESR lines as a function of the field  $h$ . As expected, these coincide with the straight lines  $\omega_B$  and  $\omega_C$  of Eq. (2.4.2) for fields  $h$  outside the intermediate phase, which bend downwards upon entering the intermediate phase to meet at the center and thus form a  $V$ -like structure. The calculated slope is  $\pm 3/2$  at the center and  $\pm 1$  at and beyond the edges of the intermediate phase. Also shown in Fig. 2.4.1 is the calculated field dependence of the matrix element  $|\langle m^* | \tilde{S}_{\text{tot}}^- | \tilde{\Omega} \rangle|^2$ , which vanishes at the center but reaches a finite value  $1/4$  that remains constant for all fields outside the intermediate phase.

The currently predicted  $V$ -like ESR spectrum with vanishing intensity at its center is consistent with our earlier prediction [49] made by a rough numerical calculation on small ( $N = 10$ ) chains within the  $S = 1$  model (1.5.1) (see Fig. 2.2.7) but disagrees with a  $Y$ -like structure with nonvanishing intensity at the center made by Cox *et al.* [80] by a calculation within the same  $S = 1$  model. Concerning possible experimental observation, the rapid vanishing of intensity near the center would make the  $V$ -mode especially sensitive to small perturbations that are ever present in effective Heisenberg models [49, 82].

Some caution is necessary with regard to the results presented in this section concerning the structure of the ESR spectrum in the intermediate phase. As stated earlier, most of the intensity is concentrated on a single resonance frequency  $\omega_{m^*}$  with a  $\delta$ -function line shape, emerging from transitions between the ground state and the excited state  $|m^*\rangle$ . Apart from this dominant contribution, the Bethe ansatz calculation revealed that the ESR spectrum consists of secondary transitions with small, but non vanishing intensity. These transitions correspond to resonance frequencies that lie above  $\omega_{m^*}$  with negligible matrix elements and are thus omitted from Fig. 2.4.1. These secondary peaks exist throughout the intermediate phase for  $-\tilde{h}_c < \tilde{h} < \tilde{h}_c$  but lose their intensity for  $\tilde{h} \geq \tilde{h}_c$  and  $\tilde{h} \leq -\tilde{h}_c$ . In this case, the only ESR transition is the one between the ferromagnetic ground state and the  $k = 0$  single magnon, with resonance frequency

$$\begin{aligned} \omega_{sm} &= 2J(1 - \Delta) + \tilde{h} \quad \text{for } \tilde{h} \geq \tilde{h}_c, \\ &= 2J(1 - \Delta) - \tilde{h} \quad \text{for } \tilde{h} \leq -\tilde{h}_c. \end{aligned} \quad (2.4.3)$$

In order to clarify this more complicated ESR spectrum, two limiting cases are considered; the isotropic chain ( $\Delta = 1$ ) and the  $XY$  model ( $\Delta = 0$ ). In the presence of isotropic interaction, the resonance frequency  $\omega_{sm} = \tilde{h}$  with a  $\delta$ -function line shape is extended in the intermediate region. The line is precisely at the Zeeman energy for any magnetic field, with intensity that gradually vanishes as  $\tilde{h} \rightarrow 0$ . In the presence of a small perturbation to the isotropic Hamiltonian, the ESR spectrum is again dominated by a single line, but the presence of anisotropy causes a shift in the position of the

resonance peak that varies with magnetic field [77, 95].

On the other hand, the picture gets more involved for  $\Delta = 0$ . A numerical calculation performed by Maeda and Oshikawa [96] showed that the single magnon picture with a  $\delta$ -function line shape at  $\omega_{sm} = 2J \pm \tilde{h}$  holds only for  $\tilde{h} \geq \tilde{h}_c$  and  $\tilde{h} \leq -\tilde{h}_c$ . This picture breaks down in the intermediate phase, where absorption takes place over a finite frequency range with boundaries  $2\tilde{h} < \omega < 4J$ .

From the discussion above it follows that the value of anisotropy considered here,  $\Delta = 1/2$ , lies approximately in the middle of the  $0 \leq \Delta \leq 1$  region, combining features from both extreme cases. The argument of a single line is substantially correct and adequately describes the ESR spectrum, while secondary peaks exist with negligible intensity. These peaks will evolve into a band of resonance frequencies in the  $\Delta = 0$  limit.

## 2.5 Discussion

As far as the general structure of the observed ESR spectrum is concerned, the theoretical predictions of the 3D model of Eq.(1.4.1) and the 1D model of Eq.(2.2.1) are qualitatively similar and in reasonable quantitative agreement with experiment. But a detailed investigation of the remaining discrepancies required a calculation of the intensities of the various ESR modes, which is not feasible within the 3D model. Thus most of our effort was devoted to a detailed numerical calculation of intensity within the 1D model. The main results are the following:

While there have been numerous theoretical predictions for the occurrence of two-magnon bound states in quantum spin systems, experimental observation has been rather slow. Perhaps, the most interesting feature of the ESR spectrum in large- $D$  systems is the evidence it provides for the existence of the so-called single-ion two-magnon bound states. The original theoretical suggestion was made some time ago [76] and was thought to explain ESR data obtained on a large- $D$  compound abbreviated as NENC [97]. But a thorough experimental investigation was carried out more recently in relation to DTN [42, 79].

Our present investigation [49] clearly suggests that the  $F$  and  $G$  lines are inseparable partners in a doubly-peaked  $FG$  band which originates in transitions between single magnons and single-ion two-magnon bound states. In fact, the  $G$  mode absorbs most of the intensity and is thus far from extraneous. This mode is especially interesting in relation to the fact that the corresponding resonance line  $\omega_G = g\mu_B H + D$  is an exact theoretical prediction both within the 3D model and the 1D model; see Eq (2.2.18).

Our numerical calculation also sheds light on the structure of the magnetic excitation spectrum in the intermediate phase  $h_1 < h < h_2$  where analytical results are

practically absent. As is evident in Fig. 2.2.6, a tail of line G with strong intensity survives in the intermediate region even at low temperature where line G itself loses its intensity for  $H > H_2$ . Such a tail should thus be attributed to a high-frequency collective excitation that appears in the intermediate phase as a shadow of the single-ion two-magnon bound state, an issue that deserves further theoretical attention.

The current calculation does not support the occurrence of a low-frequency Y structure suggested by Cox et al.[80], even though they also employ the 1D model of Eq.(2.2.1) to calculate the susceptibility  $\chi''(\omega)$ . In fact, we find a V structure with rapidly decreasing intensity near the center of the intermediate phase. Additionally, the low-lying ESR spectrum of the effective  $S = 1/2$  model is analyzed for fields in the intermediate region in order to complete our work on the  $S = 1$  model. A semi-analytical evaluation based on the Bethe ansatz also predicts that ESR lines form a V-like structure in the low-lying intermediate phase with vanishing intensity at its center.

## Chapter 3

# Thermodynamics

This chapter is devoted to the calculation of the thermodynamic quantities, such as magnetization and the specific heat for both the  $S = 1$  model of Eq.(2.2.1), using a variety of numerical techniques, and the effective  $S = 1/2$  model of Eq.(1.5.9). It is important that this calculation be done for the original Hamiltonian directly in some numerical ways in order to test the validity of the approximations used while performing the mapping. For all quantities studied here, results for both the  $S = 1$  and  $S = 1/2$  model are presented and compared. The exactly solvable XXZ model is collated to complete the theoretical description of the original  $S = 1$  model. The results presented in this chapter were originally published in [90].

### 3.0.1 $S = 1$ chain with strong anisotropy

The thermodynamics of the  $S = 1$  chain with a strong easy plane anisotropy in the absence of magnetic field have been investigated in Ref. [78] through a systematic–strong coupling expansion. Here we are interested in studying the thermodynamic quantities at the whole field–region, with special emphasis at the critical behaviour of magnetization and specific heat at the critical fields. For this reason an algorithm based on the application of the renormalization group to transfer matrices (TMRG) is employed, where the  $S = 1$  quantum chain is mapped onto a two–dimensional classical system by a Trotter–Suzuki decomposition of the partition function [98, 99]. The main advantage of this method is that the thermodynamic limit can be performed exactly and results can be obtained with satisfactory accuracy. Moreover, a second numerical calculation is carried out on the basis of the finite–temperature Lanczos method (FTLM) [100]. Although the TMRG results of thermodynamic quantities are considered to be more accurate, the FTLM applies also to the calculation of dynamic correlations such as those presented in Chapter 4 for the discussion of thermal transport. More details on TMRG and FTLM are discussed in Appendix B.

Note that central role in our discussion plays the description of the critical one-dimensional behaviour of the  $S = 1$  model, hence we are neglecting couplings perpendicular to the hard axis. Moreover, for reasons of convenience we are using the following Hamiltonian:

$$\mathcal{H} = \sum_{n=1}^N [J \mathbf{S}_n \cdot \mathbf{S}_{n+1} + D (S_n^z)^2 + H S_n^z], \quad (3.0.1)$$

and the critical fields are defined as:

$$H_1 = D - 2J + \frac{J^2}{D} + \frac{J^3}{D^2} \quad (3.0.2)$$

$$H_2 = D + 4J. \quad (3.0.3)$$

Throughout this thesis we adopt a certain choice of parameter  $D/J = 4$  in our numerical calculations in order to be consistent with earlier work on electron spin resonance (ESR) theoretical analysis (see Chapter 2). Under this choice, the critical fields are  $H_1/J = 2.28$  and  $H_2/J = 8$ .

### 3.0.2 Effective $S = 1/2$ chain

The reduced effective  $S = 1/2$  XXZ Heisenberg AFM chain in the presence of the magnetic field is described by:

$$\tilde{\mathcal{H}} = \sum_n \left[ 2J \left( \tilde{S}_n^x \tilde{S}_{n+1}^x + \tilde{S}_n^y \tilde{S}_{n+1}^y + \Delta \tilde{S}_n^z \tilde{S}_{n+1}^z \right) + \tilde{H} \tilde{S}_n^z \right], \quad (3.0.4)$$

where  $\Delta = 1/2$  and  $\tilde{H} = -J - D + H$ . Ferromagnetic order in the ground state is established when the magnetic field exceeds the critical value  $\tilde{H}_c = 2J(\Delta + 1)$ . For the first critical field, model (3.0.4) predicts  $H_1 = D - 2J$ , which coincides with Eq.(3.0.2) only at first order in terms of  $J/D$ , whereas both models predict the same value for the second critical field given by Eq.(3.0.3). This is an indication that the mapping should be more accurate close to  $H_2$  rather than  $H_1$ . For the choice of parameter  $D/J = 4$ , model (3.0.4) predicts  $H_1/J = 2$  and  $H_2/J = 8$ .

According to thermodynamic Bethe ansatz (TBA), a system of nonlinear integral equations provides all the required information for the calculation of the free energy of model (3.0.4) in the thermodynamic limit [101]. The number of these equations is determined by the value of parameter  $\Delta$ . For  $\Delta = \cos(\pi/n)$  there are  $n$  such equations with  $f_i(x)$  unknown functions, where  $i = 1, 2, \dots, n$ . The particular value of the anisotropy parameter  $\Delta = 1/2$  is especially convenient because  $n = 3$ ; therefore the full set of

equations is

$$\begin{aligned}
\ln[1 + f_1(x)] &= -\frac{2J}{T} 3\sqrt{3} \delta(x), \\
\ln f_2(x) &= -\frac{2J}{T} 3\sqrt{3} g(x) + \int_{-\infty}^{\infty} dy g(x-y) \ln \left[ 1 + 2f_3(y) \cosh(3\tilde{H}/2T) + f_3(y)^2 \right], \\
\ln f_3(x) &= \int_{-\infty}^{\infty} dy g(x-y) \ln [1 + f_2(y)],
\end{aligned} \tag{3.0.5}$$

where  $g(x) = \text{sech}(\pi x/2)/4$ . The above equations are solved numerically by an iterative process, where we generate a sequence of improving approximate solutions that converge rapidly. Once function  $f_2(x)$  is determined, the free energy is given from

$$\tilde{F} = \int_{-\infty}^{\infty} dx g(x) \ln[1 + f_2(x)]. \tag{3.0.6}$$

The specific heat and magnetization are given by

$$\tilde{C}_v = \beta^2 \frac{\partial^2 \tilde{F}}{\partial \beta^2}, \quad \tilde{M} = -\frac{\partial \tilde{F}}{\partial \tilde{H}}, \tag{3.0.7}$$

where  $\beta = 1/T$  is the inverse temperature. To avoid numerical differentiation, one can derive similar nonlinear equations and directly calculate the derivatives.

### 3.1 Magnetization

In this section, we calculate the magnetization curve as a function of temperature and applied magnetic field. In a gapped spin system in the presence of external magnetic field, the Zeeman term is responsible for the closure of the gap and spontaneous magnetization is developed in the ground state. The behaviour of the magnetization curve near a critical field  $H_{\text{cr}}$  is nontrivial and depends on the model and its dimensionality. In most cases where second-order transitions occur, the magnetization  $M$  near  $H_{\text{cr}}$  behaves like

$$M \sim (H - H_{\text{cr}})^{1/\delta}. \tag{3.1.1}$$

Models with the same critical exponent  $\delta$  are said to belong to the same universality class independently of the microscopic details of the system. In general, the universality class of the model is hard to derive prior to a direct calculation of magnetization. For the  $S = 1$  Haldane chain, the critical exponent was found equal to  $\delta = 2$ , a result based on an equivalent continuum limit of quantum chains and a mapping of the effective

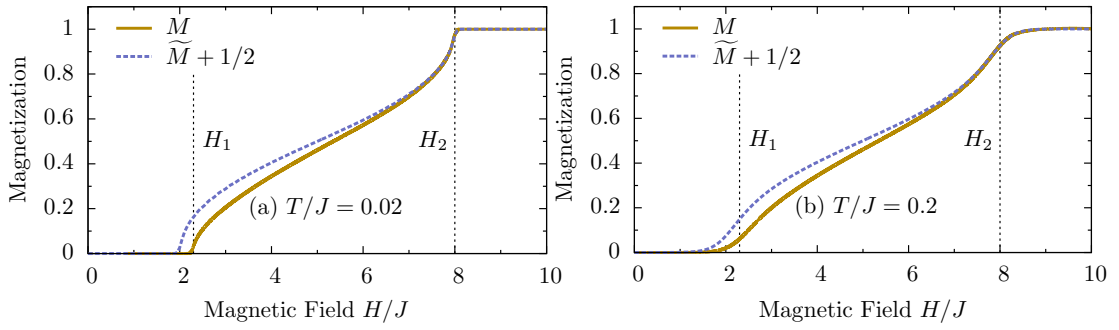


**Figure 3.1.1:** The magnetic field dependence of magnetization  $M$  at fixed temperature (a)  $T/J = 0.02$  and (b)  $T/J = 0.2$ . The solid line corresponds to TMRG results obtained for the  $S = 1$  large- $D$  chain and the dashed line corresponds to TBA results obtained for the  $S = 1/2$  XXZ chain. Vertical lines indicate the location of critical fields  $H_1/J = 2.28$  and  $H_2/J = 8$ . Satisfactory agreement between the models is achieved, particularly close to  $H_2$  where the two curves are indistinguishable.

low-energy Lagrangian to a Bose fluid with  $\delta$  repulsion [102]. Nevertheless, a similar low-energy quantum field theory is not available for the large- $D$   $S = 1$  chain and hence an independent calculation of the magnetization curve is needed. Among the models that have the same critical exponent  $\delta = 2$  are the  $S = 1/2$  ladders [103] and the  $S = 1/2$  bond-alternating chain [104].

The zero temperature magnetization of the  $S = 1/2$  XXZ model is based on a Bethe ansatz solution of the Hamiltonian. More specifically, C. N. Yang and C. P. Yang [105] studied the ground state energy as a function of  $\Delta$  and magnetization, and among the various results, they proved that  $\widetilde{M}$  close to  $\widetilde{H}_c$  behaves as follows

$$\begin{aligned} \widetilde{M} &= \frac{1}{2} - \frac{1}{\pi} \sqrt{\widetilde{H}_c - \widetilde{H}} \quad \text{for } \widetilde{H} < \widetilde{H}_c, \\ \widetilde{M} &= -\frac{1}{2} + \frac{1}{\pi} \sqrt{\widetilde{H} - \widetilde{H}_c} \quad \text{for } \widetilde{H} > \widetilde{H}_c. \end{aligned} \quad (3.1.2)$$

Note that the dependence of  $\widetilde{M}$  on the anisotropy constant  $\Delta$  enters only through the critical field  $\widetilde{H}_c = 2J(1 + \Delta)$  and thus does not affect the value of the critical exponent  $\delta = 2$ . However, finite temperature will cause a smoothing in the shape of the  $\widetilde{M}(\widetilde{H})$  curve close to  $\widetilde{H}_c$ .

In Fig. 3.1.1 we depict the magnetic field dependence of magnetization  $M$  for a  $S = 1$  large- $D$  chain, superimposed with the magnetization  $\widetilde{M} + 1/2$  for the  $S = 1/2$  XXZ chain for (a)  $T/J = 0.02$  and (b)  $T/J = 0.2$ . Among the facts that become apparent are the following: (i) Temperature  $T/J = 0.02$  is considered to be low enough that the anticipated square-root behaviour is evident for both models. The critical exponent is extracted and is found to be  $\delta \simeq 2$  close to  $H_1$ , as well as close to  $H_2$ . This foreseen result renders model (1.5.1) in the same universality class as the Haldane or  $S = 1/2$  XXZ chain. (ii) As mentioned already, we expect that the mapping close to  $H_2$  is more

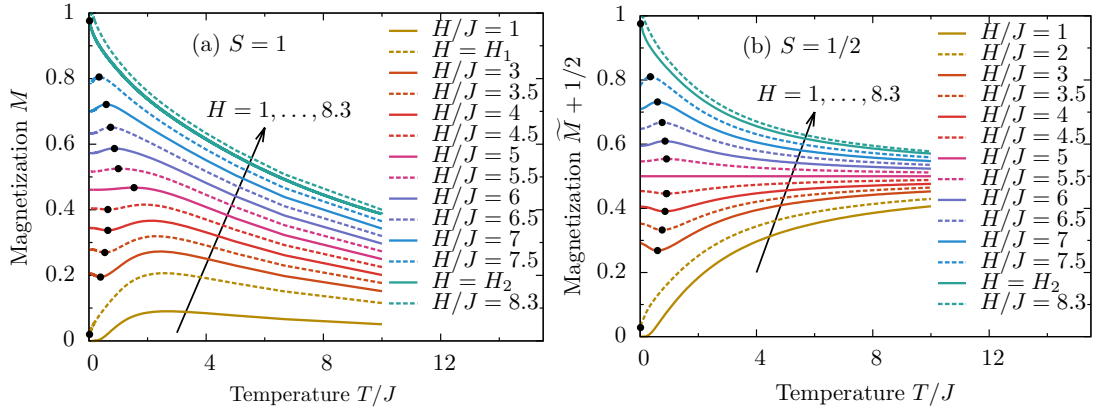


**Figure 3.1.2:** The temperature dependence of magnetization for (a) the  $S = 1$  large- $D$  model and (b) the  $S = 1/2$  XXZ model, for various fields. Dots indicate the position of extrema that correspond to the Luttinger liquid crossover.  $T_c$  decreases toward  $T = 0$  as  $H$  approaches  $H_1$  or  $H_2$ .

accurate than close to  $H_1$ . This expectation is verified by the magnetization curves close to  $H_2$  which are indistinguishable.

Let us now focus on the temperature dependence of magnetization for a wide range of fixed magnetic fields, as illustrated in Fig. 3.1.2. For  $H < H_1$ , magnetization vanishes exponentially toward  $T = 0$ ; for  $H > H_1$ , a minimum appears at low temperatures that persists up to  $H_m = (H_1 + H_2)/2$ , whereas maxima occur at larger magnetic fields for  $H_m < H < H_2$ . A further increase of the magnetic field will reopen the gap, and for  $H > H_2$  the  $M(T)$  curve decreases with increasing temperature and vanishes exponentially. In Fig. 3.1.2(a) we present the above-described behaviour of  $M$  and the position of the extrema  $T_c$  is indicated by dots.

The presence of minima and maxima at low temperatures is not a surprising result, since similar features were found for systems of  $S = 1/2$  ladders [106–108, 110] and Haldane chains [111], where this nontrivial behaviour was interpreted as a Luttinger liquid (LL) crossover, with  $T_c$  corresponding to the temperature below which the description of the system in terms of a LL is valid.

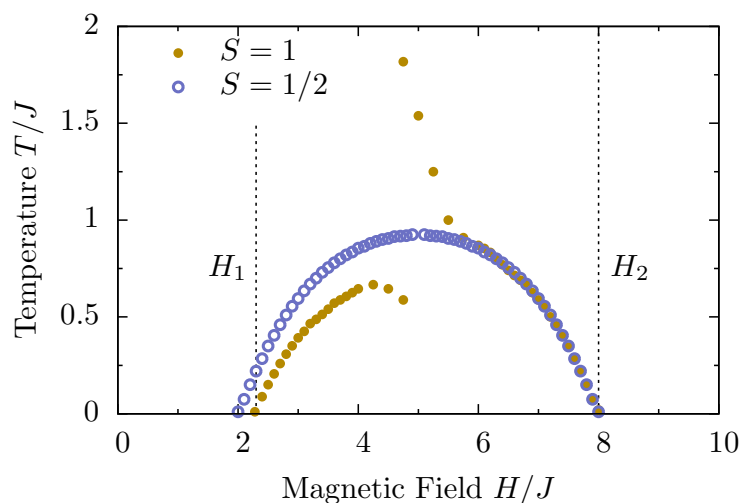
Here we examine this behaviour in terms of the  $S = 1/2$  model, and in Fig. 3.1.2(b) we have plotted the temperature dependence of magnetization for the same values of magnetic field. For small values of temperature, magnetization behaves in a similar way, with a minimum or maximum being present for every value of magnetic field. Any deviations for higher temperature can be attributed to the missing component of the doublet. At the value  $H/J = 5$  ( $\tilde{H} = 0$ ) the extrema are expected to disappear and  $\tilde{M} = 0$  for every temperature. The position of the extrema is symmetric around  $H/J = 5$ , reflecting the symmetry around  $\tilde{H} = 0$ , where every minimum for  $\tilde{H} < 0$  corresponds to a maximum under the substitution  $\tilde{H} \rightarrow -\tilde{H}$ . As expected, this symmetry holds for the  $S = 1$  model only in the  $D/J \gg 1$  limit. This lack of symmetry is easily seen in

Fig. 3.1.3, where we present the magnetic phase diagram for both models with symbols marking the crossover into a low-temperature Luttinger liquid regime. Note that the discontinuity close to  $H_m$  is an artifact of the way in which we identify the LL transition [110].

The results presented in this section, namely, the low-temperature critical exponent  $\delta = 2$  and the extrema of the  $M(T)$  curve should be accessible to experimental verification. Magnetization measurements on DTN [112, 113] revealed a linear dependence of  $M(H)$  at low temperatures and  $M(T)$  traces at fields close to  $H_1$  display a cusp-like dip that was attributed to the onset of 3D  $XY$  AFM order rather than a LL crossover. Exchange couplings perpendicular to the chain  $J_{\perp}$  play an important role in determining the dimensionality of DTN close to the QPT at  $H_1$  and  $H_2$ , where the gap closes and the system behaves as three-dimensional. The power-law behaviour of the observed phase boundary [61]  $H_1(T) - H_1(0) \propto T^{\alpha}$  has been identified as  $\alpha = 1.47 \pm 0.10$  consistent with the 3D BEC universality class. We should emphasize that the phase diagram of Fig. 3.1.3 does not correspond to a real phase transition, but to a crossover between different regimes with an  $\alpha \simeq 1$  exponent, and should lie above the phase diagram of BEC or  $XY$  AFM type.

## 3.2 Specific Heat

The magnetic field and temperature dependence of specific heat  $\mathcal{C}_v$  is now investigated. A well established result [114] is that the specific heat of the  $S = 1/2$   $XXZ$  model develops a characteristic double peak as a function of an applied longitudinal magnetic field at relatively low- $T$ . This characteristic behaviour cannot be explained by noninteracting



**Figure 3.1.3:** Magnetic phase diagram of the  $S = 1$  chain with a strong easy-plane anisotropy (full points) and of the  $S = 1/2$   $XXZ$  chain (open points). Symbols indicate the crossover into a finite-temperature LL regime present for both models.

magnons, where a single peak should be expected with its maximum at the position of the critical field.

The numerical calculation of  $\mathcal{C}_v$  for the  $S = 1$  large- $D$  chain reveals that the double peak is indeed present for adequately low temperatures. This is presented in Fig. 3.2.1, where  $\mathcal{C}_v$  is plotted as a function of magnetic field at fixed temperature  $T/J = 0.1$ . The position of the double peak is around critical fields  $H_1$  and  $H_2$ . Note that the curve is symmetric around  $H_m$  for the  $S = 1/2$  XXZ chain due to the spin-inversion symmetry, whereas some asymmetry arises for the  $S = 1$  large- $D$  chain which is apparent near the lower critical field  $H_1$ .

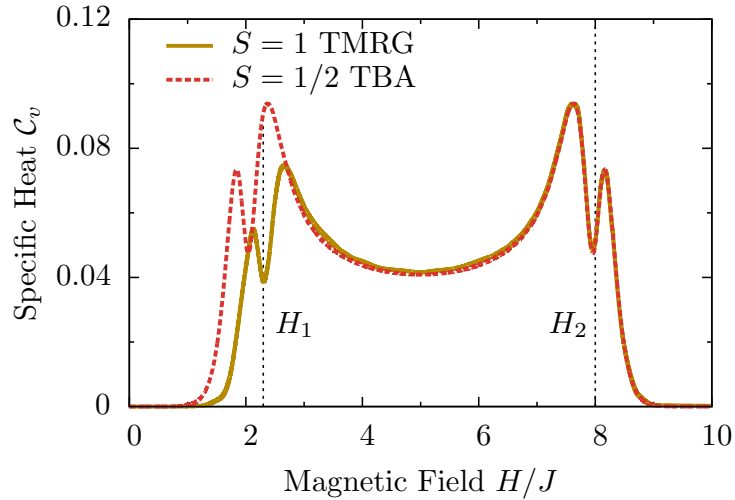


**Figure 3.2.1:** The magnetic field dependence of specific heat  $\mathcal{C}_v$  at fixed temperature  $T/J = 0.1$ . The solid line corresponds to TMRG results for the  $S = 1$  large- $D$  model and the dashed line corresponds to TBA results of the  $S = 1/2$  XXZ model.

The temperature dependence of specific heat is also studied at various magnetic fields, and the main features are depicted in Fig. 3.2.2, calculated for the original  $S = 1$  model using the TMRG algorithm. More specifically, for  $H < H_1$  specific heat decays exponentially at low temperatures due to the presence of the gap. The curve has a single peak which can be attributed to the thermal population of the  $S^z = \pm 1$  doublet excitations. An increase of  $H$  will cause a decrease of the  $\mathcal{C}_v$  curve. As  $H \rightarrow H_1$  the gap is reduced and the line shape is changed, as we find linear dependence on  $H$  at low- $T$ . For  $H_1 < H < H_2$  an additional peak is gradually developed, below which the temperature dependence remains linear. This behaviour is consistent with the LL phase where specific heat scales like  $\mathcal{C}_v/T \propto T^{d-1}$  for excitations with relativistic dispersion, where  $d$  is the dimension. Finally, for  $H > H_2$  the second peak vanishes and the reopening of the gap will again cause  $\mathcal{C}_v$  to decay exponentially at low  $T$ .

The characteristic behaviour of specific heat described in this section can be found in other models as well, for example,  $S = 1/2$  ladders. Measurements on systems of weakly coupled ladders [110] revealed qualitatively the same  $\mathcal{C}_v(T)$  behaviour, where the first

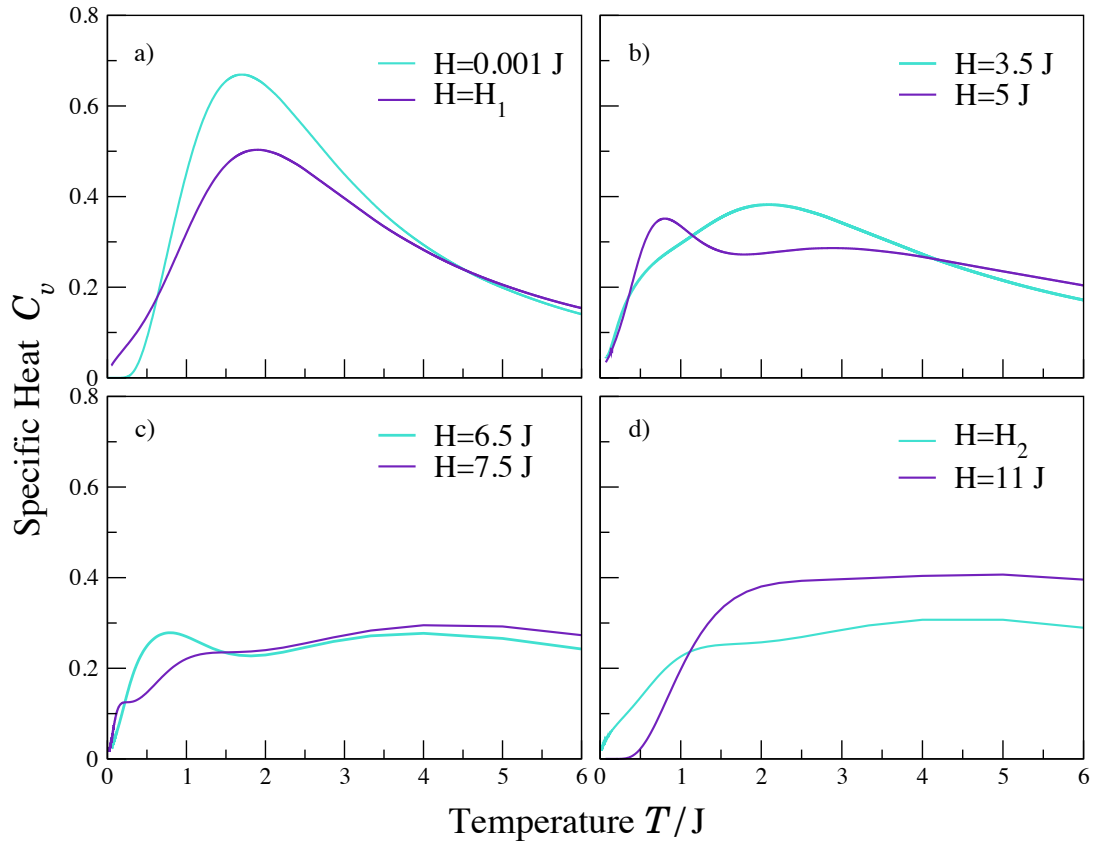


**Figure 3.2.2:** The temperature dependence of specific heat for various fields, calculated for the  $S = 1$  model using TMRG.

peak in  $T$  was explained as a sign of deviations from the LL linear regime. Moreover, the characteristic double peak of  $C_v$  as a function of magnetic field presented in Fig. 3.2.1 has been found experimentally [108, 109]. Note that the  $S = 1/2$  ladder compounds are considered to be good candidates to explore effects that occur in 1D quantum systems, with the interladder coupling being 2 orders of magnitude smaller than the intraladder couplings.

On the contrary, the specific heat data of DTN exhibit sharp peaks as a function of  $T$  and  $H$ , suggesting that DTN can partially be described as a quasi-1D system, making the inclusion of interchain couplings necessary in order to explain the experimental data. The low- $T$  dependence of specific heat data is  $T^{3/2}$  at  $H_1$ , in agreement with the expected 3D BEC [113]. In addition, the  $C_v(H)$  data exhibit sharp asymmetric peaks at the critical fields  $H_1$  and  $H_2$ , an asymmetry that was explained in terms of mass renormalization of the elementary excitations due to quantum fluctuations that exist for  $H \leq H_1$  and are absent for  $H \geq H_2$  [115]. The free magnon picture at any dimensionality is not sufficient to reproduce the double-peak shape. On the contrary, a single, rather sharp peak is predicted with a maximum at the critical fields. In Fig. 3.2.1 we notice that the asymmetry in  $C_v$  is present for the 1D case as well, with the value of

$C_v$  at the double peak around  $H_2$  being larger than the one around  $H_1$ . In terms of the effective mapping that we are discussing here, perfect symmetry is only expected in the  $D/J \gg 1$  limit.

Finally, in Fig. 3.2.3 we compare the TMRG result with FTLM calculation on the chain  $L = 16$  with periodic boundary conditions at  $T/J = 0.5$  in order to establish a reliable comparison between them. The two curves are in good agreement, especially in the vicinity of the two critical fields, with some deviations in the center of the intermediate phase that are due to finite-size effects of FTLM data.

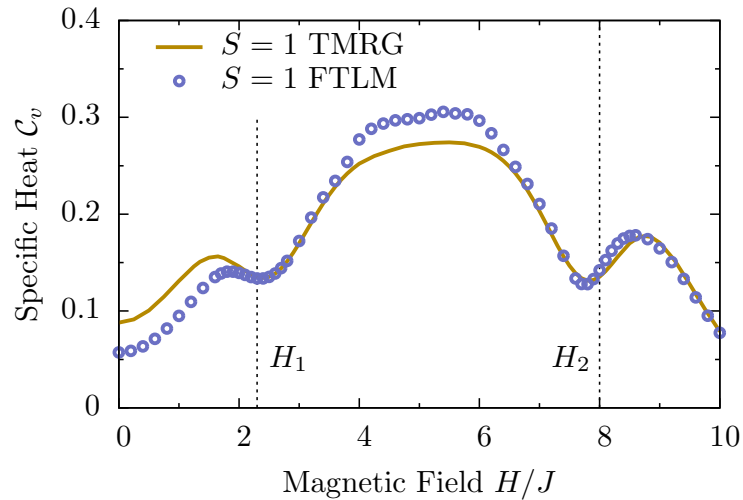


**Figure 3.2.3:** The magnetic field dependence of specific heat  $C_v$  at fixed temperature  $T/J = 0.5$  as calculated with TMRG (solid line) and FTLM (points) for the  $S = 1$  model. Deviations are due to finite-size effects of FTLM data.

### 3.3 Discussion

The temperature and magnetic field dependence of magnetization and specific heat of the  $S = 1$  model have been studied using a TMRG algorithm, which allows us to obtain these quantities with satisfactory accuracy in the thermodynamic limit. The thermodynamic Bethe ansatz is applied to derive the same quantities for the  $S = 1/2$  model. The critical exponent that describes the behaviour of magnetization near the critical fields at very low  $T$  is extracted from the numerical data of the  $S = 1$  model and found equal to  $\delta = 2$ . This result renders the considered model in the same universality class as a broad collection of various models of quantum magnetism.

Furthermore, the temperature dependence of magnetization for both models reveals the existence of extrema at some temperature  $T_c$ , which is interpreted as the critical temperature below which the description of the system in terms of Luttinger liquid is valid. A magnetic phase diagram is constructed that represents the crossover into a low- $T$  Luttinger liquid regime.

The chapter of thermodynamics is completed with the investigation of specific heat as a function of  $H$  and  $T$ . The  $\mathcal{C}_v(H)$  curve exhibits a characteristic double peak around critical fields  $H_{1,2}$  and the  $\mathcal{C}_v(T)$  curve reveals a linear dependence at low  $T$ , consistent with the LL phase.

## Chapter 4

# Thermal Transport

Transport properties of one-dimensional spin systems are currently the focus of active research, fuelled by both theoretical and experimental developments. This rapidly progressing field has been motivated by the experimental evidence that magnetic excitations can contribute significantly to the thermal conductivity of various quasi-one and two dimensional materials [116–124]. Moreover, many intensive theoretical activities have addressed the issue of heat transport in one-dimensional spin systems [125–146].

While the thermodynamic properties of low dimensional quantum magnets have been intensively studied, the transport properties are more challenging for experimental and theoretical physicists [6, 147–149]. From a theoretical perspective, the principle difficulty lies in the fact that transport theory requires the computation of nontrivial correlation functions [150]. Substantial progress has been made in the past years, but the understanding is still incomplete especially for systems involving many coupled degrees of freedom such as spins, orbitals and phonons, and for the basic understanding of scattering mechanisms and their effects.

The only strongly correlated systems for which we have a complete solution of their dynamics are the integrable ones. Most commonly, quantum systems are called integrable if an infinite set of local conserved quantities exist which are pairwise different. Exactly because of their integrability, these systems exhibit unconventional ballistic (non-diffusive) thermal transport [6], and many studies have been devoted to the question of whether integrability can stop a current from decaying completely [126, 135, 137, 140, 141, 144, 145, 151]. This ideal ballistic transport of quantum integrable models is the quantum analogue of transport by non decaying pulses (solitons) on 1D classical nonlinear integrable systems [152]. On the contrary, the theoretical work that has focused on transport properties of nonintegrable models revealed that, within linear response theory, ballistic transport is not realized [7, 129, 154, 155].

The first quantum integrable system was discovered by H. Bethe in 1931 [2], who proposed an exact treatment of the  $S = 1/2$  one-dimensional chain. One of the best

established results is the ballistic thermal transport in the integrable  $XXZ$   $S = 1/2$  chain [126, 137, 153, 154]. The transport and thermodynamic properties of integrable models can exactly be evaluated using the appropriate Bethe ansatz techniques. Among the other analytical methods used is the memory function approach [165] that has provided a complete picture of the temperature/frequency dependence and the form factor method that has also provided an exact evaluation of the frequency dependent conductivity, but it is limited to the calculation of zero temperature correlations.

The understanding of transport properties and the role of perturbations (phonons, disorder, interchain coupling) is of great importance for the interpretation of transport measurements [130, 155]. The large in magnitude heat conductivity of  $S = 1/2$  chain materials has attracted a lot of interest [120, 121], partly motivated by the prospect of ideal ballistic conductivity predicted by theory. Large thermal conductivities were also measured in ladder materials such as  $(Sr, Ca, La)_{14}Cu_{24}O_{41}$ , where the magnetic contribution to the total thermal conductivity exceeds the phonon part substantially [116–118, 156, 157]. In both cases, the large reported thermal conductivities establish a link between the thermal transport and magnetic excitations.

Here we concentrate on the conductivity of bulk clean systems where the scattering mechanisms are due to intrinsic magnetic interactions; dissipation mechanisms such as coupling to phonons or disorder are not taken into account. We also restrict to the application of linear response theory to spin and thermal transport [150], where thermal (spin) conductivity is given by the analogous Green-Kubo formula expression in terms of the energy (spin) current-current dynamic correlation function. Within the framework of linear response theory, the real part of the thermal  $\kappa$  (spin  $\sigma$ ) conductivity is defined as follows:

$$\kappa[\sigma](\omega) = D_{th}[D_s] \delta(\omega) + \kappa_{reg}[\sigma_{reg}](\omega), \quad (4.0.1)$$

where  $\kappa_{reg}(\sigma_{reg})$  is assumed to be regular at  $\omega = 0$ . Ballistic behaviour is signalled by a finite Drude weight  $D_{th,s}$ , which is the zero-frequency singular contribution to the real part of conductivity. Therefore, a finite Drude weight implies a divergent conductivity. If the current operator  $\mathcal{J}_E$  is a conserved quantity [7], the currents do not decay and the long time asymptotic of the energy current-current dynamic correlations is finite. According to the definition (4.0.1), such a scenario implies a finite thermal Drude weight at any temperature and thermal conductivity that diverges. It is well established that the energy current operator  $\mathcal{J}_E$  of the  $S = 1/2$   $XXZ$  chain is a conserved quantity [158, 159] and the thermal Drude weight  $D_{th}$  has been exactly evaluated using Bethe ansatz techniques [126] for all values of the anisotropy  $\Delta$ . It was realised that the existence of finite thermal Drude weights at all temperatures is connected with the integrability of a model and the fact that it is characterized by non-trivial conservation laws [137]. The dependence of thermal conductivity on temperature and  $\Delta$  has been

studied by means of Bethe Ansatz [126, 153] and exact diagonalization [127, 129, 154].

Concerning the spin transport the situation is more involved because in almost all the cases the spin current does not commute with the Hamiltonian. Even in the case of integrable systems, the spin-current operator is only conserved in the case of free fermions (XY). Nevertheless, it was shown [135–137] using an inequality proposed by Mazur and Suzuki [160] that for several quantum integrable systems  $D_s$  at high temperatures is bounded by the overlap of the current operator with at least one conserved quantity  $Q_n$ . Actually, only one conserved quantity  $Q_3$  is usually considered to establish a finite  $D_s$ .

Unfortunately, for the Hamiltonian of the  $S = 1/2$  model all  $Q_n$ 's, including  $\mathcal{H}$  and  $Q_3 = \mathcal{J}_E$ , are invariant under spin inversion, whereas  $\mathcal{J}_s$  is odd resulting  $\langle \mathcal{J}_s Q_n \rangle = 0$ . Only in the case of broken spin inversion symmetry, for example in the presence of a finite magnetic field, the condition  $\langle \mathcal{J}_s \mathcal{J}_E \rangle \neq 0$  is satisfied. The existence of a finite  $D_s$  at finite  $T$  has proven to be a delicate theoretical question for the zero magnetic field case.

Not until recently was an improved Mazur bound obtained [161] using a different approach based on deriving a whole family of almost conserved quasilocal conservation laws for an open XXZ chain up to boundary terms. It turns out that the quasilocal operator, with different symmetry properties than local  $Q_n$ 's, has a finite overlap with  $\mathcal{J}_s$  and provides a nonzero lower bound for the spin Drude weight. This important result was later extended to the XXZ chain with periodic boundary conditions, where a family of exactly conserved quasilocal operators was constructed [162, 163].

Integrable quantum systems show fundamentally different finite temperature transport properties than the generic non-integrable ones. In the case of nonintegrable models, both spin current and heat current are not conserved, except for the case of a dimerised  $S = 1/2$  XY chain [130]. The original conjecture by Zotos *et al.* [136, 164] stated that the Drude weights are expected to vanish in nonintegrable models. It is relevant to note that in order for the Drude weight to be finite, Mazur's inequality requires the existence of nontrivial conservation laws which have a finite overlap with the current operator in the thermodynamic limit. Since this is not the case in nonintegrable systems, Drude weights are zero and the relevant information is encoded in the frequency dependence of the conductivities.

Not only analytical approaches, but also numerical simulations are intensely employed for the study of finite temperature dynamic correlations. The exact diagonalization (ED) technique provides exact answers over the full temperature/frequency range, but only on finite size systems [166]. The finite scaling can provide useful hints on the macroscopic behaviour, but usually it is difficult to establish a definite conclusion about the thermodynamic limit. For example, any finite-size system shows a nonzero Drude weight that however scales to zero in the thermodynamic limit if the systems shows normal transport. This implies that there are limitations on the information that can

be extracted on the long time behaviour of the conductivities. Moreover, the Quantum Monte Carlo (QMC) technique [167] and the Density matrix renormalisation group (DMRG) method [169] allow the study of larger systems and they provide directly the dynamic correlations at finite temperatures but in imaginary time. By analytical continuation, one is able to extract the dependence to real frequencies. This method is not very reliable and cannot resolve singularities associated with the long-time behaviour. In fact the application of QMC has led to the conclusion that the Drude weight is finite for some nonintegrable systems [168].

In this chapter we address the calculation of dynamic correlation functions pertinent to the study of thermal transport of the  $S = 1$  large- $D$  model of (3.0.1) and  $S = 1/2$  XXZ model of (3.0.4) in the presence of finite magnetic field. In the first part, the transport theory is presented within the framework of linear response theory, and relevant issues are discussed. Next, the thermal conductivity of the  $S = 1$  model is presented, as it is calculated using the FTLM method on a chain up to  $L = 16$  sites. The frequency dependence of the conductivity is explored for a wide range of magnetic fields and various temperatures. In addition the  $S = 1/2$  XXZ chain is considered, and the comparison between the two models reveals that the magnetic field dependence of the Drude weight of the effective model includes all characteristic features of the  $S = 1$  low- $\omega$  behaviour. For the  $S = 1/2$  chain, attention is also given in the magnetic field dependence of the spin Drude weight and the magnetothermal corrections to the thermal conductivity, a term that originates from the coupling of the heat and spin currents in the presence of magnetic field.

## 4.1 Transport Theory

Most the studies on transport properties of one dimensional quantum many body systems over the last few years were within the linear response theory (Kubo formalism) [170]. Within this framework conductivities are given in terms of finite temperature  $T$  dynamic correlations calculated at the thermodynamic equilibrium. We note that alternative approaches exist, such as coupling the spin chain to heat baths [125, 171, 172].

**Transport coefficients at finite magnetic fields:** The spin current  $\mathcal{J}_s$  and heat current operator  $\mathcal{J}_Q$  are defined from the continuity equation for the density of the conserved local spin component  $S_n^z$  and local energy  $\mathcal{H}_n$  correspondingly. The continuity equation:

$$\frac{\partial S_n^z}{\partial t} + \nabla j_n^S = 0, \quad S^z = \sum_n S_n^z, \quad (4.1.1)$$

gives the spin current  $\mathcal{J}_S = \sum_n j_n^S$ . Note that the discrete gradient of a local operator is defined as  $\nabla j_n^S = j_n^S - j_{n-1}^S$ , and the time derivative is replaced by Heisenberg equation

of motion  $\partial_t S_n^z = -i[S_n^z, \mathcal{H}]$ . In most cases the spin current does not commute with the Hamiltonian. Similarly, the heat current  $\mathcal{J}_Q = \sum_n j_n^Q$  is obtained by:

$$\frac{\partial \mathcal{H}_n}{\partial t} + \nabla j_n^Q = 0, \quad \mathcal{H} = \sum_n \mathcal{H}_n, \quad (4.1.2)$$

where  $\mathcal{H}_n$  is the local energy density that includes the magnetic field term. In the absence of magnetic field  $H = 0$ , a similar continuity equation can be defined for the energy current  $\mathcal{J}_E = \sum_n j_n^E$ :

$$\frac{\partial \mathcal{H}_n|_{H=0}}{\partial t} + \nabla j_n^E = 0, \quad \mathcal{H}|_{H=0} = \sum_n \mathcal{H}_n|_{H=0}. \quad (4.1.3)$$

It is easy to show that in the case of a magnetic field applied along the  $z$  direction, the heat, energy and spin current are connected by the relation [150]:

$$\mathcal{J}_Q = \mathcal{J}_E + H \mathcal{J}_s. \quad (4.1.4)$$

In the presence of magnetic field the heat current and the spin current couple since spin-inversion symmetry is broken and hence  $\langle \mathcal{J}_Q \mathcal{J}_S \rangle \neq 0$  [137]. Within the linear response theory, the heat current  $\mathcal{J}_Q$  and the spin current  $\mathcal{J}_S$  are related to the gradients of magnetic field  $\nabla H$  and temperature  $\nabla T$  by the transport coefficients  $C_{ij}$  [150]:

$$\begin{pmatrix} \mathcal{J}_Q \\ \mathcal{J}_S \end{pmatrix} = \begin{pmatrix} C_{QQ} & C_{QS} \\ C_{SQ} & C_{SS} \end{pmatrix} \begin{pmatrix} -\nabla T \\ \nabla H \end{pmatrix}, \quad (4.1.5)$$

where  $C_{QQ} = \kappa_{QQ}$  ( $C_{SS} = \sigma_{SS}$ ) is the heat (spin) conductivity. The coefficients  $C_{ij}$  correspond to the time-dependent current-current correlation functions:

$$C_{ij}(\omega) = \lim_{\epsilon \rightarrow 0^+} \frac{\beta^r}{L} \int_0^\infty dt e^{-i(\omega - i\epsilon)t} \int_0^\infty d\tau \langle \mathcal{J}_i \mathcal{J}_j(t + i\tau) \rangle, \quad \{i, j\} = \{Q, S\}, \quad (4.1.6)$$

where  $r = 0$  for  $j = S$  and  $r = 1$  for  $j = Q$ . It is straightforward to see that due to Onsager's relation [150],  $C_{SQ} = \beta C_{QS}$ . The real part of  $C_{ij}(\omega)$  can be decomposed into a  $\delta$  function at  $\omega = 0$  and a regular part:

$$\text{Re}(C_{ij}(\omega)) = 2\pi D_{ij} \delta(\omega) + C_{ij}^{\text{reg}}(\omega). \quad (4.1.7)$$

The spectral representation of the regular part  $C_{ij}^{\text{reg}}(\omega)$  expressed in terms of eigenstates  $|n\rangle$  and eigenenergies  $\epsilon_n$  is:

$$C_{ij}^{\text{reg}}(\omega) = \frac{\pi \beta^r}{L} \frac{1 - e^{-\beta\omega}}{\omega} \sum_{\epsilon_n \neq \epsilon_m} p_n \langle m | \mathcal{J}_i | n \rangle \times \langle n | \mathcal{J}_j | m \rangle \delta(\epsilon_n - \epsilon_m - \omega), \quad (4.1.8)$$

while the dissipationless component with the Drude weight is related to the degenerate matrix elements:

$$D_{ij} = \frac{\beta^{r+1}}{2L} \sum_{\epsilon_n = \epsilon_m} p_n \langle m | \mathcal{J}_i | n \rangle \langle n | \mathcal{J}_j | m \rangle, \quad (4.1.9)$$

where  $p_n = \exp(-\beta\epsilon_n)/Z$  are corresponding Boltzmann weights and  $Z$  is the partition function.

To relate the correlation function presented so far to experimentally accessible quantities, we note that the spin conductivity  $\sigma$ , measured under the condition of  $\nabla T = 0$ , is equal to:

$$\sigma(\omega) = C_{SS}(\omega), \quad (4.1.10)$$

and the thermal conductivity under the assumption of vanishing spin current  $\mathcal{J}_S = 0$ , which is relevant to certain experimental setups, is redefined as follows:

$$\kappa(\omega) = \kappa_{QQ}(\omega) - \beta \frac{C_{QS}^2(\omega)}{C_{SS}(\omega)}, \quad (4.1.11)$$

where the second term is usually called the magnetothermal correction. Such a term originates from the coupling of the heat and spin currents in the presence of magnetic field [133, 173, 174] and is absent when  $H = 0$ .

A quantity that has attracted attention is the prefactor  $D_{SS}$  of the  $\delta$ -function of Eq.(4.1.7) for the real part of spin conductivity, named the spin Drude weight or spin stiffness. As Kohn suggested in [175], it is a criterion of ideal conducting or insulating behaviour at  $T = 0$ . For a clean system at  $T = 0$ , two possibilities exist with respect to  $D_0 = D_{SS}(T = 0)$ ; a positive  $D_0 > 0$  characterizes a conductor (metal) and a vanishing  $D_0 = 0$  characterizes an insulator [6]. A clean metallic system at  $T = 0$  is characterized by a  $\delta$ -function Drude peak, but at finite temperatures it broadens to a Drude peak of width inversely proportional to a characteristic scattering time  $\tau$ , that is in general temperature dependent. The scattering mechanisms can be intrinsic, due to interactions, or extrinsic due to coupling to other excitations such as phonons or magnons. But it is also possible that constraints on the scattering mechanisms limit the current decay, so that the system remains an ideal conductor at finite temperatures, i.e.  $D_{SS}(T > 0) > 0$  [6]. For an insulating system  $D_0 = 0$ , and in the conventional case  $D_{SS}$  remains zero at finite temperatures, while  $\sigma_{dc} = \sigma^{reg}(\omega \rightarrow 0)$  is finite. There is the possibility that  $D_{SS}$  becomes finite, turning a  $T = 0$  insulator to an ideal conductor, or that both  $D_{SS}$  and  $\sigma_{dc}$  remain zero at  $T > 0$ , a system that is called an ideal insulator [6].

On the analogy of the thermoelectric power (Seebeck coefficient) for electron systems, the thermomagnetic power  $S$  for magnetic systems is defined as [176]:

$$S = \frac{\nabla H}{\nabla T} = \frac{C_{SQ}}{C_{SS}}. \quad (4.1.12)$$

Quantity  $S$  is usually called magnetic Seebeck coefficient, and is a crucial criterion to clarify the types of carriers. When the sign of  $S$  is positive (negative) the spin and heat are dominantly carried by the carriers with up-spin (down-spin) [176]. The off-diagonal terms of (4.1.5) contribute to the determination of another important quantity that determines the efficiency of thermomagnetic devices for cooling or power generation, the thermomagnetic figure of merit  $ZT$  [176]:

$$ZT = \frac{C_{QS}^2}{C_{QQ}C_{SS} - C_{QS}^2}. \quad (4.1.13)$$

**Conservation laws and Integrability:** The effect of conservation laws on finite-temperature transport properties in one-dimensional integrable quantum models was studied in [137]. The authors showed that the energy current is related to the first non-trivial conservation law in these systems, and therefore the thermal transport coefficients are anomalous. More precisely, an inequality proposed by Mazur [160] was used in the analysis of the real part of the conductivity  $\sigma$ :

$$\text{Re}(\sigma) = \text{Re}(C_{SS}) = 2\pi D_{SS}\delta(\omega) + \sigma^{reg}(\omega). \quad (4.1.14)$$

The inequality for the spin Drude weight holds:

$$D_M \geq \frac{\beta}{2L} \sum_n \frac{\langle \mathcal{J}_S Q_n \rangle^2}{\langle Q_n^2 \rangle}, \quad (4.1.15)$$

where  $\langle \rangle$  denotes thermodynamic average, the sum is over the subset of conserved quantities  $Q_n$  orthogonal to each other,  $\langle Q_m Q_n \rangle = \delta_{mn} \langle Q_n^2 \rangle$  and it is assumed that the regular part shows a nonsingular behaviour at low frequencies. In general it is difficult to evaluate the right-hand side of inequality (4.1.15). For integrable models where at least one conserved quantity  $Q_n$  has nonzero overlap with the current operator  $\langle Q_n \mathcal{J}_S \rangle \neq 0$ , Mazur's inequality implies that the Drude weight is finite at finite temperatures. For the case of  $S = 1/2$  XXZ chain, only one conserved quantity is often considered, namely  $Q_3 = \mathcal{J}_E$ . Several authors have used this equation to infer a finite spin Drude weight for the Heisenberg chain, assuming broken particle-hole symmetry or the presence of a finite magnetic field. The Mazur's inequality provides a useful bound for integrable systems that are known to possess nontrivial conservation laws because of their integrability, but can not provide a complete picture of the Drude weight behavior.

For nonintegrable models, for which all non-trivial conservation laws are expected to be broken, the right-hand side of Mazur's inequality is expected to vanish. In these cases the dc conductivity is finite and the system is said to exhibit diffusive transport.

**Low energy effective field theories:** Effective low energy models for interacting electrons provide an alternative way to calculate the transport of quasi-one dimensional quantum models [6]. For example, the effective low-energy theoretical model for 1D interacting fermions is derived by linearising the band dispersion around the Fermi momenta and by defining left and right movers. The model is mapped onto the well-known Luttinger liquid Hamiltonian and can be analysed via the bosonization representation [177, 178]. The Bosonization of the  $S = 1/2$  XXZ Heisenberg chain leads [178] to the quantum-Sine Gordon model, which is an integrable system and has extensively been studied. The thermodynamic properties and excitation spectrum consisting of solitons-antisolitons and breather states have been established by semi-classical and Bethe ansatz techniques [179], while a rigorous evaluation of the Drude weight and frequency dependence of the conductivity at finite  $T$  is missing [6].

The low-energy physics of the  $S = 1$  Haldane chain and even-leg ladders is described by the one dimensional quantum nonlinear sigma model. A semiclassical theory applicable to gapped systems by Sachdev and collaborators, based on the idea that the spin excitations can be mapped to an integrable model describing a classical gas of impenetrable particles, predicts a normal diffusive behaviour [180]. In contrast to this semiclassical approach, using the Bethe ansatz solution of the quantum nonlinear sigma model [181], Fujimoto [182] found a finite Drude weight, exponentially activated with temperature, and he thus concluded that the spin transport at finite  $T$  is ballistic. In order to understand the origin of this discrepancy, one has to note that the low-energy model crucially depends on the choice of which operators are kept and which ones can be omitted when passing from the lattice to the continuum limit. Within the effective field theory, a possible broadening of the  $\delta$ -function peak at finite temperatures has to be related to inelastic scattering; such a process is described by an umklapp term [183]. Rosch and Andrei [184] have shown that a certain class of umklapp operators leads to the decay of all currents and hence render all conductivities finite. These umklapp terms are irrelevant for static properties but they appear to be crucial for transport, because they turn the diffusive transport to ballistic. Except for very special circumstances which could happen in certain integrable models, one should expect a vanishing Drude weight and hence a finite conductivity [185]. We should emphasise that the presence of umklapp processes is quite involved and need to be further clarified.

**Scattering mechanisms:** In order to arrive to a realistic theory of thermal transport in quasi-1D magnetic materials both intrinsic as well as extrinsic scattering processes are of relevance. This is supported by the phenomenological analysis of experimental findings for spin ladder as well as spin chain materials. When the scattering mechanism with external degrees of freedom is introduced, one may expect the infinite Drude peak

to be broadened and the transport coefficients may be replaced to:

$$\text{Re}(C_{ij}) = 2\pi D_{ij} \delta(\omega) \rightarrow \frac{D_{ij}\tau}{1 + (\omega\tau)^2} \quad (4.1.16)$$

where the relaxation time  $\tau$  depends on the particular scattering mechanism and is in general temperature and magnetic field dependent.

## 4.2 Thermal Transport in the $S = 1$ large- $D$ chain

Here we present results for the heat conductivity  $\kappa_{QQ}(\omega)$  calculated for the  $S = 1$  model with FTLM on the chain up to  $L = 16$  sites, and the results will be later compared with exact findings obtained for the  $S = 1/2$  model. According to continuity equation (4.1.2), the heat current  $\mathcal{J}_Q$  for the  $S = 1$  large- $D$  Hamiltonian of Eq.(3.0.1) is equal to:

$$\mathcal{J}_Q = \sum_n \left[ J^2 \mathbf{S}_{n-1} \cdot (\mathbf{S}_n \times \mathbf{S}_{n+1}) + (2DS_n^z + H) j_n^S \right], \quad (4.2.1)$$

where  $j_n^S = J (S_n^x S_{n+1}^y - S_n^y S_{n+1}^x)$  is the local spin current. Since our numerical calculation is performed on a finite chain, it is expected that the  $\kappa_{QQ}(\omega)$  is a sum of weighted  $\delta$  functions. Therefore in Fig. 4.2.1 we present the integrated conductivity

$$I_{QQ}(\omega) = \frac{1}{2\pi} \int_{-\omega}^{\omega} d\omega' \kappa_{QQ}(\omega'), \quad (4.2.2)$$

which is a much more reliable, monotonically increasing function, when numerically dealing with finite-system results.

From Fig. 4.2.1 it becomes apparent that  $\kappa_{QQ}(\omega)$  exhibits two, well separated regions: the low- $\omega$  part and the high- $\omega$  part that is activated around  $\omega/J \gtrsim D$ . The spectral representation of  $\kappa_{QQ}(\omega)$  of Eq. (4.1.8) implies that nonzero matrix elements exist only

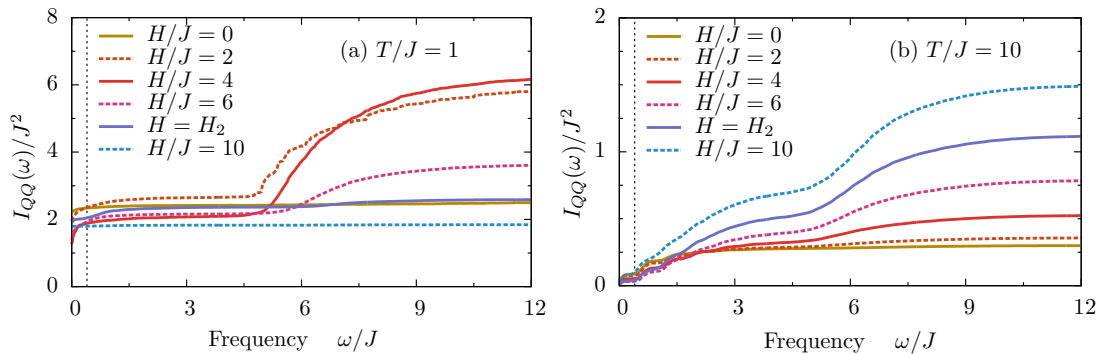


**Figure 4.2.1:** Integrated conductivity  $I_{QQ}(\omega)$  for (a)  $T/J = 1$  and (b)  $T/J = 10$  as calculated for  $L = 16$  sites and different fields  $H$ . Dashed vertical line represents  $\omega_0/J = 2\pi/L \sim 0.4$ .

for states  $|n\rangle$  and  $|m\rangle$  which obey the  $\Delta S^z = 0$  and  $\Delta k = 0$  selection rules. At low enough  $T$ , the high-frequency part of  $\kappa_{QQ}^{\text{reg}}(\omega)$  should be dominated by transitions between the ground state and the next in energy state with the same total magnetization. As mentioned already, for  $H < H_1$ , the ground state  $|\Omega\rangle$  carries zero azimuthal spin  $S^z = 0$  and the elementary excitations are the degenerate  $S^z = 1$  excitons and  $S^z = -1$  antiexcitons with energy momentum dispersion  $\epsilon(k)$  [54, 78]. The next in energy state that belongs to the total  $S^z = 0$  subspace is constructed by an exciton with crystal momentum  $k_1$  and an antiexciton with  $k_2$  and energy equal to  $\epsilon(k_1) + \epsilon(k_2)$ ; the exciton–antiexciton continuum. Therefore, at low  $T$ , the simplest possibility is a transition between the ground state and the exciton–antiexciton continuum at  $k = k_1 + k_2 = 0$ , resulting contributions from a band of frequencies with boundary lines  $\omega_{\alpha,\beta}$ , where

$$\omega_{\alpha,\beta} = 2D \mp 4J + 2J^2/D \pm J^3/D^2. \quad (4.2.3)$$

In Fig. 4.2.2 we plot the frequency dependence of  $\kappa_{QQ}(\omega)$  at  $H = 2$  and relatively low temperature  $T/J = 1$ . As predicted, the high-frequency part of  $\kappa_{QQ}^{\text{reg}}(\omega)$  is activated at frequencies around  $\omega_\alpha$  and terminates at  $\omega_\beta$ , a result consistent with the preceding analysis.

For  $H > H_2$  the ground state is fully polarized with no other state sharing the same  $S^z$  subspace; therefore it is expected that contributions at high frequencies will vanish. This is supported by our numerical results and is evident in Fig. 4.2.1(a), where for  $H \geq H_2$  only the  $\omega \sim 0$  contributions are present. In the intermediate phase for  $H_1 < H < H_2$ , the elementary excitations are difficult to calculate and there can be no analytical predictions such as lines  $\omega_{\alpha,\beta}$ . From the numerical data presented in Fig. 4.2.1(a), we conclude that for  $H_1 < H < H_2$  the high- $\omega$  part of  $\kappa_{QQ}^{\text{reg}}(\omega)$  is active at a band roughly between lines  $\omega_\alpha$  and  $\omega_\beta$  with intensity that is gradually reduced as

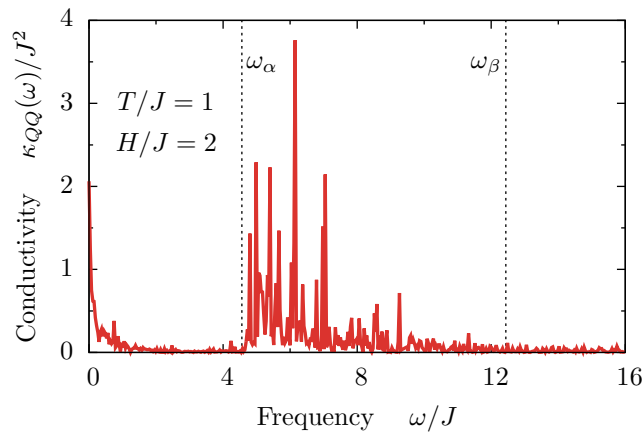


**Figure 4.2.2:** Frequency dependence of  $\kappa_{QQ}(\omega)$  at  $H = 2$  and  $T/J = 1$ . Labels  $\omega_{\alpha,\beta}$  indicate the boundaries of the band with nonvanishing weight at low  $T$ .

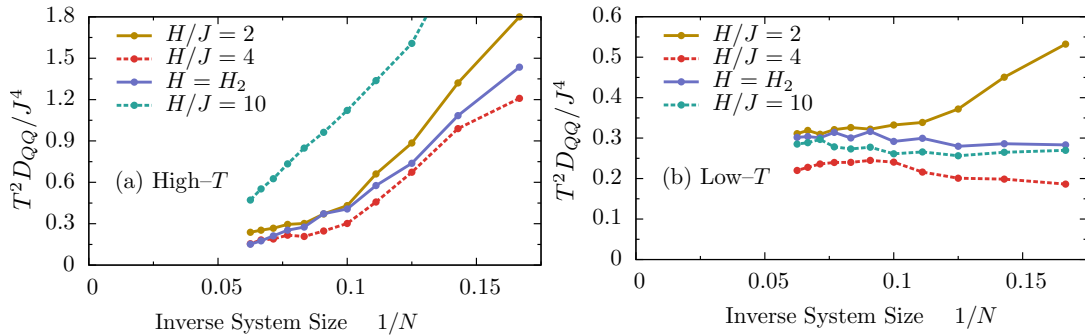


**Figure 4.2.3:** System size scaling of Drude weight  $D_{QQ}$  at (a)  $T/J = 10$  and (b)  $T/J = 1$ , obtained for systems with  $L = 6, \dots, 16$  sites with various magnetic fields  $H/J = 2, 4, 8, 10$ .

$H \rightarrow H_2$ .

Several conclusions can be drawn also for  $\omega \rightarrow 0$  behaviour of  $\kappa_{QQ}(\omega)$ . To begin with, in Fig. 4.2.1(b) an anticipated result for nonintegrable systems is illustrated, namely, that Drude weight  $D_{QQ}$  vanishes for high temperatures. On the other hand, at low temperatures,  $D_{QQ}$  remains finite at any value of  $H$ , as can be seen in Fig. 4.2.1(a). Moreover, for  $H \geq J$  the  $\omega \sim 0$  contributions are dominant in the total sum rule  $I_{QQ}(\omega = \infty)$  and almost all weight is in Drude weight itself. Since the model (1.5.1) is a nonintegrable, one would expect that  $D_{QQ}$  is vanishing exponentially fast (at least for  $T \rightarrow \infty$ ) with system size  $L$ , leading to diffusive transport in the thermodynamic limit [186].

In order to clarify this, we present in Fig. 4.2.3 inverse system size  $1/L$  scaling of the  $D_{QQ}$  for various values of  $T$  and  $H$ . For  $T \gg J$  the Drude weight is indeed vanishing exponentially fast, consistent with diffusive transport. However, this is not the case for low  $T$ , where the scaling of  $D_{QQ}$  seems to weakly depend on system size. The choice of  $H$  that determines whether the system is in the gapped or gapless phase does not seem to affect this scaling. Yet, a finite value of  $D_{QQ}$  in the thermodynamic limit is one of the features of integrable systems [137], which is clearly not the case of the considered model (3.0.1) [186]. One of the possible explanations of this phenomenon is that the intrinsic diffusive processes at low  $T$ , that will result in a zero  $D_{QQ}$  in the thermodynamic limit, become effective beyond the reachable system size or the energy resolution of the method presented here. As a result, it is expected that as one increases the system size, the spectral weight from  $D_{QQ}$  shifts to  $\kappa_{QQ}^{\text{reg}}(\omega < \omega_0)$ , with  $\omega_0/J \sim 2\pi/L$  [187, 188]. The latter completely dominates the low- $\omega$  behaviour of  $\kappa_{QQ}(\omega)$  in the thermodynamic limit ( $L \rightarrow \infty$ ). Therefore, to capture this finite-size effect, in the following we will consider integrated conductivity  $I_{QQ}(\omega_0)$  (frequency  $\omega_0$  is depicted as vertical dashed line in Fig. 4.2.1).

To gain insight into the origin of the slowly decaying Drude weight at low  $T$ , let us consider thermal transport in the effective low-energy  $S = 1/2$  Hamiltonian (3.0.4). The

heat current  $\tilde{\mathcal{J}}_Q$  is defined for this model in the same way, i.e.,  $\tilde{j}_i^Q - \tilde{j}_{i-1}^Q = -\imath[\tilde{\mathcal{H}}, \tilde{\mathcal{H}}_{i-1}]$  with  $\tilde{\mathcal{H}} = \sum_i \tilde{\mathcal{H}}_i$ , leading to

$$\tilde{\mathcal{J}}_Q = \sum_n \left[ 4J^2 \tilde{\mathbf{S}}_{n-1} \cdot \left( \tilde{\mathbf{S}}_n \times \tilde{\mathbf{S}}'_{n+1} \right) + \tilde{H} \tilde{j}_n^S \right], \quad (4.2.4)$$

with  $\tilde{\mathbf{S}}'_n = (\tilde{S}_n^x, \tilde{S}_n^y, \Delta \tilde{S}_n^z)$ . Other definitions and properties of the currents and conductivities remain the same with appropriate  $\tilde{\mathcal{J}}_\alpha$ ,  $\alpha = Q, E, S$  and  $\tilde{J} = 2J$ .

It is known that the  $S = 1/2$  Heisenberg model is integrable, with heat current being one of the conserved quantities,  $[\tilde{\mathcal{J}}_Q, \tilde{\mathcal{H}}] = 0$ , leading directly to its nondecaying behaviour and within the linear response to infinite thermal conductivity. Also, the integrability of the model (3.0.4) makes the calculation of  $\tilde{D}_{QQ}$  feasible in the thermodynamic limit. As a consequence of Eq.(4.1.4), one can decompose Drude weight in terms of the energy and spin contribution

$$\tilde{D}_{QQ} = \tilde{D}_{EE} + 2\beta \tilde{H} \tilde{D}_{ES} + \beta \tilde{H}^2 \tilde{D}_{SS}, \quad (4.2.5)$$

where Drude weights are defined in Eq.(4.1.9), with  $r = 1$  for  $i = j = Q$  or  $i = j = E$ , and  $r = 0$  for  $i = j = S$  or  $i = E, j = S$ .

The  $\tilde{D}_{EE}$  and  $\tilde{D}_{ES}$  at finite temperatures have been calculated by Sakai and Klümper [173] using a lattice path integral formulation, where a quantum transfer matrix (QTM) in the imaginary time is introduced. Correlations and thermodynamic quantities can be evaluated in terms of the largest eigenvalue of the QTM. The importance of this method yields to the fact that all quantities are found by solving two nonlinear integral equations at arbitrary magnetic fields, temperatures and anisotropy parameters. Here we repeat the calculation using  $\Delta = 1/2$ .

On the other hand, spin Drude weight  $\tilde{D}_{SS}$  at finite magnetic field is computed based on a generalization of a method that was proposed by Zotos [141], where  $\tilde{D}_{SS}$  was calculated using the Bethe ansatz technique at zero magnetic field. The presence of magnetic field will cause some changes to the TBA equations [101], but the overall analysis is essentially the same. A more detailed study of the magnetic field dependence of  $\tilde{D}_{SS}$  for a general  $\Delta$  will be presented in the subsequent section.

In Fig. 4.2.4 we compare  $\tilde{D}_{QQ}$  for the  $S = 1/2$  model with the numerically obtained integrated conductivity  $I_{QQ}$  at  $\omega_0$  for the  $S = 1$  model on  $L = 16$  sites. As is clearly visible, the overall agreement is satisfactory. The magnetic field dependence of Drude weight  $\tilde{D}_{QQ}$  includes all characteristic features of the  $S = 1$  low- $\omega$  behaviour. From the results obtained for the thermal transport, as in the case of magnetization and specific heat, we observe that the mapping is much more accurate close to  $H_2$  than close to  $H_1$ . Also, due to spin-inversion symmetry, the  $S = 1/2$  results are symmetric with respect to  $H = 5$  ( $\tilde{H} = 0$ ), where lack of such a symmetry for the  $S = 1$  model is expected.

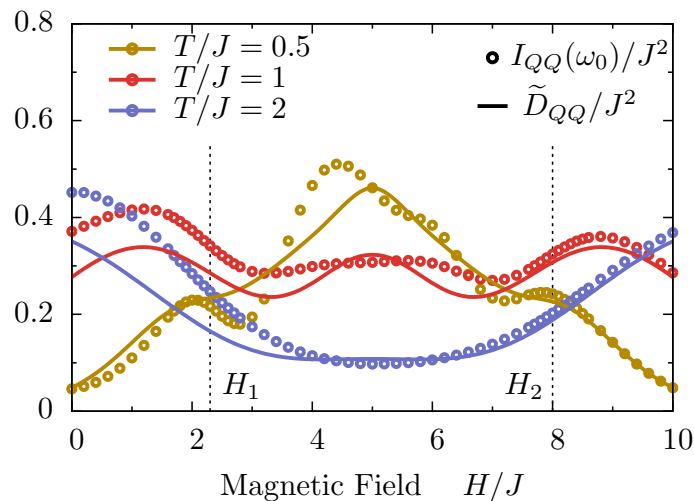


**Figure 4.2.4:** Comparison of  $S = 1$  integrated conductivity  $I_{QQ}(\omega_0)$  at  $\omega_0 = 2\pi/L$  for  $L = 16$  with exact  $S = 1/2$  Drude weight  $\tilde{D}_{QQ}$  calculated in the thermodynamic limit for  $T = 0.5, 1$  and  $2$  as a function of the magnetic field  $H$ .

Nevertheless, it is a nontrivial question as to which extent integrability of the low-energy effective  $S = 1/2$  Hamiltonian influences transport properties of the full  $S = 1$  model.

From Fig. 4.2.4 we notice, the thermal conductivity at  $T < J$  has a maximum located at  $H \simeq H_m = (H_1 + H_2)/2$ . However, this is not what is observed in the experiment. The thermal conductivity measurements at low  $T$  of the DTN compound [115, 189] exhibit sharp peaks in the vicinity of critical fields  $H_{1,2}$ . Detailed analysis of spin contribution to the total thermal conductivity is a nontrivial task due to the presence of phononic contribution. Also, the DTN compound is a quasi-1D material with  $J_{\perp}/J \simeq 0.18$ , and for temperatures below  $T_N < 1.2$  K ( $T/J \lesssim 0.5$ ) is in a 3D ordered state [41, 42, 61, 190] with long-range correlations [190, 191].

### 4.3 Thermal Transport in the $S = 1/2$ XXZ chain

The main objective of this section is the study of the thermal transport for the  $S = 1/2$  XXZ Heisenberg model in the presence of magnetic field and for values of the anisotropy parameter in the range  $1/2 < \Delta < 1$ . Before we turn our attention to the calculation of relevant correlation functions, we briefly review some main aspects of the model. The Hamiltonian for a chain of  $N$  sites with periodic boundary conditions  $S_{N+1}^{\alpha} = S_1^{\alpha}$  is given by:

$$\mathcal{H} = \sum_{n=1}^N (J(S_n^x S_{n+1}^x + S_n^y S_{n+1}^y + \Delta S_n^z S_{n+1}^z) + H S_n^z), \quad (4.3.1)$$

where  $S_i^\alpha = \frac{\sigma_i^\alpha}{2}$  are the Pauli spin operators with components  $\alpha = \{x, y, z\}$ . The energy current  $\mathcal{J}_E$  is defined from the continuity equation (4.1.3), which yields:

$$\begin{aligned} \mathcal{J}_E &= J^2 \sum_n S_{n-1}^y S_n^z S_{n+1}^x - S_{n-1}^x S_n^z S_{n+1}^y + \Delta(S_{n-1}^x S_n^y S_{n+1}^z - S_{n-1}^z S_n^y S_{n+1}^x) \\ &+ \Delta(S_{n-1}^z S_n^x S_{n+1}^y - S_{n-1}^y S_n^x S_{n+1}^z) \end{aligned} \quad (4.3.2)$$

while the spin current  $\mathcal{J}_s$  is given by Eq.(4.1.1):

$$\mathcal{J}_s = J \sum_n (S_n^x S_{n+1}^y - S_n^y S_{n+1}^x) \quad (4.3.3)$$

Based on definitions given earlier in Eqs.(4.1.4)–(4.1.11), spin conductivity is equal to :

$$\begin{aligned} \sigma(\omega) &= C_{SS}(\omega), \\ \text{Re}(C_{SS}) &= \pi D_s + C_{SS}^{reg}(\omega), \\ D_s &= \beta \langle \mathcal{J}_s \mathcal{J}_s \rangle. \end{aligned} \quad (4.3.4)$$

Similarly, the thermal conductivity can be expressed as follows:

$$\kappa(\omega) = C_{QQ} - \beta \frac{C_{Qs}^2}{C_{SS}}, \quad (4.3.5)$$

where the real part is:

$$\begin{aligned} \text{Re}(\kappa) &= \pi K_{th} + \kappa^{reg}(\omega), \\ \text{Re}(C_{QQ}) &= \pi D_{QQ} + C_{QQ}^{reg}(\omega), \\ \text{Re}(C_{Qs}) &= \pi D_{Qs} + C_{Qs}^{reg}(\omega). \end{aligned} \quad (4.3.6)$$

Note that in any case the regular parts  $C^{reg}$  are given by Eq.(4.1.8). Following the definition of the Drude weights given in Eq.(4.1.9), we derive that:

$$\begin{aligned} D_{QQ} &= \beta^2 \langle \mathcal{J}_Q \mathcal{J}_Q \rangle, \\ D_{Qs} &= \beta \langle \mathcal{J}_Q \mathcal{J}_s \rangle. \end{aligned} \quad (4.3.7)$$

Finally, combining equations (4.3.6) and (4.3.7) we obtain the following expression for the thermal Drude weight  $K_{th}$ :

$$K_{th} = D_{QQ} - \beta \frac{D_{Qs}^2}{D_s} = \beta^2 \left( \langle \mathcal{J}_Q \mathcal{J}_Q \rangle - \frac{\langle \mathcal{J}_Q \mathcal{J}_s \rangle^2}{\langle \mathcal{J}_s \mathcal{J}_s \rangle} \right), \quad (4.3.8)$$

where the first term  $D_{QQ} = \beta^2 \langle \mathcal{J}_Q \mathcal{J}_Q \rangle$  corresponds to the heat conductivity, while the

second term is the magnetothermal corrections  $MTC = \beta^2 \frac{\langle \mathcal{J}_Q \mathcal{J}_s \rangle^2}{\langle \mathcal{J}_s \mathcal{J}_s \rangle}$ , that originates from the coupling of the heat and spin currents in the presence of magnetic field. At  $H = 0$  there is no magnetothermal effect [133, 137] due to electron–hole symmetry; because of the isotropic conditions, there is no preferred direction along which a magnetization could occur. Since the heat and energy current are connected by the relation  $\mathcal{J}_Q = \mathcal{J}_E - H \mathcal{J}_s$ , the thermal Drude weight can be expressed in the equivalent form:

$$K_{th} = D_{EE} - \beta \frac{D_{Es}^2}{D_s} = \beta^2 \left( \langle \mathcal{J}_E \mathcal{J}_E \rangle - \frac{\langle \mathcal{J}_E \mathcal{J}_s \rangle^2}{\langle \mathcal{J}_s \mathcal{J}_s \rangle} \right). \quad (4.3.9)$$

Note that often in the literature [173, 174], the magnetothermal correction term is considered to be the second term of Eq.(4.3.9) and transport is studied as the combination of two competing terms,  $D_{EE}$  and  $\frac{\langle \mathcal{J}_E \mathcal{J}_s \rangle^2}{\langle \mathcal{J}_s \mathcal{J}_s \rangle}$ .

This section is organized as follows: In the first part we present a detailed calculation of the spin conductivity, focusing at the spin Drude weight  $D_s$ , at arbitrary temperature and magnetic field, while the anisotropy parameter ranges between  $1/2 < \Delta < 1$ . Next we address the calculation of the thermal conductivity with special emphasis on the competition of the two terms that contribute to  $K_{th}$ , i.e  $D_{QQ}$  and  $MTC$ . We also discuss a possible application of our results in the interpretation of experiments on the thermal transport in the  $S = 1/2$  isotropic chain compound  $Cu(C_4H_4N_2)(NO_3)_2$ . Finally, two quantities relevant to the magnetothermal effect in spin systems are provided, the magnetic Seebeck coefficient  $S$  and the figure of merit  $ZT$ .

### 4.3.1 Spin Conductivity

The spin Drude weight of the  $S = 1/2$   $XXZ$  Heisenberg model has been extensively studied by numerical and analytical techniques and a lot is known about its temperature and magnetic field dependence. Nevertheless the issue of diffusive or ballistic behaviour in the absence of magnetic field has proven to be a very delicate theoretical question, and a lot of effort has been put over the years to provide an adequate description of the behaviour of the spin conductivity.

Because of its integrability, model (4.3.1) is characterized by nontrivial conservation laws. Mazur’s inequality (4.1.15), evaluated in terms of model (4.3.1) is [6]:

$$D_M(T) \geq \frac{\beta \Delta^2 m^2 (1/4 - m^2)}{1 + 8 \Delta^2 (1/4 + m^2)}, \quad (4.3.10)$$

where  $m$  is equal to the magnetization density. Quantity  $D_M$  provides a lower bound of  $D_s$  in the high temperature limit; if  $D_M > 0$  then  $D_s$  is finite and the spin transport is ballistic. Note that Mazur’s inequality provides a useful bound but can not provide a complete picture of the Drude weight behaviour. This can be shown by considering two special cases where the right hand side of Eq.(4.3.10) vanishes. For the special case

of  $\Delta = 0$ , Hamiltonian (4.3.1) reduces to the XY model, where the spin current  $J_s$  commutes with  $\mathcal{H}$  and  $D_s$  is finite. Also, for the  $m = 0$  case, Bethe ansatz calculations [141, 151] and numerical simulations [129, 136, 140, 144, 154] have shown that  $D_s$  is finite for  $\Delta < 1$ .

A very convenient method for the calculation of the spin Drude weight at zero temperature is the one proposed by Kohn [175], where  $D_s(T = 0)$  is expressed as the sensitivity of the ground state energy  $\epsilon_0$  to an applied flux  $\phi = eA$ :

$$D_s(T = 0) = \frac{1}{2L} \frac{\partial^2 \epsilon_0}{\partial^2 \phi} \Big|_{\phi \rightarrow 0}. \quad (4.3.11)$$

The generalization of Eq.(4.3.11) at finite temperatures is [164]:

$$D_s = \frac{1}{2L} \sum_n p_n \frac{\partial^2 \epsilon_n}{\partial^2 \phi} \Big|_{\phi \rightarrow 0}, \quad (4.3.12)$$

where  $p_n$  are the Boltzmann weights. Expression (4.3.12) is extremely useful, as it allows for the calculation of the Drude weight just from the eigenvalues of the Hamiltonian.

For the gapped  $\Delta > 1$  regime, numerical [136] and analytical [192] studies indicate that the spin Drude weight vanishes at all temperatures. Numerical results for the gapped phase can also be found in Refs.[129, 154, 195].

For  $|\Delta| < 1$ , the spin Drude weight at  $T = 0$  and  $H = 0$  has been calculated from Kohn's formula (4.3.12) using the Bethe ansatz method [193, 194]:

$$D_s(T = 0) = \frac{\pi \sin(\pi/\nu)}{8 \frac{\pi}{\nu} (\pi - \frac{\pi}{\nu})}, \quad (4.3.13)$$

where the anisotropy parameter has been parametrized as  $\Delta = \cos(\pi/\nu)$ . In the special case of  $\Delta = 0$ , the spin current  $\mathcal{J}_s$  is a constant of motion, such that  $[\mathcal{H}, \mathcal{J}_s] = 0$ . For the calculation of the correlation functions, it is convenient to transform the system to the spinless fermion system by performing the Jordan–Wigner transformation on the XY chain. This results an exact evaluation of the spin and thermal Drude weight at arbitrary temperature and magnetic field. A detailed analysis of the thermal Drude weight and the magnetic Seebeck coefficient can be found in Ref. [176].

For  $0 < \Delta < 1$  and at finite temperatures, the Bethe ansatz calculation depends on the approximations made in the treatment of the excited states. The one suggested by Zotos [141] follows a method proposed by Fujimoto and Kawakami [196] based on the calculation on finite size corrections of the energy eigenvalues obtained by the Bethe ansatz method [197]. This construction is based on the string assumption for the excitations and it is significantly complex for arbitrary  $\Delta$ . The requirement that  $\nu$  is integer, so that only a finite number of strings is allowed, provides a certain simplification in the

analysis. The main results of this calculations are:

- (a) In the AFM regime ( $0 < \Delta < 1$ ),  $D_s(T)$  is nonzero, with power-law behaviour at low temperatures as  $D(T) = D(T=0) - \text{const.}T^\alpha$ , where  $\alpha = 2/(\nu - 1)$ .
- (b) In the FM regime ( $-1 < \Delta < 0$ ),  $D_s(T)$  decreases quadratically with temperature.
- (c) At the isotropic AFM point  $\Delta = 1$   $D_s(T)$  vanishes at all temperatures.
- (d) In the high temperature limit  $\beta \rightarrow 0$ , spin Drude weight behaves like  $D_s(T) = \beta C(\Delta)$  [151], that also holds for finite magnetic fields  $H$ , where  $C(\Delta)$  equals:

$$C(\Delta) = J^2 \frac{\frac{\pi}{\nu} - \frac{1}{2}\sin(2\frac{\pi}{\nu})}{16\frac{\pi}{\nu}}, \quad (4.3.14)$$

An alternative Bethe ansatz calculation was presented by Benz *et al.* [151], based on the spinon and antispinon particle basis, that predicted a different temperature dependence of the Drude weight. In particular, for values of anisotropy near the isotropic point and for sufficiently low temperatures,  $D_s(T)$  increases with temperature, and after reaching a maximum, it decreases. Moreover, the values of  $D_s(T)$  at the isotropic point  $\Delta$  are non-zero for any  $T$ . These contradictory results rendered the application of the Bethe ansatz method to the calculation of spin Drude weight, an unresolved issue.

Not until recently was an improved Mazur bound obtained [198] using a different approach based on deriving a whole family of quasilocal conservation laws. This nontrivial improvement of the Drude weight bound remarkably agrees with one of the debatable Bethe ansatz results; the one proposed by Zotos [141]. In light of this advancement, we generalize the calculation of [141] for finite magnetic fields. A detailed analysis of the calculation and relevant expressions for the Drude weight can be found in Appendix B.2. The computation relies on a numerical calculation of coupled integral equations, whose number depends on the value of parameter  $\nu$ ; there are 3 such equations for  $\Delta = \cos(\pi/3)$ , 4 equations for  $\Delta = \cos(\pi/4)$  and so on. Therefore, the isotropic Heisenberg point  $\Delta = 1$  is unreachable, because one would need to solve an infinite number of coupled equations.

At finite magnetic field and zero temperature, the calculation of the magnetic field dependence of the spin Drude weight is feasible by considering the low-energy effective Hamiltonian of the  $XXZ$  mode using abelian bosonization. Within the Luttinger Liquid description, the spin Drude weight is expressed as [194]

$$D_s = u(\Delta, H)K(\Delta, H)/\pi, \quad (4.3.15)$$

where the Fermi velocity  $u(\Delta, H)$  and the so-called Luttinger parameter  $K(\Delta, H)$  depend on both the magnetic field  $H$  and anisotropy parameter  $\Delta$ . For zero magnetic

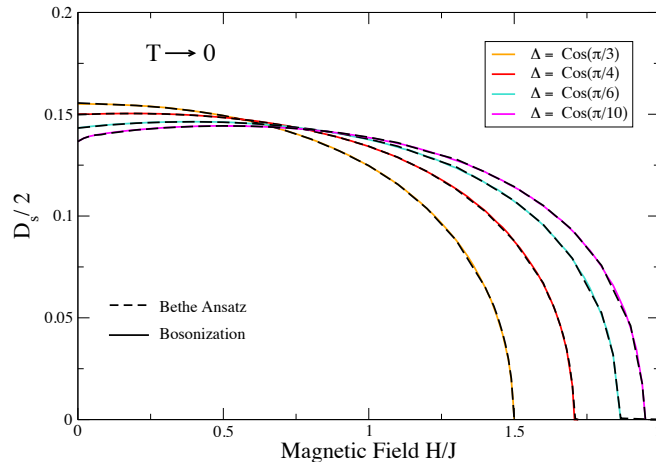


**Figure 4.3.1:** Magnetic field dependence of the spin Drude weight  $D_s(H)$  for four values of the anisotropy parameter  $\Delta = \cos(\pi/3)$ ,  $\cos(\pi/4)$ ,  $\cos(\pi/6)$  and  $\cos(\pi/10)$ . Solid lines correspond to results obtained from bosonization and dashed lines from Bethe ansatz.

field they can be found in closed form:

$$K(\Delta) = \frac{\pi}{2(\pi - \frac{\pi}{\nu})}, \quad u(\Delta) = \frac{\pi \sin(\pi/\nu)}{2\pi/\nu}. \quad (4.3.16)$$

At finite magnetic field, both parameters can be computed exactly from the Bethe ansatz solution [199, 200]. The corresponding Bethe Ansatz equations for the evaluation of the Fermi velocity and the Luttinger parameter can be found in Appendix B.4.

In Fig. 4.3.1 the magnetic field dependence of the spin Drude weight at zero temperature is presented, calculated using the Luttinger Liquid description and the Bethe ansatz technique. The lines are indistinguishable providing a reliable test about the validity of the Bethe ansatz calculation at low  $T$ . We also observe that  $D_s(H)$  abruptly terminates at  $H = H_{cr} = J(1 + \cos(\pi/\nu))$ , above which the system enters at its massive phase and  $D_s$  vanishes at all  $H$ .

We now turn our attention to the magnetic field dependence of  $D_s$  at finite temperature. In Fig. 4.3.2 we depict  $D_s$  as a function of magnetic field  $H$  for two values of temperature  $T/J = 0.5, 1$  and various values of the anisotropy  $\Delta$ . Among the facts that become apparent are the following: (i) At small magnetic fields spin Drude weight goes like  $D_s \simeq AH^2$ , a behaviour that is significantly different from the one at  $T = 0$ . (ii) Upon increase of the magnetic field,  $D_s$  increases until it reaches a maximum at a field  $H_M$  and then it exponentially goes to zero. In the vicinity of  $H_{cr}$ ,  $D_s$  is a smooth function of  $H$  that is in direct contrast with the  $T = 0$  result. (iii) Upon increase of  $\Delta$ , starting from  $\Delta = 1/2$  and approaching the isotropic point  $\Delta = 1$ , spin Drude weight seems to converge to a limiting behaviour that remains unaffected as one further increases the values of  $\Delta$ . Already at  $\Delta = \cos(\pi/9)$  and for magnetic fields  $H/J \gtrsim 0.5$ ,

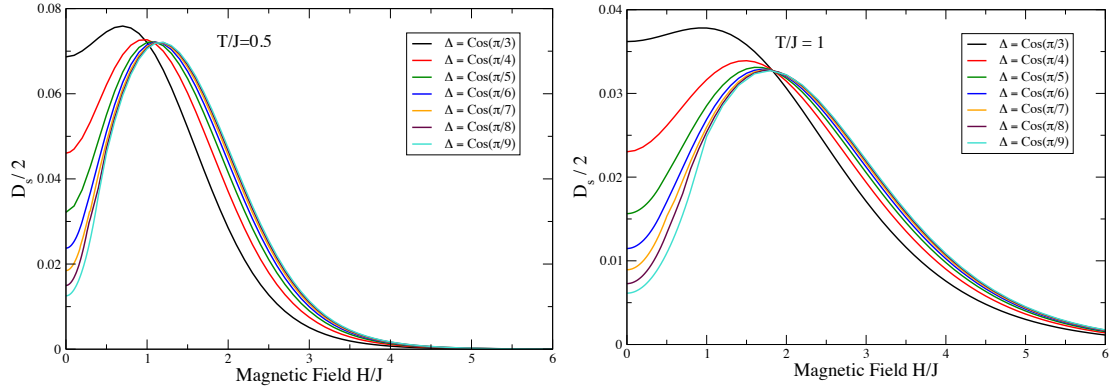


**Figure 4.3.2:** Magnetic field dependence of spin Drude weight at (a)  $T/J = 0.5$  and (b)  $T/J = 1$  and various values of the anisotropy parameter  $\Delta$ . The  $D_s(H)$  curve seems to converge to a limiting behaviour for  $\Delta \gtrsim \cos(\pi/9)$  and practically remains the same upon increase of  $\Delta$  for  $H/J \gtrsim 0.5$ .

$D_s$  has approached its limiting behaviour. This is not true for small magnetic fields  $H/J \lesssim 0.5$ , where such a convergence should not be expected. The  $D_s(H = 0)$  value strongly depends on  $\Delta$  and goes to zero as  $\Delta \rightarrow 1$ .

The temperature dependence of the spin Drude weight is also studied for three typical magnetic fields and  $\Delta$  and the main features are depicted in Figs. 4.3.3 and 4.3.4. At  $H < H_{cr}$  the system is at its gapless phase, and  $D_s$  is finite at small temperatures and decreases like:

$$D_s(T) \simeq D_s(0) - Ae^{-H/T}T^{\gamma(H,T)}, \quad (4.3.17)$$

provided that  $A$  is constant and the exponent  $\gamma$  depends on both the  $T$  and  $H$ . At elevated temperatures, the  $D_s(T)$  curve vanishes exponentially. This is evident in Fig. 4.3.3(a) where we plot  $D_s(T)$  for  $H/J = 0.5$  for four values of the anisotropy  $\Delta$ . The low  $T$  behaviour is in contrast with the  $H = 0$  results given in [141], where a power-law behaviour at low  $T$  was observed.

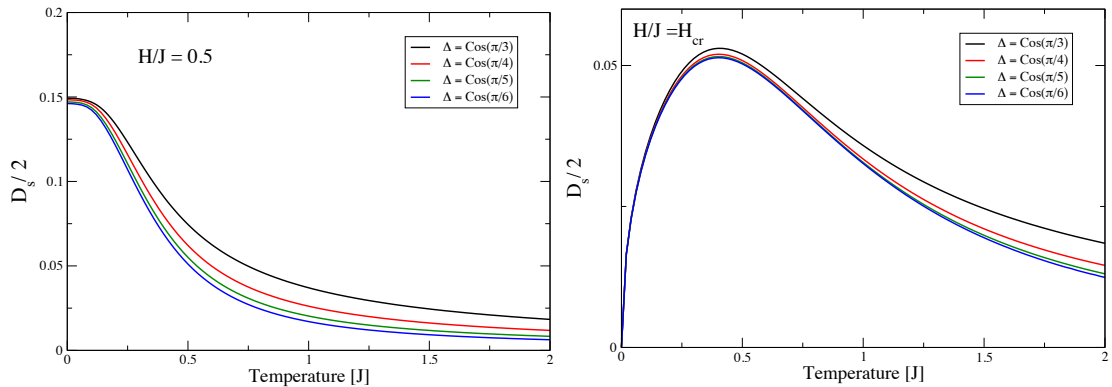


**Figure 4.3.3:** Temperature dependence of spin Drude weight at (a)  $H/J = 0.5$  where the system is at its gapless phase and (b)  $H/J = H_{cr}$  where the system enters the gapped regime, and various values of the anisotropy  $\Delta$ .

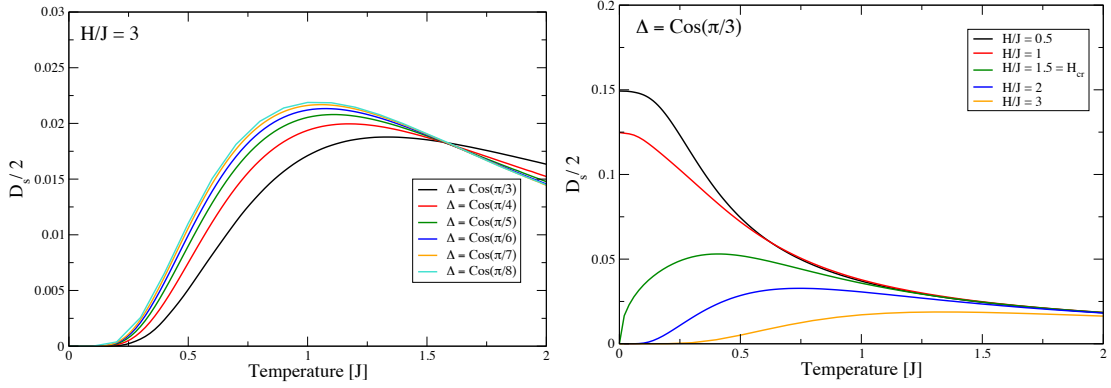


**Figure 4.3.4:** Temperature dependence of spin Drude weight at (a)  $H/J = 3$  and various values of  $\Delta$  (b)  $\Delta = \cos(\pi/3)$  and various magnetic fields. In the high temperature limit, spin Drude weight behaves like  $D_s(T) = \beta C(\Delta)$ , where  $C(\Delta)$  does not depend on  $H$ .

At  $H = H_{cr}$  the system enters its gapped regime and  $D_s$  vanishes at  $T = 0$ . Nevertheless,  $D_s$  becomes finite upon a small increase of temperature, exhibiting a  $\sqrt{T}$  critical behaviour at low  $T$ . The curve increases with  $T$  until it reaches a maximum and then drops exponentially. This behaviour is summarized in Fig. 4.3.3(b). Additionally, in Fig. 4.3.4(a) we plot  $D_s(T)$  for  $H/J = 3$  and we notice that at low  $T$  Drude weight is zero, it is exponentially activated upon increase of  $T$  and vanishes after taking a maximum. From Figs. 4.3.3 and 4.3.4(a) it is evident that as we increase the value of anisotropy  $\Delta$ , the  $D_s(T)$  curve approaches a limiting behaviour that is acquired approximately for  $\Delta = \cos(\pi/8)$ .

Finally, the main results of the  $D_s(T)$  behaviour are summarized in Fig. 4.3.4(b), where the temperature dependence of spin Drude weight is depicted for  $\Delta = \cos(\pi/3)$  and various magnetic fields. Also note that in the high temperature limit, spin Drude weight behaves like  $D_s(T) = \beta C(\Delta)$ , where  $C(\Delta)$  is magnetic field independent and is given by Eq.(4.3.14).

Before proceeding with the analysis of the thermal Drude weight, we present one more figure that illustrates the main features of the temperature as well as the magnetic field dependence of  $D_s$ . In Fig. 4.3.5 the coloured surface represents  $D_s(H, T)$  for  $\Delta = \cos(\pi/3)$  and by simple inspection several conclusions can be drawn. To begin with, we observe that  $D_s$  acquires its higher values in the gapless phase for  $0 < H < H_{cr}$ . In the gapped phase for  $H > H_{cr}$ , although  $D_s$  is finite, its values in this region are too low to make a distinct contribution. We also notice that at  $T \simeq 0$ ,  $D(H)$  vanishes abruptly at  $H \simeq H_{cr}$ , while upon a small increase of  $T$ , the exponential decay of the curve is established. Finally, as far as the temperature dependence is concerned, we notice that spin Drude weight becomes larger at low temperatures, while at  $T/J \approx 1$ ,  $D_s$  has lost almost  $2/3$  of its weight.

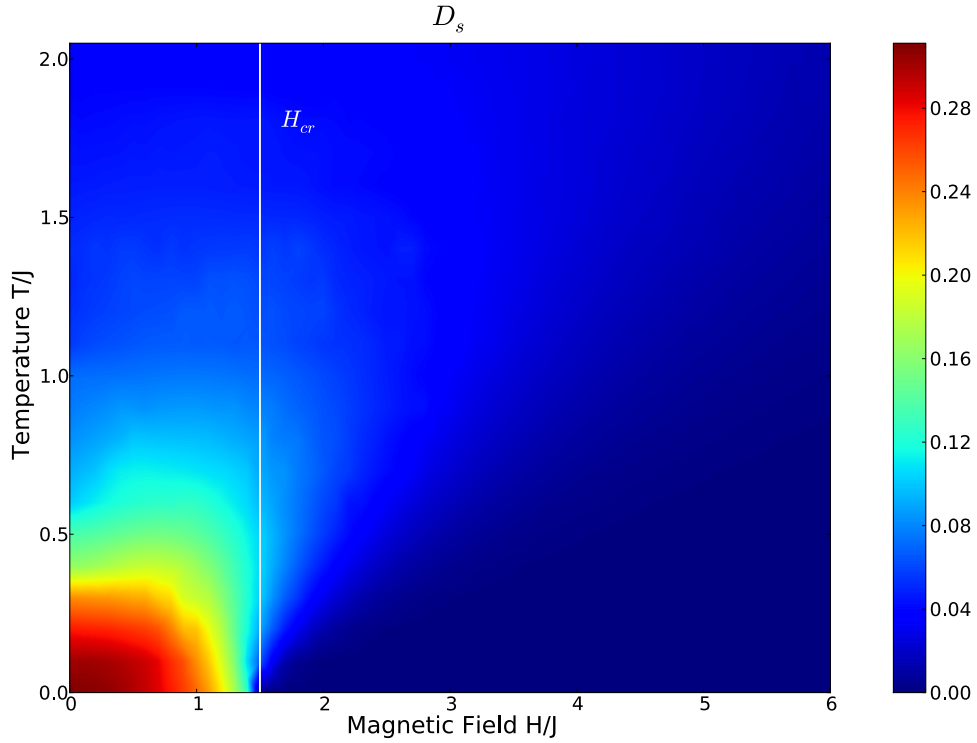


**Figure 4.3.5:** Coloured surface represents  $D_s(H, T)$  calculated for  $\Delta = \cos(\pi/3)$  as a function of temperature  $T/J$  and magnetic field  $H/J$ . Vertical line indicates the position of the critical field  $H_{cr} = 1.5$ .

### 4.3.2 Thermal Conductivity

Two main quantities play central role in the study of thermal conductivity in the  $S = 1/2$  XXZ chain; the heat Drude weight  $D_{QQ}$  and the thermal Drude weight  $K_{th}$ . From Eq.(4.3.8) it becomes apparent that the full term  $K_{th}$  is the result of a combination of two competing terms, the  $D_{QQ}$  Drude weight and the magnetothermal corrections  $MTC = \beta^2 \frac{\langle J_Q J_s \rangle^2}{\langle J_s J_s \rangle}$ . It is interesting to explore the behaviour of all three terms as a function of temperature and magnetic field, and to examine the regions of  $H$  and  $T$  at which the  $MTC$  terms becomes important.

We remind the reader that one can decompose the heat Drude weight  $D_{QQ}$  in terms of the energy and spin contribution, which yields:

$$D_{QQ} = D_{EE} + 2\beta H D_{Es} + \beta H^2 D_s. \quad (4.3.18)$$

Similarly the  $MTC$  term, and consequently the  $K_{th}$  term, can be decomposed in terms of  $D_{EE}$ ,  $D_{Es}$  and  $D_s$ . The  $D_{EE}$  and  $D_{Es}$  at finite temperatures have been calculated by Sakai and Klümper [173] using a lattice path integral formulation, where a quantum transfer matrix (QTM) in the imaginary time is introduced. This method produces all relevant correlations by solving two nonlinear integral equations at arbitrary

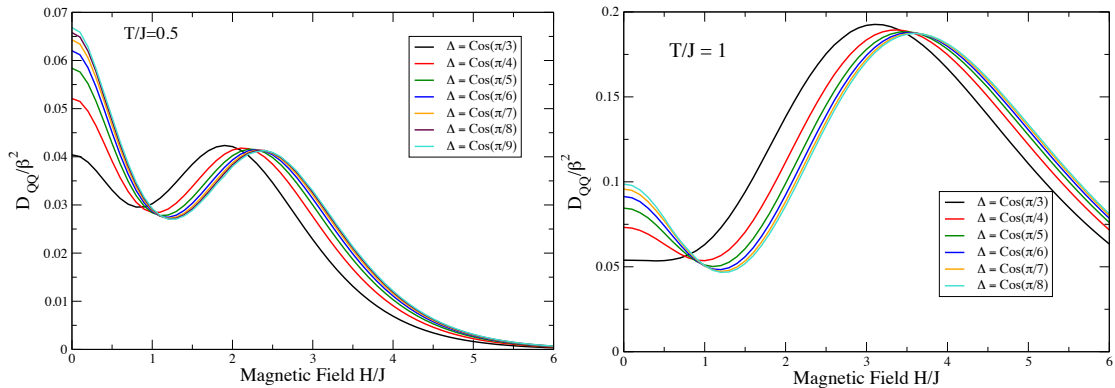


**Figure 4.3.6:** Magnetic field dependence of heat Drude weight at (a)  $T/J = 0.5$  and (b)  $T/J = 1$  and various values of the anisotropy parameter  $\Delta$ . The  $D_{QQ}(H)$  curve seems to converge to a limiting behaviour for  $\Delta \gtrsim \cos(\pi/9)$  and practically remains the same upon increase of  $\Delta$  for  $H/J \gtrsim 0.25$ . The  $D_{QQ}(H)$  curve exhibits a pronounced nonmonotonic behaviour as a function of  $H$ .

magnetic fields and temperatures. The parametrization  $\Delta = \cos(\pi/\nu)$  with  $\nu$  integer is not required, and all anisotropy parameters are accessible, including the isotropic point. Details for the QTM method and the corresponding nonlinear integral equations are included in Appendix A.

The thermal transport of the  $XXZ$  chain in finite magnetic fields has been studied using exact diagonalization for finite chains of length up to  $N = 20$  sites and mean-field theory for various exchange anisotropies [174]. The results presented here are based on the Bethe ansatz method that makes the calculation of Drude weights feasible in the thermodynamic limit. This is among the reasons that render Bethe ansatz technique a perfect tool for understanding complex phenomena such as thermal transport, leaving aside finite-size effects. Nevertheless, finite scaling can provide useful hints on the macroscopic behaviour and we expect that the Bethe ansatz results will agree, at least qualitatively, with the ED results on finite chains.

Let us begin by considering the magnetic field dependence of the various quantities. In Fig. 4.3.6 we depict the heat Drude weight  $D_{QQ}$  as a function of  $H$  for various values of  $\Delta$ , ranging from  $\Delta = 1/2$  up to  $\Delta = 0.94$ , and two values of temperature  $T/J = 0.5, 1$ . An important fact of Fig. 4.3.6 is that  $D_{QQ}(H)$  exhibits a pronounced nonmonotonic behaviour as a function of  $H$ . At small magnetic fields it decreases quadratically and then it rises again creating a peak before it vanishes at large magnetic fields. If one increases temperature, the overall curve is decreased and the position of the peak is shifted to higher magnetic fields. Another feature suggested by Fig. 4.3.6 is that as the anisotropy parameter approaches the isotropic point  $\Delta = 1$ , the  $D_{QQ}(H)$  curve in the field region  $H/J \gtrsim 0.25$  approaches a limiting behaviour and seems to be insensitive to changes in the parameter  $\Delta$ .

We now consider the behaviour of the  $MTC$  term as a function of  $H$  as illustrated

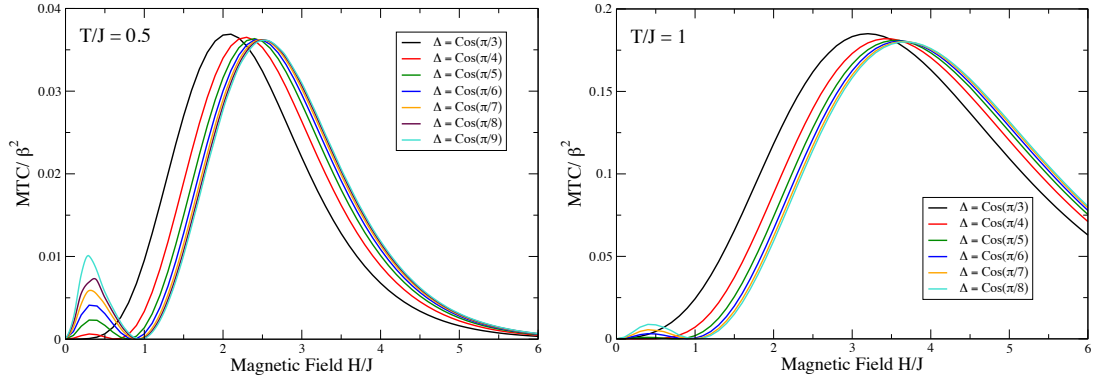


**Figure 4.3.7:** Magnetic field dependence of  $MTC$  term at (a)  $T/J = 0.5$  and (b)  $T/J = 1$  and various values of the anisotropy parameter  $\Delta$ . The  $MTC$  term is zero at  $H = 0$ , but becomes finite at finite  $H$ , where it develops two peaks. The first peak is located at small magnetic fields while the second and more dominant peak is centered close to the critical field at low- $T$ .

in Fig. 4.3.7 for various values of  $\Delta$  and two values of temperature  $T/J = 0.5, 1$ . As expected, the  $MTC$  term is exactly zero at  $H = 0$ , but becomes finite at finite  $H$ , where it develops two peaks. The first peak is located at small magnetic fields while the second and more dominant peak is centered close to the critical field at low- $T$ . Upon increase of  $T$ , the peaks are shifted at higher magnetic fields. Fig. 4.3.7 implies that the  $MTC$  term becomes significant for a wide range of magnetic fields and temperature, and it should be taken into account for a complete description of thermal transport. The resulting behaviour of the total thermal Drude weight  $K_{th}$ , as a sum of two competing terms, is summarised in Fig. 4.3.8, where it is plotted as a function of  $H$  for two values of temperature  $T/J = 0.5, 1$ . Fig. 4.3.8 allows for two major observations: (i) thermal Drude weight turns out to be a smooth function of magnetic field with no peaks observed

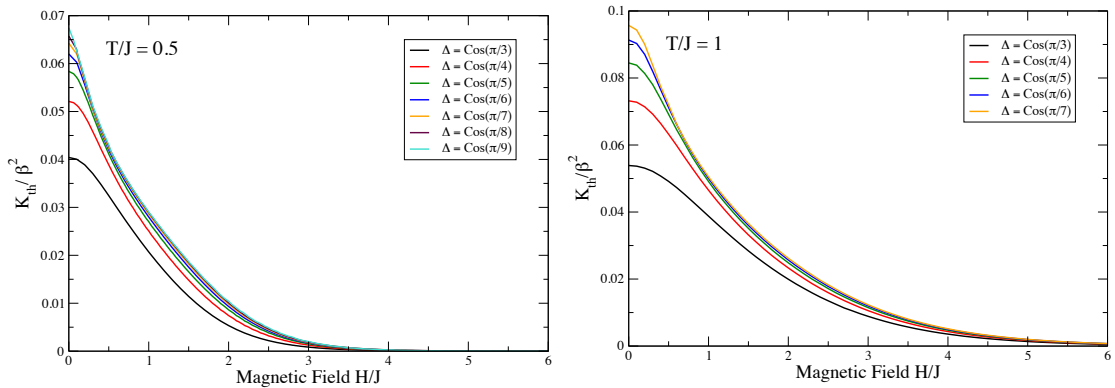


**Figure 4.3.8:** Magnetic field dependence of thermal Drude weight at (a)  $T/J = 0.5$  and (b)  $T/J = 1$  and various values of the anisotropy parameter  $\Delta$ . The  $K_{th}(H)$  is a smooth function of  $H$  and in the field region  $H/J \gtrsim 0.25$  seems to converge to a limiting behaviour for  $\Delta \gtrsim \cos(\pi/8)$  and practically remains the same upon increase of  $\Delta$ .

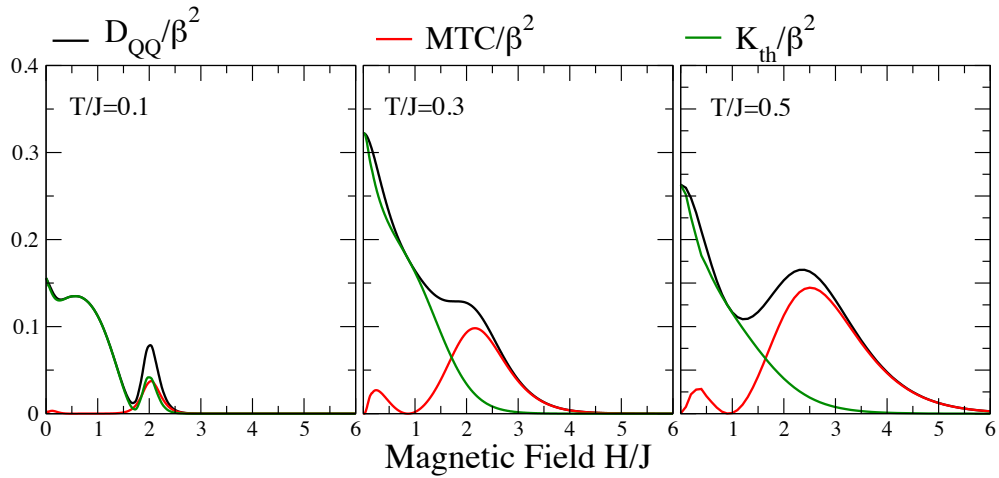


**Figure 4.3.9:** Magnetic field dependence of thermal Drude  $K_{th}$ , heat Drude weight  $D_{QQ}$  and the  $MTC$  term scaled with temperature  $T^2$  at  $\Delta = \cos(\pi/8)$  and (a)  $T/J = 0.1$ , (b)  $T/J = 0.3$  and (c)  $T/J = 0.5$ . We observe that as  $T$  increases, the  $MTC$  and  $D_{QQ}$  term develop a peak located at the same field, so that the combination of these two terms results a  $K_{th}$  curve that is a smooth function of  $H$ .

as a function of  $H$ . The inclusion of the  $MTC$  term results in an overall suppression of  $K_{th}$  and the cancellation of the nonmonotonic peaked behaviour of  $D_{QQ}$ . This finding is confirmed by a numerical study of the thermal transport in the  $S = 1/2$   $XXZ$  chain in the presence of a magnetic field [174] based on exact diagonalization of a finite chain. (ii) As in the case of  $D_{QQ}(H)$ , thermal Drude weight  $K_{th}(H)$  is also approaching a limiting behaviour in the  $H/J \gtrsim 0.25$  region as  $\Delta \rightarrow 1$ .

To give a quantitative picture of the difference between thermal and heat Drude weight, in Fig. 4.3.9 we present the field dependence of  $K_{th}$ ,  $D_{QQ}$  and the  $MTC$  term for three different temperatures at  $\Delta = \cos(\pi/8)$ . The overall picture suggested by Fig. 4.3.9 is the following: at low temperature  $T/J = 0.1$  the  $MTC$  term is finite but small to cause significant deviations so that the total  $K_{th}$  is suppressed but in general follows the nonmonotonic behaviour of  $D_{QQ}$ . As the temperature is increased at  $T/J = 0.3$  the  $MTC$  and  $D_{QQ}$  term develop a peak located exactly at the same field; the subtraction of these two terms results a  $K_{th}$  that is a smooth function of  $H$ . This behaviour also holds for higher values of  $T$ . In addition, in the high-field region  $H \gg H_{cr}$  the  $MTC$  and  $D_{QQ}$  term become equal, leading to a vanishing  $K_{th}$ . We would also like to explore the temperature dependence of the thermal and heat Drude weight. From Fig. 4.3.10 it becomes apparent that at the low-field region,  $D_{QQ}(T)$  and  $K_{th}(T)$  exhibit approximately the same behaviour at almost every temperature, while at larger fields the  $MTC$  term becomes stronger causing a suppression of  $K_{th}$ . As  $H$  is further increased, the  $MTC$  term grows approaching  $D_{QQ}$  almost at all temperatures. Note that in Fig. 4.3.10 we have plotted the various quantities scaled with temperature  $T^2$  to avoid numerical singularities at  $T = 0$ . To remedy this situation, we extract the

leading contributions at low temperature  $T \ll 1$  of all quantities scaled with  $T^2$ , that are nonsingular functions of  $T$ . We are mostly interested in the temperature dependence of  $D_{QQ}$  and  $K_{th}$  in the massless  $0 < H < H_{cr}$  region; in the gapped region  $H > H_{cr}$  we expect an exponential suppression of both quantities at low- $T$ . The outcome of this calculation is that both  $D_{QQ}/\beta^2$  and  $K_{th}/\beta^2$  scale as  $T^3$ , so that heat and thermal Drude weight are characterized by a linear behaviour. The low-temperature asymptotics of correlation functions  $\langle \mathcal{J}_E \mathcal{J}_E \rangle$  and  $\langle \mathcal{J}_E \mathcal{J}_s \rangle$  for  $T \ll 1$  and  $T \ll H$  is given by [173]:

$$\begin{aligned} \langle \mathcal{J}_E \mathcal{J}_E \rangle &= H^2 D_s(0) T + B_1(H, \Delta) T^3 \\ \langle \mathcal{J}_E \mathcal{J}_s \rangle &= -H D_s(0) T + B_2(H, \Delta) T^3 \end{aligned} \quad (4.3.19)$$

where  $B_1$  and  $B_2$  can be found by solving a set of two nonlinear integral equations within the framework of QTM [173]. Combining Eqs.(4.3.17), (4.3.19) with (4.3.18) we obtain  $D_{QQ}$  for  $T \ll 1$  and  $T \ll H$ :

$$D_{QQ} \simeq (B_1 + 2B_2)T. \quad (4.3.20)$$

It is easy to derive that the thermal Drude weight  $K_{th}$  also approaches  $T = 0$  with a linear form. We should emphasize that this result agrees with the expected low temperature asymptotics of the thermal Drude weight, given by [127, 173]:

$$K_{th} = \frac{\pi}{3} u(\Delta, H) T, \quad (4.3.21)$$

where  $u(\Delta, H)$  is the Fermi velocity. The validity of Eq.(4.3.21) is verified at  $H = 0$  [126] and for the XY model. Additionally, mean field approximation of the Hartree-Fock

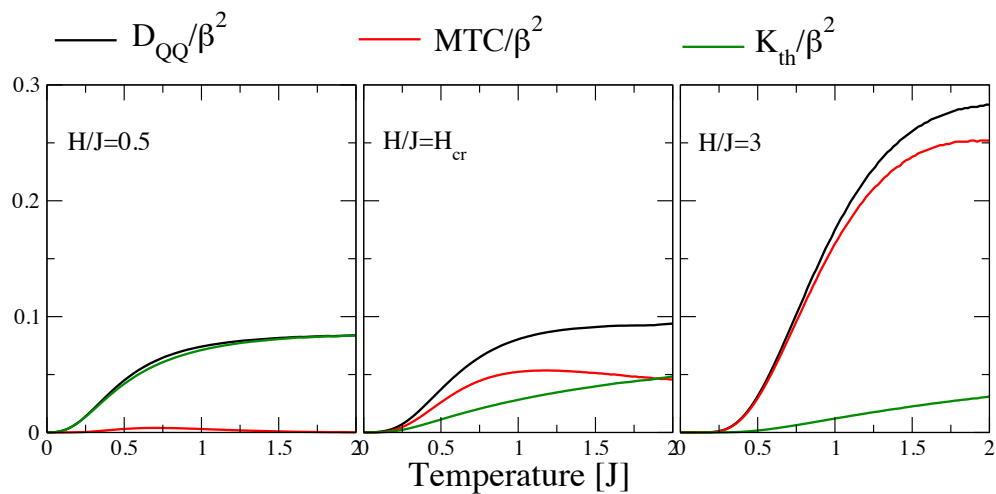


**Figure 4.3.10:** Temperature dependence of thermal Drude  $K_{th}$ , heat Drude weight  $D_{QQ}$  and the  $MTC$  term scaled with temperature  $T^2$  at  $\Delta = \cos(\pi/6)$  and (a)  $H/J = 0.5$ , (b)  $H/J = H_{cr}$  and (c)  $H/J = 3$ .

type confirm that the low-temperature dependence of  $K_{th}$  is linear in  $T$  [174].

The main features of the temperature and magnetic field dependence of heat and thermal Drude weights are depicted in Fig. 4.3.11 and Fig. 4.3.12 respectively, where the coloured surface represents  $D_{QQ}(H, T)$  and  $K_{th}(H, T)$  for  $\Delta = \cos(\pi/3)$ . The most important fact of Fig. 4.3.11 is that  $D_{QQ}$  presents an involved structure as a function of both  $T$  and  $H$ . At low temperatures, most of the weight is concentrated at the low-field region, while upon increase of temperature a peak appears, that is located at the critical field  $H_{cr}$  at low enough  $T$ . The peak is further enhanced and shifted to higher magnetic fields in the high- $T$  region. On the contrary, the thermal Drude weight is a smooth function of  $H$  and  $T$ , and no feature is observed in the vicinity of  $H_{cr}$ . This is a consequence of the inclusion of the magnetothermal correction term  $MTC$ , that causes an overall suppression of  $K_{th}$  and the cancellation of the nonmonotonic peaked behaviour of  $D_{QQ}$ .

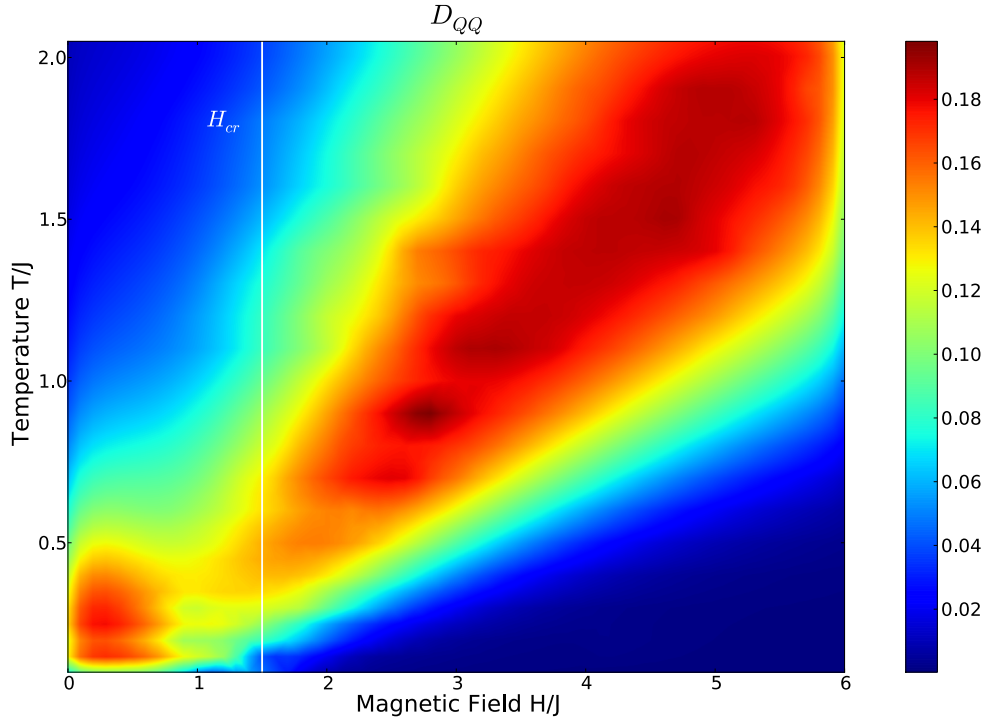


**Figure 4.3.11:** Coloured surface represents  $D_{QQ}(H, T)$  calculated for  $\Delta = \cos(\pi/3)$  as a function of temperature  $T/J$  and magnetic field  $H/J$ . Vertical line indicates the position of the critical field  $H_{cr} = 1.5$ .

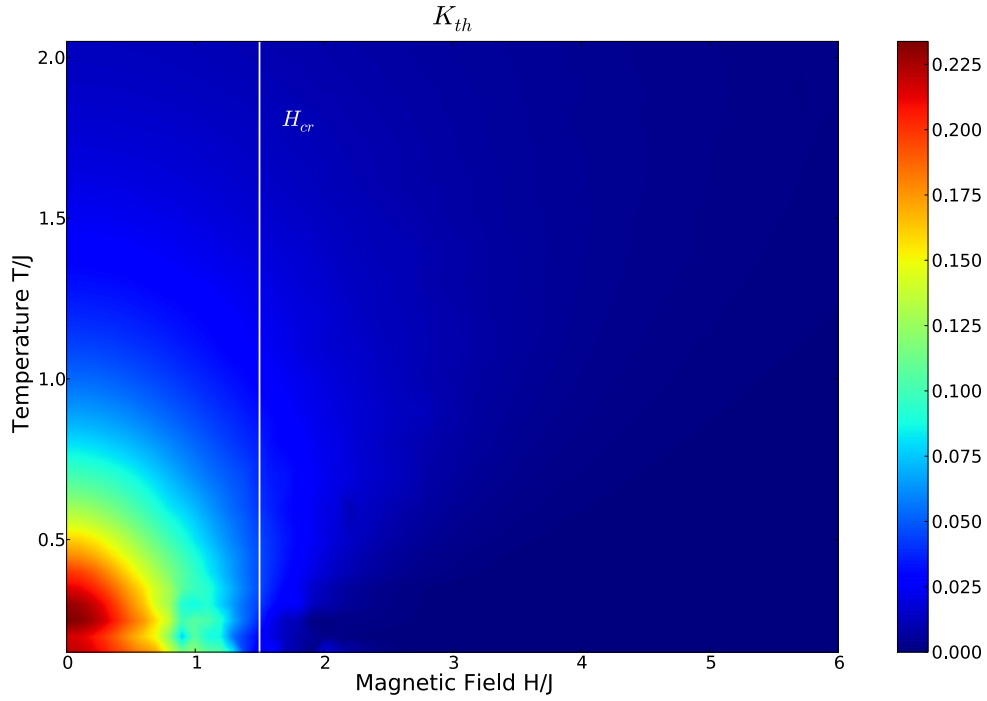


**Figure 4.3.12:** Coloured surface represents  $K_{th}(H, T)$  calculated for  $\Delta = \cos(\pi/3)$  as a function of temperature  $T/J$  and magnetic field  $H/J$ . Vertical line indicates the position of the critical field  $H_{cr} = 1.5$ .

**Connection with the experiment:** A connection between the transport properties calculated in this section and the experimental measurements of thermal conductivity should be possible. The measured thermal conductivity however includes contributions from all itinerant particles or quasi-particles, such as spin excitations, phonons and charge carriers. Even in the case of insulators, where the thermal conductivity carried by electronic quasi-particles is small or zero, the phonon contribution  $\kappa_{ph}$  is significant and has to be accurately estimated and subtracted from the total measured thermal conductivity  $\kappa$ .

Since in spin chain materials the exchange interaction along the chain is much stronger than perpendicular to it, the magnetic thermal conductivity  $\kappa_{mag}$  is expected to be negligible when  $\kappa$  is measured perpendicular to the chain. In this case the phonon thermal conductivity is found [148], i.e.  $\kappa_{\perp}(T) = \kappa_{ph}(T)$ , and in most of the materials studied exhibits a peak at low temperatures which is followed by a continuous decrease as  $T$  rises [148]. The situation is different when  $\kappa$  is measured parallel to the chain, where on top of the phonon contribution a distinct additional feature is observed at higher temperatures [149]. This anisotropy in the temperature dependence of  $\kappa_{\perp}$  and  $\kappa_{\parallel}$  is attributed to large magnetic contributions to  $\kappa_{\parallel}$ . As it is argued in [148, 149] the phononic contribution  $\kappa_{ph}$  can be subtracted from  $\kappa_{\parallel}$  only when  $\kappa_{\perp}$  is a smooth and featureless function of  $T$  and the strong features of  $\kappa_{mag}$  appear at a much higher  $T$ -scale than the low- $T$  phonon peak.

Additionally, when thermal conductivity is measured as a function of magnetic field no significant changes have been observed in  $\kappa_{\perp}$  as  $H$  varies, while the  $\kappa_{\parallel}$  is strongly influenced by  $H$  [201]. Therefore, the thermal conductivity perpendicular to the chain has phononic origin,  $\kappa_{\perp} = \kappa_{ph}$  and along the chain is equal to  $\kappa_{\parallel} = \kappa_{mag} + \kappa_{ph}$ . In the magnetic part  $\kappa_{mag}$  one should take into account three terms [201]:

$$\kappa_{mag} = \kappa_s + \kappa_{s-ph} + \Delta\kappa_{ph}, \quad (4.3.22)$$

where the first term  $\kappa_s$  corresponds to the spin contribution, the second term  $\kappa_{s-ph}$  describes the drag of spin heat currents by phononic heat currents and the last term  $\Delta\kappa_{ph}$  accounts for the decrease of the phononic thermal conductivity due to spin-phonon scattering. Scattering to magnetic defects of the crystal is another source for the reduction of the  $\kappa_{mag}$  and should be taken into account.

When the magnetic thermal conductivity is extracted from the total measured conductivity, the analysis of the experimental data usually relies on the quasi-particle approach employing Boltzmann's kinetic transport theory. The  $T$ -dependence of  $\kappa$  is given by [149]:

$$\kappa = \sum_k \frac{df(k, T, H)}{dT} \epsilon(k) u_s(k) l_s(k, T, H), \quad (4.3.23)$$

where  $f(k, T, H)$ ,  $\epsilon(k)$ ,  $u_s(k)$  and  $l_s(k, T, H)$  are respectively the distribution function, the energy, the velocity and the mean free path of spin excitations with wave-vector  $k$ . In most of the cases it is assumed that the scattering rates are  $k$ -independent, i.e.  $l_s(k, T, H) = l_s(T, H)$ . The magnetic mean free path  $l_s$  reflects the density of static defects in the material that have proven to be important scatterers of spin excitations in 1D magnetic systems.

The application of Kubo formalism in analysing the experimental results is possible and is considered to be more general than the kinetic transport theory because it does not rely on the quasi-particle approach. The experimental accessible quantity is the dc conductivity,  $\kappa_{dc} = \kappa(\omega \rightarrow 0)$ , which in the case of the  $S = 1/2$   $XXZ$  chain equals to the thermal Drude weight  $K_{th}$  since the regular part is such that  $\kappa_{reg}(\omega \rightarrow 0) = 0$ . Although the integrability of the model suggests ballistic transport in the sense of infinite thermal conductivity, in any real system in the presence of external scattering mechanisms, the  $\delta$ -peak broadens into a Lorentzian with a width inversely proportional to the relaxation time  $\tau(T, H)$ , a finite external lifetime that incorporates all independent scattering mechanisms. The relaxation time  $\tau$  is linked with the mean free path  $l_s$  and the spin-wave velocity  $u_s$  through the relation  $l_s = u_s \tau$ . A comparison between the experimental results and the dc limit of the theoretically calculated  $\kappa(\omega)$  is possible through the relation:

$$\kappa_{exp} = K_{th} \tau. \quad (4.3.24)$$

Numerous experimental works have been devoted in the study of thermal transport in materials that are well described by the Heisenberg  $S = 1/2$  Hamiltonian at the isotropic point  $\Delta = 1$  and weak exchange interactions perpendicular to the chain. Good examples are the  $\text{CaCu}_2\text{O}_3$  with  $J/k_B = 2000$  K, where linear  $T$ -dependence of  $\kappa_{mag}$  was measured in [202], and the cuprate chains  $\text{Sr}_2\text{CuO}_3$  and  $\text{SrCuO}_2$  where  $J/k_B$  is between 2150 and 3000 K [120].

In most of these experiments the thermal conductivity has often been found to be insensitive to the application of an external magnetic field due to the large value of the exchange coupling  $J$  of these materials. The magnetic fields available are too small to cause effects on the measured thermal conductivity. An ideal compound for thermal conductivity experiments in magnetic field turned out to be the  $S = 1/2$  chain compound copper pyrazine dinitrate  $\text{Cu}(\text{C}_4\text{H}_4\text{N}_2)(\text{NO}_3)_2$  where  $J/k_B = 10.3$  K and the critical field is  $H_{cr} = 15$  T, while the ration of interchain  $J'$  to intrachain  $J$  couplings is estimated around  $J'/J = 4.4 \cdot 10^{-3}$  [203]. The thermal conductivity was measured [201] by a standard steady-state heat flow technique, in the temperature region between 0.37 and 10 K and for magnetic fields up to 17 T. Special emphasis in the interpretation of the data was put in analysing the behaviour of thermal conductivity in the vicinity of critical field  $H_{cr}$ . Moreover, thermal transport perpendicular  $\kappa_{\perp}$  and parallel  $\kappa_{\parallel}$  to the chain was investigated in order to subtract the the phononic contribution. It was argued that since the phononic part  $\kappa_{ph}$  does not significantly changes with  $H$ , the difference between the total measured  $\kappa_{\parallel}(H)$  and its zero field value  $\kappa_{\parallel}(0)$  will yield the field dependence of the magnetic heat conductivity  $\kappa_{mag}(H) - \kappa_{mag}(0)$ .

Fig. 4.3.13 summarizes experimental results of the thermal conductivity measured parallel to the chains of  $\text{Cu}(\text{C}_4\text{H}_4\text{N}_2)(\text{NO}_3)_2$  as a function of magnetic field at several fixed temperatures. The analysis of the experimental data suggests that the observed field dependence arises dominantly from thermal transport in the spin system  $\kappa_s$  and that the  $\kappa_{s-ph}$  and  $\Delta\kappa_{ph}$  terms are not important. Moreover, within the framework of kinetic transport theory, experimental results imply a mean free path that is momentum and magnetic free independent.

In Fig. 4.3.14 we plot  $D_{QQ}(H) - D_{QQ}(0)$  and  $K_{th}(H) - K_{th}(0)$  for  $\Delta = \cos(\pi/8)$  and several fixed temperatures ranging from 0.64 K up to 5.15 K. A comparison with the experimental data presented in Fig. 4.3.13 will provide information on the behaviour of the relaxation time  $\tau$  as a function of both  $T$  and  $H$ . Particular attention should be paid to the fact that the copper pyrazine dinitrate compound used for the experiment is well described by the Heisenberg  $S = 1/2$  Hamiltonian at the isotropic point  $\Delta = 1$ , while the theoretical calculation was performed for  $\Delta = \cos(\pi/8) = 0.92$ . The Bethe ansatz technique relies on a numerical calculation of coupled integral equations, whose number increases as  $\Delta \rightarrow 1$ , making the calculation of correlation functions infeasible for the isotropic point. Nevertheless, Figs. 4.3.6–4.3.8 suggest that as  $\Delta \rightarrow 1$ , both  $D_{QQ}(H)$

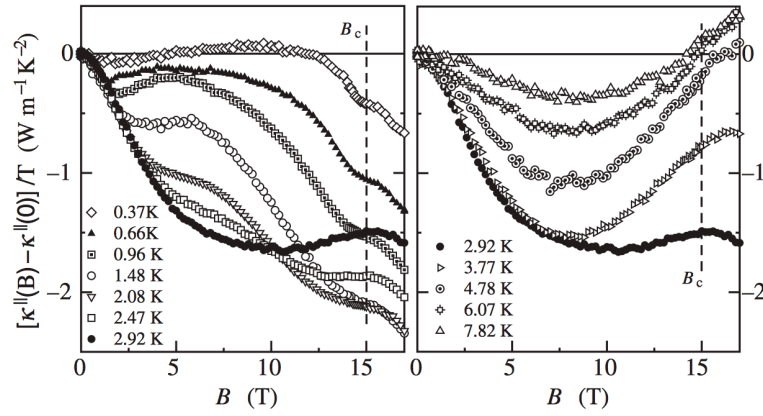


**Figure 4.3.13:** Thermal conductivity measured parallel to the chains of  $Cu(C_4H_4N_2)(NO_3)_2$  as a function of magnetic field at several fixed temperatures. Figure taken from [201].

and  $K_{th}(H)$  approach a limiting behaviour in the field range  $H/J \gtrsim 0.25$ , and seem to be insensitive to changes in the parameter  $\Delta$ . We therefore arrive at the conclusion that  $\Delta = \cos(\pi/8) = 0.92$  provides a satisfactory description of the isotropic point, while minor deviations are expected in the low field region  $H/J \lesssim 0.25$ .

Among the facts that become apparent from a comparison between Figs. 4.3.13 and 4.3.14 are the following: (i) In the low- $T$  region up to 1 K (see insets of Fig. 4.3.14) the theoretical findings suggest that both  $D_{QQ}$  and  $K_{th}$  strongly depend on  $H$ , specially for magnetic fields close to  $H_{cr}$ . On the contrary, experimental data display a plateaulike feature close to  $H_{cr}$ . This observed discrepancy points to the existence of a weighty relaxation time  $\tau$  that also strongly depends on  $H$  and becomes important at low enough  $T$ . (ii) At higher temperatures, a satisfactory agreement between theory and experiment is achieved for the whole field range, which implies that  $\tau$  becomes less important for  $T \gtrsim 1$  K. (iii) The presence of the magnetothermal correction term is not conspicuous at low temperatures; the field dependence of  $D_{QQ}$  and  $K_{th}$  is almost indistinguishable. Certain deviations occur at higher temperatures around 2 K and a simple inspection of Fig. 4.3.14 reveals that the experimental data are best described by  $D_{QQ}$  rather than  $K_{th}$ . Similar results are found in Ref. [201] where thermal conductivity and the magnetothermal correction term were calculated using the kinetic transport theory. In Ref. [155] it was argued that the MTC terms are absent in real materials due to the broken conservation of the total magnetization by spin-orbit coupling.

We would like to argue that one of the assumptions used to compare theoretical findings with experimental results is not fully verified and requires further investigation. We have assumed that the relaxation time  $\tau$  is common for all correlation functions involved in the study of thermal transport. Actually, a more formal definition of  $\tau$  given in Eq. (8) of Ref. [204], where the  $S = 1/2$  Heisenberg chain is coupled to phonons,

reveals that this is not the case. Each correlation function  $\langle \mathcal{J}_i \mathcal{J}_j \rangle$  is accompanied by a characteristic relaxation time  $\tau_{ij}$ . We believe that this should also hold for other sources of scattering, such as magnetic defects of the crystal. A detailed investigation of  $\tau_{ij}$  as a function of  $T$  and  $H$  is required to provide a better description of the experimental data.

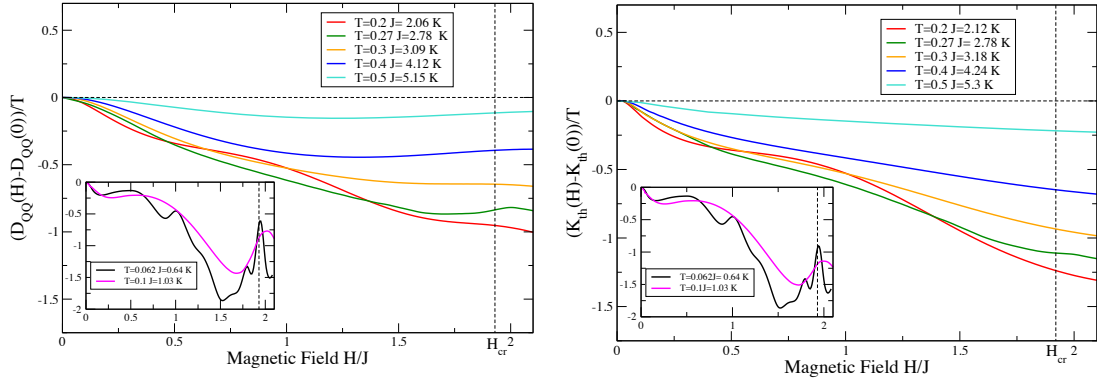


**Figure 4.3.14:** (a) Heat and (b) Thermal Drude weight as a function of magnetic field at several fixed temperatures and  $\Delta = \cos(\pi/8)$ . Magnetic field is measured in units of 7.81 T, given that the critical field is  $H_{cr} = J(1 + \Delta) = 15$  T.

### 4.3.3 Magnetothermal effects

There are several intriguing phenomena in which the interplay of spin and heat plays a crucial role. For example it was suggested [133, 176] that by analogy with the thermoelectric Seebeck effect in electronic conductors, the thermomagnetic Seebeck effect should arise in the presence of a temperature gradient and a magnetic field in electronic insulators.

According to the conventional Seebeck effect when a temperature gradient is maintained in a metal and no electric current is allowed to flow, there will be generated a steady-state electrostatic potential difference between the high- and low-temperature regions of the specimen [205]. This generation of electromotive force by a temperature gradient was discovered by T. J. Seebeck in the 1820's [206] and leads to measurable voltages and currents. The current density  $\mathbf{J}$  is related to the voltage gradient  $\nabla V$  and the temperature gradient  $\nabla T$  by:

$$\mathbf{J} = -\sigma \nabla V - \sigma S \nabla T, \quad (4.3.25)$$

where  $\sigma$  is the electrical conductivity and  $S$  is the Seebeck coefficient. Therefore the conventional definition of  $S$  is the portion of electric current driven by temperature gradients. The steady state special case corresponds to  $\mathbf{J} = 0$  which suggests that the two terms have cancelled out so that  $S = -\frac{\nabla V}{\nabla T}$ .

In recent years, a spin analogue of the Seebeck effect has drawn considerable attention, where the charge transport is replaced with spin transport [207]. The spin Seebeck effect in a magnet stands for the generation of spin voltage, a potential for driving nonequilibrium spin currents, as a result of a temperature gradient. In a spin Seebeck device, when a nonmagnetic metal is attached to a part of a magnet, the spin voltage injects a spin current  $\mathbf{J}_s$  into the conductor. In the metal, the spin current  $\mathbf{J}_s$  is converted into a charge current  $\mathbf{J}_c$  with the help of the inverse spin Hall effect [208]. Therefore, the spin Seebeck effect enables the generation of electromotive force from the temperature gradient as in conventional charge Seebeck devices [207].

In 2008, spin Seebeck effect was originally discovered in a ferromagnetic metal [209] and in 2010 it was also observed in a ferromagnetic semiconductor [210, 211]. It was later revealed that, despite the absence of conduction electrons, the spin Seebeck effect appears even in ferrimagnetic insulators [212–214], indicating it is a universal phenomenon in magnetic materials. There is a consensus that the spin Seebeck effect relies on spin currents that can be carried by low-lying collective excitations of localized spins, such as spin waves or magnons. Certain advantages of one-dimensional spin systems that are electric insulators, like the large and anisotropic reported thermal and spin conductivity, might render these materials as good candidates for the experimental observation of the spin Seebeck effect.

In the presence of magnetic fields and in analogy with the thermoelectric effects, interesting thermomagnetic phenomena occur. In Ref.[133] it was pointed out that in spin systems a current of magnetic moments will flow in the presence of magnetic field  $H$  and a temperature gradient  $\nabla T$  along the chain. For the  $S = 1/2$  XXZ chain, this magnetothermal effect is zero in the absence of magnetic field for symmetry reasons; there is no preferred direction along which a nonzero magnetization could occur [133]. In the presence of magnetic field, a temperature gradient will cause a magnetization vector parallel to the field. The spin current  $\mathcal{J}_s$  is related to the gradients of magnetic field  $\nabla H$  and temperature  $\nabla T$  by the following relation:

$$\mathcal{J}_s = C_{SQ}(-\nabla T) + C_{SS}\nabla H. \quad (4.3.26)$$

Therefore, the magnetic Seebeck coefficient  $S$ , under the condition of zero spin current  $\mathcal{J}_s = 0$  is obtained by:

$$S = \frac{\nabla H}{\nabla T} = \frac{C_{SQ}}{C_{SS}}. \quad (4.3.27)$$

Based on the preceding results, it is easily seen that the Seebeck effect is infinite for the integrable  $S = 1/2$  Heisenberg model:

$$S = \beta \frac{\langle \mathcal{J}_Q \mathcal{J}_s \rangle}{\langle \mathcal{J}_s \mathcal{J}_s \rangle}. \quad (4.3.28)$$

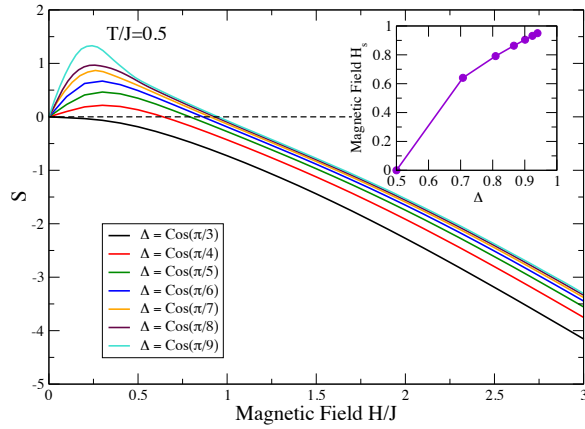


**Figure 4.3.15:** Thermal Seebeck coefficient  $S$  for  $T/J = 0.5$  and several values of  $\Delta$  as a function of  $H$ . The inset depicts the magnetic field  $H_s$  at which  $S$  changes sign, as a function of  $\Delta$ .

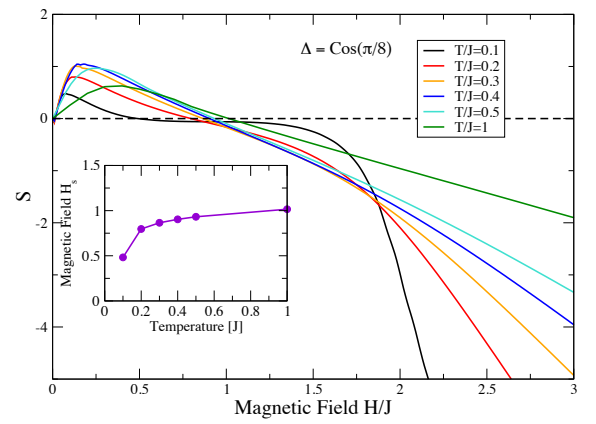


**Figure 4.3.16:** Thermal Seebeck coefficient  $S$  for  $\Delta = \cos(\pi/8)$  and several values of  $T$  as a function of  $H$ . The inset depicts the magnetic field  $H_s$  at which  $S$  changes sign, as a function of  $T$ .

The study of the magnetic Seebeck coefficient for the  $S = 1/2$   $XXZ$  chain was initially addressed in Ref.[133], where the magnetothermal response was calculated via the Jordan–Wigner transformation for the  $XY$  chain and using numerical techniques for  $\Delta \neq 0$ . Several studies followed but they are restricted either in the low–temperature limit [173] or in finite chains [176]. Here we take advantage of Bethe ansatz technique to calculate  $S$  as a function of  $H$  for various temperatures and anisotropy parameters in the thermodynamic limit.

In Fig. 4.3.15 we depict the magnetic field dependence of  $S$  for  $T/J = 0.5$  and several values of  $\Delta$ . We note that at small magnetic fields  $S$  is positive, while at a certain magnetic field  $H_s$  it changes sign and remains negative. In Ref. [176] it was suggested that the sign of  $S$  is a criterion to clarify the types of carriers; a positive  $S$  implies that the spin and heat are dominantly carried by carriers with up spin while a negative  $S$  implies that the majority of carriers have down spin. We note that the value of  $H_s$  shifts to higher values as  $\Delta$  is increased (see inset in Fig. 4.3.15), a feature that has also been observed in [176].

We also examine the behaviour of  $S$  for different temperatures, and for this reason in Fig. 4.3.16 we have plotted  $S(H)$  for  $\Delta = \cos(\pi/8)$  and a number of temperatures. Upon increase of  $T$  the structure of  $S$  changes, but at any  $T$  there is a single  $H_s$  at which the Seebeck coefficient changes sign (see inset in Fig. 4.3.15).

The thermomagnetic effect results measurable currents exactly like the thermoelectric analogue. In a letter recently [215] authors claim to have provided the first evidence for the magnetic Seebeck effect. The experimental set up is based on the prediction that a temperature gradient in the presence of magnetization waves induces a magnetic

induction field. This was tested on a yttrium iron garnet (YIG) thin crystals, a compound that is known to be a ferrimagnetic insulator [207]. We should emphasize that the underlying physics of the magnetic Seebeck effect in a ferrimagnet is formulated using an alternative framework [216]. In this case, the lattice sites carry a magnetic dipole  $\mathbf{m}_A$  and if a constant external magnetic field  $H_{ext}$  and a temperature gradient  $\nabla T$  are applied the time evolution of  $\mathbf{m}_A$  is given by the Landau–Lifschitz–Gilbert equation [217]. The magnetic field appearing in the time evolution equation consists of not only the contribution of the external field  $H_{ext}$ , but also from the induced  $H_{ind}$  magnetic field by the temperature gradient  $\nabla T$ . Inclusion of  $H_{ind}$  into the time evolution equation has certain modifications on how magnetization waves propagate. This effect implies that magnetization waves propagating in the direction of  $\nabla T$  and  $H_{ext}$  are less attenuated than those propagating in the opposite direction. This conjuncture has been experimentally confirmed in Ref.[215].

Using the appropriate experimental procedure it is possible that the magnetic Seebeck effect can be observed using one–dimensional  $S = 1/2$  Heisenberg chains as an electric insulator. As far as theory is concerned, an infinite Seebeck coefficient is predicted for integrable models. This section is completed with the study of the ability of a given material to efficiently produce thermoelectric power, that is related to its dimensionless figure of merit  $ZT$  [176] given by:

$$ZT = \frac{C_{QS}^2}{C_{QQ}C_{SS} - C_{QS}^2} = \frac{\langle \mathcal{J}_Q \mathcal{J}_S \rangle^2}{\langle \mathcal{J}_Q \mathcal{J}_Q \rangle \langle \mathcal{J}_S \mathcal{J}_S \rangle - \langle \mathcal{J}_Q \mathcal{J}_S \rangle^2}. \quad (4.3.29)$$

In Fig. 4.3.17 we plot the magnetic field dependence of  $ZT$  for  $T/J = 0.5$  and several values of the anisotropy parameter  $\Delta$ . We observe that  $ZT$  is small at small fields but increases exponentially for magnetic fields  $H \gtrsim 1$ .

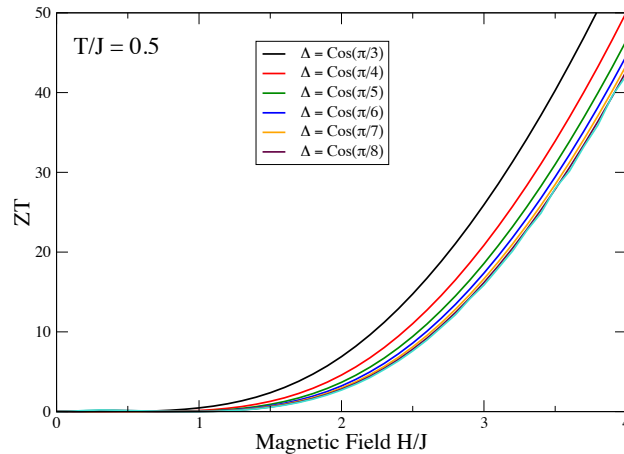


**Figure 4.3.17:** Magnetic field dependence of the figure of merit  $ZT$  for  $T/J = 0.5$  and several values of  $\Delta$ .

## 4.4 Discussion

In this chapter, an attempt has been made to present thermal transport for the  $S = 1$  large- $D$  nonintegrable chain and the  $S = 1/2$   $XXZ$  integrable chain, both in the presence of magnetic field, under the assumptions that the only scattering mechanisms are due to intrinsic magnetic interactions and within the framework of linear response theory.

A description of the heat conductivity  $\kappa_{QQ}$  is given, calculated for the  $S = 1$  model with a FTLM algorithm on a finite chain of length  $L = 16$ . The frequency dependence of the conductivity is explored for a wide range of magnetic fields and various temperatures. The  $\kappa_{QQ}(\omega)$  exhibits two well separated regions the low- $\omega$  part and the high- $\omega$  part, that is activated around  $\omega/J \gtrsim D$ . The high- $\omega$  part is attributed to transitions between the ground state and the exciton-antiexciton continuum.

We also observe that the singular part of  $\kappa_{QQ}$ , namely, the Drude peak  $D_{QQ}$ , vanishes for high  $T$ , an anticipated result for nonintegrable systems. On the contrary, at low  $T$ ,  $D_{QQ}$  remains the significant contribution to the total sum rule of  $\kappa_{QQ}$  at all considered fields. Since the considered model is nonintegrable, a possible explanation of this phenomenon is that the intrinsic diffusive processes at low  $T$ , that will result in a zero  $D_{QQ}$  in the thermodynamic limit, become effective beyond the reachable system size or the energy resolution of the method presented here. Moreover, the low- $\omega$  part of the integrated conductivity  $I_{QQ}$  is compared with the  $S = 1/2$  Drude weight  $\tilde{D}_{QQ}$  calculated in the thermodynamic limit. The overall agreement is satisfactory, with  $\tilde{D}_{QQ}$  including all the characteristic features of the  $S = 1$  behaviour.

A detailed study of the thermal transport for the  $S = 1/2$   $XXZ$  Heisenberg model in the presence of magnetic field and for values of the anisotropy parameter in the range  $1/2 < \Delta < 1$  is given, where all correlation functions are calculated in the thermodynamic limit using the Bethe ansatz technique. As far as the spin conductivity is concerned, the zero  $T$  results agree with the ones calculated using the Luttinger Liquid description, providing a reliable test about the validity of our findings.  $D_s(H, T = 0)$  abruptly terminates at  $H = H_{cr} = J(1 + \cos(\pi/\nu))$ , above which the system enters at its massive phase and  $D_s$  vanishes at all  $H$ .

As far as the magnetic field dependence of  $D_s$  is concerned, at small magnetic fields spin Drude weight goes like  $D_s \simeq AH^2$ . Additionally, upon increase of  $\Delta$ , starting from  $\Delta = 1/2$  and approaching the isotropic point  $\Delta = 1$ , spin Drude weight in the field region  $H/J \gtrsim 0.5$  seems to converge to a limiting behaviour that remains unaffected as one further increases the values of  $\Delta$ . The temperature dependence of the spin Drude weight is also studied and at  $H < H_{cr}$  decreases like  $D_s(T) \simeq$

$D_s(0) - Ae^{-H/T}T^{\gamma(H,T)}$ . This is in contrast with the  $H = 0$  results where a power-law behaviour at low  $T$  was observed.

Attention is also given in the thermal conductivity of the  $S = 1/2$  *XXZ* model. Two main quantities play central role; the heat Drude weight  $D_{QQ}$  and the thermal Drude weight  $K_{th}$ . The full term  $K_{th}$  is the result of a combination of two competing terms, the  $D_{QQ}$  Drude weight and the magnetothermal corrections *MTC* that originate from the coupling of the heat and spin currents in the presence of magnetic field.

Heat Drude weight  $D_{QQ}(H)$  exhibits a pronounced nonmonotonic behaviour as a function of  $H$ . Furthermore, as the anisotropy parameter approaches the isotropic point  $\Delta = 1$ , the  $D_{QQ}(H)$  curve in the field region  $H/J \gtrsim 0.25$  approaches a limiting behaviour and seems to be insensitive to changes in the parameter  $\Delta$ . The *MTC* term is exactly zero at  $H = 0$ , but becomes finite at finite  $H$ , where it develops two peaks.

The resulting behaviour of the total thermal Drude weight  $K_{th}$ , as a sum of two competing terms is that it turns out to be a smooth function of magnetic field with no peaks observed as a function of  $H$ . The inclusion of the *MTC* term results in an overall suppression of  $K_{th}$  and the cancellation of the nonmonotonic peaked behaviour of  $D_{QQ}$ . As in the case of  $D_{QQ}(H)$ , thermal Drude weight  $K_{th}(H)$  is also approaching a limiting behaviour in the  $H/J \gtrsim 0.25$  region as  $\Delta \rightarrow 1$ .

The temperature dependence of the thermal and heat Drude weight is also explored. Finally, two quantities relevant to the magnetothermal effect in spin systems are provided, the magnetic Seebeck coefficient  $S$  and the figure of merit  $ZT$ . At small magnetic fields  $S$  is positive, while at a certain magnetic field  $H_s$  it changes sign and remains negative. The value of  $H_s$  shifts to higher values as  $\Delta$  is increased.

# Conclusions

The main results of this work are summarized in the following:

- (a) **Effective  $S = 1/2$  description of the  $S = 1$  chain:** We show that the  $S = 1$  Heisenberg AFM with strong easy– plane anisotropy in a magnetic field can be systematically mapped onto a  $S = 1/2$  XXZ Heisenberg model in a longitudinal magnetic field. This mapping enables us to gain a better physical understanding of the original  $S = 1$  model, since the  $S = 1/2$  model is exactly solvable and a lot is known about its thermodynamical and dynamical quantities. By a straightforward comparison of the critical fields predicted by each model, we have an indication that the mapping is more accurate close to  $H_2$  rather than  $H_1$ .
- (b) **Electron Spin Resonance:** A detailed theoretical as well as experimental study of the ESR spectrum of a  $S = 1$  chain with strong anisotropy is presented. The principal results are:
- As far as the general structure of the observed ESR spectrum is concerned, the theoretical predictions of the 3D and 1D model are qualitatively similar and in reasonable quantitative agreement with experiment.
  - The most interesting feature of the ESR spectrum is that our current experiment supports the interpretation that the  $F$  and  $G$  lines are inseparable partners in a doubly–peaked  $FG$  band which originates in transitions between single magnons and single–ion two–magnon bound states. In fact, the  $G$  mode absorbs most of the intensity.
  - Structure of the Spectrum in the Intermediate phase: A tail of line  $G$  with strong intensity survives in the intermediate region even at low temperature where line  $G$  itself loses its intensity for  $H > H_2$ . Such a tail should thus be attributed to a high–frequency collective excitation that appears in the intermediate phase. On the low–frequency end of the intermediate phase we reveal a  $V$ –like structure with intensity that gradually vanishes as one approaches the center. An evaluation of the low–lying ESR spectrum of the effective  $S = 1/2$  model also predicts that ESR lines form a  $V$ –like structure. The calculation is based on the Bethe ansatz using a state that is highly unusual one in the Bethe ansatz literature.

(c) **Magnetization  $M$ :**

- As far as the magnetic field dependence of  $M$  is concerned, the critical exponent that describes the behaviour of magnetization near the critical fields at very low  $T$  is extracted found equal to  $\delta = 2$ . This result renders the considered model in the same universality class as a broad collection of various models of quantum magnetism.
- The temperature dependence of  $M$  for both models reveals the existence of extrema at some temperature  $T_c$ , which is interpreted as the critical temperature below which the description of the system in terms of Luttinger liquid is valid. A magnetic phase diagram is constructed that represents the crossover into a low- $T$  Luttinger liquid regime.

(d) **Specific Heat  $C_v$ :**

- The  $C_v(H)$  curve exhibits a characteristic double peak around critical fields  $H_{1,2}$ . This characteristic behaviour cannot be explained by noninteracting magnons and is a signature of the strong correlations of the system.
- The  $C_v(T)$  curve reveals a linear dependence at low  $T$  for magnetic fields between  $H_1 < H < H_2$ , consistent with the Luttinger liquid phase.

(e) **Thermal Transport in the  $S=1$  large  $-D$  chain:** The heat conductivity  $\kappa_{QQ}(\omega)$  exhibits two well separated regions the low- $\omega$  part and the high- $\omega$  part, that is activated around  $\omega/J \gtrsim D$ . The high- $\omega$  part is attributed to transitions between the ground state and the exciton-antiexciton continuum. The heat Drude peak  $D_{QQ}$ , vanishes for high  $T$ , an anticipated result for nonintegrable systems. On the contrary, at low  $T$ ,  $D_{QQ}$  remains the significant contribution to the total sum rule of  $\kappa_{QQ}$  at all considered fields. Since the considered model is nonintegrable, a possible explanation of this phenomenon is that the intrinsic diffusive processes at low  $T$ , that will result in a zero  $D_{QQ}$  in the thermodynamic limit, become effective beyond the reachable system size or the energy resolution of the our method. The low- $\omega$  part of the integrated conductivity  $I_{QQ}$  is compared with the  $S = 1/2$  Drude weight  $\tilde{D}_{QQ}$  calculated in the thermodynamic limit. The overall agreement is satisfactory, with  $\tilde{D}_{QQ}$  including all the characteristic features of the  $S = 1$  behaviour.(f) **Thermal Transport in the  $S=1/2$  large  $-D$  chain:**

- Spin Conductivity: At small magnetic fields spin Drude weight goes like  $D_s \simeq AH^2$ . Additionally, upon increase of  $\Delta$ , starting from  $\Delta = 1/2$  and approaching the isotropic point  $\Delta = 1$ , spin Drude weight in the field region  $H/J \gtrsim 0.5$  seems to converge to a limiting behaviour that remains unaffected as one further increases the values of  $\Delta$ . The temperature dependence of the spin Drude weight is also studied and at  $H < H_{cr}$  decreases like  $D_s(T) \simeq D_s(0) - Ae^{-H/T}T^{\gamma(H,T)}$ . This is in contrast with the  $H = 0$  results where a power-law behaviour at low  $T$  was observed.

- **Thermal Conductivity:** Heat Drude weight  $D_{QQ}(H)$  exhibits a pronounced nonmonotonic behaviour as a function of  $H$ . Furthermore, as the anisotropy parameter approaches the isotropic point  $\Delta = 1$ , the  $D_{QQ}(H)$  curve in the field region  $H/J \gtrsim 0.25$  approaches a limiting behaviour and seems to be insensitive to changes in the parameter  $\Delta$ . The *MTC* term is exactly zero at  $H = 0$ , but becomes finite at finite  $H$ , where it develops two peaks. The resulting behaviour of the total thermal Drude weight  $K_{th}$ , as a sum of two competing terms is that it turns out to be a smooth function of magnetic field with no peaks observed as a function of  $H$ . The inclusion of the *MTC* term results in an overall suppression of  $K_{th}$  and the cancellation of the nonmonotonic peaked behaviour of  $D_{QQ}$ . As in the case of  $D_{QQ}(H)$ , thermal Drude weight  $K_{th}(H)$  is also approaching a limiting behaviour in the  $H/J \gtrsim 0.25$  region as  $\Delta \rightarrow 1$ .
- **Magnetothermal effects:** At small magnetic fields the magnetic Seebeck effect  $S$  is positive, while at a certain magnetic field  $H_s$  it changes sign and remains negative. The value of  $H_s$  shifts to higher values as  $\Delta$  is increased.

# Appendix A

## Two-magnons bound states in the 3D model

In this Appendix we give a detailed description of the derivation of the single-ion bound state in three dimensions. This is done by a direct method developed long time ago by Wortis [68] for the calculation of two-magnon bound states in ferromagnets with arbitrary lattice dimension. The method is here generalized to account for easy-plane anisotropy with strength  $D$ .

To begin with, consider a finite cubic array of points,  $i$ , which may be thought of as the vertices of a lattice of unit spacing and site  $L$ . There are a total of  $N = L^3$  lattice points. It is convenient to assume that the lattice has periodic connectivity, i.e., that the point  $i + Lj$  is identical with the point  $i$  for all  $i, j$  lattice vectors. The considered  $S = 1$  model is described by the Hamiltonian:

$$\mathcal{H} = \sum_{i,m} J_m(\mathbf{S}_i \cdot \mathbf{S}_{i+e_m}) + \sum_i [D(S_i^z)^2 + g\mu_B H S_i^z], \quad (\text{A.0.1})$$

where  $i$  denotes a generic site of a 3D lattice and  $e_m$  with  $m = \{x, y, z\}$  count nearest neighbors. We assume that  $H > H_2$  in order for the ground state of the system  $|\Omega_0\rangle$  to be fully ferromagnetic. The spin deviation number is:

$$n = NS + \sum_m S_m^z \quad (\text{A.0.2})$$

It is easy to see that the unique state with  $n = 0$  is the ground state of Eq.(A.0.1) with energy  $E_0 = -g\mu_B H N + N \sum_m J_m + DN$ . The normalized states of the  $n = 1$  and  $n = 2$  subspaces are simply generated from  $|\Omega_0\rangle$ :

$$\begin{aligned} S_\nu^+ |\Omega_0\rangle &= \sqrt{2} |\nu\rangle, \\ S_\nu^+ S_\mu^+ |\Omega_0\rangle &= \sqrt{2(1 + \delta_{\mu,\nu} h_2(\mu, \nu))} |\nu, \mu\rangle, \quad \text{where } h_2(\mu, \nu) = 1 - \delta_{\mu,\nu}/2 \end{aligned} \quad (\text{A.0.3})$$

The notation  $|\nu, \mu, \dots\rangle$  stands for a *normalized* state in which a unit of spin has been flipped away from total alignment on each of the sites  $\nu, \mu, \dots$

Now we define the one- and two-particle Green functions:

$$\begin{aligned} G_1(\nu; \mu; t) &= (-i) \langle \Omega_0 | S_\nu^-(t) S_\mu^+(0) | \Omega_0 \rangle \theta(t) \\ G_2(\nu, \mu; \nu', \mu'; t) &= (-i) \langle \Omega_0 | S_\nu^-(t) S_\mu^-(t) S_{\nu'}^+(0) S_{\mu'}^+(0) | \Omega_0 \rangle \theta(t), \end{aligned} \quad (\text{A.0.4})$$

where  $\theta(t) = 1$  for  $t > 0$  and  $\theta(t) = 0$  for  $t < 0$ . The standard time development is taken as:

$$\mathbf{S}_\nu(t) = e^{iHt} \mathbf{S}_\nu(0) e^{-iHt}. \quad (\text{A.0.5})$$

**Solution of the one-particle problem:** The equation of motion for  $G_1(\nu; \mu; t)$  following from Eq.(A.0.1) is:

$$\begin{aligned} &\left( i \frac{\partial}{\partial t} + 2 \sum_m J_m + D - g\mu_b H \right) G_1(\nu; \mu; t) \\ &- \sum_m J_m ((G_1(\nu + e_m; \mu; t) + G_1(\nu - e_m; \mu; t)) = 2\delta(t)\delta_{\nu,\mu}, \end{aligned} \quad (\text{A.0.6})$$

where  $m = \{x, y, z\}$ . Note that there is a difference in index  $m$  between Eq.(A.0.1) and Eq.(A.0.6). While in the first case  $m$  counts nearest neighbors, in the second case for convenience it only counts nearest neighbors in the positive direction. The negative direction is explicitly taken into account as  $\nu - e_m$ . The periodicity requirement

$$G_1(\nu; \mu; t) = G_1(\nu + Li; \mu; t), \quad \text{where } \nu, \mu, i \text{ are lattice points,} \quad (\text{A.0.7})$$

is incorporated by expressing  $G_1$  as a spatial Fourier series with respect to the  $\mathbf{k}$  vectors of the reciprocal lattice. This is expressed as follows:

$$G_1(\nu; \mu; t) = \frac{2}{N} \sum_{\mathbf{k} \in F} e^{i\mathbf{k}(\nu-\mu)} G_1(\mathbf{k}; t). \quad (\text{A.0.8})$$

The sum in Eq.(A.0.8) is over the set  $F$  containing the reciprocal lattice vectors with components  $k_j = (2\pi/L)p_j$  where:

$$\begin{aligned} - & \left(\frac{1}{2}L - 1\right) \leq p_j \leq \frac{1}{2}L, & \text{for } L \text{ even,} \\ - & \left(\frac{1}{2}L - \frac{1}{2}\right) \leq p_j \leq \left(\frac{1}{2}L - \frac{1}{2}\right), & \text{for } L \text{ odd.} \end{aligned}$$

The temporal Fourier transformation of  $G_1$  is defined by:

$$G_1(\nu; \mu; t) = i \int_{-\infty}^{\infty} \frac{d\omega}{2\pi} e^{-i\omega t} G_1(\nu; \mu; \omega). \quad (\text{A.0.9})$$

Eq.(A.0.6) is trivially solved using Eq.(A.0.8) and Eq.(A.0.9), and the result is:

$$G_1(\nu; \mu; t) = \frac{2}{N} \sum_{\mathbf{k} \in F} e^{ik(\nu-\mu)} \int_{-\infty}^{\infty} \frac{d\omega}{2\pi} \frac{e^{-i\omega t}}{2\pi(\omega - \Omega(\mathbf{k}) + i\eta)}, \quad (\text{A.0.10})$$

where  $\Omega(\mathbf{k})$  is the magnon dispersion

$$\Omega(\mathbf{k}) = 2 \sum_m J_m (\cos k_m - 1) - D + g\mu_B H, \quad (\text{A.0.11})$$

**Solution of the two-particle problem:** We are now in a position to calculate  $G_2$ .

The equation of motion obeyed by  $G_2$  is:

$$\begin{aligned} & \left( i \frac{\partial}{\partial t} + 4 \sum_m J_m + 2D - 2g\mu_B H \right) G_2(\nu_A, \nu_B; \mu_A, \mu_B; t) \\ & - \sum_m J_m (G_2(\nu_A + e_m, \nu_B; \mu_A, \mu_B; t) + G_2(\nu_A, \nu_B + e_m; \mu_A, \mu_B; t) \\ & + G_2(\nu_A - e_m, \nu_B; \mu_A, \mu_B; t) + G_2(\nu_A, \nu_B - e_m; \mu_A, \mu_B; t)) \\ & + 2D G_2(\nu_A, \nu_B; \mu_A, \mu_B; t) \delta_{\nu_A, \nu_B} \\ & + \sum_m J_m (G_2(\nu_A, \nu_B + e_m; \mu_A, \mu_B; t) + G_2(\nu_A, \nu_B - e_m; \mu_A, \mu_B; t) \\ & - \sum_m J_m (\delta_{\nu_A, \nu_B + e_m} + \delta_{\nu_A, \nu_B - e_m}) G_2(\nu_A, \nu_B; \mu_A, \mu_B; t) \\ & = (-i) 4 (\delta_{\nu_A, \mu_A} \delta_{\nu_B, \mu_B} + \delta_{\nu_A, \mu_B} \delta_{\nu_B, \mu_A}) \left( 1 - \frac{\delta_{\mu_A, \mu_B}}{2} \right) \delta(t). \end{aligned} \quad (\text{A.0.12})$$

The last three terms in the left hand side of this equation may be regarded as interactions between particles whose free motion is described by the two first terms. To exploit this analogy we introduce the symmetrical function:

$$\Gamma(\nu_A, \nu_B; \mu_A, \mu_B; t) = G_1(\nu_A; \mu_A; t) G_1(\nu_B; \mu_B; t) + G_1(\nu_A; \mu_B; t) G_1(\nu_B; \mu_A; t). \quad (\text{A.0.13})$$

It can be verified that  $\Gamma(\nu_A, \nu_B; \mu_A, \mu_B; t)$  satisfies the following equation:

$$\begin{aligned}
 & \left( i \frac{\partial}{\partial t} + 4 \sum_m J_m + 2D - 2g\mu_B H \right) \Gamma(\nu_A, \nu_B; \mu_A, \mu_B; t) \\
 & - \sum_m J_m (\Gamma(\nu_A + e_m, \nu_B; \mu_A, \mu_B; t) + \Gamma(\nu_A, \nu_B + e_m; \mu_A, \mu_B; t) \\
 & \quad + \Gamma(\nu_A - e_m, \nu_B; \mu_A, \mu_B; t) + \Gamma(\nu_A, \nu_B - e_m; \mu_A, \mu_B; t)) \\
 & = (-i)4(\delta_{\nu_A, \mu_A} \delta_{\nu_B, \mu_B} + \delta_{\nu_A, \mu_B} \delta_{\nu_B, \mu_A}). \quad (\text{A.0.14})
 \end{aligned}$$

With the help of  $\Gamma$  the equation of motion Eq.(A.0.12) may be now transformed into an integral equation, which incorporates the boundary conditions through the structure of  $G_1$ . This is done as follows. We define the  $\mathcal{Q}$ ,  $\delta\mathcal{Q}$  and  $\mathcal{D}$  operators as:

$$\begin{aligned}
 \mathcal{D}(\nu_A, \nu_B, t; \mu_A, \mu_B, t') &= (\delta_{\nu_A, \mu_A} \delta_{\nu_B, \mu_B} + \delta_{\nu_A, \mu_B} \delta_{\nu_B, \mu_A}) \delta(t - t') \\
 \mathcal{Q}(\nu_A, \nu_B, t; n_A, n_B, t') &= \left( -\frac{\partial}{\partial t} + 4 \sum_m (J_m) + D - g\mu_B H \right) \delta(t - t') \delta_{n_A, \nu_A} \delta_{n_B, \nu_B} \\
 & - \delta(t - t') \sum_m J_m (\delta_{\nu_A + e_m, n_A} \delta_{\nu_B, n_B} + \delta_{\nu_A - e_m, n_A} \delta_{\nu_B, n_B} + \delta_{\nu_A, n_A} \delta_{\nu_B + e_m, n_B} + \delta_{\nu_A, n_A} \delta_{\nu_B - e_m, n_B}) \quad (\text{A.0.15}) \\
 \delta\mathcal{Q}(\nu_A, \nu_B, t; \mu_A, \mu_B, t') &= -2D \delta_{\nu_A, \nu_B} \delta_{n_A, \nu_A} \delta_{n_B, \nu_B} \\
 & + \sum_m (\delta_{\nu_A, n_A} \delta_{\nu_B + e_m, n_B} + \delta_{\nu_A, n_A} \delta_{\nu_B - e_m, n_B} - \delta_{\nu_A, n_A} \delta_{\nu_B, n_B} (\delta_{\nu_A, \nu_B + e_m} + \delta_{\nu_A, \nu_B - e_m})) \quad (\text{A.0.16})
 \end{aligned}$$

Using definition (A.0.15), Eq.(A.0.14) can be written in a more compact form as:

$$\sum_{n_A, n_B} \int dt' \mathcal{Q}(\nu_A, \nu_B, t; n_A, n_B, t') \Gamma(n_A, n_B, t; \mu_A, \mu_B, t'') = (-i)4\mathcal{D}(\nu_A, \nu_B, t; \mu_A, \mu_B, t''). \quad (\text{A.0.17})$$

Similarly, a more concise formula of Eq.(A.0.12) is:

$$\begin{aligned}
 \sum_{n_A, n_B} \int dt' (\mathcal{Q}(\nu_A, \nu_B, t; n_A, n_B, t') + \delta\mathcal{Q}(\nu_A, \nu_B, t; n_A, n_B, t')) G_2(n_A, n_B, t; \mu_A, \mu_B, t'') \\
 = (-i)4\mathcal{D}(\nu_A, \nu_B, t; \mu_A, \mu_B, t'') h_2(\mu_A, \mu_B). \quad (\text{A.0.18})
 \end{aligned}$$

It is easy to notice that the  $\delta\mathcal{Q}$  operator corresponds to the last three terms in the left hand side of Eq.(A.0.12). Now, from Eq.(A.0.17) we obtain

$$\mathcal{Q}(\nu_A, \nu_B, t; n_A, n_B, t') = -i4 \sum_{m_A, m_B} \int dt'' \mathcal{D}(\nu_A, \nu_B, t; m_A, m_B, t'') \Gamma^{-1}(m_A, m_B, t'', n_A, n_B, t'). \quad (\text{A.0.19})$$

Replacing  $\mathcal{Q}$  in Eq.(A.0.18), and after some algebraic manipulation, we arrive at the following expression:

$$G_2(\nu_A, \nu_B; \mu_A, \mu_B, t) = \Gamma(\nu_A, \nu_B; \mu_A, \mu_B, t)h_2(\mu_A, \mu_B) - \frac{i}{8} \sum_{m_A, m_B} \int dt'' \left[ \sum_{n_A, n_B} \int dt' \Gamma(\nu_A, \nu_B, n_A, n_B, t') \delta \mathcal{Q}(n_A, n_B, t'; m_A, m_B, t'') \right] G_2(m_A, m_B, t''; \mu_A, \mu_B) \quad (\text{A.0.20})$$

or equivalently, if we introduce an interaction kernel  $K_2$  such that:

$$K_2(\nu_A, \nu_B; m_A, m_B, t'') = \sum_{n_A, n_B} \int dt' \Gamma(\nu_A, \nu_B; n_A, n_B, t') \delta \mathcal{Q}(n_A, n_B, t'; m_A, m_B, t''), \quad (\text{A.0.21})$$

then Eq.(A.0.20) is expressed as:

$$G_2(\nu_A, \nu_B; \mu_A, \mu_B; t) = \Gamma(\nu_A, \nu_B; \mu_A, \mu_B; t)h_2(\mu_A, \mu_B) - \frac{i}{8} \sum_{n_A, n_B} \int_{-\infty}^{\infty} dy K_2(\nu_A, \nu_B; n_A, n_B; t - y) G_2(n_A, n_B; \mu_A, \mu_B; y), \quad (\text{A.0.22})$$

The asymmetry between indices  $\nu_{A,B}$  and  $\mu_{A,B}$  seems to be an unavoidable consequence of the spin commutation relations. The next step is to Fourier transform Eq.(A.0.22) and attempt to solve it in the Fourier space. Sum and difference variables are introduced according to:

$$\begin{aligned} 2\mathbf{R} &= \nu_A + \nu_B, & \mathbf{r} &= \nu_A + \nu_B \\ \mathbf{K} &= \mathbf{k}_1 + \mathbf{k}_2, & 2\mathbf{k} &= \mathbf{k}_1 - \mathbf{k}_2 \end{aligned} \quad (\text{A.0.23})$$

Spatial and temporal Fourier transformations are defined as:

$$\begin{aligned} G_2(\nu_A, \nu_B; \mu_A, \mu_B; t) &= \frac{1}{N} \sum_{\mathbf{K} \in F} e^{i\mathbf{K} \cdot (\mathbf{R} - \mathbf{R}')} \int_{-\infty}^{\infty} \frac{d\omega}{2\pi} e^{-i\omega t} G_2(\mathbf{r}; \mathbf{r}'; \mathbf{K}, \omega) \\ \Gamma(\nu_A, \nu_B; \mu_A, \mu_B; t) &= \frac{i}{N} \sum_{\mathbf{K} \in F} e^{i\mathbf{K} \cdot (\mathbf{R} - \mathbf{R}')} \int_{-\infty}^{\infty} \frac{d\omega}{2\pi} e^{-i\omega t} \Gamma(\mathbf{r}; \mathbf{r}'; \mathbf{K}, \omega) \\ K_2(\nu_A, \nu_B; \mu_A, \mu_B; t) &= \frac{i}{N} \sum_{\mathbf{K} \in F} e^{i\mathbf{K} \cdot (\mathbf{R} - \mathbf{R}')} \int_{-\infty}^{\infty} \frac{d\omega}{2\pi} e^{-i\omega t} K_2(\mathbf{r}; \mathbf{r}'; \mathbf{K}, \omega) \end{aligned} \quad (\text{A.0.24})$$

where

$$\Gamma(\mathbf{r}; \mathbf{r}'; \mathbf{K}, \omega) = \frac{-8}{N} \sum_{\mathbf{k} \in G} \frac{\cos(\mathbf{k} \cdot \mathbf{r}) \cos(\mathbf{k} \cdot \mathbf{r}')}{\omega - S(\mathbf{k}, \mathbf{K}) + i\eta}. \quad (\text{A.0.25})$$

$G$  denotes the set of modified reciprocal lattice vectors with components  $2k_j = (2\pi/L)p_j$  where:

- $(L - 2) \leq p_j \leq L$ , for L and L  $K_j/2\pi$  same parity ,
- $(L - 1) \leq p_j \leq (L - 1)$ , for L and L  $K_j/2\pi$  opposite parity . (A.0.26)

and  $S(\mathbf{k}, \mathbf{K})$  is the energy of two noninteracting magnons with wavevectors  $\mathbf{k}_1$  and  $\mathbf{k}_2$ :

$$S(\mathbf{k}, \mathbf{K}) = \Omega(\mathbf{k}_1) + \Omega(\mathbf{k}_2) = 4 \sum_m J_m \left( \cos\left(\frac{K_m}{2}\right) \cos(k_m) - 1 \right) - 2D + 2g\mu_B H . \quad (\text{A.0.27})$$

The symmetry of  $G_2$  in  $\nu_A, \nu_B$  and  $\mu_A, \mu_B$  requires that  $G_2(\mathbf{r}; \mathbf{r}'; \mathbf{K}, \omega)$  be even in  $\mathbf{r}$  and  $\mathbf{r}'$ . Once representations (A.0.24) are substituted into (A.0.22) one finds:

$$G_2(\mathbf{r}; \mathbf{r}'; \mathbf{K}, \omega) = \Gamma(\mathbf{r}; \mathbf{r}'; \mathbf{K}, \omega) h_2(\mathbf{r}') + \frac{1}{8} \sum_{\mathbf{r}_1} K_2(\mathbf{r}; \mathbf{r}_1; \mathbf{K}, \omega) G_2(\mathbf{r}_1; \mathbf{r}'; \mathbf{K}, \omega) \quad (\text{A.0.28})$$

It can be easily proven that the following equality holds:

$$\begin{aligned} \sum_{\mathbf{r}_1} K_2(\mathbf{r}; \mathbf{r}_1; \mathbf{K}, \omega) G_2(\mathbf{r}_1; \mathbf{r}'; \mathbf{K}, \omega) &= -2D \Gamma(\mathbf{r}, 0; \mathbf{K}, \omega) G_2(0; \mathbf{r}'; \mathbf{K}, \omega) \\ &\quad - 2 \sum_m J_m \Lambda_2(\mathbf{r}, j_m; \mathbf{K}, \omega) \end{aligned} \quad (\text{A.0.29})$$

where  $j_m$  denotes a unit vector in the  $m = \{x, y, z\}$  direction, and function  $\Lambda_2$  is defined as follows:

$$\Lambda_2(\mathbf{r}; \mathbf{r}'; \mathbf{K}, \omega) = \frac{-8}{N} \sum_{\mathbf{k} \in G} \frac{\cos(\mathbf{k} \cdot \mathbf{r}) \left( \cos(\mathbf{k} \cdot \mathbf{r}') - \cos\left(\frac{\mathbf{K} \cdot \mathbf{r}'}{2}\right) \right)}{\omega - S(\mathbf{k}, \mathbf{K}) + i\eta} . \quad (\text{A.0.30})$$

Finally, incorporating equality (A.0.29) into Eq.(A.0.28) we obtain:

$$\begin{aligned} G_2(\mathbf{r}; \mathbf{r}'; \mathbf{K}, \omega) &= \Gamma(\mathbf{r}; \mathbf{r}'; \mathbf{K}, \omega) h_2(\mathbf{r}') - \frac{D}{4} \Gamma(\mathbf{r}; 0; \mathbf{K}, \omega) G_2(0; \mathbf{r}'; \mathbf{K}, \omega) \\ &\quad - \frac{1}{4} \sum_m J_m K_2(\mathbf{r}; j_m; \mathbf{K}, \omega) G_2(j_m; \mathbf{r}'; \mathbf{K}, \omega) . \end{aligned} \quad (\text{A.0.31})$$

If  $\mathbf{r}$  is replaced by a unit lattice vector  $l$ , Eq.(A.0.31) becomes for each  $\mathbf{r}'$ ,  $\mathbf{K}$ , and  $\omega$  a set of 3 equations for the 3 unknowns  $G_2(l; \mathbf{r}'; \mathbf{K}, \omega)$ . By reinserting the solution on the right-hand side of Eq.(A.0.31), we may compute the full  $G_2(\mathbf{r}; \mathbf{r}'; \mathbf{K}, \omega)$  from which the wavefunctions and energy eigenvalues can be found. For general L and  $\mathbf{K}$  the difficulty of performing the summations (A.0.25) makes this full program unfeasible.

For our purposes it will be sufficient to restrict to analyzing the structure of  $G_2$  as a function of its energy variable,  $\omega$ . For  $|\gamma\rangle$  a complete orthonormal set of two-particle energy eigenstates we use the representation:

$$G_2(\nu_A, \nu_B; \mu_A, \mu_B; \omega) = - \sum_{\gamma} \frac{\langle \Omega_0 | S_{\nu_A}^- S_{\nu_B}^- |\gamma\rangle \langle \gamma | S_{\mu_A}^+ S_{\mu_B}^+ (t) | \Omega_0 \rangle}{\omega - (E_{\gamma} - E_0) + i\eta}, \quad (\text{A.0.32})$$

to show that the poles of  $G_2$  are the two-magnons eigenenergies. More specifically, if we choose to regard  $\omega$  as a complex variable  $z$ , the poles of  $G_2(\mathbf{r}; \mathbf{r}'; \mathbf{K}, z)$  as a function of  $z$  lie on the real  $z$  axis at values given by the differences between the two-magnon eigenstates and  $E_0$ . Formulas (A.0.25) show that the functions  $\Gamma(\mathbf{r}; \mathbf{r}'; \mathbf{K}, z)$  and  $K_2(\mathbf{r}; \mathbf{r}'; \mathbf{K}, z)$  have poles at the energies  $S(\mathbf{k}, \mathbf{K})$  of two noninteracting magnons.  $G_2$  appears to have poles both at  $S(\mathbf{k}, \mathbf{K})$  and at the zeros of the denominator which arise in the solution of Eq.(A.0.31). These later poles can be found as follows. If we replace  $\mathbf{r} \rightarrow l_a$  and  $\mathbf{r}' \rightarrow l_b$ , with  $l_a, l_b$  unit vectors, we get from Eq.(A.0.31):

$$\begin{aligned} G_2(l_a; l_b; \mathbf{K}, \omega) &= \Gamma(l_a; l_b; \mathbf{K}, \omega) h_2(l_b) - \frac{D}{4} \Gamma(l_a; 0; \mathbf{K}, \omega) G_2(0; l_b; \mathbf{K}, \omega) \\ &- \frac{1}{4} \sum_m J_m K_2(l_a; j_m; \mathbf{K}, \omega) G_2(j_m; l_b; \mathbf{K}, \omega), \end{aligned} \quad (\text{A.0.33})$$

For  $l_a, l_b = 0, x, y, z$ , where  $x, y, z$  are unit vectors in the  $x, y, z$  direction respectively, from Eq.(A.0.33) we get 16 equations, which in matrix form are expressed as:

$$\begin{aligned} &\left( \mathcal{I} + \frac{D}{4} \begin{bmatrix} 0 & 0 & 0 & 0 \\ \Gamma(x, 0) & 0 & 0 & 0 \\ \Gamma(y, 0) & 0 & 0 & 0 \\ \Gamma(z, 0) & 0 & 0 & 0 \end{bmatrix} + \frac{1}{4} \begin{bmatrix} 0 & K_2(0, x) & K_2(0, y) & K_2(0, z) \\ 0 & K_2(x, x) & K_2(x, y) & K_2(x, z) \\ 0 & K_2(y, x) & K_2(y, y) & K_2(y, z) \\ 0 & K_2(z, x) & K_2(z, y) & K_2(z, z) \end{bmatrix} \cdot \begin{bmatrix} 0 & 0 & 0 & 0 \\ 0 & Jx & 0 & 0 \\ 0 & 0 & Jy & 0 \\ 0 & 0 & 0 & Jz \end{bmatrix} \right) \times \\ &\begin{bmatrix} G_2(0, 0) & G_2(0, x) & G_2(0, y) & G_2(0, z) \\ G_2(x, 0) & G_2(x, x) & G_2(x, y) & G_2(x, z) \\ G_2(y, 0) & G_2(y, x) & G_2(y, y) & G_2(y, z) \\ G_2(z, 0) & G_2(z, x) & G_2(z, y) & G_2(z, z) \end{bmatrix} = \\ &\begin{bmatrix} \Gamma(0, 0) & \Gamma(0, x) & \Gamma(0, y) & \Gamma(0, z) \\ \Gamma(0, x) & \Gamma(x, x) & \Gamma(x, y) & \Gamma(x, z) \\ \Gamma(0, y) & \Gamma(y, x) & \Gamma(y, y) & \Gamma(y, z) \\ \Gamma(0, z) & \Gamma(z, x) & \Gamma(z, y) & \Gamma(z, z) \end{bmatrix} \cdot \begin{bmatrix} h_2(0) & 0 & 0 & 0 \\ 0 & h_2(x) & 0 & 0 \\ 0 & 0 & h_2(y) & 0 \\ 0 & 0 & 0 & h_2(z) \end{bmatrix} \end{aligned} \quad (\text{A.0.34})$$

where  $\mathcal{I}$  is the identity matrix, and  $\mathbf{K}$  and  $z$  have been left implicit. Note that the unit vectors can equal zero ( $l_a, l_b = 0$ ) as a direct consequence of the single-ion term in Hamiltonian (A.0.1). Thus, we obtain a linear system of 16 equations, one for each

combination of  $l_a, l_b = \{0, x, y, z\}$ . In the absence of this anisotropy, the second term in the right-hand side of Eq.(A.0.31) would not be present and the linear system would consist of 9 equations with  $l_a, l_b = \{x, y, z\}$ .

The poles of  $G_2$  which correspond to bound states are located at the roots of equation:

$$0 = \det \left( 2\mathcal{I} + \begin{bmatrix} 0 & 0 & 0 & 0 \\ \Gamma(x, 0) & 0 & 0 & 0 \\ \Gamma(y, 0) & 0 & 0 & 0 \\ \Gamma(z, 0) & 0 & 0 & 0 \end{bmatrix} + \begin{bmatrix} 0 & K_2(0, x) & K_2(0, y) & K_2(0, z) \\ 0 & K_2(x, x) & K_2(x, y) & K_2(x, z) \\ 0 & K_2(y, x) & K_2(y, y) & K_2(y, z) \\ 0 & K_2(z, x) & K_2(z, y) & K_2(z, z) \end{bmatrix} \cdot \begin{bmatrix} 0 & 0 & 0 & 0 \\ 0 & \rho_x & 0 & 0 \\ 0 & 0 & \rho_y & 0 \\ 0 & 0 & 0 & \rho_z \end{bmatrix} \right) \quad (\text{A.0.35})$$

where  $\rho_m = J_m/D$ . In the thermodynamic limit, the summations in Eq.(A.0.25) may be replaced by integrations,

$$\frac{1}{N} \sum_{\mathbf{k} \in G} \rightarrow \frac{1}{(2\pi)^3} \int_{-\pi}^{\pi} d\mathbf{k}, \quad (\text{A.0.36})$$

and functions  $K_2$  and  $\Gamma$  are written as integrals in the  $k$ -space as:

$$\begin{aligned} K_2(l, p) &= \frac{1}{\pi^3} \int_{-\pi}^{\pi} d\mathbf{k} \frac{\cos k_l (\cos k_p - a_p)}{-t + \sum_m \rho_m a_m \cos k_m} \\ \Gamma(l, p) &= \frac{1}{\pi^3} \int_{-\pi}^{\pi} d\mathbf{k} \frac{\cos k_l \cos k_p}{-t + \sum_m \rho_m a_m \cos k_m} \end{aligned} \quad (\text{A.0.37})$$

where

$$t = \frac{1}{4D} (z + 2D - 2g\mu_B H + 4(J_x + J_y + J_z)), \quad \text{and} \quad a_m = \cos(K_m/2) \quad (\text{A.0.38})$$

As functions of the variable  $t$ ,  $K_2$  and  $\Gamma$  have a cut along the real axis  $-\sum_m \rho_m a_m \leq t \leq \sum_m \rho_m a_m$ . This cut corresponds to two-magnon scattering states. Any bound state must lie therefore on the real  $t$  axis for  $t \geq |\sum_m \rho_m a_m|$ . If  $t_B(\mathbf{K})$  is a solution of Eq.(A.0.35) in this region for given  $\mathbf{K}$ , then

$$E(\mathbf{K}) = 2g\mu_B H - 2D + 4D(t_B(\mathbf{K}) - \rho_x - \rho_y - \rho_z) \quad (\text{A.0.39})$$

is the energy of a two-particle bound state. The calculation requires to evaluate integrals (A.0.37) for  $t \geq |\sum_m \rho_m a_m|$ , look for solutions  $t_B$  of the bound states condition (A.0.35) and use Eq.(A.0.39) to compute the corresponding energy eigenvalues. The principle difficulty of this calculation lies in the evaluation of the three-dimensional integrals (A.0.37), for which an analytical form is not available. To remedy this situation, we perform a series expansion of the integrand in terms of  $J_m/D$  prior the integration, and we are in position to derive analytical expressions for the energy of the two-magnons bound state up to third order in  $J_m/D$ . Alternatively we could resort to a numerical

calculation of (A.0.37). Starting from the bound-state condition (A.0.35) the final formula for  $t_B(\mathbf{K})$  is:

$$t_B(\mathbf{K}) = \frac{1}{2} + \frac{a_x^2}{2}\rho_x^2 + \frac{a_x^2}{4}\rho_x^3 + \frac{a_y^2}{2}\rho_y^2 + \frac{a_y^2}{4}\rho_y^3 + \frac{a_z^2}{2}\rho_z^2 + \frac{a_z^2}{4}\rho_z^3, \quad (\text{A.0.40})$$

and

$$E(\mathbf{K}) = 2g\mu_B H + \sum_{m=\{x,y,z\}} \left[ -4J_m + \cos^2(K_m/2) \left( \frac{2J_m^2}{D} + \frac{J_m^3}{D^2} \right) \right]. \quad (\text{A.0.41})$$

Eq.(A.0.41) is the three-dimensional generalization of Eq.(1.2.41) and corresponds to the single ion bound state. The solution  $t_B(\mathbf{K})$  is not unique; if one was interested in finding the 3D generalization of the exchange bound state, he should search for a different solution  $t'_B(\mathbf{K})$  of Eq.(A.0.35), with  $t_B(\mathbf{K}) > t'_B(\mathbf{K}) \geq |\sum_m \rho_m a_m|$ .

## Appendix B

# Analytical Techniques

### B.1 ESR spectrum for the $S=1/2$ XXZ chain using the Bethe ansatz technique

In this section we briefly review all elements necessary for the calculation of the zero-temperature low-lying ESR spectrum of the  $S = 1/2$  XXZ model presented in Section 2.4. A rigorous solution can be obtained using the Bethe ansatz, where the relevant to the ESR intensity matrix elements are calculated exactly. The total magnetization commutes with the Hamiltonian of Eq.(4.3.1) and the Hilbert space separates into subspaces of fixed magnetization, determined from the number of reversed spins  $M$ . Eigenstates are completely characterized by a set of rapidities  $\{\lambda_j\}$ ,  $j = 1, \dots, M$ , solutions to the Bethe ansatz equations [70, 71]:

$$\left[ \frac{\sinh(\lambda_j + i\gamma/2)}{\sinh(\lambda_j - i\gamma/2)} \right]^N = \prod_{k \neq j}^M \frac{\sinh(\lambda_j - \lambda_k + i\gamma)}{\sinh(\lambda_j - \lambda_k - i\gamma)}, \quad j = 1, \dots, M, \quad (\text{B.1.1})$$

where  $n$  is the number of spins and  $\Delta = \cos(\gamma)$ . Note that we only consider the case where  $-1 < \Delta \leq 1$ . The logarithmic version of the Bethe ansatz equations is:

$$\tan^{-1} \left[ \frac{\tanh(\lambda_j)}{\tan(\gamma/2)} \right] - \frac{1}{N} \sum_{k=1}^M \tan^{-1} \left[ \frac{\tanh(\lambda_j - \lambda_k)}{\tan(\gamma)} \right] = \pi \frac{I_j}{N}. \quad (\text{B.1.2})$$

Each choice of a set  $\{I_j\}$  uniquely satisfies a set of rapidities and an eigenstate with energy  $E$  and momentum  $q$ :

$$\begin{aligned} E &= J \sum_{j=1}^M \frac{-\sin^2 \gamma}{\cosh 2\lambda_j - \cos \gamma} + H \left( \frac{N}{2} - M \right), \\ q &= \pi M + \frac{2\pi}{N} \sum_{j=1}^M I_j \quad \text{mod } 2\pi. \end{aligned} \quad (\text{B.1.3})$$

The ground state  $|\Omega\rangle$  is given by  $I_j = -(M+1)/2 + j$ ,  $j = 1, \dots, M$ , and all excited states are obtained from a different set of  $\{I_j\}$ .

The intensity of the ESR spectrum per site is defined up to an overall multiplicative constant by  $I \sim \omega \chi''(\omega)/N$ , where the imaginary part of the susceptibility is (see Section 2.1):

$$\chi''(\omega) = \frac{\pi}{Z} \sum_{a,b} (e^{-\beta E_b} - e^{-\beta E_a}) |\langle a | \mu_x | b \rangle|^2 \delta(E_a - E_b - \hbar\omega). \quad (\text{B.1.4})$$

Here sums extend over all eigenstates  $|a\rangle$  of Hamiltonian of Eq.(4.3.1),  $E_a$  are the corresponding eigenvalues,  $\beta = 1/T$  is the inverse temperature, and  $Z = \sum_a e^{-\beta E_a}$  is the total partition function. The matrix elements involve the total spin operator in the x-direction  $\mu_x = \sum_n S_n^x$ . Using the fact that  $S^x = (S^+ + S^-)/2$  and that the spin operators can be Fourier-transformed as

$$S_q^\alpha = \frac{1}{\sqrt{N}} \sum_{n=1}^n e^{iqn} S_n^\alpha, \quad (\text{B.1.5})$$

the calculation of  $\chi''(\omega)$  boils down to the evaluation of the  $|\langle a | S_q^- | b \rangle|^2$  matrix elements. For two eigenstates  $a, b$  with  $M$  and  $M-1$  reversed spins correspondingly, characterized by two sets of rapidities  $a\{\mu\}$  and  $b\{\lambda\}$ , the Bethe ansatz predicts that [91, 92, 242]:

$$\begin{aligned} |\langle \{\mu\} | S_q^- | \{\lambda\} \rangle|^2 &= N \delta_{q, q\{\lambda\} - q\{\mu\}} |\sin\gamma| \frac{\prod_{j=1}^M |\sinh(\mu_j - i\gamma/2)|^2}{\prod_{j=1}^{M-1} |\sinh(\lambda_j - i\gamma/2)|^2} \\ &\times \prod_{j>k=1}^M |\sinh(\mu_j - \mu_k) + \sin^2\gamma|^{-1} \prod_{j>k=1}^{M-1} |\sinh(\lambda_j - \lambda_k) + \sin^2\gamma|^{-1} \\ &\times \frac{|\det \mathbf{H}^{-1}(\{\mu\}, \{\lambda\})|^2}{|\det \Phi(\{\mu\}) \det \Phi(\{\lambda\})|} \end{aligned} \quad (\text{B.1.6})$$

The matrix  $H^{-1}$  is defined as:

$$\begin{aligned} \mathbf{H}_{a,b}^{-1}(\{\mu\}, \{\lambda\}) &= \frac{1}{\sinh(\mu_a - \lambda_b)} \left[ \prod_{j \neq a}^M \sinh(\mu_j - \lambda_b - i\gamma) - \left[ \frac{\sinh(\lambda_b + i\gamma/2)}{\sinh(\lambda_b - i\gamma/2)} \right]^N \right. \\ &\times \left. \prod_{j \neq a}^M \sinh(\mu_j - \lambda_b + i\gamma) \right], \quad b < M, \\ \mathbf{H}_{a,M}^{-1}(\{\mu\}, \{\lambda\}) &= \frac{1}{\sinh^2 \mu_a + \sin^2 \gamma/2}, \end{aligned} \quad (\text{B.1.7})$$

and

$$\begin{aligned} \Phi(\{\lambda\}) &= \delta_{ab} \left[ N \frac{\sin\gamma}{\sinh^2\lambda_a + \sin^2\gamma/2} - \sum_{k \neq a} \frac{\sin 2\gamma}{\sinh^2(\lambda_a - \lambda_k) + \sin^2\gamma} \right] \\ &+ (1 - \delta_{ab}) \frac{\sin 2\gamma}{\sinh^2(\lambda_a - \lambda_b) + \sin^2\gamma}. \end{aligned} \quad (\text{B.1.8})$$

At zero temperature only contributions between the ground state  $|\Omega\rangle$  and the lowest excited states are expected to contribute significantly, while other allowed transitions acquire vanishing intensity. The calculation of the  $T = 0$  ESR spectrum reduces to the calculation of the  $|\langle m|\mu_x|\Omega\rangle|^2$ , where  $|m\rangle$  is a low-lying excited state. Within the Bethe ansatz and for  $\gamma = \pi/\nu$  the excited states are usually searched for in the form of strings of order  $n_j = j$ ,  $j = 1, \dots, \nu - 1$  and parity  $u_j = +1$ :

$$\lambda_{a,+}^{n,k} = \lambda_a^n + (n+1-2k)i + \mathcal{O}(e^{-\delta N}), \quad (\text{B.1.9})$$

and strings of order  $n_\nu = 1$  and parity  $u_\nu = -1$  of the form:

$$\lambda_{a,-} = \lambda_a + i\nu + \mathcal{O}(e^{-\delta N}). \quad (\text{B.1.10})$$

These states have imaginary parts symmetrically arranged around the real axis. In a string configuration the parameter  $e^{-\delta N}$  is exponentially suppressed with the system size. Nevertheless, it is found [90] that there is essentially one excited state  $|m^*\rangle$  that has significant weight in the spectrum. This state is highly unusual in the Bethe ansatz literature and deviates from the string hypothesis; this state has all the  $\lambda$ 's real except one that is complex with an imaginary part  $i\pi/2$ . The existence of this state was recently discussed [93] and it physically corresponds to a uniform change of the  $S^z$  component of the magnetization by 1.

From a computational point of view, it turns out to be rather difficult to find the pseudomomenta  $\lambda$  for this state. The nonlinear Bethe ansatz equations at finite magnetization, in general, do not converge by iteration. To circumvent this problem, it was suggested [94] to study chains with an odd number  $N$  of spins, where indeed the problem is far less crucial [92]. We should emphasize that the calculation in this thesis and in [90] was made for the particular choice of  $\Delta = 1/2$ . Apart from the dominant contribution of  $|m^*\rangle$ , the Bethe ansatz calculation revealed that the ESR spectrum consists of secondary transitions with small, but non vanishing intensity. The appearance of secondary peaks strongly depends on the choice of parameter  $\Delta$ . This is further discussed in Section 2.4.

## B.2 Spin Drude weight for the $S=1/2$ XXZ chain using the Bethe ansatz technique

The main issue addressed in this section is the calculation of the spin Drude weight  $D_s$  for the  $S = 1/2$  XXZ chain in the presence of magnetic field. The calculation relies on the generalization of the approach proposed in [141], where procedure is based on evaluating the finite size corrections of the energy eigenvalues obtained by the Bethe ansatz method. The analysis starts by noting that  $D_s$  is the prefactor of the low-frequency imaginary part of the conductivity [194]:

$$D_s = \frac{1}{2} [\omega \sigma''(\omega)]_{\omega \rightarrow 0} = \frac{1}{N} \left( \frac{1}{2} \langle -T \rangle - \sum_n p_n \sum_{m \neq n} \frac{|\langle n | \mathcal{J}_s | m \rangle|^2}{\epsilon_m - \epsilon_n} \right), \quad (\text{B.2.1})$$

where  $\langle T \rangle$  denotes the thermal expectation value of the kinetic energy. An equivalent convenient expression for the spin Drude weight has been derived [135, 175], where  $D_s$  equals the thermal average of curvatures of energy levels in a Hamiltonian subject to a fictitious flux coupled to the hopping or spin-flipping term. More specifically, the Hamiltonian (4.3.1) in the presence of a fictitious flux  $\phi$  has the form:

$$\mathcal{H} = \sum_{n=1}^N \left( J \left( \frac{1}{2} e^{i\phi} \sigma_n^+ \sigma_{n+1}^- + \frac{1}{2} e^{-i\phi} \sigma_n^- \sigma_{n+1}^+ + \Delta S_n^z S_{n+1}^z \right) + H S_n^z \right) \quad (\text{B.2.2})$$

We can evaluate using second order perturbation theory the shift of the energy level:

$$E_n(\phi) = \langle n | \mathcal{H}(\phi = 0) | n \rangle - \phi \langle n | \mathcal{J}_s | n \rangle - \phi^2 \sum_{m \neq n} \frac{|\langle n | \mathcal{J}_s | m \rangle|^2}{\epsilon_m - \epsilon_n} - \phi^2 \langle n | T | n \rangle. \quad (\text{B.2.3})$$

By taking the second derivative with respect to  $\phi$  we arrive at the following expression:

$$D_s = \frac{1}{N} \sum_n p_n \frac{1}{2} \frac{\partial^2 E_n(\phi)}{\partial \phi^2}. \quad (\text{B.2.4})$$

The aim is to calculate the second derivative of the eigenvalues  $\epsilon_n$  with respect to  $\phi$ , where  $\epsilon_n$  are generated using the Bethe ansatz technique. Within this formalism, eigenstates are completely characterized by a set of rapidities  $\lambda_j$  solutions to the Bethe ansatz equations (see section B.1). The Bethe ansatz relations are generalized in the presence of the flux  $\phi$  and they are given in great detail in Ref. [141]. This construction is based on the string assumption for the excitations given in Eqs.(B.1.9)–(B.1.10). Following Ref. [197], the finite size corrections for a system of size  $N$  are calculated by introducing the functions  $g_{1j}$ ,  $g_{2j}$ :

$$\lambda_N^j = \lambda_\infty^j + \frac{g_{1j}}{N} + \frac{g_{2j}}{N^2}, \quad (\text{B.2.5})$$

where  $\lambda_N$  ( $\lambda_\infty$ ) are the rapidities for a system of size  $N(\infty)$ . The Bethe ansatz relations are expanded to orders of  $1/N$  and in the thermodynamic limit the densities of excitations  $\rho_j$  and hole densities  $\rho_j^h$  are introduced. We therefore arrive at a set of integral equations, whose solutions provide the  $\rho_j$  and  $\rho_j^h$  densities. The main objective of this section is to outline the main steps of the calculation of  $D_s$ . Detailed analysis and explicit formulas can be found in Ref. [141]. The final expression for the Drude weight is:

$$D_s = \frac{1}{2} \sum_j \int_{-\infty}^{\infty} d\lambda \left[ (\rho_j + \rho_j^h) \frac{\partial g_{1j}}{\partial \phi} \right]^2 \frac{d}{d\lambda} \left( \frac{-1}{1 + e^{\beta \epsilon_j}} \right) \left( \frac{1}{\rho_j + \rho_j^h} \frac{d\epsilon_j}{d\lambda} \right), \quad (\text{B.2.6})$$

where  $\epsilon_j = \frac{1}{\beta} \ln \left( \frac{\rho_j^h}{\rho_j} \right)$  is the temperature dependent effective dispersion.

### B.3 Quantum Transfer Matrix Approach (QTM)

This section is devoted in introducing an analytical method used for the calculation of dynamic correlation functions pertinent to the study of thermal transport, known as the Quantum Transfer Matrix approach. The main objective is to described the technique used to calculate the correlation functions  $\langle \mathcal{J}_E^2 \rangle$  and  $\langle \mathcal{J}_E \mathcal{J}_s \rangle$  of the  $S = 1/2$  *XXZ* chain. The discussion here follows the lines of Refs. [173, 219].

Let us begin by considering a one dimensional lattice with  $L$  sites and periodic boundary conditions. A  $q$ -state variable  $\alpha_i$  is assigned to each site  $i$  and  $\alpha$  has its own statistics number  $\epsilon_\alpha = (-1)^{\xi_\alpha} = \pm 1$ . A spin with  $\epsilon_\alpha = 1$  is called bosonic and a spin with  $\epsilon_\alpha = -1$  is called fermionic. We introduce the Hamiltonian of the permutation model as:

$$\mathcal{H} = \sum_{i=1}^L P_{i,i+1}, \quad (\text{B.3.1})$$

where  $P_{i,i+t}$  is the permutation operator that acts like:

$$P_{i,i+1} |\alpha_1, \alpha_2, \dots, \alpha_i, \alpha_{i+1}, \dots, \alpha_L\rangle = (-1)^{\xi_{\alpha_i \alpha_{i+1}}} |\alpha_1, \alpha_2, \dots, \alpha_{i+1}, \alpha_i, \dots, \alpha_L\rangle, \quad (\text{B.3.2})$$

where  $\xi_{\alpha_i \alpha_{i+1}}$  is one if both  $\alpha_i$  and  $\alpha_{i+1}$  are fermionic and 0 otherwise.

The  $S = 1/2$  Heisenberg chain

$$\mathcal{H} = 2 \sum_{i=1}^L \mathbf{S}_i \cdot \mathbf{S}_{i+1} + L/2, \quad (\text{B.3.3})$$

is of type (B.3.1) with  $q = 2$  and  $\epsilon_1 = \epsilon_2 = +1$ .

A classical counterpart is defined on a two dimensional square lattice of  $L \times N$  sites, where we impose periodic boundary conditions and Boltzmann weights  $R_{\beta\nu}^{\alpha\mu}$  are

associated with local vertex configurations  $\alpha$ ,  $\beta$ ,  $\mu$ ,  $\nu$ . The classical counterpart to (B.3.1) is the Perk–Schultz model [220] with Boltzmann weights:

$$R_{\beta\nu}^{\alpha\mu} = \delta_{\alpha\nu}\delta_{\beta\mu} + (u - v)(-1)^{\xi_\alpha\xi_\mu}\delta_{\alpha\beta}\delta_{\mu\nu}, \quad (\text{B.3.4})$$

where  $u$  and  $v$  are parameters assigned to the entire horizontal and vertical lines intersecting in the particular vertex under consideration. These weights satisfy the Yang–Baxter equations (YBE). The total Boltzmann weight of some fixed lattice configuration is given by the product of all local Boltzmann weights, and the partition function of the model is the sum of the Boltzmann weights over all possible lattice configurations.

The transfer matrices of the classical model are defined as:

$$T_\nu^\mu(u) = \sum_{\{\alpha\}} \prod_{i=1}^L R_{\alpha_{i+1}\nu_i}^{\alpha_i\mu_i}(u, v_i). \quad (\text{B.3.5})$$

The object  $T(u)$  represents a family of commuting matrices,  $T(u)T(w) = T(w)T(u)$ . Row-to-row transfer matrix corresponds to the case of vanishing spectral parameters  $v_i = 0$  and the following limiting case is of special importance:

$$T(0) = e^{iP}, \quad \mathcal{H} = \frac{d}{du} \ln T(u)|_{u=0}. \quad (\text{B.3.6})$$

Therefore, the Hamiltonian is a member of a family of infinitely many commuting operators and conserved quantities; any element of the family commutes with  $\mathcal{H}$ . This is the typical proof of integrability for the case of isotropic  $SU(m, n)$ -symmetric systems, based on classical models satisfying the YBE. All conserved quantities can be generated from  $\ln T(u)$  as:

$$\mathcal{J}^{(n)} = \left( \frac{\partial}{\partial u} \right)^n \ln T(u)|_{u=0}, \quad (\text{B.3.7})$$

For the  $XXZ$  model with  $\Delta = \cos(\gamma)$  the first three conserved currents ( $n = 0, 1, 2$ ) are related to the momentum operator, the Hamiltonian and the thermal current via

$$\begin{aligned} P &= -i\mathcal{J}^{(0)}, \\ \mathcal{H} &= 2\frac{\sin\gamma}{\gamma}\mathcal{J}^{(1)} - \frac{L\Delta}{2}, \\ \mathcal{J}_E &= i\left(2\frac{\sin\gamma}{\gamma}\right)^2\mathcal{J}^{(2)} + iL. \end{aligned} \quad (\text{B.3.8})$$

The central idea of the quantum matrix approach is a lattice path–integral formulation of the partition function of the Hamiltonian and the definition of a suitable transfer matrix [224–226]. If we define a new set of vertex weights  $\bar{R}$  by rotating  $R$  by 90 degrees and introduce the transfer matrix  $\bar{T}(u)$  as a product of  $\bar{R}(-u, 0)$ , the partition function

of the quantum chain of length  $L$  at finite  $T$  reads:

$$Z_L = \text{Tr}[e^{-\beta H}] = \lim_{N \rightarrow \infty} Z_{L,N} \quad (\text{B.3.9})$$

where  $Z_{L,N}$  is defined by:

$$Z_{N,L} = \text{Tr}[T(-\tau)\bar{T}(-\tau)]^{N/2}, \quad \tau = \frac{\beta}{N}. \quad (\text{B.3.10})$$

This is the partition function of a staggered vertex model with alternating rows corresponding to the transfer matrices  $\bar{T}(-\tau)$  and  $T(-\tau)$  (see Fig. B.3.1). The evaluation of the partition function of this classical model can be done by choosing a different transfer direction along the chain, with a corresponding transfer matrix  $T^{QTM}$  which is defined for the columns of the lattice (see Fig. B.3.1). The partition function of the quantum chain at temperature  $1/\beta$  is given by:

$$Z_{L,N} = \text{Tr}(T^{QTM})^L \quad (\text{B.3.11})$$

We will refer to  $T^{QTM}$  as the “quantum transfer matrix” of the quantum spin chain, because it is the closest analogue to the transfer matrix of a classical spin chain. Due to this analogy the free energy  $f$  per lattice site is given just by the largest eigenvalue  $\Lambda_{max}$ :

$$f = -k_B T \lim_{N \rightarrow \infty} \log \Lambda_{max}. \quad (\text{B.3.12})$$

provided that  $\Lambda_{max}$  is positive, non-degenerate and greater than the absolute value of

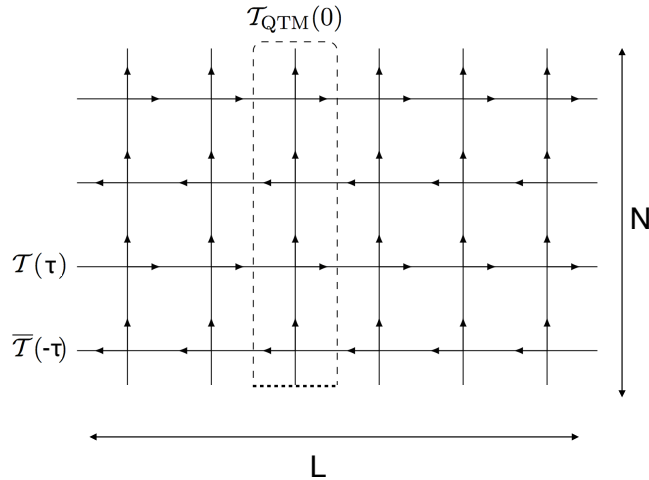


**Figure B.3.1:** Illustration of the Perk–Schultz model. The square lattice has width  $L$  equal to the chain length and height  $N$  equal to the Trotter number. Alternating rows correspond to transfer matrices  $T(\tau)$  and  $\bar{T}(-\tau)$  and the dashed box corresponds to the column-to-column quantum transfer matrix  $T^{QTM}$ . The arrows indicate the type of local Boltzmann weights that are either  $R$  or  $\bar{R}$ .

any other eigenvalue [227]. In Eq.(B.3.12) we have implicitly employed the interchangeability of the two limits ( $L, N \rightarrow \infty$ ) and the existence of a gap between the largest and the next-largest eigenvalues of  $T^{QTM}$  for finite temperatures. The next-leading eigenvalues give the exponential correlation lengths  $\xi$  of the equal time correlators at finite temperature:

$$\frac{1}{\xi} = \lim_{N \rightarrow \infty} \ln \left[ \frac{\Lambda_{max}}{\Lambda} \right]. \quad (\text{B.3.13})$$

In the presence of an external magnetic field  $H$  partition function is changed trivially:

$$Z_{N,L} = \text{Tr}[T(-\tau)\bar{T}(-\tau)^{N/2} e^{\beta HS}]. \quad (\text{B.3.14})$$

The classical counterpart of the XXZ model is the six-vertex model. For  $\Delta = \cos(\gamma)$ , the relation of the Hamiltonian and the row-to-row transfer matrix is:

$$\mathcal{H} = 2 \frac{\sin \gamma}{\gamma} \frac{d}{du} \ln T(u)|_{u=0}. \quad (\text{B.3.15})$$

The TBA and the QTM are not at all independent. An approach based on the ‘‘fusion hierarchy’’ leads to a set of infinitely many NLIEs that are identical to the TBA equations though completely different reasoning has been applied.

Our aim is to diagonalize the row-to-row transfer matrix and the QTM by means of the algebraic Bethe ansatz. By use of the YBE, algebraic expressions of the eigenstates and explicit expressions of the eigenvalues are derived. It turns out that the row-to-row transfer matrix and the QTM can be treated in parallel. The large number of coupled Bethe ansatz equations is transformed into a simple finite set of non-linear integral equations, and the numerical study of these equations enable us to derive explicit results for the specific heat and susceptibility. For more details we refer the reader to [219, 230].

The expectation values of conserved quantities related to thermal transport may be calculated by use of an extended Hamiltonian [173]:

$$\tilde{\mathcal{H}} = \lambda_0 \mathcal{H}_0 + H \mathcal{M} + \lambda_1 \mathcal{J}_E, \quad \mathcal{M} = \sum_n S_n^z \quad (\text{B.3.16})$$

where  $H_0$  is the  $S = 1/2$  XXZ Hamiltonian (4.3.1) without the Zeeman term. The parameters  $\lambda_0, \lambda_1$  will be set to 0 and 1 correspondingly after taking the necessary derivatives. We also introduce the partition function

$$Z = \text{Tr}[e^{-\beta \tilde{\mathcal{H}}}], \quad (\text{B.3.17})$$

from which we find the expectation value by derivatives with respect to  $\lambda_1$  at  $\lambda_1 = 0$ :

$$\langle \mathcal{J}_E^2 \rangle = \frac{1}{\beta^2 L} \left( \frac{\partial}{\partial \lambda_1} \right)^2 \ln Z|_{\lambda_1=0}, \quad (\text{B.3.18})$$

In the formalism of the QTM,  $Z$  can be expressed as the largest eigenvalue of the QTM  $\Lambda(\lambda_0, \lambda_1)$ ,

$$\lim_{L \rightarrow \infty} \frac{1}{L} \ln Z = \ln \Lambda(\lambda_0, \lambda_1), \quad (\text{B.3.19})$$

where

$$\ln \Lambda(\lambda_0, \lambda_1) = -\frac{\beta H}{2} + \oint_C \alpha_1(x+1) \ln(1 + 1/\eta(x+1)) dx, \quad \alpha_n = \frac{\gamma \sin n\gamma}{2\pi(\cosh(\gamma x) - \cos(n\gamma))}. \quad (\text{B.3.20})$$

The contour  $C$  encloses the real axis, and the unknown function  $\eta(x)$  is determined by the following non-linear integral equation:

$$\ln \eta(x) = \beta(\lambda_0 + \lambda_1 A \partial_x) \epsilon(x) - \beta H + \oint_C \alpha_2(x-y-i) \ln(1 + \eta^{-1}(y+i)) dy, \quad (\text{B.3.21})$$

where  $\epsilon(x) = -2\pi A \alpha_1(x)$  and  $A = J \sin(\gamma)/\gamma$ . Consequently we obtain:

$$\langle \mathcal{J}_E^2 \rangle = \frac{1}{\beta^2} \left( \frac{\partial}{\partial \lambda_1} \right)^2 \ln \Lambda(1, \lambda_1)|_{\lambda_1=0}. \quad (\text{B.3.22})$$

For the full description of the thermal transport for finite magnetic fields, the quantity  $\langle \mathcal{J}_E \mathcal{J}_s \rangle$  is also necessary. The spin current is not a constant of motion and the quantity  $\mathcal{J}_E \mathcal{J}_s$  is no longer conserved. The above procedure can only be applied to conserved quantities, thus an alternative is necessary. The following nontrivial identity [228]

$$\langle \mathcal{J}_E \mathcal{J}_s \Delta \mathcal{H}_0 \rangle = \langle \mathcal{J}_E^2 \Delta \mathcal{M} \rangle, \quad (\text{B.3.23})$$

is used, provided that  $\Delta \mathcal{H}_0 = \mathcal{H}_0 - \langle \mathcal{H}_0 \rangle$  and  $\Delta \mathcal{M} = \mathcal{M} - \langle \mathcal{M} \rangle$ . Using this identity and some algebra we arrive at:

$$\langle \mathcal{J}_E \mathcal{J}_s \rangle = \frac{1}{2\pi A \beta^2} \oint_C \partial_{\lambda_1}^2 \ln(1 + \eta^{-1}(x+i)) dx. \quad (\text{B.3.24})$$

To summarize, the evaluation of  $\langle \mathcal{J}_E^2 \rangle$  and  $\langle \mathcal{J}_E \mathcal{J}_s \rangle$  correlation functions given in Eq.(B.3.22) and Eq.(B.3.24) correspondingly, requires the calculation of the largest eigenvalue of the QTM given in Eq.(B.3.20), where the unknown function  $\eta(x)$  is obtained by solving the nonlinear integral equation (NLIE) of Eq.(B.3.21). An analytical calculation is not possible, so we have to attempt a numerical calculation based on iteration. The rest of this section is dedicated in the numerical treatment of the NLIE (B.3.21).

The fact that the integral of Eq.(B.3.21) is along the complex contour  $C$ , (see Fig. B.3.2) necessitates some care. The outcome of the integration along the line  $C_2$  is exactly opposite than the one along  $C_4$ , providing a certain simplification. Therefore



**Figure B.3.2:** Integration contour  $C$  surrounding the real axis.

the integral should be performed along lines  $C_1$  and  $C_3$ :

$$\begin{aligned} \ln \eta(x) = f(x) &+ \int_{-\infty}^{\infty} \alpha_2(x-y) \ln(1 + \eta^{-1}(y)) dy \\ &- \int_{-\infty}^{\infty} \alpha_2(x-y-2i) \ln(1 + \eta^{-1}(y+2i)) dy, \end{aligned} \quad (\text{B.3.25})$$

provided that  $f(x) = \beta(\lambda_0 + \lambda_1 A \partial_x) \epsilon(x) - \beta H$ . Eq.(B.3.25) is solved numerically by iteration process starting with  $\ln \eta(x) = f(x)$ . For this numerical procedure all involved functions are discretized, ranging from  $-N$  to  $+N$  with a  $dx$  step. Integration from  $-\infty$  to  $\infty$  is replaced by integration from  $-N$  to  $+N$ . Both  $N$  and  $dx$  are sources of systematic error and should be chosen such that if the integrand vanishes for every  $|x| < M$ , then  $M \ll N$ . It is useful to define functions  $F(x)$ ,  $G(x)$  and  $g(x)$  as:

$$F(x) = \ln \eta(x), \quad G(x) = \ln \eta(x+2i), \quad \text{and} \quad g(x) = f(x+2i), \quad (\text{B.3.26})$$

and rewrite Eq.(B.3.25) in the following form:

$$\begin{aligned} F(x) &= f(x) + \int_{-\infty}^{\infty} \alpha_2(x-y) \ln(1 + e^{-F(y)}) dy - \int_{-\infty}^{\infty} \alpha_2(x-y-2i) \ln(1 + e^{-G(y)}) dy \\ G(x) &= g(x) + \int_{-\infty}^{\infty} \alpha_2(x-y+2i) \ln(1 + e^{-F(y)}) dy - \int_{-\infty}^{\infty} \alpha_2(x-y) \ln(1 + e^{-G(y)}) dy \end{aligned} \quad (\text{B.3.27})$$

We have therefore arrived at a set of two nonlinear coupled equations with two unknown functions  $F(x)$  and  $G(x)$  where integrals now are along the real axis. The convolutions at the right-hand sides of the equations are easily evaluated in Fourier

space. The Fourier transform (FT) of a continuous function  $h(x)$  is defined as:

$$\begin{aligned} H(f) &= \int_{-\infty}^{\infty} h(x)e^{2\pi ifx} dx \\ h(x) &= \int_{-\infty}^{\infty} H(f)e^{-2\pi ifx} df. \end{aligned} \quad (\text{B.3.28})$$

The convolution theorem suggests that:

$$\int_{-\infty}^{\infty} \kappa(x-y)h(y)dy = \int_{-\infty}^{\infty} e^{-2\pi ifx} K(f)H(f)df, \quad (\text{B.3.29})$$

where  $K(f)$  and  $H(f)$  are the FT of functions  $\kappa(x)$  and  $h(x)$  correspondingly. Taking into account that the integrands are discrete functions of  $x$ , the discrete version of FT should be introduced. Let us consider a sampled function  $h(x)$  at evenly spaced intervals in  $x$  and let  $dx$  denote the space interval between consecutive samples. The sequence of  $\mathcal{N}$  complex numbers  $h_0, h_1, \dots, h_{\mathcal{N}-1}$  is transformed into an  $\mathcal{N}$ -periodic sequence of complex numbers:

$$H_n = \sum_{k=0}^{\mathcal{N}-1} h_k e^{2\pi i kn/\mathcal{N}}, k \in Z. \quad (\text{B.3.30})$$

The relation between the discrete FT of a set of numbers  $H_k$  and their continuous FT when they are viewed as samples of a continuous function  $h(x)$  sampled at an interval  $dx$  can be expressed as  $H(f_n) = dxH_n$ , where  $f_n = \frac{n}{\mathcal{N}dx}$  and  $n = -\mathcal{N}/2, \dots, \mathcal{N}/2$ .

The necessary Fourier transformations of the integrands appearing in Eq.(B.3.25) can be calculated with the use of the Fast Fourier algorithm (FFT). The efficiency of this method relies on the fact that while the discrete FT is an  $\mathcal{O}(\mathcal{N}^2)$  process, the FFT needs  $\mathcal{O}(\mathcal{N}\log_2\mathcal{N})$  operations [229]. One last comment concerning the evaluation of the  $\langle \mathcal{J}_E \mathcal{J}_s \rangle$  correlation function. From Eq.(B.3.24) we notice that a second derivative with respect to  $\lambda_1$  is necessary. In order to avoid numerical derivatives, equivalent equations for the  $\partial_{\lambda_1}^2 F(x)$  and  $\partial_{\lambda_1}^2 G(x)$  can be derived and solved using the same procedure.

## B.4 Bosonization of the S=1/2 chain: Calculation of the Spin Drude weight at zero temperature

In this section we develop the necessary formalism for the calculation of the spin Drude weight  $D_s$  at finite magnetic field and zero temperature within the formalism of the Luttinger Liquid. The outcome of the bosonization of the XXZ chain in the gapless regime at zero field is the following effective model [183, 236–238]:

$$\begin{aligned}
 \mathcal{H} &= \mathcal{H}_0 + \mathcal{H}_u + \mathcal{H}_{bc}, \\
 \mathcal{H}_0 &= \frac{u}{2} \int dx [\Pi^2 + (\partial_x \phi)^2], \\
 \mathcal{H}_u &= \lambda \int dx \cos(\sqrt{8\pi K} \phi), \\
 \mathcal{H}_{bc} &= -2\pi u \lambda_+ \int dx (\partial_x \phi_R)^2 (\partial_x \phi_L)^2 - 2\pi u \lambda_- \int dx [(\partial_x \phi_R)^4 + (\partial_x \phi_L)^4] \tag{B.4.1}
 \end{aligned}$$

where  $\mathcal{H}_0$  is the standard Luttinger model and  $\mathcal{H}_u$  and  $\mathcal{H}_{bc}$  are the leading irrelevant perturbations due to umklapp scattering and band curvature respectively. The bosonic field  $\phi = \phi_R + \phi_L$  and its conjugate momentum  $\Pi$  obey the canonical commutation relation  $[\phi(x), \Pi(x')] = i\delta(x - x')$ . The Fermi velocity  $u$  and the so-called Luttinger parameter  $K$  depend on both the magnetic field and the anisotropy parameter  $\Delta$ . These two parameters determine completely the low energy dynamics of the lattice model and they can be computed from the Bethe ansatz solution. For zero magnetic field, both  $K$  and  $u$  can be computed in a closed form:

$$K(\Delta) = \frac{\pi}{2(\pi - \frac{\pi}{\nu})}, \quad u(\Delta) = \frac{\pi \sin(\pi/\nu)}{2\pi/\nu}. \tag{B.4.2}$$

where the anisotropy parameter has been parametrized as  $\Delta = \cos(\pi/\nu)$ . In this notation,  $K = 1$  corresponds to the free fermion point ( $\Delta = 0$ ) and  $K = 1/2$  at the isotropic point ( $\Delta = 1$ ). The amplitudes  $\lambda_{+,-}$  are known exactly [183, 238]. The parameters  $K$  and  $u$  at finite magnetic fields can be obtained by solving integral equations in the following way. The eigenfunctions of the  $S = 1/2$   $XXZ$  Hamiltonian are constructed by means of the Bethe ansatz. They correspond to several "particles" with spectral parameters  $\lambda_j$ . The bare energy and bare momentum of each particles are  $p_0(\lambda_j)$  and  $\epsilon_0(\lambda_j)$  where [71, 239]

$$\begin{aligned}
 p_0(\lambda) &= i \ln \frac{\cosh(\lambda - i\gamma/2)}{\cosh(\lambda + i\gamma/2)}, \\
 \epsilon_0(\lambda) &= H - \frac{2\sin^2(\gamma)}{\cosh(\lambda) - \cos(\gamma)}, \tag{B.4.3}
 \end{aligned}$$

provided that  $\gamma = \pi/\nu$ . The sum of the bare energies of particles will result the eigenvalue of the Hamiltonian. For the gapless regime and for  $0 < H < H_{cr}$ , the ground state is constructed by filling the Dirac sea with elementary particles having negative energies. The distribution function of these particles in spectral parameters

$\rho(\lambda) = N^{-1}(\lambda_{j+1} - \lambda_j)^{-1}$  satisfies the following equation:

$$\begin{aligned}\rho(\lambda) &= p'_0(\lambda)/(2\pi) - \frac{1}{2\pi} \int_{-\Lambda}^{\Lambda} \mathcal{K}(\lambda, \mu) \rho(\mu) d\mu, \\ \mathcal{K}(\lambda, \mu) &= \frac{\sin 2\gamma}{\cosh(\lambda - \mu) - \cos(2\gamma)}.\end{aligned}\tag{B.4.4}$$

The dressed energy of the corresponding particles satisfies the integral equation:

$$\epsilon(\lambda) = \epsilon_0(\lambda) - \frac{1}{2\pi} \int_{-\Lambda}^{\Lambda} \mathcal{K}(\lambda, \mu) \epsilon(\mu) d\mu.\tag{B.4.5}$$

Parameter  $\Lambda$  is the spectral parameter value at the Fermi surface determined by the requirement  $\epsilon(\Lambda) = 0$ . The dressed momentum is:

$$p(\lambda) = p_0(\lambda) - \int_{-\Lambda}^{\Lambda} p'_0(\mu) F(\mu, \lambda) d\mu,\tag{B.4.6}$$

where the structure function  $F$  obeys the equation:

$$\begin{aligned}F(\lambda, \mu) &= \frac{1}{2\pi} \Phi(\lambda - \mu) + \frac{1}{2\pi} \int_{-\Lambda}^{\Lambda} \mathcal{K}(\lambda, \nu) F(\nu, \mu) d\nu, \\ \Phi(\lambda) &= i \ln \left[ \frac{\sinh(\lambda + i\gamma)}{\sinh(\lambda - i\gamma)} \right].\end{aligned}\tag{B.4.7}$$

The Fermi velocity  $u(\Delta, H)$ , the group velocity of particles at the Fermi surface, is:

$$u(\Delta, H) = \frac{\partial \epsilon}{\partial p} \Big|_{\lambda=\Lambda} = \frac{\partial \epsilon}{\partial \lambda} \frac{\partial \lambda}{\partial p} \Big|_{\lambda=\Lambda} = \frac{\frac{\partial \epsilon}{\partial \lambda} \Big|_{\lambda=\Lambda}}{2\pi \rho(\lambda) \Big|_{\lambda=\Lambda}},\tag{B.4.8}$$

because  $p'(\lambda) = 2\pi \rho(\lambda)$ . Finally, the dressed charge function  $Z(\lambda)$  is given by:

$$Z(\lambda) = 1 - \frac{1}{2\pi} \int_{-\Lambda}^{\Lambda} K(\lambda, \mu) Z(\mu) d\mu.\tag{B.4.9}$$

The Luttinger parameter  $K$  is equal to  $K = Z(\Lambda)$  [240]. The exact zero Drude weight  $D_s$  at  $T = 0$  is evaluated by [194]:

$$D_s = \frac{1}{\pi} K(\Delta, H) u(\Delta, H).\tag{B.4.10}$$

In general, the parameter  $\Lambda$  is adjusted numerically by first solving Eq. (B.4.5) and then checking if the requirement  $\epsilon(\Lambda) = 0$  is satisfied. Once  $\Lambda$  is determined iteratively, the integral equations (B.4.4) and (B.4.9) are solved by an iteration process to yield functions  $\rho(\lambda)$  and  $Z(\lambda)$ . To avoid numerical differentiation, one can derive a similar nonlinear equations for the quantity  $\epsilon'(\lambda)$  instead of solving Eq.(B.4.5) and then differentiate.

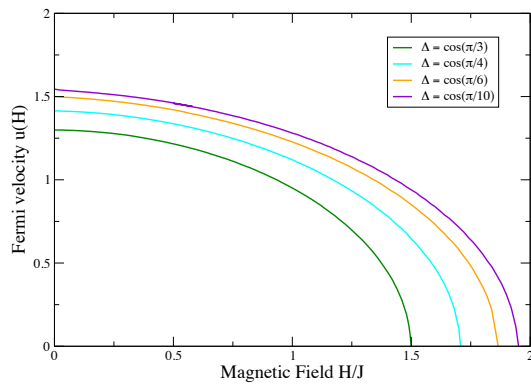


**Figure B.4.1:** Fermi velocity  $u(H)$  as a function of magnetic field for four values of anisotropy parameter  $\Delta$ .

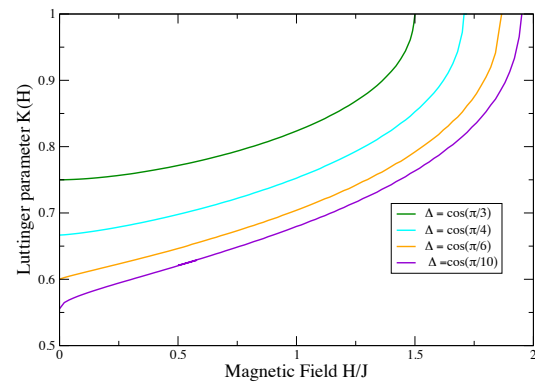


**Figure B.4.2:** Luttinger parameter  $K(H)$  as a function of magnetic field for four values of anisotropy parameter  $\Delta$ .

# Appendix C

## Numerical Techniques

In view of the absence of analytical methods, numerical methods have proven to be a perfect tool for understanding the composite nature of many-body quantum systems and provide important insights into the underlying physics. This appendix summarizes the techniques used to calculate various dynamical and thermodynamic quantities.

### C.1 Exact Diagonalization (ED)

Exact diagonalization (ED) method is extensively employed in the investigations of strongly correlated many-body quantum systems because it provides an exact straightforward description of the problem without any assumptions or approximations. The main restriction of the method is that it applies to finite systems, usually small, due to computational limitations. For example, if we study the  $S = 1/2$  Heisenberg Hamiltonian on a lattice of  $N$  sites, we have two possible states for each site: spin up and spin down. Thus the lattice has  $2^N$  states, and this is the dimension of the Hamiltonian matrix. Similarly for the  $S = 1$  chain that is a three level system, we find  $3^N$ . This exponential growth of the matrix with lattice size makes even small lattices of typically 10 sites difficult to handle with standard diagonalization techniques.

To start with, in order to build the Hamiltonian matrix, we have to choose a basis set that is easily generated, allows fast computation of matrix elements and is economical with memory. Apart from that we also have to find a numerical representation of the basis set. For representing two-level systems like  $S = 1/2$  chains we can use the integers  $n_i = \sigma_i + 1/2$ , where  $\sigma_i = \{1/2, -1/2\}$  is the eigenvalue of the  $S_i^z$  operator. If we identify the sequence of  $n_i$  with the bit pattern of the integer  $I = \sum_{l=1}^N n_l 2^{l-1}$  the basis state  $|\psi\rangle = |-1/2, +1/2, -1/2, +1/2\rangle$  is represented by  $\mathbf{n} = \{0101\}$  with  $I = 4$ . This representation saves memory and speeds up some numerical operations. If the number of sites is  $N = 16$ , there are  $2^N = 65536$  basis states in total.

In order to make the matrix size for a given lattice size accessible to the available computing power, it is important to exploit the model symmetries. It is often the

case that the considered model shows conservation of total spin in the  $z$  direction, i.e.  $[\mathcal{H}, S^z = 0]$  and the eigenvalues of  $\mathcal{H}$  and  $S^z$  are simultaneous good quantum numbers. As  $S_z$  commutes with the Hamiltonian, the  $\mathcal{H}$  matrix is block diagonal in the sectors with fixed  $S^z$  values. For a given  $S^z$  vector, the number of ones in the bit patten (or the number of up spins) is fixed, which reduces the number of basis states to  $L = \frac{N!}{N^\uparrow N^\downarrow}$ . For  $N = 16$ , there are 12870 possible states with  $S^z = 0$ , 11440 with  $S^z = 1$ , and so on. Other symmetries can be used to decompose the Hamiltonian into separate blocks, like translation and rotation symmetries that could be exploited to reduce the number of basis states even further.

## C.2 Finite Temperature Lanczos Method (FTLM)

The diagonalization of Hamilton matrices can be made possible if we employ special methods. Among them, the Lanczos algorithm is one of the simplest methods for the calculation of the ground state energies and wavefunctions and corresponding expectation values. It was developed by C. Lanczos [218] who proposed the diagonalization of sparse matrices using the iterative procedure, allowing for much bigger Hilbert spaces  $N$  relative to the full ED method. The discussion here follows the lines of Ref. [100].

The Lanczos method is an example of a family of projection techniques known as Krylov subspace methods, a general procedure to transform and reduce a symmetric  $N \times N$  matrix  $\mathcal{H}$  to a symmetric  $M \times M$  tridiagonal matrix  $T_M$ . It is an iterative power method which is known to converge fast for the extreme lower and upper eigenvalues of  $\mathcal{H}$ . Typically,  $M > 50$  are enough to reach very high accuracy for both eigenvalues. The basic structure of the algorithm is very simple. Starting from a random initial state  $|\phi_0\rangle$  we generate orthogonal Lanczos vectors  $L_M = |\phi_0, \mathcal{H}\phi_0, \mathcal{H}^2\phi_0, \dots, \mathcal{H}^M\phi_0\rangle$  by repeatedly applying the matrix  $\mathcal{H}$ . Proceeding with the iteration one gets in  $i$  steps:

$$\mathcal{H}|\phi_i\rangle = b_i|\phi_{i-1}\rangle + \alpha_i|\phi_i\rangle + b_{i+1}|\phi_{i+1}\rangle, \quad 0 \leq i \leq M, \quad (\text{C.2.1})$$

with  $|\phi_{-1}\rangle = 0$ ,  $|\phi_{M+1}\rangle = 0$  and  $|\phi_0\rangle$  a random normalized state. The coefficients  $\alpha_n$  and  $b_n$  are determined by the requirement that the  $L_M = |\phi_0, \phi_1, \dots, \phi_M\rangle$  set is orthonormal. Expressed in terms of this basis, the matrix  $\mathcal{H}$  turns out to be tridiagonal. Such a matrix is easily diagonalized using standard numerical routines to obtain approximate eigenvalues  $\epsilon_j$  and corresponding orthonormal eigenvectors  $|\psi_j\rangle$ . With increasing recursion order  $M$  the eigenvalues  $\epsilon_j$  converge to the eigenvalues of the original matrix  $\mathcal{H}$ .

At  $T > 0$ , the Finite Temperature Lanczos Method (FTLM) is employed for the calculation of static and dynamical quantities. In a general orthonormal basis  $|n\rangle$  for finite system with  $N$  basis states one can express the canonical expectation value  $\langle A \rangle$

as:

$$\begin{aligned}\langle A \rangle &= \frac{1}{Z} \sum_{n=1}^N \langle n | e^{-\beta \mathcal{H}} A | n \rangle \\ Z &= \sum_{n=1}^N \langle n | e^{\beta \mathcal{H}} | n \rangle.\end{aligned}\tag{C.2.2}$$

The FTLM is based on the evaluation of the expectation value for each  $|n\rangle$  using the Lanczos basis. Starting with the vector  $|\phi_0^n\rangle = |n\rangle$ , produces the Lanczos basis  $L_M$  along with approximate eigenstates  $|\psi_j^n\rangle$  and  $\epsilon_j^n$ . It can be shown that the final result can be expressed as:

$$\begin{aligned}\langle A \rangle &= \frac{1}{Z} \sum_{n=1}^N \sum_{i=0}^M e^{-\beta \epsilon_i^n} \langle n | \psi_i^n \rangle \langle \psi_i^n | A | n \rangle \\ Z &= \sum_{n=1}^N \sum_{i=0}^M e^{-\beta \epsilon_i^n} \langle n | \psi_i^n \rangle \langle \psi_i^n | n \rangle.\end{aligned}\tag{C.2.3}$$

The computation of static quantities still involves the summation over the complete set of  $N$  states  $|n\rangle$ , which is clearly not feasible in practice. A further approximation replaces the full summation over  $|n\rangle$  by a partial one over a much smaller set of random states. This procedure leads to a statistical error which can be well estimated and is generally quite small. At  $T \rightarrow \infty$  the statistical error goes to zero.

For the computation of dynamical quantities we have to consider the following quantity:

$$C(t) = \frac{1}{Z} \sum_n \langle n | e^{(-\beta+it)\mathcal{H}} A^\dagger e^{-iHt} A | n \rangle.\tag{C.2.4}$$

In analogy with the example given for the expectation value  $\langle A \rangle$ , the dynamical quantities can be again obtained via the Lanczos method, performing two Lanczos iterations with  $M$  steps. The first one, starting with the vector  $|\phi_0^n\rangle = |n\rangle$  produces the Lanczos basis  $L_M$  along with approximate eigenstates  $|\psi_i^n\rangle$  and  $\epsilon_i^n$ . The second Lanczos procedure is started with the normalized vector  $A|\phi_0^n = A|n\rangle$  and generates  $K_M$  with corresponding  $|\chi_i^n\rangle$  and  $\omega_i^n$ . Finally we obtain:

$$C(t) = \frac{1}{Z} \sum_{n=1}^N \sum_{i,j=0}^M e^{-\beta \epsilon_i^n} e^{it(\epsilon_i^n - \omega_j^n)} \langle n | \psi_i^n \rangle \langle \psi_i^n | A^\dagger | \chi_j^n \rangle \langle \chi_j^n | A | n \rangle.\tag{C.2.5}$$

For dynamical correlation functions, the application of the FTLM is limited to  $50 < M < 500$  where the lower bound is determined by the convergence of the ground state and the upper exhaust the limitations of CPU time and memory requirements.

The limitations of both ED and FTLM are confronted by other several variations of these methods, like the Microcanonical Lanczos Method (MCLM), the Low-Temperature

Lanczos Method (LTLM) and the Exact Diagonalization method in Limited Functional Space (EDLFS). A detailed description of these techniques, along with applications are given in Ref. [100].

### C.3 Transfer Matrix Renormalization Group (TMRG)

This numerical method relies on a mapping of the  $D$ -dimensional quantum system to a  $D+1$ -dimensional classical system through a Trotter–Suzuki decomposition [233]. A path–integral formulation in imaginary time  $\tau$  is performed leading to a classical model on a lattice where the imaginary time is discretized in steps  $\tau = \beta/N$ , where  $\beta$  is the inverse temperature and  $N$  is the so called Trotter number.

For the 1D chain of length  $L$  the classical counterpart is a two–dimensional system, where the second axis corresponds to the discrete imaginary time  $\tau = \beta/M$ . A quantum transfer matrix  $T_M$  is defined in analogy with Appendix B.3 with the only difference that  $T_M$  is two columns wide and the partition function is given by  $Z = \ln T_M^{L/2}$ . The calculation of thermodynamic properties in the exact thermodynamic limit  $L \rightarrow \infty$  is based on the application of the density–matrix renormalization group to transfer matrices of the classical model.

It was first suggested by Nishino in 1995 [231] that the DMRG method developed few years earlier by White [232] can be applied to the transfer matrix of a 2D classical system, allowing to calculate its partition function at finite temperature. An improved algorithm was presented by Wang and Xiang [98] and Shibata [99] and showed that the TMRG method provides results with satisfactory accuracy.

The transfer matrix formalism is extremely useful for numerical calculations because of the eigenspectrum of  $T_M$ . At infinite temperature the largest eigenvalue of the QTM is given by  $S^2$  ( $S$ ) and all other eigenvalues are zero. Here  $S$  denotes the number of degrees of freedom of the physical system per lattice site. Decreasing the temperature, the gap between the leading eigenvalue  $\Lambda_0$  and next–leading eigenvalues  $\Lambda_n$  ( $n > 0$ ) of the transfer matrix shrinks. The ratio between  $\Lambda_0$  and each of the other eigenvalues  $\Lambda_n$  defines a correlation length  $\xi_n$ :

$$\frac{1}{\xi_n} = \ln \left| \frac{\Lambda_0}{\Lambda_n} \right|. \quad (\text{C.3.1})$$

Because an 1D quantum system cannot order at finite temperature, any correlation length  $\xi_n$  will stay finite for  $T > 0$ , i.e., the gap between the leading and any next–leading eigenvalue stays finite. Therefore the calculation of the free energy in the thermodynamic limit at non–zero temperature boils down to the calculation of the largest eigenvalue  $\Lambda_0$

of the QTM:

$$\begin{aligned}
f &= -T \lim_{L \rightarrow \infty} \frac{1}{L} \ln Z = -T \lim_{L \rightarrow \infty} \ln \left[ \sum_n \Lambda_n^{L/2} \right] \\
&= -T \lim_{L \rightarrow \infty} \frac{1}{L} \ln \left[ \Lambda_0^{L/2} \left( 1 + \left( \frac{\Lambda_1}{\Lambda_0} \right)^{L/2} + \left( \frac{\Lambda_2}{\Lambda_0} \right)^{L/2} + \dots \right) \right] \\
&= -\frac{1}{2} T \ln \Lambda_0.
\end{aligned} \tag{C.3.2}$$

Note that the error of the mapping due to a finite  $\tau$  is of the order  $\mathcal{O}(\tau^2)$ , i.e we have omitted terms of order  $\mathcal{O}(\tau^2)$  in the partition function and an additional limit  $\tau \rightarrow 0$  is necessary, or equivalently the limit  $N \rightarrow \infty$ . With increasing  $N$  the dimension of the transfer matrix grows exponentially. Nevertheless the length of the transfer matrix  $N$  in imaginary time can be extended iteratively using the DMRG scheme, so that the eigenvalues of the QTM are computed for very large Trotter numbers up to  $N \sim 2000$ . In the numerical calculation,  $\tau$  is fixed and the temperature  $T = 1/(\tau N)$  decreases with increasing  $N$ .

The main advantage of the TMRG algorithm is that the thermodynamic limit can be performed exactly and no extrapolation in system size is required. No statistical errors are present and results can be obtained with an accuracy comparable to ( $T = 0$ ) DMRG calculations. We should emphasize that the  $T = 0$  limit is impossible within this method. A detailed analysis of the method and possible applications can be found in [234, 235].

# Bibliography

- [1] E. Ising: Z. Physik **31**, 253 (1925).
- [2] H. A. Bethe, "Zur Theorie der Metalle. I. Eigenwerte und Eigenfunktionen der linearen Atomkette". (On the theory of metals. I. Eigenvalues and eigenfunctions of the linear atom chain), Z. Phys. **71**, 205 (1931).
- [3] R. M. White, *Quantum Theory of Magnetism*, Springer Series in Solid-State Sciences, (1970).
- [4] Γ. Ψαλτάκης, Κβαντικά συστήματα πολλών σωματιδίων, Πανεπιστημιακές εκδόσεις Κρήτης, (2008).
- [5] S. Sachdev, *Quantum Phase Transitions* (Cambridge University Press, Cambridge, England), (1999).
- [6] X. Zotos, and P. Prelovsek, *Transport in one dimensional quantum systems*, Kluwer Academic Publishers (Dordrecht), (2004).
- [7] X.Zotos, *High Temperature Thermal Conductivity of Two-Leg Spin-1/2 Ladders*, Phys. Rev. Lett. **92**, 067202 (2004).
- [8] V. Zapf, M. Jaime, and C. D. Batista, *Bose-Einstein condensation in quantum magnets*, Rev. Mod. Phys. **86**, 563 (2014).
- [9] F. D. M. Haldane, *Continuum dynamics of the 1-D Heisenberg Antiferromagnet: Identification with the O(3) Nonlinear sigma model*, Phys. Lett. A **93**, 464 (1983).
- [10] J. des Cloizeaux and J.J. Pearson, *Spin-Wave Spectrum of the Antiferromagnetic Linear Chain*, Phys. Rev. **128**, 2131 (1962).
- [11] Ian Affleck, *Quantum spin chains and the Haldane gap*, J. Phys. :Condens. Matter **1** 3047-3072 (1989).
- [12] N. D. Mermin, and H. Wagner, *Absence of Ferromagnetism or Antiferromagnetism in One- or Two-Dimensional Isotropic Heisenberg Models*, Phys. Rev. Lett. **17**, 1133 (1966).

- 
- [13] P. W. Anderson, *An Approximate Quantum Theory of the Antiferromagnetic Ground State*, Phys. Rev. **86** 694 (1952).
- [14] R. Kubo, *The Spin-Wave Theory of Antiferromagnetics*, Phys. Rev. **87**, 568 (1952).
- [15] R. Botet and R. Jullien, *Ground-state properties of a spin-1 antiferromagnetic chain*, Phys. Rev. B, **27**, 613 (1983).
- [16] R. Botet, R. Jullien, and M. Kolb, *Finite-size-scaling study of the spin-1 Heisenberg-Ising chain with uniaxial anisotropy*, Phys. Rev. B, **28**, 3914, (1983).
- [17] M. P. Nightingale and H. W. Blöte, *Gap of the linear spin-1 Heisenberg antiferromagnet: A Monte Carlo calculation*, Phys. Rev. B, **33** 659 (1986) .
- [18] Takahashi, *Monte Carlo Calculation of Elementary Excitation of Spin Chains*, Phys. Rev. Lett., **62**, 2313, (1989).
- [19] Takahashi, *Elementary excitations of an anisotropic spin-1 chain*, Phys. Rev. B, **48** 311 (1993) .
- [20] I. Affleck, *Theory of Electron spin Resonance in Haldane-Gap Antiferromagnet*, Phys. Rev. B **46**, 9002 (1992).
- [21] S. R. White, D. A. Huse, *Density Matrix Formulation for Quantum Renormalization Groups* , Phys. Rev. Lett. **69**, 2863 (1992).
- [22] S. R. White, *Numerical renormalization-group study of low-lying antiferromagnetic  $S = 1$  Heisenberg eigenstates chain*, Phys. Rev. B **48**, 3844 (1993).
- [23] O. Golinelli, Th. Jolicoeur and R. Lacaze, *Finite-lattice extrapolations for a Haldane-gap antiferromagnet*, Phys. Rev. B **50**, 3037 (1994).
- [24] H. J. Mikeska and A. K. Kolezhuk, *One-Dimensional Magnetism*, Lect. Notes Phys. **645**, 1–83 (2004).
- [25] A. M. Polyakov, *Compact gauge fields and the infrared catastrophe*, Phys. Lett. B **59**, 82 (1975); A.A. Belavin, A.M. Polyakov, A.S. Schwartz, and Yu.S. Tyupkin, *Pseudoparticle solutions of the Yang-Mills equations*, Phys. Lett. B **59**, 85 (1975).
- [26] E. Brézin, J. Zinn-Justin, *Spontaneous breakdown of continuous symmetries near two dimensions*, Phys. Rev. B **14**, 3110 (1976).
- [27] E. Lieb, T. D. Schultz, D. C. Mattis, *Two soluble models of an antiferromagnetic chain*, Ann. Phys. (NY) **16**, 407 (1961).
- [28] I. Affleck, E. H. Lieb, *A proof of part of Haldane's conjecture on spin chains*, Lett. Math. Phys. **12**, 57 (1986).

- [29] M. Oshikawa, M. Yamanaka and I. Affleck, *Magnetization Plateaus in Spin Chains: “Haldane Gap” for Half-Integer Spins*, Phys. Rev. Lett. **78**, 1984 (1997).
- [30] C. K. Majumdar and D. K. Ghosh, *On the next-nearest neighbor interaction in Linear Chain. I*, J. Math. Phys. **10** 1388 (1969).
- [31] I. Affleck, T. Kennedy, E. H. Lieb and H. Tasaki, *Rigorous results on valence-bond ground states in antiferromagnets*, Phys. Rev. Lett. **59**, 799 (1987); *Valence bond ground states in isotropic quantum antiferromagnets*, Commun. Math. Phys. **115**, 477 (1988).
- [32] P. Kulish, N. Yu Reshetikhin and E. Sklyanin, *Yang-Baxter equation and representation theory: I*, Lett. Math. Phys. **5** 393 (1981); L. Takhtajan, *The picture of low-lying excitations in the isotropic Heisenberg chain of arbitrary spins*, Phys. Lett. **87A** 479 (1982).
- [33] A. Lauchli, G. Schmid, S. Trebst, *Spin nematics in the bilinear- biquadratic  $S=1$  spin chain*, Phys. Rev. B **74**, 144426 (2006).
- [34] I. Affleck, *Theory of Haldane-gap antiferromagnets in applied fields*, Phys. Rev. B, **41** 6697 (1990); Phys. Rev. Lett. **62** 474 (1989).
- [35] A. M. Tsvelik, *Field-theory treatment of the Heisenberg spin-1 chain*, Phys. Rev. B, **42** 10499 (1990).
- [36] O. Golinelli, Th. Jolicoer and R. Lacaze, *Haldane gaps in a spin-1 Heisenberg chain with easy plane single-ion anisotropy*, Phys. Rev. B, **45** 9798 (1992).
- [37] O. Golinelli, Th. Jolicoer and R. Lacaze, *Dispersion of magnetic excitations in a spin-1 chain with easy-plane anisotropy*, Phys. Rev. B, **46** 10854 (1992).
- [38] W. Chen, K. Hida and B. C. Sanctuary, *Ground-state phase diagram of  $S=1$  XXZ chains with uniaxial single-ion-type anisotropy*, Phys. Rev. B **67** 104401 (2003).
- [39] A. Langari, F. Pollmann, and M. Siahatgar, *Ground-state fidelity of the spin-1 Heisenberg chain with single ion anisotropy: quantum renormalization group and exact diagonalization approaches*, J. Phys.: Condens. Matter **25**, 406002 (2013).
- [40] H. .J. Schulz, *Phase diagrams and correlation exponents for quantum spin chains of arbitrary spin quantum number*, Phys. Rev. B **34** 6372–85 (1986).
- [41] V. S. Zapf, D. Zocco, B. R. Hansen, M. Jaime, N. Harrison, C.D. Batista, M. Kenzelmann, C. Niedermayer, A. Lacerda, and A. Paduan-Filho, *Bose-Einstein Condensation of  $S=1$  Nickel Spin Degrees of Freedom in  $NiCl_2 - 4SC(NH_2)_2$* , Phys. Rev. Lett. **96**, 077204 (2006).

- [42] S. A. Zvyagin, J. Wosnitza, C. D. Batista, M. Tsukamoto, N. Kawashima, J. Krzystek, V. S. Zapf, M. Jaime, N. F. Oliveira, and A. Paduan-Filho, *Magnetic Excitations in the Spin-1 Anisotropic Heisenberg Antiferromagnetic Chain System  $NiCl_2 - 4SC(NH_2)_2$*  Phys. Rev. Lett. **98**, 047205 (2007).
- [43] W. J. L. Buyers, R. L. Armstrong, P. Gerlach, and K. Hirakawa, *Experimental Evidence for the Haldane Gap in a Spin-1, Nearly Isotropic, Antiferromagnetic Chain*, Phys. Rev. Lett. **56**, 371 (1986); W. J. L. Buyers, R. L. Armstrong, and K. Hirakawa, Phys. Rev. **38** 543 (1988).
- [44] J. P. Renard, M. Verdagner, L. P. Regnault, W. A. C. Erkelens, J. Rossat-Mignod, and W. G. Stirling, *Presumption for a Quantum Energy Gap in the Quasi-One-Dimensional  $S = 1$  Heisenberg Antiferromagnet  $Ni(C_2H_8N_2)_2NO_2(ClO_4)$* , Europhys. Lett. **3** 945 (1987).
- [45] M. Steiner, J. Villain, and C. G. Windsor, *Theoretical and experimental studies on one-dimensional magnetic systems*, Adv. Phys. **25**, 87 (1975); M. Steiner, K. Kakurai, and J. K. Kjems, *Experimental study of the spin dynamics in the 1-D-ferromagnet with planar anisotropy,  $CsNiF_3$ , in an external magnetic field*, Z. Phys. B **53**, 117 (1983).
- [46] M. Steiner, K. Kakurai, W. Knop, B. Dorner, R. Pynn, U. Hapek, P. Day and G. McLeen, *Collective excitations in the 1D-ferromagnet  $CsFeCl_3$  with singlet ground state*, Solid State Commun. **38** 1179 (1981).
- [47] B. Dorner, D. Visser, U. Steigenberger, K. Kakurai and M. Steiner, *Magnetic excitations in the quasi one-dimensional antiferromagnetic singlet groundstate system  $CsFeBr_3$* , Z. Phys. B **72** 487 (1988); B. Dorner, D. Visser, U. Steigenberger, K. Kakurai and M. Steiner, *Magnetic excitations in the quasi one-dimensional antiferromagnetic singlet groundstate system  $CsFeBr_3$* , Physica B **156** 263 (1989).
- [48] M. Sieling, U. Löw, B. Wolf, S. Schmidt, S. Zvyagin, and B. Lüthi, *High magnetic-field ESR in the Haldane spin chains  $NENP$  and  $NINO$* , Phys. Rev. B **61**, 88 (2000).
- [49] C. Psaroudaki, S. A. Zvyagin, J. Krzystek, A. Paduan-Filho, X. Zotos, and N. Papanicolaou, *Magnetic excitations in the spin-1 anisotropic antiferromagnet  $NiCl_2 - 4SC(NH_2)_2$* , Phys. Rev. B **85**, 014412 (2012).
- [50] N. Papanicolaou, *Pseudospin approach for planar ferromagnets*, Nucl. Phys. B **240**, 281 (1984); *On the Phase Structure of Spin-1 Planar Magnetic Chains*, Z. Phys. B **61**, 159 (1985).
- [51] N. Papanicolaou, *Unusual phases in quantum spin-1 systems*, Nucl. Phys. B **305**, 386 (1984).

- [52] N. Papanicolaou, *Ground-state properties of spin-1 nematics*, Phys. Lett **A116**, 89 (1986).
- [53] N. Papanicolaou, and P. Spathis, *Quantum spin-1 chains with strong planar anisotropy*, J. Phys.: Condens. Matter **2**, 6575-6591 (1990).
- [54] N. Papanicolaou, and P. Spathis, *Bound excitons in quantum spin-1 chains with strong planar anisotropy*, J. Phys.: Condens. Matter **1**, 5555-5560 (1989).
- [55] I. Affleck, *Bose condensation in quasi-one-dimensional antiferromagnets in strong fields*, Phys. Rev. B, **43** 3215 (1991).
- [56] P. Jordan, and E. Wigner, *Über das Paulische Äquivalenzverbot* Z. Phys. A **47**, 631 (1928).
- [57] E. H. Lieb, and W. Liniger, *Exact Analysis of an Interacting Bose Gas. I. The General Solution and the Ground State*, Phys. Rev. **130**, 1605 (1963); E. H. Lieb, *ibid.* **130**, 1616 (1963).
- [58] C. D. Batista, and G. Ortiz, *Generalized Jordan-Wigner Transformations*. Phys. Rev. Lett. **86** 1082 (2001).
- [59] T. Matsubara, and H. Matsuda, *A Lattice Model of Liquid Helium, I*, Prog. Theor. Phys. **16**, 569 (1956).
- [60] C. D. Batista, and G. Ortiz, *Algebraic Approach to Interacting Quantum Systems*, Adv. Phys. **53**, 1 (2004).
- [61] L. Yin, J. S. Xia, V. S. Zapf, N. S. Sullivan, and A. Paduan-Filho, *Direct Measurement of the Bose–Einstein Condensation Universality Class in  $\text{NiCl}_2-4\text{SC}(\text{NH}_2)_2$  at Ultralow Temperatures*, Phys. Rev. Lett. **101**, 187205 (2008).
- [62] Z. Zhang, K. Wierschem, I. Yap, Y. Kato, C. D. Batista, and P. Sengupta, *Phase diagram and magnetic excitations of anisotropic spin-one magnets*, Phys. Rev. B **87** 174405 (2013).
- [63] A. F. Albuquerque, C. J. Hamer, and J. Oitmaa, *Quantum phase diagram and excitations for the one-dimensional  $S=1$  Heisenberg antiferromagnet with single-ion anisotropy* Phys. Rev. B **79**, 054412 (2009).
- [64] D. C. Mattis, *Phase Transitions and Critical phenomena*, edited by C. Domb and M. S. Green (Academic, New York, 1972), Vol. 1, p.177.
- [65] N. Papanicolaou, and G. C. Psaltakis, *Bethe ansatz for two-magnon bound states in anisotropic magnetic chains of arbitrary spin*, Phys. Rev. **35** 342.

- [66] M. Marder, N. Papanicolaou, and G. C. Psaltakis, *Phase separation in a  $t$ - $J$  model*, Phys. Rev. B **41** 6920 (1990).
- [67] A. V. Sizanov, and A. V. Syromyatnikov, *Bosonic representation of quantum magnets with large single-ion easy-plane anisotropy*, Phys. Rev. B **84**, 054445 (2011).
- [68] M. Wortis, *Bound States of Two Spin Waves in the Heisenberg Ferromagnet*, Phys. Rev. **132**, 85 (1963).
- [69] T. Giamarchi, and A. M. Tsvelik, *Coupled ladders in a magnetic field* Phys. Rev. B **59**, 11398 (1999); F. Mila, *Ladders in a magnetic field: a strong coupling approach*, Eur. Phys. J. B **6**, 201 (1998).
- [70] M. Takahashi, *Thermodynamics of One-Dimensional Solvable Models*, Cambridge University Press.
- [71] V. E. Korepin, N. M. Bogoliubov, and A. G. Izergin, *Quantum Inverse Scattering Method and Correlation Functions*, Cambridge University Press.
- [72] C. P. Slichter, *Principles of Magnetic Resonance*, Springer Series in Solid-State Sciences; v. 1 (1978).
- [73] R. Kubo, and K. Tomita, *A General Theory of Magnetic Resonance Absorption*, J. Phys. Soc. Jpn. **9**, 888 (1954).
- [74] H. Mori, and K. Kawasaki, *Theory of Dynamical Behaviors of Ferromagnetic Spins*, Prog. Theor. **27** 529 (1962); *Antiferromagnetic Resonance Absorption*, *ibid* **28**, 971 (1962).
- [75] R. E. Dietz, F. R. Merritt, R. Dingle, D. Hone, B. G. Silbernagel, and P. M. Richards, *Exchange Narrowing in One-Dimensional Systems*, Phys. Rev. Lett. **26** 1186 (1971).
- [76] N. Papanicolaou, A. Orendáčová, and M. Orendáč, *Electron-spin resonance in spin-1 planar magnetic chains*, Phys. Rev. B **56**, 8786 (1997).
- [77] M. Oshikawa, and I. Affleck, *Electron spin resonance in  $S=1/2$  antiferromagnetic chains*, Phys. Rev. **65**, 134410 (2002).
- [78] N. Papanicolaou, and P. Spathis, *Strong-coupling theory for the thermodynamics of spin-1 planar magnetic chains*, Phys. Rev. B **52**, 16001 (1995).
- [79] S. A. Zvyagin, C. D. Batista, J. Krzystek, V. S. Zapf, M. Jaime, A. Paduan-Filho, and J. Wosnitza, *Observation of two-magnon bound states in the spin-1 anisotropic Heisenberg antiferromagnetic chain system  $NiCl_2 - 4SC(NH_2)_2$* , Physica B **403**, 1497 (2008).

- [80] S. Cox, R. D. McDonald, M. Armanious, P. Sengupta, and A. Paduan-Filho, *Unusual Magneto–Optical Phenomenon Reveals Low Energy Spin Dispersion in the Spin–1 Anisotropic Heisenberg Antiferromagnetic Chain System  $NiCl_2 - 4SC(NH_2)_2$* , Phys. Rev. Lett. **101**, 087602 (2008).
- [81] T. Moriya, Phys. Rev. **117**, 635 (1960).
- [82] S. A. Zvyagin, J. Wosnitza, A. K. Kolezhuk, V. S. Zapf, M. Jaime, A. Paduan-Filho, V. N. Glazkov, S. S. Sosin, and A. I. Smirnov, *Spin dynamics of  $NiCl_2 - 4SC(NH_2)_2$  in the field-induced ordered phase*, Phys. Rev. B **77**, 092413 (2008).
- [83] A. Paduan-Filho et al., *Field–induced magnetic ordering in uniaxial nickel systems: A second example*, J. Chem. Phys. **74**, 4103 (1981); A. Paduan-Filho, X. Gratens, and N. F. Oliveira, Jr., *Field-induced magnetic ordering in  $NiCl_2 - 4SC(NH_2)_2$* , Phys. Rev. B **69**, 020405(R) (2004).
- [84] A. Lopez-Castro and M. R. Truter, *The crystal and molecular structure of dichlorotetrakis thiourea nickel,  $[(NH_2)_2CS]_4NiCl_2$* , J. Chem. Soc. 1963, 1309.
- [85] V. S. Zapf, V. F. Correa, P. Sengupta, C. D. Batista, M. Tsukamoto, N. Kawashima, P. Egan, C. Pantea, A. Migliori, J. B. Betts, M. Jaime, and A. Paduan-Filho, *Direct measurement of spin correlations using magnetostriction*, Phys. Rev. B **77**, R020404 (2008).
- [86] O. Chiatti, S. Zherlitsyn, A. Sytcheva, J. Wosnitza, A. A. Zvyagin, V. S. Zapf, M. Jaime, and A. Paduan-Filho, *Ultrasonic investigation of  $NiCl_2 - 4SC(NH_2)_2$* , J. Phys. **150**, 042016 (2009).
- [87] V. S. Zapf, P. Sengupta, C. D. Batista, F. Nasreen, F. Wolff-Fabris, and A. Paduan-Filho, *Magnetoelectric effects in an organometallic quantum magnet*, Phys. Rev. B **83**, 140405(R).
- [88] S. A. Zvyagin, J. Krzystek, P.H.M. van Loosdrecht, G. Dhalenne, and A. Revcolevschi, *High-field ESR study of the dimerized-incommensurate phase transition in the spin-Peierls compound  $CuGeO_3$* , Physica B **346-347**, 1 (2004).
- [89] A. V. Sizanov, and A. V. Syromyatnikov, *Bosonic representation of quantum magnets with large single-ion easy-plane anisotropy*, Phys. Rev. B **84**, 054445 (2011).
- [90] C. Psaroudaki, J. Herbrych, J. Karadamoglou, P. Prelovček, X. Zotos, and N. Papanicolaou, *Effective  $S=1/2$  description of the  $S=1$  chain with strong easy plane anisotropy*, Phys. Rev. B **89**, 224418 (2014).
- [91] N. Kitanine, J.M. Maillet, V. Terras, *Form factors of the XXZ Heisenberg finite chain*, Nucl. Phys. B **554**, 647 (1999).

- [92] J-S. Caux, R. Hagemans and J. M. Maillet, *Computation of dynamical correlation functions of Heisenberg chains: the gapless anisotropic regime*, J. Stat. Mech., P09003 (2005).
- [93] A. A. Ovchinnikov, *On the particle excitations in the XXZ spin chain*, Phys. Lett. **A377**, 3067 (2013).
- [94] R. J. Baxter, *Completeness of the Bethe Ansatz for the Six and Eight-Vertex Models*, J. Stat. Phys. **108**, 1 (2002).
- [95] M. Oshikawa and I. Affleck, *Electron spin resonance in  $S=1/2$  antiferromagnetic chains*, Phys. Rev. B **65**, 134410 (2002); Y. Maeda, K. Sakai, and M. Oshikawa, *Exact Analysis of ESR Shift in the Spin-1/2 Heisenberg Antiferromagnetic Chain*, Phys. Rev. Lett. **95**, 037602 (2005); M. Brockmann, F. Göhmann, M. Karbach, A. Klümper, and A. Weisse, *Theory of Microwave Absorption by the Spin-1/2 Heisenberg-Ising Magnet*, *ibid.* **107**, 017202 (2011).
- [96] Y. Maeda, and M. Oshikawa, *Numerical analysis of electron-spin resonance in the spin-1/2 XY model*, Phys. Rev. B **67**, 224424, (2003).
- [97] S. A. Zvyagin, V. V. Eremin, V. V. Pishko, A. Feher, M. Orendáč, and A. Orendáčová, *Low. Temp. Phys.* **21**, 680 (1995); S. A. Zvyagin, T. Rieth, M. Sieling, S. Schmidt, and B. Luthi, *Magnetic excitation spectrum in large- $D$  chain NENC*, Czech. J. Phys. **46**, 1937 (1996); A. K. Kolezhuk, and H.-J. Mikeska, *Electron spin resonance in high-field critical phase of gapped spin chains*, Phys. Rev. B **65**, 014413 (2001).
- [98] X. Wang, T. Xiang, *Transfer-matrix density-matrix renormalization-group theory for thermodynamics of one-dimensional quantum systems*, Phys. Rev. B **56**, 5061 (1997).
- [99] N. Shibata, *Thermodynamics of the Anisotropic Heisenberg Chain Calculated by the Density Matrix Renormalization Group Method*, J. Phys. Soc. Jpn. **66**, 2221 (1997).
- [100] For a recent review, see P. Prelovšek and J. Bonča, in *Strongly Correlated Systems - Numerical Methods*, edited by A. Avella and F. Mancini (Springer Series in Solid-State Sciences Vol. 176 (Springer, Berlin, 2013), pp. 1–29.
- [101] M. Takahashi and M. Suzuki, *One-Dimensional Anisotropic Heisenberg Model at Finite Temperatures*, Prog. Theor. Phys. **48**, 2187 (1972).
- [102] I. Affleck, *Bose condensation in quasi-one-dimensional antiferromagnets in strong fields*, Phys. Rev. B **43**, 3215 (1991).

- [103] R. Chitra, and T. Giamarchi, *Critical properties of gapped spin-chains and ladders in a magnetic field*, Phys. Rev. B **55**, 5816 (1997).
- [104] T. Sakai, and M. Takahashi, *Critical exponent in the magnetization curve of quantum spin chains*, Phys. Rev. B **57**, R8091 (1998).
- [105] C. N. Yang, and C. P. Yang, *One-Dimensional Chain of Anisotropic Spin-Spin Interactions. II. Properties of the Ground-State Energy Per Lattice Site for an Infinite System*, Phys. Rev. **150**, 327 (1966); *One-Dimensional Chain of Anisotropic Spin-Spin Interactions. III. Applications* Phys. Rev. **151**, 258 (1966).
- [106] X. Wang, and L. Yu, *Magnetic-Field Effects on Two-Leg Heisenberg Antiferromagnetic Ladders: Thermodynamic Properties*, Phys. Rev. Lett. **84**, 5399 (2000).
- [107] S. Wessel, M. Olshanii, and S. Haas, *Field-Induced Magnetic Order in Quantum Spin Liquids*, Phys. Rev. Lett. **87**, 206407 (2001).
- [108] C. Rüegg, K. Kiefer, B. Thielemann, D. F. McMorrow, V. Zapf, B. Normand, M.B. Zvonarev, P. Bouillot, C. Kollath, T. Giamarchi, S. Capponi, D. Poilblanc, D. Biner, and K.W. Krämer, *Thermodynamics of the Spin Luttinger Liquid in a Model Ladder Material*, Phys. Rev. Lett. **101**, 247202 (2008).
- [109] A. V. Sologubenko, T. Lorenz, J. A. Mydosh, B. Thielemann, H. M. Rønnow, C. Rüegg, K. W. Krämer, *Evidence for spinon localization in the heat transport of the spin-12 ladder compound  $(C_5H_{12}N)_2CuBr_4$* , Phys. Rev. B **80**, 220411(R) (2009).
- [110] P. Bouillot, C. Kollath, A.M. Läuchli, M. Zvonarev, B. Thielemann, C. Rüegg, E. Orignac, R. Citro, M. Klanjšek, C. Berthier, M. Horvatić, and T. Giamarchi, *Statics and dynamics of weakly coupled antiferromagnetic spin-12 ladders in a magnetic field*, Phys. Rev. B **83**, 054407 (2011).
- [111] Y. Maeda, C. Hotta, and M. Oshikawa, *Universal Temperature Dependence of the Magnetization of Gapped Spin Chains*, Phys. Rev. Lett. **99**, 057205 (2007).
- [112] A. Paduan-Filho, X. Gratens, and N.F. Oliveira, Jr., *Field-induced magnetic ordering in  $NiCl_2 - 4SC(NH_2)_2$* , Phys. Rev. B **69**, 020405 (2004).
- [113] F. Weickert, R. Küchler, A. Steppke, L. Pedrero, M. Nicklas, M. Brando, F. Steglich, M. Jaime, V.S. Zapf, A. Paduan-Filho, K. A. Al-Hassanieh, C. D. Batista, and P. Sengupta, *Low-temperature thermodynamic properties near the field-induced quantum critical point in  $NiCl_2 - 4SC(NH_2)_2$* , Phys. Rev. B **85**, 184408 (2012).
- [114] N. Papanicolaou, and P. Spathis, *The magnetic field dependence of the specific heat in quantum spin chains with axial symmetry*, J. Phys. C: Solid State Phys. **20**, L783.

- [115] Y. Kohama, A. V. Sologubenko, N. R. Dilley, V. S. Zapf, M. Jaime, J.A. Mydosh, A. Paduan-Filho, K.A. Al-Hassanieh, P. Sengupta, S. Gangadharaiah, A. L. Chernyshev, and C. D. Batista, *Thermal Transport and Strong Mass Renormalization in  $NiCl_2 - 4SC(NH_2)_2$* , Phys. Rev. Lett. **106**, 037203 (2011).
- [116] C. Hess, C. Baumann, U. Ammerahl, B. Büchner, F. Heidrich-Meisner, W. Brenig, and A. Revcolevschi, *Magnon heat transport in  $(Sr, Ca, La)_{14}Cu_{24}O_{41}$* , Phys. Rev. B **64**, 184305 (2001).
- [117] A. V. Sologubenko, K. Giannó, H. R. Ott, U. Ammerahl, and A. Revcolevschi, *Thermal Conductivity of the Hole-Doped Spin Ladder System  $Sr_{14-x}Ca_xCu_{24}O_{41}$* , Phys. Rev. Lett. **84**, 2714 (2000).
- [118] K. Kudo, S. Ishikawa, T. Noji, T. Adachi, Y. Koike, K. Maki, S. Tsuji, and Ken-ichi Kumagai, *Spin Gap and Hole Pairing in the Spin-Ladder Cuprate  $Sr_{14-x}A_xCu_{24}O_{41}$  ( $A = Ca$  and  $La$ ) Studied by the Thermal Conductivity*, J. Phys. Soc. Jpn. **70**, 437 (2001).
- [119] C. Hess, U. Ammerahl, C. Baumann, B. Büchner, and A. Revcolevschi, *Magnon hole scattering in  $(Sr, Ca, La)_{14}Cu_{24}O_{41}$* , Physica B **312-313**, 612 (2002).
- [120] A. V. Sologubenko, E. Felder, K. Giannó, H. R. Ott, A. Vietkine, and A. Revcolevschi, *Thermal conductivity and specific heat of the linear chain cuprate  $Sr_2CuO_3$ : Evidence for thermal transport via spinons*, Phys. Rev. B **62**, R6108 (2000); A. V. Sologubenko, K. Giannó, H. R. Ott, A. Vietkine, and A. Revcolevschi, *Heat transport by lattice and spin excitations in the spin-chain compounds  $SrCuO_2$  and  $Sr_2CuO_3$* , *ibid.* **64**, 054412 (2001).
- [121] A. V. Sologubenko, H. R. Ott, G. Dhalenne, and A. Revcolevschi, *Universal behavior of spin-mediated energy transport in  $S = 1/2$  chain cuprates  $BaCu_2Si_2O_7$  as an example*, Europhys. Lett. **62**, 540 (2003).
- [122] M. Hofmann, T. Lorenz, K. Berggold, M. Grüniger, A. Freimuth, G. S. Uhrig, and E. Brück, *Evidence for a large magnetic heat current in insulating layered cuprates*, Phys. Rev. B **67**, 184502 (2003).
- [123] C. Hess, B. Büchner, U. Ammerahl, L. Colonescu, F. Heidrich-Meisner, W. Brenig, and A. Revcolevschi, *Magnon Heat Transport in Doped  $La_2CuO_4$* , Phys. Rev. Lett. **90**, 197002 (2003).
- [124] Yoichi Ando, J. Takeya, D.L. Sisson, S.G. Doettinger, I. Tanaka, R.S. Feigelson, and A. Kapitulnik, *Thermal conductivity of the spin-Peierls compound  $CuGeO_3$* , Phys. Rev. B **58**, R2913 (1998). Phys. Rev. B **67**, 104503 (2003).

- [125] K. Saito, S. Takesue, and S. Miyashita, *Thermal conduction in a quantum system*, Phys. Rev. E **54**, 2404 (1996).
- [126] A. Klümper and K. Sakai, *The thermal conductivity of the spin-1/2 XXZ chain at arbitrary temperature*, J. Phys. A **35**, 2173 (2002).
- [127] J. V. Alvarez and C. Gros, *Anomalous Thermal Conductivity of Frustrated Heisenberg Spin Chains and Ladders*, Phys. Rev. Lett. **89**, 156603 (2002).
- [128] K. Saito and S. Miyashita, *Enhancement of the Thermal Conductivity in Gapped Quantum Spin Chains*, J. Phys. Soc. Jpn. **71**, 2485 (2002).
- [129] F. Heidrich-Meisner, A. Honecker, D. C. Cabra, and W. Brenig, *Thermal conductivity of anisotropic and frustrated spin-1/2 chains*, Phys. Rev. B **66**, 140406(R) (2002).
- [130] E. Orignac, R. Chitra, and R. Citro, *Thermal transport in one-dimensional spin gap systems*, Phys. Rev. B **67**, 134426 (2003).
- [131] K. Saito, *Strong evidence of normal heat conduction in a one-dimensional quantum system*, Europhys. Lett. **61**, 34 (2003).
- [132] K. Saito, *Transport anomaly in the low-energy regime of spin chains*, Phys. Rev. B **67**, 064410 (2003).
- [133] K. Louis and C. Gros, *Diverging magnetothermal response in the one-dimensional Heisenberg chain*, Phys. Rev. B **67**, 224410 (2003).
- [134] J. Bonča, J. P. Rodriguez, J. Ferrer, and K. S. Bedell, *Direct calculation of spin stiffness for spin-1/2 Heisenberg models*, Phys. Rev. B **50**, 3415 (1994).
- [135] H. Castella, X. Zotos, and P. Prelovšek, *Integrability and Ideal Conductance at Finite Temperatures*, Phys. Rev. Lett. **74**, 972 (1995).
- [136] X. Zotos and P. Prelovšek, *Evidence for ideal insulating or conducting state in a one-dimensional integrable system* Phys. Rev. B **53**, 983 (1996).
- [137] X. Zotos, F. Naef, and P. Prelovšek, *Transport and conservation laws*, Phys. Rev. B **55**, 11029 (1997).
- [138] K. Fabricius and B. M. McCoy, *Spin diffusion and the spin-1/2 XXZ chain at  $T = \infty$  from exact diagonalization*, Phys. Rev. B **57**, 8340 (1998).
- [139] F. Naef and X. Zotos, *Spin and energy correlations in the one dimensional spin-1/2 Heisenberg model*, J. Phys.: Condens. Matter **10**, L183 (1998).

- [140] B. N. Narozhny, A. J. Millis, and N. Andrei, *Transport in the XXZ model*, Phys. Rev. B **58**, R2921 (1998).
- [141] X. Zotos, *Finite Temperature Drude Weight of the One-Dimensional Spin-1/2 Heisenberg Model*, Phys. Rev. Lett. **82**, 1764 (1999).
- [142] N. Laflorencie, S. Capponi, and E. S. Sørensen, *Finite size scaling of the spin stiffness of the antiferromagnetic  $S = 1/2$  XXZ chain* Eur. Phys. J B **24**, 77 (2001).
- [143] X. Zotos, *Ballistic Transport in Classical and Quantum Integrable Systems*, J. Low Temp. Phys. **126**, 1185 (2002).
- [144] J. V. Alvarez and C. Gros, *Low-Temperature Transport in Heisenberg Chains*, Phys. Rev. Lett. **88**, 077203 (2002); *Conductivity of quantum spin chains: A quantum Monte Carlo approach*, Phys. Rev. B **66**, 094403 (2002).
- [145] S. Fujimoto and N. Kawakami, *Drude Weight at Finite Temperatures for Some Nonintegrable Quantum Systems in One Dimension*, Phys. Rev. Lett. **90**, 197202 (2003).
- [146] M. W. Long, P. Prelovšek, S. El Shawish, J. Karadamoglou, and X. Zotos, *Finite-temperature dynamical correlations using the microcanonical ensemble and the Lanczos algorithm*, Phys. Rev. B **68**, 235106 (2003).
- [147] F. Heidrich-Meisner, A. Honecker, and W. Brenig, *Transport in quasi one-dimensional spin-1/2 systems*, Eur. J. Phys. Special Topic **151**, 135 (2007).
- [148] C. Hess, *Heat conduction in low-dimensional quantum magnets*, Eur. J. Phys. Special Topic **151**, 73 (2007).
- [149] A. V. Sologubenko, T. Lorenz, H. R. Ott, and A. Freimuth, *Thermal Conductivity via magnetic excitations in spin-chain materials*, J. Low. Temp. Phys. **147**, 387 (2007).
- [150] G. D. Mahan, *Many-Particle Physics*, Plenum Press, New York London, 1990.
- [151] J. Benz, T. Fukui, A. Klümper, and C. Scheeren, *On the Finite Temperature Drude Weight of the Anisotropic Heisenberg Chain*, J. Phys. Soc. Jpn. Suppl. **74**, 181 (2005).
- [152] *Optical solitons: theoretical challenges and industrial perspectives*, editors: V.E. Zakharov and S. Wabnitz, Les Houches Workshop, Springer (1998).
- [153] K. Sakai and A. Klümper, *Non-dissipative thermal transport in the massive regimes of the XXZ chain*, J. Phys. A **36**, 11617 (2003).

- [154] F. Heidrich-Meisner, A. Honecker, D. C. Cabra, and W. Brenig, *Zero-frequency transport properties of one dimensional spin-1/2 systems*, Phys. Rev. B **68**, 134436 (2003).
- [155] E. Shimshoni, N. Andrei, and A. Rosch, *Thermal conductivity of spin-1/2 chains*, Phys. Rev. B **68**, 104401 (2003).
- [156] C. Hess, H. Elaes, B. Büchner, U. Ammerahl, M. Hücker, and A. Revcolevschi, *Magnon-Hole Scattering and Charge Order in  $Sr_{14-x}Ca_xCu_{24}O_{41}$* , Phys. Rev. Lett. **93**, 027005 (2004).
- [157] C. Hess, P. Ribeiro, B. Büchner, H. Elaes, G. Roth, U. Ammerahl, and A. Revcolevschi, *Magnon heat conductivity and mean free paths in two-leg spin ladders: A model-independent determination*, Phys. Rev. B **73**, 104407 (2006).
- [158] D. L. Huber, and J. S. Semura, *Spin and Energy Transport in Anisotropic Magnetic Chains with  $S=1/2$*  Phys. Rev. **182**, 602 (1969).
- [159] T. Niemeijer, and H. A. W. van Vianen, *A note on the thermal conductivity of linear magnetic chains*, Phys. Lett. **34A**, 401 (1971).
- [160] P. Mazur, Physica **43**, 533 (1969); M. Suzuki, *Ergodicity, constants of motion, and bounds for susceptibilities*, Physica **51**, 277 (1971).
- [161] T. Prosen, Phys. Rev. Lett. **106** 217206 (2011); T. Prosen, and E. Illievski, Phys. Rev. Lett. **111**, 057203 (2013).
- [162] R. G. Pereira, V. Pasquier, J. Sirker and I. Affleck, J. Stat. Mech. P09037 (2014).
- [163] T. Prosen / Nucl. Phys. B **886**, 1177 (2014).
- [164] H. Castella, X. Zotos, and P. Prelovšek, *Integrability and Ideal Conductance at Finite Temperatures*, Phys. Rev. Lett. **74**, 972 (1995).
- [165] W. Götze and P. Wölfle, *Homogeneous Dynamical Conductivity of Simple Metals*, Phys. Rev. B **6**, 1226 (1972).
- [166] J. Jaklič, and P. Prelovšek, *Lanczos method for the calculation of finite-temperature quantities in correlated systems*, Phys. Rev. B **49**, 5065 (1994).
- [167] M. Jarrel, and J.E. Gubernatis, *Bayesian inference and the analytic continuation of imaginary-time quantum Monte Carlo data*, Phys. Rep. **269**, 133 (1996).
- [168] S. Kirchner, H. G. Evertz, and W. Hanke, *Transport properties of one-dimensional Hubbard models*, Phys. Rev. B **59**, 1825 (1999); D. Heidarian, and S. Sorella, *Finite Drude weight for one-dimensional low-temperature conductors*, Phys. Rev. B **75**, 241104 (2007).

- [169] F. Naef, X. Wang, X. Zotos, W. von der Linden, *Autocorrelations from the transfer-matrix density-matrix renormalization-group method*, Phys. Rev. B **60**, 359 (1999).
- [170] R. Kubo, *Statistical-Mechanical Theory of Irreversible Processes. I. General Theory and Simple Applications to Magnetic and Conduction Problems*, J. Phys. Soc. Jpn. **12**, 570 (1957).
- [171] C. Meja-Monasterio, T. Prosen, and S. Miyashita, *Fourier's law in a quantum spin chain and the onset of quantum chaos*, Europhys. Lett. **72**, 520 (2006).
- [172] T. Prosen, and E. Illievski, *Families of Quasilocal Conservation Laws and Quantum Spin Transport*, Phys. Rev. Lett. **111**, 057203 (2013).
- [173] K. Sakai, and A. Klümper, *Non-dissipative Thermal Transport and Magnetothermal Effect for the Spin-1/2 Heisenberg Chain*, J. Phys. Soc. Jpn. Suppl. **74**, 196 (2005).
- [174] F. Heidrich-Meisner, A. Honecker, and W. Brenig, *Thermal transport of the XXZ chain in a magnetic field*, Phys. Rev. B **71**, 184415 (2005).
- [175] W. Kohn, *Theory of the Insulating State*, Phys. Rev. **133**, A171 (1964).
- [176] S. Furukawa, D. Ikeda, and K. Sakai, *Thermomagnetic Power and Figure of Merit for Spin-1/2 Heisenberg Chain*, J. Phys. Soc. Jpn. **74** 3241 (2005).
- [177] *Luttinger liquids: the basic concepts*, K. Schönhammer, Chapter 4.
- [178] *Highly Conducting One-dimensional Solids*, V. J. Emery, ed. by J. Devreese, Plenum, New York (1979).
- [179] *Quantum Inverse Scattering Method and Correlation Functions*. V. E. Korepin, N. M. Bogoliubov, and A. G. Izargin, Cambridge University Press (1993).
- [180] S. Sachdev, and K. Damle, *Low Temperature Spin Diffusion in the One-Dimensional Quantum  $O(3)$  Nonlinear  $\sigma$  Model*, Phys. Rev. Lett. **78**, 943 (1997); K. Damle, and S. Sachdev, *Spin dynamics and transport in gapped one-dimensional Heisenberg antiferromagnets at nonzero temperatures*, Phys. Rev. B **57**, 8307 (1998).
- [181] P. B. Wiegmann, *Exact solution of the  $O(3)$  nonlinear  $\sigma$ -model*, Phys. Lett. **152B** 209 (1985); JETP Lett. **41** 95 (1985).
- [182] S. Fujimoto, *Spin Transport Properties of the Quantum One-Dimensional Non-Linear Sigma Model: an Application to Haldane Gap Systems*, J. Phys. Soc. Jpn., **68**, 2810 (1999).

- [183] J. Sirker, R. G. Pereira, and I. Affleck, *Conservation laws, integrability, and transport in one-dimensional quantum systems*, Phys. Rev. B **83**, 035115 (2011).
- [184] A. Rosch, and N. Andrei, *Conductivity of a Clean One-Dimensional Wire*, Phys. Rev. Lett. **85** 1092 (2000).
- [185] X. Zotos, *Issues on the transport of one dimensional quantum systems* Zotos, J. Phys. Soc. Jpn **74**, Suppl. 173-180 (2005).
- [186] J. Karadamoglou and X. Zotos, *Diffusive Transport in Spin-1 Chains at High Temperatures*, Phys. Rev. Lett. **93**, 177203 (2004).
- [187] M. W. Long, P. Prelovšek, S. El Shawish, J. Karadamoglou, and X. Zotos, *Finite-temperature dynamical correlations using the microcanonical ensemble and the Lanczos algorithm*, Phys. Rev. B **68**, 235106 (2003).
- [188] F. Naef and X. Zotos, *Spin and energy correlations in the one dimensional spin-1/2 Heisenberg model*, J. Phys.: Condens. Matter **10**, L183 (1998).
- [189] X. F. Sun, W. Tao, X. M. Wang, and C. Fan, *Low-Temperature Heat Transport in the Low-Dimensional Quantum Magnet  $NiCl_2 - 4SC(NH_2)_2$* , Phys. Rev. Lett. **102**, 167202 (2009).
- [190] S. Mukhopadhyay, M. Klanjšek, M. S. Grbić, R. Blinder, H. Mayaffre, C. Berthier, M. Horvatić, M. A. Continentino, A. Paduan-Filho, B. Chiari, and O. Piovesana, *Quantum-Critical Spin Dynamics in Quasi-One-Dimensional Antiferromagnets*, Phys. Rev. Lett. **109**, 177206 (2012).
- [191] O. Chiatti, A. Sytcheva, J. Wosnitza, S. Zherlitsyn, A. A. Zvyagin, V. S. Zapf, M. Jaime, and A. Paduan-Filho, *Character of magnetic excitations in a quasi-one-dimensional antiferromagnet near the quantum critical points: Impact on magnetoacoustic properties*, Phys. Rev. B **78**, 094406 (2008).
- [192] N.M.R Peres, P. D. Sacramento, D. K. Campbell, and J. M. P. Carmelo, *Curvature of levels and charge stiffness of one-dimensional spinless fermions*, Phys. Rev. B **59**, 7382 (1999).
- [193] F. D. M. Haldane, *General Relation of Correlation Exponents and Spectral Properties of One-Dimensional Fermi Systems: Application to the Anisotropic  $S=1/2$  Heisenberg Chain*, Phys. Rev. Lett. **45**, 1358 (1980).
- [194] B. S. Shastry, and B. Sutherland, *Twisted boundary conditions and effective mass in Heisenberg-Ising and Hubbard rings*, Phys. Rev. Lett. **65**, 243 (1990).

- [195] P. Prelovšek, S. El Shawish, X. Zotos, and M. Long, *Anomalous scaling of conductivity in integrable fermion systems*, Phys. Rev. B **70**, 205129 (2004).
- [196] S. Fujimoto, and N. Kawakami, *Exact Drude weight for the one-dimensional Hubbard model at finite temperatures*, J. Phys. A **31**, 465 (1998).
- [197] A. Berkovits, and N. G. Murthy, *Operator dimensions and surface exponents for the non-linear Schrodinger model at  $T=0$* , J. Phys. A **21**, 3703 (1988).
- [198] T. Prosen, and Enej Ilievski, *Families of Quasilocal Conservation Laws and Quantum Spin Transport*, Phys. Rev. Lett. **111**, 057203 (2013).
- [199] N. M. Bogoliubov, A. G. Izergin, and V. E. Korepin, *Critical exponents for integrable models*, Nucl. Phys. B **275**, 687 (1986).
- [200] V. E. Korepin, N. M. Bogoliubov, and A. G. Izergin, *Quantum Inverse Scattering Method and Correlation Functions*, Cambridge University Press, Cambridge, 1993.
- [201] A. V. Sologubenko, K. Berggold, T. Lorenz, A. Rosch, E. Shimshoni, M. D. Phillips, and M. M. Turnbull, *Magneto-thermal transport in the  $S = 1/2$  chains of copper pyrazine Dinitrate*, Phys. Rev. Lett. **98**, 107201 (2007).
- [202] C. Hess, H. ElHaes, A. Waske, B. Büchner, C. Sekar, G. Krabbes, F. Heidrich-Meisner, and W. Brenig, *Linear Temperature Dependence of the Magnetic Heat Conductivity in  $\text{CaCu}_2\text{O}_3$* , Phys. Rev. Lett. **98**, 027201 (2007).
- [203] T. Lancaster, S. J. Blundell, M. L. Brooks, P. J. Baker, F. L. Pratt, J. L. Manson, C. P. Landee, and C. Baines, *Magnetic order in the quasi-one-dimensional spin-1/2 molecular chain compound copper pyrazine dinitrate*, Phys. Rev. B **73**, 020410(R) (2006).
- [204] K. Louis, P. Prelovšek, and X. Zotos, *Thermal conductivity of one-dimensional spin-1/2 systems coupled to phonons*, Phys. Rev. B **74**, 235118 (2006).
- [205] N. W. Ashcroft and N. D. Mermin, *Solid State Physics*, Saunders College (1976).
- [206] T. J. Seebeck, *Ueber den magnetismus der galvanische kette*, Abh. K. Akad. Wiss. Berlin, **289**, 1821; T. J. Seebeck, *Magnetische polarisation der metalle und erze durch temperatur-differenz*, Abh. K. Akad. Wiss. Berlin, **265**, 1823; T. J. Seebeck, *Ann. Phys (Leipzig)*; T. J. Seebeck, *Methode, Platinatiegel auf ihr chemische reinheit durck thermomagnetismus zu prufen*, Schweigger's J. Phys., **46**, 101 (1826).
- [207] *Recent Advances in Magnetic Insulators - From Spintronics to Microwave Applications*, Edited by M. Wu and A. Hoffmann, Solid State Physics Vol. **64**, Academic Press, (2013); *Magnonics-From Fundamentals to Applications*, Edited by

- S. O. Demokritov and A. N. Slavin, *Topics in Applied Physics* Vol. 125, Springer (2013).
- [208] E. Saitoh, M. Ueda, H. Miyajima, and G. Tatara, *Conversion of spin current into charge current at room temperature: Inverse spin-Hall effect*, *Appl. Phys. Lett.* **88** 182509 (2006); S. O. Valenzuela, and M. Tinkham, *Direct electronic measurement of the spin Hall effect*, *Nature* **442** 176 (2006).
- [209] K. Uchida, S. Takahashi, K. Harii, J. Ieda, W. Koshibae, K. Ando, S. Maekawa, E. Saitoh, *Observation of the spin Seebeck effect*, *Nature* **455** 778 (2008).
- [210] C.M. Jaworski, J. Yang, S. Mack, D.D. Awschalom, J.P. Heremans, R.C. Myers, *Observation of the spin-Seebeck effect in a ferromagnetic semiconductor*, *Nat. Mater.* **9** 898 (2010) .
- [211] C.M. Jaworski, J. Yang, S. Mack, D.D. Awschalom, R.C. Myers, J.P. Heremans, *Spin-Seebeck Effect: A Phonon Driven Spin Distribution*, *Phys. Rev. Lett.* **106** 186601 (2011).
- [212] K. Uchida, H. Adachi, T. Ota, H. Nakayama, S. Maekawa, E. Saitoh, *Observation of longitudinal spin-Seebeck effect in magnetic insulators*, *Appl. Phys. Lett.* **97** 172505 (2010).
- [213] K. Uchida, J. Xiao, H. Adachi, J. Ohe, S. Takahashi, J. Ieda, T. Ota, Y. Kajiwara, H. Umezawa, H. Kawai, G.E.W. Bauer, S. Maekawa, E. Saitoh, *Spin Seebeck insulator*, *Nat. Mater.* **9** 894 (2010).
- [214] K. Uchida, T. Nonaka, T. Ota, E. Saitoh, *Longitudinal spin-Seebeck effect in sintered polycrystalline  $(Mn, Zn)Fe_2O_4$* , *Appl. Phys. Lett.* **97** 262504 (2010).
- [215] S. D. Brechet, F. A. Vetro, E. Papa, S. E. Barnes, and J. Ansermet, *Evidence for a Magnetic Seebeck Effect*, *Phys. Rev. Lett.* **111**, 087295 (2013).
- [216] S. D. Brechet, and J. Ansermet, *Thermodynamics of a continuous medium with electric and magnetic dipoles*, *Eur. Phys. J. B* **86**, 318 (2013).
- [217] T. L. Gilbert, *A Phenomenological Theory of Damping in Ferromagnetic Materials*, *IEEE Trans. Magn.* **40**, 3443 (2004); T. L. Gilbert, *A Lagrangian formulation of the gyromagnetic equation of the magnetic field*, *Physical Review* **100**, 1243 (1955).
- [218] C. Lanczos, *An iteration method for the solution of the eigenvalue problem of linear differential and integral operators*, *J. Res. Nat. Bur. Stand.* **45**, 255 (1950).
- [219] A. Klümper, *Integrability of quantum chains: theory and applications to the spin-1/2 XXZ chain*, arxiv:cond-mat/0502431v1 (2005).

- [220] J. H. H. Perk, and C. L. Schultz, in *Nonlinear Integrable Systems Classical–Theory and Quantum Theory*, edited by M. Jimbo and T. Miwa (World Scientific, Singapore, 1983), p. 135; C. L. Schultz, *Solvable  $q$ -State Models in Lattice Statistics and Quantum Field Theory*, Phys. Rev. Lett. **46**, 629 (1981); J. H. H. Perk and C. L. Schultz, *New families of commuting transfer matrices in  $q$ -state vertex models*, Phys. Lett. A **84**, 407 (1981).
- [221] M. Takahashi, *Thermodynamics of the Heisenberg-Ising model for  $|\Delta| < 1$  in one dimension*, Phys. Lett. A **36**, 325 (1971); M. Takahashi, *One-Dimensional Heisenberg Model at Finite Temperature*, Prog. Theor. Phys. **46**(2), 401 (1971).
- [222] M. Gaudin, *Thermodynamics of the Heisenberg-Ising Ring for  $\Delta > \sim 1$* , Phys. Rev. Lett. **26**, 1301 (1971).
- [223] C. N. Yang and C. P. Yang, *Thermodynamics of a One-Dimensional System of Bosons with Repulsive Delta-Function Interaction*, J. Math. Phys. **10**, 1115 (1969).
- [224] T. Koma, *Thermal Bethe-Ansatz Method for the One-Dimensional Heisenberg Model*, Prog. Theor. Phys. **78**, 1213 (1987); M. Suzuki and M. Inoue, *The ST-Transformation Approach to Analytic Solutions of Quantum Systems. I General Formulations and Basic Limit Theorems*, Prog. Theor. Phys. **78**, 787 (1987); R. Z. Bariev, *Two-dimensional ice-type vertex model with two types of staggered sites*, Theor. and Math. Phys. **49**, 1021 (1982).
- [225] T. T. Truong and K. D. Schotte, *Quantum inverse scattering method and the diagonal-to-diagonal transfer matrix of vertex models*, Nucl. Phys. B **220**, 77 (1983); J. Suzuki, Y. Akutsu, and M. Wadati, *A New Approach to Quantum Spin Chains at Finite Temperature*, J. Phys. Soc. Japan **59**, 2667 (1990); M. Takahashi, *Correlation length and free energy of the  $S=1/2$  XYZ chain*, Phys. Rev. B **43**, 5788 (1991).
- [226] J. Suzuki, T. Nagao, and M. Wadati, *Exactly solvable models and finite size corrections*, Int. J. Mod. Phys. B **6**, 1119 (1992); A. Klümper, *Free energy and correlation lengths of quantum chains related to restricted solid-on-solid lattice models*, Ann. Physik **1**, 540 (1992); A. Klümper, Z. Physik B **91**, 507 (1993).
- [227] F. Ninio, *A simple proof of the Perron–Frobenius theorem for positive symmetric matrices*, J. Phys. A: Math. Gen. **9**, 1281 (1976).
- [228] K. Louis, and C. Gros, *Diverging magnetothermal response in the one-dimensional Heisenberg chain*, Phys. Rev. B **67** 224410 (2003).
- [229] *Numerical Recipes in Fortran 77*, W. H. Press, S. A. Teukolsky, W. T. Vetterling, and B. P. Flannery, 1986-1992 Cambridge University Press.

- [230] *Nonlinear Integral Equations for the Thermodynamics of Integrable Quantum Chains*, J. Damerau, (Doctoral dissertation) (2008) Bergischen Universität Wuppertal, <http://d-nb.info/989766209>.
- [231] T. Nishino, *Density Matrix Renormalization Group Method for 2D Classical Models*, J. Phys. Soc. Jpn. **64**, 3598 (1995).
- [232] S. White, *Density matrix formulation for quantum renormalization groups*, Phys. Rev. Lett. **69**, 2863 (1992).
- [233] H. F. Trotter, *On the product of semi-groups of operators*, Proc. Amer. Math. Soc. **10**, 545 (1959); M. Suzuki, *Generalized Trotter's formula and systematic approximants of exponential operators and inner derivations with applications to many-body problems*, Commun. Math. Phys. **51**, 183 (1976); M. Suzuki, *Transfer-matrix method and Monte Carlo simulation in quantum spin systems*, Phys. Rev. B **31**, 2957 (1985).
- [234] *Computational Many-Particle Physics* edited by H. Fehske, R. Schneider, and A. Weiß, Lect. Notes Phys. 739 (Springer, Berlin Heidelberg 2008), Chapter 22  
25 Density-Matrix Renormalization Group for Transfer Matrices: Static and Dynamical Properties of 1D Quantum Systems at Finite Temperature S. Glocke, A. Klümper, and J. Sirker.
- [235] *Transfer matrix approach to thermodynamics and dynamics of one-dimensional quantum systems*, J. Sirker (Doctoral dissertation) (2002) Universität Dortmund.
- [236] T. Giamarchi, *Quantum Physics in One Dimension*, (Clarendon Press, Oxford, 2004).
- [237] S. Eggert, and I. Affleck, *Magnetic impurities in half-integer-spin Heisenberg antiferromagnetic chains*, Phys. Rev. B **46**, 10866 (1992).
- [238] S. Lukyanov, *Low energy effective Hamiltonian for the XXZ spin chain*, Nucl. Phys. B **522**, 533 (1998).
- [239] D. C. Cabra, and P. Pujol, *Field-Theoretical Methods in Quantum Magnetism*, Lect. Notes Phys. **645** 253 (2004).
- [240] D. C. Cabra, A. Honecker, and P. Pujol, *Magnetization plateaux in N-leg spin ladders*, Phys. Rev. B **58**, 6241 (1998).
- [241] J. Caux, R. Hagemans, and J. Maillet, *Computation of dynamical correlation functions of Heisenberg chains: the gapless anisotropic regime*, J. Stat. Mech. P09003 (2005).

- [242] V. E. Korepin, *Calculation of norms of Bethe wave functions*, Commun. Math. Phys. **86** 391 (1982).

# List of Figures

|  |    |
|--|----|
| 1.1.1 The Haldane gap as a function of lattice size $L$ , as it has been calculated by the real-space renormalization-group method. The figure is taken from [21]. . . . .   | 8  |
| 1.1.2 Low-lying states for an infinite $S=1$ chain. The figure is taken from [22]. . . . .   | 8  |
| 1.1.3 The ground state of the AKLT Hamiltonian with a single valence bond connecting every neighboring pair of sites. . . . .  | 11 |
| 1.2.1 Gap of the spin-1 AF chain as a function of the single-ion easy-plane anisotropy $D$ . The Haldane phase extends from $D = 0$ up to $D = 1$ . Figure is taken from [36]. . . . .   | 13 |
| 1.2.2 The phase diagram of $S = 1$ XXZ chains with uniaxial single-ion-type anisotropy. The solid lines and symbols are the transition lines. Figure is taken from [38]. . . . .   | 13 |
| 1.3.1 Schematic representation of the ground state Eq. 1.3.3 of the $S = 1$ AFM Heisenberg chain. Yellow indicates a site with azimuthal spin $S^z = 0$ . . . . .  | 16 |
| 1.3.2 Diagram of the various phases of model (1.3.1) as a function of magnetic field. Vertical lines correspond to field-induced phase transitions located at critical fields $h_1$ and $h_2$ . Paramagnetic phase is characterized by a singlet ground state with $S_i^z = 0$ at any site, and lowest excitations have a gap. At $h_1$ level crossing occurs and the ground state becomes increasingly ferromagnetic, while gapless excitations are expected. Magnetization develops in the ground state that ranges from zero to one. At $h_2$ a second transition occurs, where the ground state is a completely ordered ferromagnetic state with a gapped excitation spectrum. . . . . | 17 |
| 1.3.3 Diagram of the spin-particle correspondence. The $S^z = 0$ state is mapped into a state with zero bosons per site, the $S^z = -1$ with one boson per site and the $S^z = 1$ with two bosons per site. Magnetic field plays the role of the chemical potential and the density of bosons corresponds to magnetization. . . . .  | 19 |
| 1.3.4 Illustration of the elementary excitations of the $S = 1$ AFM Heisenberg chain with strong easy-plane anisotropy in the paramagnetic phase. From left to right: Exciton with $S^z = +1$ and antiexciton with $S^z = -1$ . Yellow indicates a site with azimuthal spin $S^z = 0$ , red with $S^z = -1$ and blue with $S^z = +1$ . . . . .   | 21 |
| 1.3.5 Energy-momentum dispersion of the (anti)exciton dispersion for a typical coupling $\rho = 0.1$ . Orange line corresponds to the strong-coupling expansion result given in Eq.(1.3.11) and purple line to the modified semiclassical method given in Eq.(1.3.12). . . . .   | 22 |
| 1.3.6 Illustration of two-body states. From left to right: exciton-exciton pairs ( $ee$ ) with $S^z = 2$ , antiexciton-antiexciton pairs ( $\bar{e}\bar{e}$ ) with $S^z = -2$ and exciton-antiexciton pairs ( $e\bar{e}$ ) with $S^z = 0$ . . . . .  | 23 |

|   |    |
|---|----|
| 1.3.7 A schematic view of the energy–momentum dispersions of magnetic excitations in an $S = 1$ AFM Heisenberg chain with strong easy-plane anisotropy for $\rho = 0.1$ and $h = 0.4 < h_1$ . Blue lines correspond to the exciton and antiexciton mode, and purple lines indicate the boundaries of the two–body continuum. Black lines denote the bound states. The $ee$ ( $e\bar{e}$ ) bound state lies above the continuum, while the $e\bar{e}$ bound state emerges below the continuum. . . . .   | 25 |
| 1.3.8 Illustration of the ground state and magnon excitation of the $S = 1$ AFM Heisenberg chain with strong easy plane anisotropy in the fully ferromagnetic phase. . . . .  | 27 |
| 1.3.9 Illustration of the two–magnon states. The bound character of the single–ion state manifests itself in the enhanced probability that the two magnons are at the same site. Similarly for the exchange bound state, that the two spins are on neighboring sites of the chain. . . . .  | 28 |
| 1.3.10 One and two–magnons excitation energies (in units of $D$ ) for an AFM chain with a small exchange interaction $\rho = 0.1$ and a typical field $h = 2 > h_2$ . Blue line corresponds to the single magnon and purple lines indicate the boundaries of the two–magnon continuum. Black lines denote the bound states. The single–ion bound state is well separated above the continuum, while the exchange bound state branches off the continuum near the zone boundary. . . . .   | 29 |
| 1.5.1 Illustration of the low–energy subspaces (1.5.2) and (1.5.7) in the vicinity of $h_1$ and $h_2$ . . . . .   | 34 |
| 2.1.1 Left: Illustrations of the possible ESR transitions in a magnetic system. It is assumed that the uniform magnetic field is along the symmetry axis of the model, causing a splitting of the energy levels. Right: Sketch of the expected ESR absorption spectrum as a function of frequency. . . . .  | 39 |
| 2.2.1 Field dependence of the resonance lines at vanishing exchange interaction and zero temperature. Colored surface represents the ESR intensity $P \sim \omega\chi'(\omega)$ , where $\chi''(\omega)$ is given by Eq.(2.2.2). The intensity of $\omega_D$ vanishes at zero temperature, because the transition takes place between excited states. . . . .   | 43 |
| 2.2.2 A schematic view of the energy–momentum dispersions of magnetic excitations in an $S = 1$ Heisenberg chain with strong easy-plane ( $D > 0$ ) anisotropy for two typical fields $h < h_1$ (left) and $h > h_2$ (right). Note that the ESR transitions denoted by $A, B, C, E$ and $F$ occur at $k = 0$ , whereas transition $G$ occurs at $k = \pi$ . Two-particle continua are not shown for simplicity. . . . .   | 45 |
| 2.2.3 Field dependence of the ESR spectrum for an AFM chain with a small exchange interaction $\rho = 0.25$ at zero temperature. Colored surface represents the ESR intensity $P \sim \omega\chi'(\omega)$ , where $\chi''(\omega)$ is given by Eq.(2.2.6) and (2.2.8). The location of critical fields $h_1 = 0.57$ and $h_2 = 2$ is indicated by vertical dashed lines. At the zero– $T$ limit, there is an absence of intensity of the $FG$ band. The resonance lines $A, B$ , and $C$ are continued as dashed lines into the intermediate phase $h_1 < h < h_2$ to indicate the lack of analytical calculations of the low-lying excitation spectrum for such field values. . . . . | 47 |

|  |    |
|--|----|
| 2.2.4 Energy gap of the (anti)exciton dispersion at $k = \pi$ . Orange line corresponds to the theoretical value obtained within a strong-coupling expansion in the thermodynamic limit and purple line to the one obtained through a numerical exact diagonalization of a finite chain of length $N = 10$ .   | 49 |
| 2.2.5 Calculated normalized intensity $I(f, h, \tau)$ as a function of frequency $f$ for $\rho = 0.25$ at a fixed temperature $\tau = 0.2$ and four typical values of magnetic field $h$ . Field $h_m = (h_1 + h_2)/2$ denotes approximately the center of the intermediate phase. Vertical lines $A, B, C$ indicate the location of resonance frequencies $\omega_A, \omega_B$ and $\omega_C$ , while line $G$ indicates the position of the one of the boundaries of the single-ion (FG) band. | 50 |
| 2.2.6 Colored surface represents the normalized ESR intensity $I(f, h, \tau)$ calculated for a spin chain with $N = 10$ as a function of frequency $f$ and magnetic field $h$ , at fixed temperature $\tau = 0.2$ . Solid lines correspond to analytical results and are deliberately extended as dashed lines into the intermediate region $h_1 < h < h_2$ . The location of critical fields $h_1 = 0.57$ and $h_2 = 2$ is indicated by vertical dashed lines.                                  | 51 |
| 2.2.7 Same as Fig. 2.2.6 but now focusing on the low-frequency end of the intermediate phase $h_1 < h < h_2$ . Note the formation of a $V$ -like structure with rapidly decreasing intensity as one approaches the center of the intermediate phase.   | 51 |
| 2.2.8 Calculated normalized intensity $I(f, h, \tau)$ scaled with temperature $\tau$ , as a function of frequency $f$ at a fixed field $h = 2.5$ and four typical values of temperature $\tau$ . Vertical lines $C, F$ and $G$ indicate the location of the single-magnon resonance $C$ and the boundaries of the single-ion (FG) band.  | 52 |
| 2.2.9 Same as Fig. 2.2.6 but with intensity now calculated at a much higher temperature $\tau = 2$ . Note that we concentrate on the high-field region $h > h_2$ in order to emphasize the significant enhancement of intensity in the FG band (especially near the $G$ boundary).   | 53 |
| 2.2.10 Calculated normalized intensity $I(f, h, \tau)$ scaled with temperature $\tau$ , as a function of frequency $f$ at two fixed field $h = 2.5, 3$ and two typical values of temperature $\tau = 10, 100$ . In the high- $\tau$ limit, intensity scales as $\Phi(f, h)/\tau$ as a function of temperature.   | 53 |
| 2.3.1 One unit cell of the full crystal structure of $NiCl_2 - 4SC(NH_2)_2$ . The Ni magnetic spins (green) occupy a tetragonal body-centered structure with antiferromagnetic interactions between nearest neighbors.   | 55 |
| 2.3.2 Molecular structure of $NiCl_2 - 4SC(NH_2)_2$ . Figure taken from [83].  | 55 |
| 2.3.3 Temperature-field diagram of the AFM-ordered phase obtained from magnetocaloric-effect measurements (opened squares), and the magnetization data taken at $T = 16$ mK (opened circles). Closed squares and circles denote results of the quantum Monte Carlo calculations. Figure taken from [42].   | 56 |
| 2.3.4 ESR transmittance spectra for three characteristic frequencies and a wide field range up to 25 T. Note that the specific choice of frequencies is such that all possible modes appear in the figure.   | 57 |
| 2.3.5 ESR transmittance spectra in DTN taken at frequency 647 GHz for three representative temperature values. Note that experiments were performed in magnetic fields up to 25 T and thus the single-magnon ( $C$ ) resonance is not shown in this figure.  | 57 |

|        |   |    |
|--------|---|----|
| 2.3.6  | Frequency-field dependence of magnetic excitations in DTN, with a uniform magnetic field $H$ applied along the tetragonal $c$ axis. Blue symbols denote experimental data taken at $T = 1.7$ K and red symbols at $T = 4.3$ K. Note that the mode $E$ was observed in the Voight configuration [42, 79] while the rest of the modes were observed in the Voight as well as in the Faraday geometry. Solid lines correspond to results of calculations presented in Sec. 2.2.3 and are continued as dashed lines into the intermediate region $H_1 < H < H_2$ . The location of critical fields $H_1 = 2.1$ T and $H_2 = 12.6$ T is indicated by vertical dashed lines. . . . .  | 58 |
| 2.3.7  | DTN dispersion of magnetic excitations at zero field calculated along three directions in the Brillouin zone using Eq.(1.4.2) and parameters taken from Eq.(2.3.1) (dashed lines) and Eqs.(2.3.2)–(2.3.3) (solid lines). Symbols denote inelastic neutron scattering data taken from [41]. Energy is measured in degrees K. . . . .   | 59 |
| 2.3.8  | Calculated normalized intensity $I(f, h, \tau)$ scaled with temperature $\tau$ as a function of magnetic field $h$ at a fixed frequency $f = 3.5$ (649 GHz) and two values of temperature $\tau = 0.2, 5$ (1.78 K, 44.5K). Note that resonance field of line $C$ shifts from its zero-temperature limit upon increasing of temperature. . . . .   | 60 |
| 2.3.9  | The temperature dependence of resonance field $H_C$ at frequency $f = 220$ GHz. Symbols denote experimental data. . . . .   | 61 |
| 2.3.10 | Integrated intensity $I_{FG}$ at fixed frequency $f = 647$ GHz (left) and $I_C$ at fixed frequency $f = 220$ GHz (right) as a function of temperature calculated within the 1D model. Symbols denote experimental data extracted from field integration of ESR spectra. . . . .   | 62 |
| 2.4.1  | Field dependence of $T = 0$ low-lying ESR lines calculated from the effective $S = 1/2$ model diagonalized through the Bethe ansatz. Lines $B$ and $C$ are the straight lines $\omega_B$ and $\omega_C$ given in Eq. (2.4.2) for fields outside the intermediate phase but bend downwards in a nontrivial manner upon entering the intermediate phase to meet at the center and thus form a $V$ -like structure. The inset depicts the field dependence of the matrix element $ \langle m^*   \tilde{S}_{\text{tot}}^-   \tilde{\Omega} \rangle ^2$ , which is directly relevant for the calculation of the intensity of ESR modes. Vertical dotted lines indicate the location of the critical fields $h_1$ and $h_2$ calculated from Eq. (2.4.1). . . . . | 64 |
| 3.1.1  | The magnetic field dependence of magnetization $M$ at fixed temperature (a) $T/J = 0.02$ and (b) $T/J = 0.2$ . The solid line corresponds to TMRG results obtained for the $S = 1$ large- $D$ chain and the dashed line corresponds to TBA results obtained for the $S = 1/2$ $XXZ$ chain. Vertical lines indicate the location of critical fields $H_1/J = 2.28$ and $H_2/J = 8$ . Satisfactory agreement between the two models is achieved, particularly close to $H_2$ where the two curves are indistinguishable. . . . .  | 71 |
| 3.1.2  | The temperature dependence of magnetization for (a) the $S = 1$ large- $D$ model and (b) the $S = 1/2$ $XXZ$ model, for various fields. Dots indicate the position of extrema that correspond to the Luttinger liquid crossover. $T_c$ decreases toward $T = 0$ as $H$ approaches $H_1$ or $H_2$ . . . . .  | 72 |
| 3.1.3  | Magnetic phase diagram of the $S = 1$ chain with a strong easy-plane anisotropy (full points) and of the $S = 1/2$ $XXZ$ chain (open points). Symbols indicate the crossover into a finite-temperature LL regime present for both models. . . . .   | 73 |

|  |    |
|--|----|
| 3.2.1 The magnetic field dependence of specific heat $\mathcal{C}_v$ at fixed temperature $T/J = 0.1$ . The solid line corresponds to TMRG results for the $S = 1$ large- $D$ model and the dashed line corresponds to TBA results of the $S = 1/2$ XXZ model. . . . .   | 74 |
| 3.2.2 The temperature dependence of specific heat for various fields, calculated for the $S = 1$ model using TMRG. . . . .   | 75 |
| 3.2.3 The magnetic field dependence of specific heat $\mathcal{C}_v$ at fixed temperature $T/J = 0.5$ as calculated with TMRG (solid line) and FTLM (points) for the $S = 1$ model. Deviations are due to finite-size effects of FTLM data. . . . .  | 76 |
| 4.2.1 Integrated conductivity $I_{QQ}(\omega)$ for (a) $T/J = 1$ and (b) $T/J = 10$ as calculated for $L = 16$ sites and different fields $H$ . Dashed vertical line represents $\omega_0/J = 2\pi/L \sim 0.4$ . . . . .   | 86 |
| 4.2.2 Frequency dependence of $\kappa_{QQ}(\omega)$ at $H = 2$ and $T/J = 1$ . Labels $\omega_{\alpha,\beta}$ indicate the boundaries of the band with nonvanishing weight at low $T$ . . . . .  | 87 |
| 4.2.3 System size scaling of Drude weight $D_{QQ}$ at (a) $T/J = 10$ and (b) $T/J = 1$ , obtained for systems with $L = 6, \dots, 16$ sites with various magnetic fields $H/J = 2, 4, 8, 10$ . . . . .   | 88 |
| 4.2.4 Comparison of $S = 1$ integrated conductivity $I_{QQ}(\omega_0)$ at $\omega_0 = 2\pi/L$ for $L = 16$ with exact $S = 1/2$ Drude weight $\tilde{D}_{QQ}$ calculated in the thermodynamic limit for $T = 0.5, 1$ and $2$ as a function of the magnetic field $H$ . . . . .   | 90 |
| 4.3.1 Magnetic field dependence of the spin Drude weight $D_s(H)$ for four values of the anisotropy parameter $\Delta = \cos(\pi/3), \cos(\pi/4), \cos(\pi/6)$ and $\cos(\pi/10)$ . Solid lines correspond to results obtained from bosonization and dashed lines from Bethe ansatz. . . . .   | 95 |
| 4.3.2 Magnetic field dependence of spin Drude weight at (a) $T/J = 0.5$ and (b) $T/J = 1$ and various values of the anisotropy parameter $\Delta$ . The $D_s(H)$ curve seems to converge to a limiting behaviour for $\Delta \gtrsim \cos(\pi/9)$ and practically remains the same upon increase of $\Delta$ for $H/J \gtrsim 0.5$ . . . . .   | 96 |
| 4.3.3 Temperature dependence of spin Drude weight at (a) $H/J = 0.5$ where the system is at its gapless phase and (b) $H/J = H_{cr}$ where the system enters the gapped regime, and various values of the anisotropy $\Delta$ . . . . .  | 96 |
| 4.3.4 Temperature dependence of spin Drude weight at (a) $H/J = 3$ and various values of $\Delta$ (b) $\Delta = \cos(\pi/3)$ and various magnetic fields. In the high temperature limit, spin Drude weight behaves like $D_s(T) = \beta C(\Delta)$ , where $C(\Delta)$ does not depend on $H$ . . . . .  | 97 |
| 4.3.5 Coloured surface represents $D_s(H, T)$ calculated for $\Delta = \cos(\pi/3)$ as a function of temperature $T/J$ and magnetic field $H/J$ . Vertical line indicates the position of the critical field $H_{cr} = 1.5$ . . . . .  | 98 |
| 4.3.6 Magnetic field dependence of heat Drude weight at (a) $T/J = 0.5$ and (b) $T/J = 1$ and various values of the anisotropy parameter $\Delta$ . The $D_{QQ}(H)$ curve seems to converge to a limiting behaviour for $\Delta \gtrsim \cos(\pi/9)$ and practically remains the same upon increase of $\Delta$ for $H/J \gtrsim 0.25$ . The $D_{QQ}(H)$ curve exhibits a pronounced nonmonotonic behaviour as a function of $H$ . . . . . | 99 |

|        |  |     |
|--------|--|-----|
| 4.3.7  | Magnetic field dependence of $MTC$ term at (a) $T/J = 0.5$ and (b) $T/J = 1$ and various values of the anisotropy parameter $\Delta$ . The $MTC$ term is zero at $H = 0$ , but becomes finite at finite $H$ , where it develops two peaks. The first peak is located at small magnetic fields while the second and more dominant peak is centered close to the critical field at low- $T$ .  | 100 |
| 4.3.8  | Magnetic field dependence of thermal Drude weight at (a) $T/J = 0.5$ and (b) $T/J = 1$ and various values of the anisotropy parameter $\Delta$ . The $K_{th}(H)$ is a smooth function of $H$ and in the field region $H/J \gtrsim 0.25$ seems to converge to a limiting behaviour for $\Delta \gtrsim \cos(\pi/8)$ and practically remains the same upon increase of $\Delta$ .  | 100 |
| 4.3.9  | Magnetic field dependence of thermal Drude $K_{th}$ , heat Drude weight $D_{QQ}$ and the $MTC$ term scaled with temperature $T^2$ at $\Delta = \cos(\pi/8)$ and (a) $T/J = 0.1$ , (b) $T/J = 0.3$ and (c) $T/J = 0.5$ . We observe that as $T$ increases, the $MTC$ and $D_{QQ}$ term develop a peak located at the same field, so that the combination of these two terms results a $K_{th}$ curve that is a smooth function of $H$ . | 101 |
| 4.3.10 | Temperature dependence of thermal Drude $K_{th}$ , heat Drude weight $D_{QQ}$ and the $MTC$ term scaled with temperature $T^2$ at $\Delta = \cos(\pi/6)$ and (a) $H/J = 0.5$ , (b) $H/J = H_{cr}$ and (c) $H/J = 3$ .  | 102 |
| 4.3.11 | Coloured surface represents $D_{QQ}(H, T)$ calculated for $\Delta = \cos(\pi/3)$ as a function of temperature $T/J$ and magnetic field $H/J$ . Vertical line indicates the position of the critical field $H_{cr} = 1.5$ .   | 103 |
| 4.3.12 | Coloured surface represents $K_{th}(H, T)$ calculated for $\Delta = \cos(\pi/3)$ as a function of temperature $T/J$ and magnetic field $H/J$ . Vertical line indicates the position of the critical field $H_{cr} = 1.5$ .   | 104 |
| 4.3.13 | Thermal conductivity measured parallel to the chains of $Cu(C_4H_4N_2)(NO_3)_2$ as a function of magnetic field at several fixed temperatures. Figure taken from [201].  | 107 |
| 4.3.14 | (a) Heat and (b) Thermal Drude weight as a function of magnetic field at several fixed temperatures and $\Delta = \cos(\pi/8)$ . Magnetic field is measured in units of 7.81 T, given that the critical field is $H_{cr} = J(1 + \Delta) = 15$ T.  | 108 |
| 4.3.15 | Thermal Seebeck coefficient $S$ for $T/J = 0.5$ and several values of $\Delta$ as a function of $H$ . The inset depicts the magnetic field $H_s$ at which $S$ changes sign, as a function of $\Delta$ .  | 110 |
| 4.3.16 | Thermal Seebeck coefficient $S$ for $\Delta = \cos(\pi/8)$ and several values of $T$ as a function of $H$ . The inset depicts the magnetic field $H_s$ at which $S$ changes sign, as a function of $T$ .   | 110 |
| 4.3.17 | Magnetic field dependence of the figure of merit $ZT$ for $T/J = 0.5$ and several values of $\Delta$ .   | 111 |
| B.3.1  | Illustration of the Perk–Schultz model. The square lattice has width $L$ equal to the chain length and height $N$ equal to the Trotter number. Alternating rows correspond to transfer matrices $T(\tau)$ and $\bar{T}(-\tau)$ and the dashed box corresponds to the column-to-column quantum transfer matrix $T^{QTM}$ . The arrows indicate the type of local Boltzmann weights that are either $R$ or $\bar{R}$ .                   | 132 |
| B.3.2  | Integration contour $C$ surrounding the real axis.   | 135 |
| B.4.1  | Fermi velocity $u(H)$ as a function of magnetic field for four values of anisotropy parameter $\Delta$ .   | 139 |

B.4.2 Luttinger parameter  $K(H)$  as a function of magnetic field for four values  
of anisotropy parameter  $\Delta$ . . . . . 139